23 March 2012 | $10

Science

AAAS

page 1444

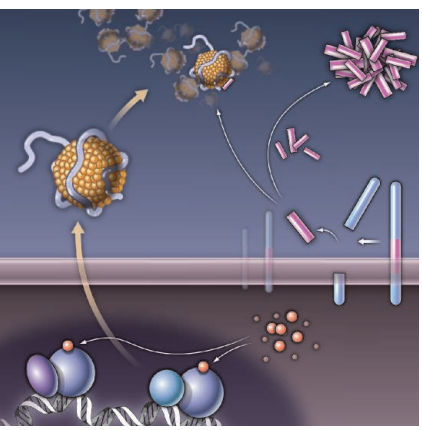

pages 1447 & 1503

COVER

Spring sun lights up signaling pathways. In plants, the UVR8 protein senses ultraviolet-B (UV-B) wavelengths in sunlight, triggering changes in growth and development, including the production of a protective chemical sunscreen. Pyramids of tryptophan rings intrinsic to UVR8 create a built-in light switch; no separate chromophore is required. Understanding how plant growth varies with changes in sunlight becomes more important as we adapt to climate change. See page 1492.

Photo: iStockphoto.com

DEPARTMENTS

Published by AAAS

BREVIA

REPORTS

CONTENTS continued >>

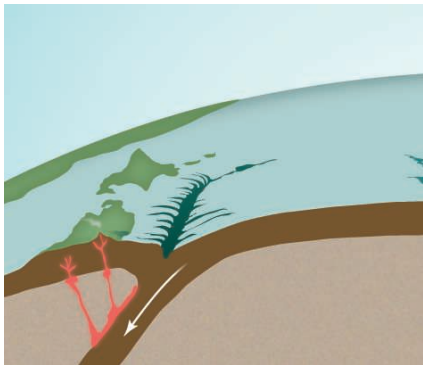

pages 1448 & 1480

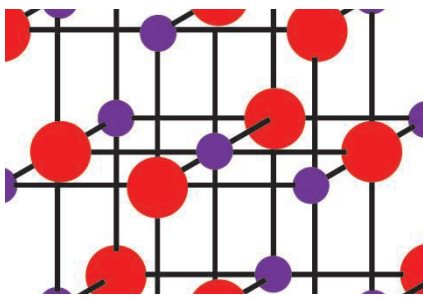

page 1464

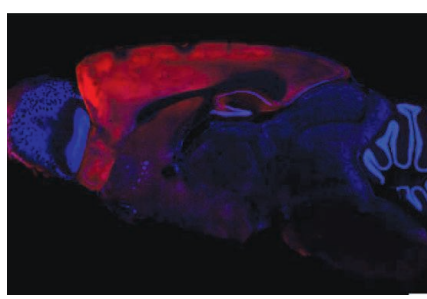

pages 1455 & 1513

Published by AAAS

SCIENCEONLINE

SCIENCEXPRESS
www.sciencexpress.org

Topography of the Northern Hemisphere of Mercury from MESSENGER Laser Altimetry
M. T. Zuber et al.
Mercury's topography indicates sustained geophysical activity for most of the planet's geological history.
10.1126/science.1218805

Gravity Field and Internal Structure of Mercury from MESSENGER
D. E. Smith et al.
Mercury's outer solid shell is denser than expected, suggesting a deep reservoir of high-density material, possibly iron-sulfur.
10.1126/science.1218809

A Lineage of Myeloid Cells Independent of Myb and Hematopoietic Stem Cells
C. Schulz et al.
In mice, a population of tissue-resident macrophages arises independently of bone marrow–derived stem cells.
10.1126/science.1219179

Microbial Exposure During Early Life Has Persistent Effects on Natural Killer T Cell Function
T. Olszak et al.
Early exposure of germ-free mice to microbes keeps later inflammation in check by modulating immune cells.
10.1126/science.1219328
>> News story p. 1428; Science *Podcast*

Enantioselective C-H Crotylation of Primary Alcohols via Hydrohydroxyalkylation of Butadiene
J. R. Zbieg et al.
A catalyst facilitates complex carbon-carbon bond formation using a bulk commodity feedstock compound.
10.1126/science.1219274

TECHNICALCOMMENTS

Comment on "Productivity Is a Poor Predictor of Plant Species Richness"
X. Pan et al.
Full text at www.sciencemag.org/cgi/content/full/335/6075/1441-a

Comment on "Productivity Is a Poor Predictor of Plant Species Richness"
J. D. Fridley et al.
Full text at www.sciencemag.org/cgi/content/full/335/6075/1441-b

Response to Comments on "Productivity Is a Poor Predictor of Plant Species Richness"
J. B. Grace et al.
Full text at www.sciencemag.org/cgi/content/full/335/6075/1441-c

SCIENCENOW
www.sciencenow.org
Highlights From Our Daily News Coverage

Were Some Neandertals Brown-Eyed Girls?
A study finds brown eyes and dusky skin in human relatives.
http://scim.ag/Neandertals_Eyes

Insight Into a Shocking Therapy for Depression
An imaging study reveals why jolting patients with electricity can lift mood.
http://scim.ag/Depression_Therapy

Enzyme 'Melts' Cancer Drug Barrier
Breaking down the tough matrix around pancreatic tumors makes chemotherapy work better in mice.
http://scim.ag/Drug_Barrier

SCIENCESIGNALING
www.sciencesignaling.org
The Signal Transduction Knowledge Environment
20 March issue: http://scim.ag/ss032012

RESEARCH ARTICLE: Cellular Inhibitors of Apoptosis Are Global Regulators of NF-κB and MAPK Activation by Members of the TNF Family of Receptors
E. Varfolomeev et al.
Signaling downstream of tumor necrosis factor family receptors hinges on the presence or absence of c-IAP proteins.

RESEARCH ARTICLE: Cannabinoids Induce Pancreatic β-Cell Death by Directly Inhibiting Insulin Receptor Activation
W. Kim et al.
Activation of cannabinoid 1 receptors prevents insulin receptors from promoting β-cell survival in the pancreas.

PERSPECTIVE: The Structure of the TLR5-Flagellin Complex—A New Mode of Pathogen Detection, Conserved Receptor Dimerization for Signaling
J. Lu and P. D. Sun
TLR5 exhibits a distinct ligand-binding mechanism compared with those used by other TLRs.

EVENTS
Plan to attend a signaling-relevant meeting; six new meetings added since February.

GLOSSARY
Find out what p70S6K, Deptor, and PRAS40 mean in the world of cell signaling.

SCIENCECAREERS
www.sciencecareers.org/career_magazine
Free Career Resources for Scientists

Experimental Error: How to Write Like a Scientist
A. Ruben
Why do we require scientists to write badly?
http://scim.ag/EE_Writing

Enhance Your Career With Leadership Skills
S. A. Holgate
It's important to begin building leadership skills even before you take on a managerial role.
http://scim.ag/EnhanceLeadership

Career Q&A: Myron Cohen
B. Mole
The infectious disease expert and recipient of *Science*'s 2011 Breakthrough of the Year award reflects on his career and keys to success.
http://scim.ag/QA_MyronCohen

SCIENCETRANSLATIONAL MEDICINE
www.sciencetranslationalmedicine.org
Integrating Medicine and Science
21 March issue: http://scim.ag/stm032112

RESEARCH ARTICLE: Characterization of Circulating Endothelial Cells in Acute Myocardial Infarction
S. Damani et al.
Features of endothelial cells in blood samples may eventually permit prediction of atherosclerotic plaque rupture events.

RESEARCH ARTICLE: Prostaglandin D_2 Inhibits Hair Growth and Is Elevated in Bald Scalp of Men with Androgenetic Alopecia
L. A. Garza et al.
Prostaglandin D_2 inhibits hair growth through its receptor, GPR44, and this pathway could serve as a new target for developing treatments for male pattern baldness.

RESEARCH ARTICLE: Restoring Methicillin-Resistant *Staphylococcus aureus* Susceptibility to β-Lactam Antibiotics
C. M. Tan et al.
Methicillin-resistant *Staphylococcus aureus* (MRSA) infection can be treated effectively by combining a β-lactam antibiotic with a drug that targets FtsZ.

PERSPECTIVE: Merging Systems Biology with Pharmacodynamics
R. Iyengar et al.
Enhanced pharmacodynamic models combine favorable features of systems biology and traditional models and may form the basis of precision medicine.

SCIENCEPODCAST
www.sciencemag.org/multimedia/podcast
Free Weekly Show
On the 23 March *Science* Podcast: entrepreneurship in the developing world, microbes and the immune response, flying robots, and more.

SCIENCEINSIDER
news.sciencemag.org/scienceinsider
Science Policy News and Analysis

SCIENCE (ISSN 0036-8075) is published weekly on Friday, except the last week in December, by the American Association for the Advancement of Science, 1200 New York Avenue, NW, Washington, DC 20005. Periodicals Mail postage (publication No. 484460) paid at Washington, DC, and additional mailing offices. Domestic individual membership and subscription (51 issues): $149 ($74 allocated to subscription). Domestic institutional subscription (51 issues): $990; Foreign postage extra: Mexico, Caribbean (surface mail) $55; other countries (air assist delivery) $85. First class, airmail, student, and emeritus rates on request. Canadian rates with GST available upon request, GST #1254 88122. Publications Mail Agreement Number 1069624. **Printed in the U.S.A.**

Change of address: Allow 4 weeks, giving old and new addresses and 8-digit account number. **Postmaster:** Send change of address to AAAS, P.O. Box 96178, Washington, DC 20090–6178. **Single-copy sales:** $10.00 current issue, $15.00 back issue prepaid includes surface postage; bulk rates on request. The identification code for *Science* is 0036-8075. *Science* is indexed in the *Reader's Guide to Periodical Literature* and in several specialized indexes.

AAAS
ADVANCING SCIENCE, SERVING SOCIETY

EDITED BY STELLA HURTLEY

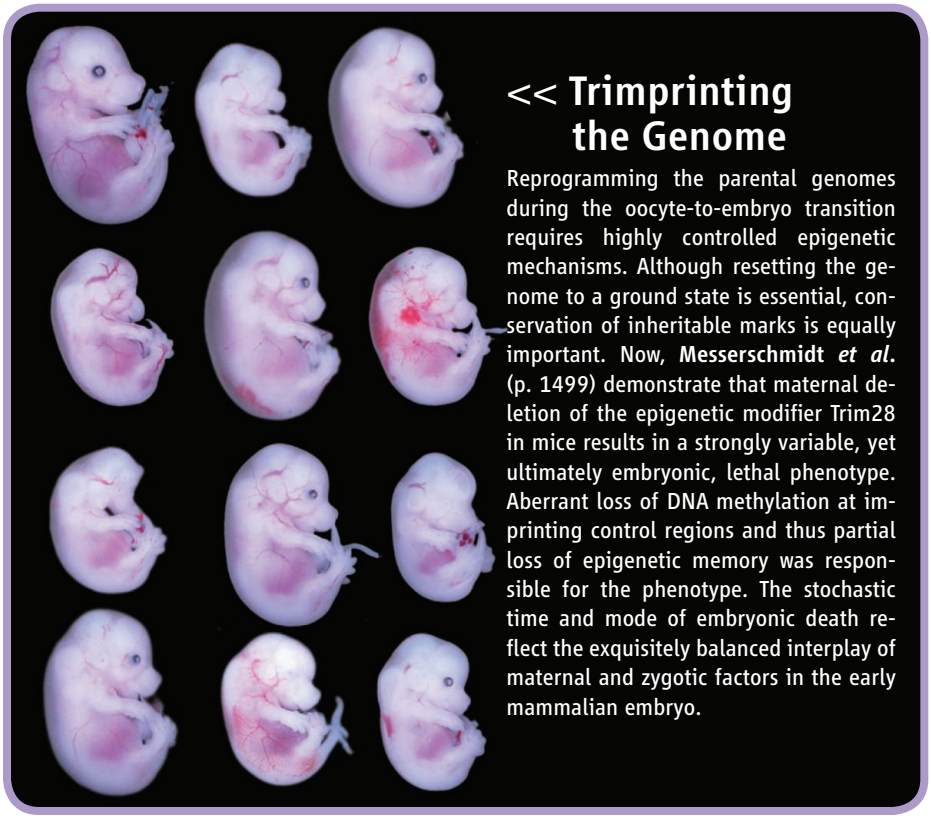

<< Trimprinting the Genome

Reprogramming the parental genomes during the oocyte-to-embryo transition requires highly controlled epigenetic mechanisms. Although resetting the genome to a ground state is essential, conservation of inheritable marks is equally important. Now, **Messerschmidt *et al.*** (p. 1499) demonstrate that maternal deletion of the epigenetic modifier Trim28 in mice results in a strongly variable, yet ultimately embryonic, lethal phenotype. Aberrant loss of DNA methylation at imprinting control regions and thus partial loss of epigenetic memory was responsible for the phenotype. The stochastic time and mode of embryonic death reflect the exquisitely balanced interplay of maternal and zygotic factors in the early mammalian embryo.

CREDITS (TOP TO BOTTOM): MESSERSCHMIDT *ET AL.*; GÖMÖRY *ET AL.*

Interacting Topological Insulator

Topological insulators (TIs) hold great promise as a setting for exotic fundamental phenomena, as well as for more practical applications such as quantum computing. This new state of matter has been discovered in materials such as Bi_2Se_3, where electrons' spins are correlated with their orbital motion, but interactions between the electrons themselves are negligible. For a TI to fulfill its potential, a material with interacting electrons is desirable. **Zhang *et al.*** (p. 1464) used density functional calculations to predict that strong interactions in actinide compounds such as AmN may drive a transition into a TI state, with a large insulating gap favorable for device applications.

Tamer Triangulations

Diazomethane is a broadly useful precursor to carbene (CH_2), which, in turn, reacts with olefins to form triangular carbon cycles known as cyclopropanes. These small rings are of fundamental interest for their strained bonds and turn up periodically in natural products, as well as in pharmaceutical and agrochemical research. Unfortunately, the flip side of diazomethane's facile reactivity is its dangerous tendency to explode—a hazard exacerbated by the need to isolate the compound after its preparation in highly basic water before it can be reacted with hydrophobic olefins. **Morandi and Carreira** (p. 1471) now show that an iron cyclopropanation catalyst can circumvent the need for the isolation step, inducing reaction of the hazardous compound in a biphasic aqueous/organic medium immediately after its generation.

Lignin to the Rescue?

The increasing demand for rechargeable batteries is putting a strain on the availability of certain key raw materials. Lignin is the second most common biopolymer and typically makes up 25% of wood. Lignin derivatives are also readily available as by-products from the pulp and paper industry. **Milczarek and Inganäs** (p. 1468) combined lignin derivatives, which are electronic insulators, with polypyrole, a conductive polymer, into an interpenetrating composite suitable for use as a cathode.

Waste Not

The organic matter in wastewater is a potentially vast and sustainable energy source; however, most wastewater treatment plants consume energy. **Cusick *et al.*** (p. 1474, published online 1 March) combined a microbial fuel cell with a reverse-electrodialysis system to boost the voltage output and the power density over a simple microbial fuel cell. The use of ammonium bicarbonate as a fuel for reverse electrodialysis while microorganisms simultaneously turn organic matter into electricity not only allows for the capturing of waste heat, but could eventually produce enough energy to offset the energy used in conventional wastewater treatment systems.

Building Blocks of Earth

Earth formed from an explosive and energetic series of collisions that accreted material over millions of years. Comparisons between rocks from Earth's interior and more primitive extraterrestrial samples can help tease apart the composition of Earth's starting material; however, discrepancies between the abundance of certain elements or their isotope ratios often obscure their origin. **Fitoussi and Bourdon** (p. 1477, published online 1 March) analyzed the silicon isotopes of a suite of rocks from chondritic meteorites and the Moon to reconcile some of the previous models. By tuning Earth accretion models to account for these Si isotope signatures, enstatite chondrites could be ruled out as the sole end-member composition for bulk Earth. Instead, a heterogeneous mixture of several types of chondritic meteorites is more likely.

Hidden from Magnetic View

An electromagnetic cloak is a device within which electromagnetic fields cannot penetrate, but, more importantly, the device itself does not disturb the electromagnetic fields surrounding it. An article placed in the cloak therefore vanishes from view, creating no shadow or reflection.

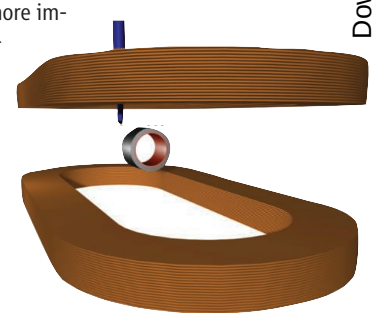

Such devices have been demonstrated, but only for a particular band of frequencies. Confirming theoretical work that predicts such cloaking should be possible down to zero frequency, **Gömöry *et al.*** (p. 1466) designed a cloak for a dc magnetic field. With a composite design of ferromagnetic and superconducting material, together with a relatively simple structure, the device could potentially find immediate application.

Continued on page 1407

Published by AAAS

Continued from page 1405

Human Impact?

Following the arrival of humans in Australia 40- to 50,000 years ago, many species of large vertebrates rapidly became extinct. By analyzing sediment cores from a site in northeastern Australia, **Rule et *al.*** (p. 1483; see the Perspective by **McGlone**) show that the extinction of the Australian megafauna caused important ecosystem shifts. Prominent among these were a shift from rainforest vegetation to sclerophyllous vegetation and a sustained increase in the incidence of fire. The cores also provide evidence of the cause of megafaunal extinction in Australia, ruling out climate and anthropogenic fire as possible causes while confirming that the extinctions closely followed human arrival. These findings show how landscapes sometimes have been fundamentally changed by the indirect effects of early humans—which underscores the impact that even prehistoric human societies had on natural systems.

Untangling the Web

Interspecific interactions link species within complex trophic and nontrophic webs (see the Perspective by **Lewinsohn and Cagnolo**). Theoretical work has suggested that certain characteristics of species, or even interactions, may predispose them to extinction from a network. **Aizen *et al.*** (p. 1486) provide empirical evidence that plant-pollinator interactions are lost nonrandomly following habitat reduction in isolated hills in the Argentine pampas. Some types of interaction were more vulnerable to disruption than others, particularly when the specialization of the interacting was high and when the interactions were infrequent. **Stouffer *et al.*** (p. 1489) applied network theory to predict the dynamical importance of species across different food webs. Characteristic three-node motifs were identified, and species were characterized according to the relative frequencies with which they occupied unique positions within the motifs. These relative frequencies and the dynamic importance of the motifs were then used to identify a species-level importance within a food web.

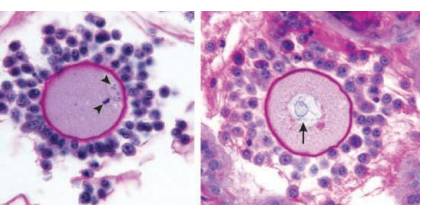

Mistress of Meiosis

Meiosis is essential for proper distribution of maternal chromosomes to eggs during oogenesis. **Su *et al.*** (p. 1496) identified a gene, meiosis arrest female 1 (*Marf1*), which is indispensable for meiosis and other oogenic processes. In mice, *Marf1* mutations resulted in meiotic arrest and an increase in nuclear DNA double-strand breaks, phenotypes linked to up-regulated levels of specific messenger RNAs (mRNA). These findings place MARF1 as a key regulator of mammalian female fertility through its integration of oocyte mRNA homeostasis, meiosis, and maintenance of genomic integrity.

Reversing Decline?

Apolipoprotein E (apoE) normally helps in the clearance of β-amyloid from the brain, a process that is compromised in Alzheimer's disease. **Cramer *et al.*** (p. 1503, published online 9 February; see the Perspective by **Strittmatter**) now show that a drug that increases apoE expression rapidly promoted soluble β-amyloid clearance in a mouse model of Alzheimer's disease. The drug also improved cognitive, social, and olfactory performance and rapidly improved neural circuit function. Similar therapeutics may potentially help to ameliorate the symptoms of Alzheimer's disease and its prodromal states.

Remembering Stressful Events

Situations surrounding emotional events are better remembered than others that accompany neutral events. However, in severe pathological states such as posttraumatic stress disorder (PTSD), exposure to threatening situations can also result in memory impairment. In this case, a hypermnesia for a salient trauma-related cue is associated with loss of memory for important aspects of the traumatic event. The memory for the core traumatic event is enhanced, but the capacity to place it in the right place and in response to the right cues is reduced. **Kaouane *et al.*** (p. 1510, published online 23 February) associated a high-intensity threat with the infusion of corticosterone in the hippocampus to induce PTSD-like memory impairments in mice. The animals became unable to identify the threat context as the right predictor of the threat, and they showed a fear response for discrete salient cues normally identified as safe. The neural activation patterns in the amygdala and hippocampal regions of these mice were similar to those observed in human PTSD.

CREDIT: SU *ET AL.*

Published by AAAS

Judy C. Miner is the president of Foothill College, Los Altos Hills, CA. E-mail: minerjudy@foothill.edu.

America's Community Colleges

IN THE 2009 AMERICAN GRADUATION INITIATIVE, PRESIDENT OBAMA ENTHUSIASTICALLY HIGHLIGHTED the importance of community colleges—publicly funded 2-year institutions—for meeting the projected growth in jobs requiring a college degree. Increasing the number of college graduates earning science- and math-related degrees depends on these institutions increasing workforce preparation through science, technology, engineering, and mathematics (STEM) education. Community colleges are accessible, affordable, diverse, and flexible, and thus well positioned to meet this need. However, the current demand for courses far exceeds capacity,* thereby calling for more government, business, and local resources to support these institutions.

More than 1100 community colleges enroll about 44% of all undergraduate students in U.S. higher education. Responding to a wide range of student readiness, community colleges offer a wealth of services, including academic and career counseling, tutoring, and developmental education. Faculty are selected, tenured, and otherwise rewarded on the basis of pedagogical expertise and classroom effectiveness; thus, the teaching function takes center stage. My own institution, Foothill College, currently has more than 16,000 students, aged 16 to over 90. The nominal time to obtain our "associate degree" is 2 years, but many students work full time, making the mean time to graduation 4 years. Community college programs enable students to either enter the workforce directly or transfer to a 4-year college to complete a bachelor's degree. Each year, Foothill College sends more than 300 students to the University of California alone, many pursuing STEM degrees. As to affordability, in 2011 community college students paid an average of $2713 a year in tuition and fees, as compared to an average of $7605 at U.S. 4-year public universities.

Community colleges can play a pivotal role in preparing underrepresented students for STEM careers. People of color will make up 45% of the working-age population in the United States by 2030, up from 18% in 1980. According to the U.S. National Academies, they "embody a vastly underused resource and a lost opportunity for meeting our nation's technology needs."† Community colleges currently enroll more than 50% of undergraduate Hispanic students and about 45% of African American and Asian undergraduates. Among those currently holding a baccalaureate or master's degree in science or engineering, 55% of Hispanics and 50% of African Americans attended a community college.‡ For immigrants pursuing the American dream, community colleges are a vital resource.They provide English language instruction, citizenship preparation, job skills, and assistance in navigating American bureaucracy. The Community College Consortium for Immigrant Education was established to highlight immigrant education issues and share models from leading institutions such as the City College of San Francisco, Miami Dade Community College, and Westchester Community College.

Online
sciencemag.org
Listen to the author podcast at http://scim.ag/ed_pod

There is a flexibility in community college curricula that allows prompt responses to workforce needs. For example, Northern Virginia Community College has developed the SySTEMic Solutions model, in collaboration with local corporations including Micron Technology and Lockheed Martin, to increase the availability of skilled workers. Part-time employment and internships serve the needs of employers while giving students opportunities for hands-on learning.

Community colleges have emerged as essential national players in the evolving landscape of STEM education, worthy of increased public and private support. To ensure a bright future, America needs to invest more in these critical resources. **– Judy C. Miner**

10.1126/science.1219366

*G. R. Boggs, *Science* **329**, 1151 (2010). †*Minority Participation: America's Science and Technology Talent at the Crossroads* (National Academies Press, Washington, DC, 2011). ‡P. Bradley, *Community College Week* (1 February 2011).

Published by AAAS

EDITORS' CHOICE

EDITED BY KRISTEN MUELLER AND JAKE YESTON

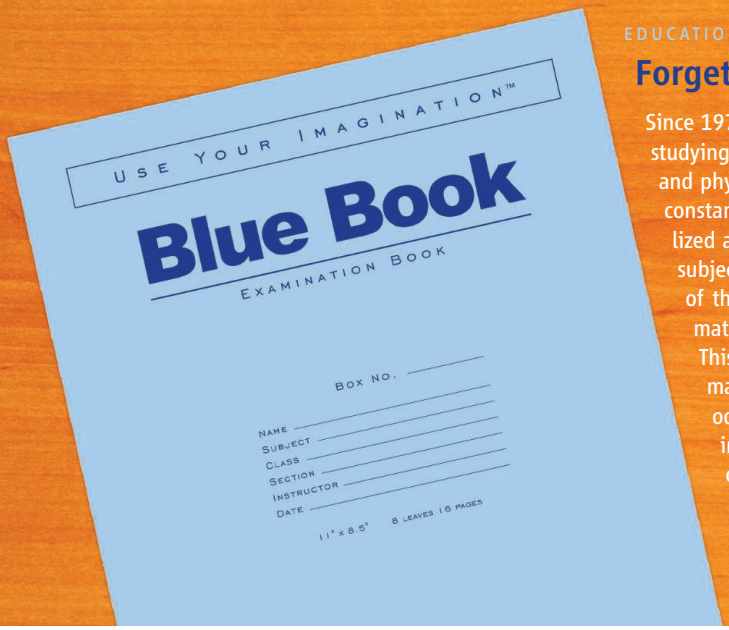

EDUCATION

Forget Me Not

Since 1975, the same Prior Knowledge Test (PKT) has been given to incoming students studying physics at the University of Bristol, UK. Designed to identify areas of math and physics that might need extra attention in the curriculum, PKT scores remained constant through 1991, decreased dramatically between 1992 and 2000, and stabilized after 2001, suggesting a clear change in the ability of students in the tested subjects. Barham argues that the decrease in scores was caused by modularization of the secondary education curriculum, which resulted in students learning the material required for each module examination and failing to retain it afterward. This highlights the dangers of a "learn and forget" approach to physics and math, and the author suggests that university faculty adapt their teaching methods to allow for the changes in preparedness of incoming students, particularly in math, where large parts of multistage calculations should not be skipped over. Furthermore, he argues for encouraging the understanding that physics and math are coherent disciplines, wherein material taught at all levels must be retained for a complete understanding of the subject. — MM

Phys. Educ. **47**, 162 (2012).

APPLIED PHYSICS

Optically Adapting

When light passes through the atmosphere, fluctuations in air density can introduce distortions in the optical wavefront, resulting in aberrations of an image. For high-end astronomical telescopes, adaptive optics in the form of deformable mirrors can be used to iron out the distortions in the wavefronts and effectively remove the twinkle from the stars. The dense arrays of microelectromechanical systems used for such adaptive optics applications tend to be costly add-ons because of the detailed fabrication and control hardware required. Bonora *et al.* introduce a simpler adaptive optics system in which the deformable mirror is controlled by light. Their deformable mirror is an electrostatic membrane mirror with one of the electrodes replaced by a photoconductive material. The electrostatic coupling and thus the extent of the local deformation can therefore be controlled by varying the intensity of light hitting the photoconductive electrode. The authors argue that such a simple design should make adaptive optics readily available for other applications. — ISO

Opt. Express **20**, 5178 (2012).

CHEMISTRY

Core Function

Numerous metalloenzymes make use of their metal centers to promote substrate oxidations in a highly controlled fashion. Chemists have long wondered in this context how much of the reactivity is intrinsic to the local coordination environment of the active site, and how much relies on the extended scaffolding of the surrounding protein. Citek *et al.* now show that in the particular case of tyrosinase—an enzyme that oxidizes phenols in the service of melanin biosynthesis—a bimetallic complex that essentially constitutes the bare active site manifests its central reactivity pattern at low temperature. In the enzyme, two copper ions, each held in place by three imidazole rings tethered to histidines, bind oxygen via a bridging side-on coordination motif. The authors find that combining a copper salt, imidazole, and oxygen in solution at −125°C in arbitrary order leads directly to assembly of a complex that mimics the active site structurally (based on x-ray, ultraviolet, and optical absorption spectroscopy) and functionally (based on the relative kinetics of reactions with phenols of varying electronic properties). The complex falls apart as the temperature goes up, suggesting that the primary role of the protein in this case is to keep the naturally reactive coordination sphere intact and inhibit destructive side reactions. — JSY

Nat. Chem. **4**, 10.1038/NCHEM.1284 (2012).

BIOTECHNOLOGY

Rare Sightings

The isolation and analysis of rare cells, particularly circulating tumor cells (CTCs), is central to advances in personalized medicine. Various approaches have been used to isolate these cells, which are typically present at concentrations of just 1 to 10 cells per milliliter of blood, below the threshold of conventional flow cytometry techniques. However, it has been difficult to ensure detection of all cells, to avoid stressing or damaging the cells during isolation, and to recover the cells after imaging. To overcome these problems, Schiro *et al.* have developed a microfluidic platform, in which blood is broken down into nanoliter aliquots that are ranked for the presence or absence of CTCs. CTCs were

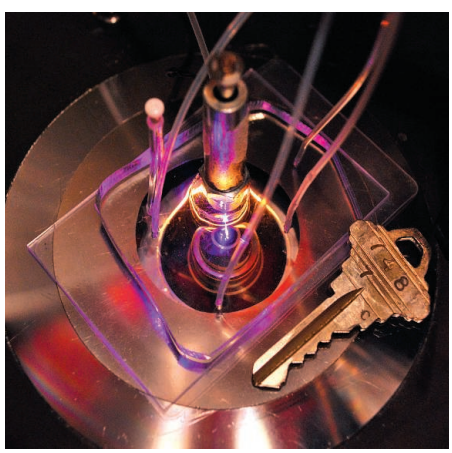

labeled with fluorescent antibodies to enable detection. Those aliquots containing CTCs were then sorted into a collection channel and filtered to enrich the rare cells within a small area. In this area, individual live CTCs could be imaged with minimal stress or could be removed for further studies. The method allows analysis of 1 ml of blood within 20 min, with no false positives and a recovery efficiency of 93%. The method should also be applicable to other rare cell types. — JFU

Angew. Chem. Int. Ed. **51**, 10.1002/anie.201108695 (2012).

CREDITS (TOP TO BOTTOM): PHOTO COURTESY OF ROARING SPRING PAPER PRODUCTS; ISTOCKPHOTO; SCHIRO *ET AL., ANGEW. CHEM. INT. ED.* **51**, 10.1002/ANIE.201108695 (2012)

Published by AAAS

AROUND THE WORLD

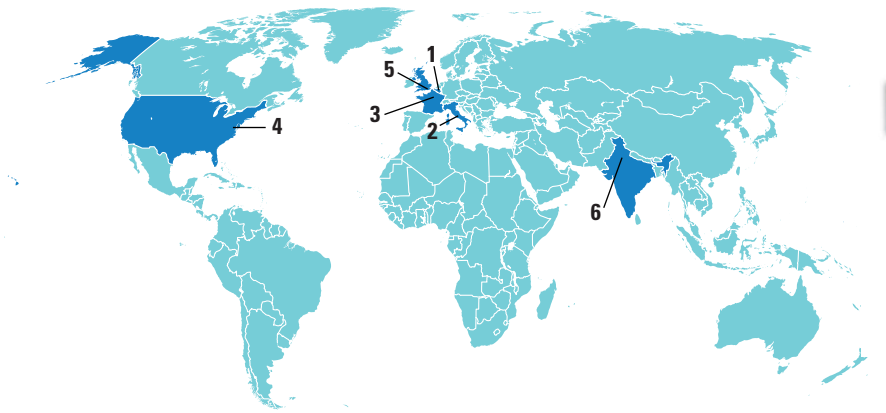

Antwerp and Brussels, Belgium **1**

Schmallenberg Vectors Found

Researchers in Belgium have identified three species of biting midges as the vectors for the newly recognized Schmallenberg virus, which has been causing birth defects in livestock across western Europe (*Science*, 2 March, p. 1028). The midges, commonly called no-see-ums, also transmit bluetongue, another livestock virus that emerged in Europe a few years ago. Scientists at the Institute of Tropical Medicine (ITG) in Antwerp and the Belgian Veterinary and Agrochemical Research Centre (VAR) analyzed

Tiny pest. A biting midge (*bottom*) is dwarfed by a mosquito.

the heads of midges caught in September and October as part of a bluetongue surveillance project. (The researchers looked only at the heads because the virus must reach the salivary glands to be transmitted.) They detected the virus in *Culicoides obsoletus*, *C. dewulfi*, and *C. pulicaris*, three of the five species that have been shown to transmit bluetongue. The researchers say they are continuing their survey.

Gran Sasso D'Italia, Italy **2**

Adieu, Superluminal Neutrinos

A new measurement appears to torpedo the claim that subatomic particles called neutrinos travel faster than light (*Science*, 30 September 2011, p. 1809).

That spectacular claim came from physicists working with a particle detector called OPERA in Italy's subterranean Gran Sasso National Laboratory. They found that neutrinos fired from CERN, the European particle physics laboratory 730 kilometers away in Switzerland, arrived 60 nanoseconds faster than they should if they traveled at light speed. However, last month the OPERA team also reported that a loose cable could have produced a spurious timing shift (*Science*, 2 March, p. 1027). Now, researchers using a detector called ICARUS, also at Gran Sasso, have timed neutrinos from CERN and found that they travel exactly at light speed, they announced last week.

"There is no superluminal effect, what else can I say?" says CERN's Carlo Rubbia, spokesperson for the ICARUS team. Antonio Ereditato of University of Bern, who is a spokesperson for the OPERA team, says "the result from ICARUS is well in line with our recent findings about a possible malfunctioning of some components of the experimental apparatus."

Paris **3**

NASA Out, Russia in for ESA's ExoMars Missions

The European Space Agency's (ESA's) governing council decided last week to press ahead with two Mars exploration missions, known as ExoMars. The agency had planned to collaborate with NASA, but NASA pulled out last month after President Barack Obama proposed steep cuts in the agency's Mars funding for next year (*Science*, 24 February, p. 900). The Russian Federal Space Agency will replace NASA in providing the launchers and a number of experiments, according to ESA spokesperson Franco Bonacina.

Up in the air? ESA's Trace Gas Orbiter remains on track, but funding is unsure.

The ExoMars project will send two missions to Mars. In 2016, the Trace Gas Orbiter will study the planet's atmosphere, and an environmental-science lander will test entry, descent, and landing technologies. The 2018 mission will carry a rover, originally expected to be delivered by NASA's Sky Crane craft, to look for signatures of past or present life.

Revamping the missions will likely push their cost beyond the €1 billion that ESA has allocated for ExoMars. The governing council instructed the agency to see whether it could shift funds from other accounts or raise the additional money from member states or from Russia.

Washington, D.C. **4**

Highway Bill Puts Brakes On Some Research

Less money, more competition. That's what archeologists and environmental scientists who want funding from a little-known transportation program will face if a massive highway bill approved by the U.S. Senate last week becomes law. The measure, passed on a 74–22 vote, authorizes the government to spend $109 billion on road and transit projects over 2 years. It includes up to $400 million per year for mainstream transportation research, but reorganizes and reduces funds for an "enhancements" program which has pumped more than $50 million into hundreds of archeology and environmental projects since 1992 (*Science*, 18 November 2011, p. 884). Overall, funding for those efforts would fall by some 20%, to about $833 million. But much of that money is expected to go to walking and biking trails, leaving less for researchers. The action now moves to the House of Representatives, which has so far failed to agree on its version of the bill.
http://scim.ag/highwaybill

London **5**

Gene Therapy Trial for Cystic Fibrosis Saved

A gene therapy trial for cystic fibrosis (CF) has found funding from the U.K. government and will go ahead this spring. The phase II trial faced cancellation last summer after the researchers conducting it ran out of funding. But the U.K. Medical Research Council (MRC) and National Institute for Health Research are now providing £3.1 million to support the trial, with an additional £1.2 million from MRC for basic research on using a viral vector to deliver the gene. CF causes a buildup of mucus in the lungs and digestive tract that leads to life-threatening health problems. Scientists will use lipids to deliver a working copy of the gene that causes CF into the lungs of 130 patients, who will inhale the therapy once a month for a year.

New Delhi **6**

India's Budget Plan Disappoints Scientists

The announcement of India's maiden mission to Mars is not cheering Indian scientists who are disappointed with proposed spending increases for research in a new government budget plan. The annual budget proposal presented to India's parliament on 16 March by Finance Minister Pranab Mukherjee calls for the operating budgets for science to rise, on average, by about 5% in 2012–2013—less than many scientists expected.

Prime Minister Manmohan Singh had raised expectations in parts of India's scientific community when he said earlier this year that India needed to double the share of its gross domestic product spent on research to 2% over the next 5 years.

But the new budget "is not good news" because the increases don't keep pace with inflation, which has been running at about 10%, says physicist Ajay K. Sood, president of the Indian Academy of Sciences in Bangalore.

"Things may look up in the coming years," says space scientist Krishnaswamy Kasturirangan, a member of a government planning commission that is preparing a 5-year science spending plan for the government. But he warns that "some serious prioritization needs to be undertaken by the scientific departments."

http://scim.ag/Indiabudget

Grazed Grasslands Biodiverse, Too

Tropical rainforests may boast the highest number of plant species per hectare, but at smaller scales, the grasslands of Eastern Europe (above) and Argentina top the biodiversity list. A mountain grassland in central Argentina packs 89 species into a single square meter and several meadows in Romania and the Czech Republic are on par, researchers reported last week in the *Journal of Vegetation Science*. The researchers scanned millions of published and unpublished plant surveys in different sized plots to learn how maximum diversity changes across different spatial scales.

Species-rich grasslands tend to be over limestone, and such grasslands were once quite common in Europe. However, changes in land-use practices have made these meadows quite rare. Unlike in rainforests, where preservation requires minimizing human activity, protecting these grasslands involves ongoing management: mowing or grazing—in some cases for centuries—is part of the secret to the grasslands' richness.

NEWSMAKERS

Three Q's


Birgeneau

Physicist **Robert Birgeneau** announced last week that he will step down at the end of 2012 after 8 years as chancellor of the University of California, Berkeley. His tenure coincided with an economic crisis in California that resulted in drastically reduced state funding for the university.

Q: How well has Berkeley managed to maintain its strength in the sciences in the face of these cuts?

The funding we get from the state to run Berkeley has dropped by more than a factor of two, but our research funding has gone up by 40%. They've almost cancelled each other out. … But I would say most importantly, as measured by Sloan Research Fellowships [which provide funding for early-career scientists] we've hired really, really talented young faculty. So I don't think I'm being Pollyannaish to say that we have largely weathered this storm.

Q: But I've heard faculty say it's getting harder to attract and retain top talent. Isn't that true?

That's one of these urban myths. In the past year our faculty retention rate is the highest it's been in the past decade.

Q: What are you most looking forward to after you step down?

Doing physics! I have a small research group and our focus has been on these new iron chalcogenide and iron pnictide superconductors, which are fascinating materials. It's an unexpectedly rich new area of solid state physics.

FINDINGS

Immune Cells Alleviate Symptoms Of Rett Syndrome in Mice

One out of about every 10,000 girls is born with Rett syndrome, a genetic condition that stunts growth, causes autism-like behavior, and impairs sleeping, breathing, and movement. A new study with mice suggests that microglia, a type of immune cell in the brain, play a role in the disorder and may >>

Published by AAAS

Random Sample

Charting the Culture of Science

Graphene research scooped the 2010 Nobel Prize in physics—but when did it really begin to take hold in the scientific community? What about carbon nanotubes? Or string theory? A team of scientists based at Harvard University has created a tool, called Bookworm, which can reveal such historical trends in the language of research with the click of a button.

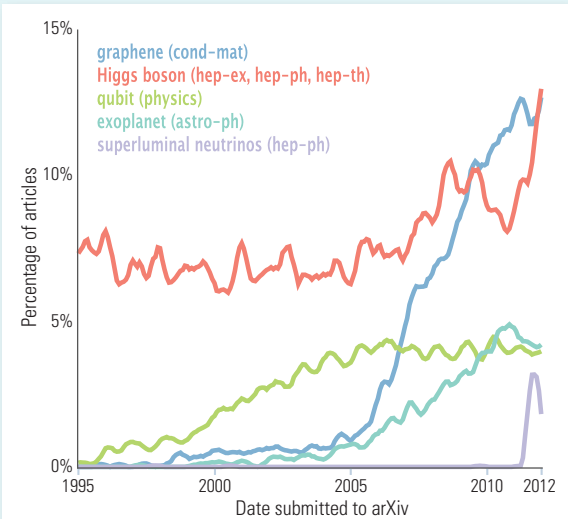

What's hot? Bookworm reveals the popularity of topics in a research area, such as high-energy physics (hep). Graphene is booming, but faster-than-light neutrinos were a flash in the pan.

The research papers were provided by Paul Ginsparg, a physicist at Cornell University, and the founder of arXiv, the online archive of preprint articles for mathematical sciences. arXiv is the perfect data set for this tool because its articles are open access, which "implies being able to treat articles as computable objects, to ingest them into a database and number-crunch them," Ginsparg says. And as of today, Bookworm for arXiv is available for anyone to use at arxiv.culturomics.org.

Converting the 7 billion words from 730,000 arXiv research articles into useable data isn't trivial. But the team is led by Jean-Baptiste Michel and Erez Lieberman Aiden, the Harvard scientists who converted millions of books digitized by Google into useable data, spawning a field called culturomics (*Science*, 17 December 2010, p. 1600). So the Bookworm team—including Benjamin Schmidt, Neva Cherniavsky, and Martin Camacho—were able to build from the same underlying code.

The term "graphene," it turns out, was no more common than the more general term "fullerene" until 2006. Then it exploded onto the scene, sucking attention away from earlier trendsetting fullerenes such as "carbon nanotubes."

BY THE NUMBERS

$10 million Price tag to name Max Planck Florida Institute's new medical research lab, part of its campaign to raise $50 million in private donations over the next 5 years.

21 km Height above Earth from which Austrian skydiver Felix Baumgartner jumped on 15 March. The jump was a test run for a 37-kilometer, record-breaking jump this summer—of interest to NASA engineers working on astronaut escape systems.

10 km^3 The volume of sand—enough to bury Manhattan by 160 meters—spewed by undersea geysers in the North Sea hundreds of thousands of years ago, according to a study reported online 19 March in *Geology*.

(PHOTO) NASA/JOHNS HOPKINS UNIVERSITY APPLIED PHYSICS LABORATORY/CARNEGIE INSTITUTION OF WASHINGTON

>>FINDINGS

even be a promising therapeutic target.

Neuroimmunologist Jonathan Kipnis of the University of Virginia in Charlottesville and colleagues transplanted bone marrow from normal mice into mice with a gene mutation like the one that causes Rett syndrome, thereby giving the mutants a new set of immune cells. Untreated mice got sick and died within a few weeks of birth, but the treated mice had far fewer symptoms and longer lifespans, the team reports in *Nature*. The benefit seems to come from repopulating the brain with genetically normal microglia, whose job it is to clean up cellular debris. Any clinical trials are a long way off, but Kipnis says the findings raise the possibility of using bone marrow transplants to treat girls with Rett syndrome. **http://scim.ag/RettSyn**

More, More Iron for Mercury

The solar system's Iron Planet is living up to its name. A team on the MESSENGER mission orbiting Mercury reports online in this week's issue of *Science* the discovery of more iron than previously thought deep in the planet's interior.

Finding unseen iron required exquisitely sensitive measurements of the motions of both the MESSENGER spacecraft and Mercury. Using measurements of the Doppler frequency shift in the spacecraft's radio signal, the team gauged the variations of gravity across Mercury. Those, in turn, depend on where mass is concentrated in the interior. The internal mass distribution also affects the tilt of Mercury's axis of rotation and the speed of rotation, which were measured using Earth-based radar.

The combined gravity and radar data point to plenty of iron in Mercury. Much of it is likely in the liquid core, now seen to extend 2030 kilometers from the center of Mercury, or 83% of the planetary radius. And the team sees another, unexpected place iron may be stored: a layer of iron sulfide that could have frozen out of the liquid core. That electrically conductive layer might explain Mercury's oddly weak magnetic field. **http://scim.ag/mercuryiron**

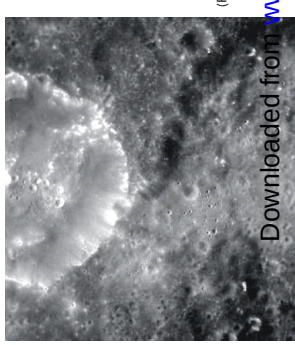

Iron inside. An iron sulfide layer may extend Mercury's iron core.

(PHOTO) NASA/JOHNS HOPKINS UNIVERSITY APPLIED PHYSICS LABORATORY/CARNEGIE INSTITUTION OF WASHINGTON; (GRAPH SOURCE) ARXIV.CULTUROMICS.ORG;

Science LIVE

Join us on **Thursday, 29 March**, at 3 p.m. EDT for a live chat on **the future of personalized genomics**. Talk with experts about how full genome scans could revolutionize personal medicine. **http://scim.ag/science-live**

Published by AAAS

Glimmers of hope. At a landmark meeting in Pyongyang, experts mulled ideas for restoring North Korea's degraded ecosystems and strengthening research at test beds like this tree nursery near the capital.

CREDITS: COURTESY OF JUNGUO LIU

ECOLOGICAL RESTORATION

Seeking Cures for North Korea's Environmental Ills

Margaret Palmer got a firsthand look earlier this month at a looming ecological catastrophe that few other scientists have witnessed. On a rare foray into North Korea's countryside, Palmer, director of the University of Maryland's National Socio-Environmental Synthesis Center in Annapolis, saw a landscape of wasted soil and rivers choked with silt from erosion. "Farmers were working the land right down to the water's edge," she says. Draped with camouflage netting, apparently reflecting their deep distrust of South Korea–U.S. military exercises, the farmers would trudge in and out of waterways with ox-pulled carts and plows; some scooped sediments from streambeds to use as fertilizer for nutrient-depleted fields. "The situation is very, very bleak," Palmer says.

Her sobering glimpse of an environment under siege came during a field trip following a landmark seminar on ecological restoration in Pyongyang, capital of the Democratic People's Republic of Korea (DPRK). The conference, held from 7 to 9 March and sponsored by the American Association for the Advancement of Science (AAAS, *Science*'s publisher), brought together 85 North Koreans and 14 experts from eight other countries to take stock of DPRK's ecological misery, share ideas on how to restore its ecosystems, and improve the country's food security. "It was an utterly remarkable, unprecedentedly real and substantive seminar," says Norman Neureiter, director of AAAS's Center for Science, Technology and Security Policy, who led the foreign delegation. In a boost for Korean scientists, it was the first international conference in DPRK since Kim Jong Un took power in December.

Bringing North Korea's environment back into equilibrium will be a monumental challenge. And securing help from outside could become more difficult, thanks to growing political tensions. Last week, DPRK announced that it will launch an Earth-observation satellite in mid-April to celebrate the 100th anniversary of the birth of the nation's founder, Kim Il Sung. Analysts assert that the launch is a long-range ballistic missile test in defiance of U.N. sanctions. If DPRK follows through, nascent attempts to cooperate in science and other areas could be derailed for months, a U.S. State Department official told *Science*.

There's no question North Korea needs assistance. Wide swaths of land have been stripped of biomass, says Richard Hardiman, an expert on natural resource management at the Hebrew University of Jerusalem, who attended the Pyongyang meeting. "The soil in many areas is in terrible shape. There's no organic matter left."

Many other aspects of DPRK's ecological degradation are sketchy, with the true extent of deforestation and pollution loads unknown. "It was impossible for us to get solid data on the scale and magnitude of the problem," says Palle Madsen, a forest ecologist at the University of Copenhagen. Although many North Korean presentations were enlightening, "a lot of analysis was superficial and qualitative," says Junguo Liu, a water specialist at Beijing Forestry University. Informal interactions between the two sides were also limited and chaperoned, frustrating attempts by the visiting researchers to get a more nuanced picture and size up North Korean expertise.

Despite the obstacles, several of the foreign meeting participants are forging ahead with proposals for restoration projects within North Korea. DPRK scientists, they say, are eager to collaborate. At the seminar, organized by Pyongyang International Information Center on New Technology and Economy in Pyongyang and the Environmental Education Media Project in Beijing, "we met some very smart people with an absolute thirst for knowledge," Hardiman says.

North Koreans "recognize that they need to do something, and do something fast," says ecologist Keith Bowers, president of Biohabitats Inc., an ecological restoration company in North America. "They also recognize that their livelihoods and food security depend on a restored and healthy ecosystem."

DPRK's environment took a turn for the worse during the Korean War, which ignited forest fires that razed vast tracts of its hilly terrain. After the 1953 armistice, some

areas, including picturesque Mount Myohyang Biodiversity Reserve, were restored through tree-planting campaigns. By 1990, about two-thirds of the country was forested. Conditions deteriorated again in the 1990s, when the nation endured droughts and floods that ruined harvests, touching off a famine that claimed hundreds of thousands of lives. Desperate villagers scoured forests for food and fuel. During this "arduous time," forest cover shrank from 8.2 million to 7.6 million hectares, says Hoh Man Suk, director of the Institute of Forest Management in Pyongyang. (Satellite imagery suggests steeper losses in recent years.) At the seminar, Ryo Song Hwa, director of the Central Forestry Design Institute in Pyongyang, described how the deforestation led to desertification, spawned pest outbreaks, and perturbed local climate regimes.

As a step toward healing its ecosystems, DPRK passed a law in 2009 to protect specific areas. Since then it has set aside more than 2 million hectares as forest reserves. North Korean scientists also recently completed a national land-cover assessment that will serve as a basis for a 10-year forestation plan. Bowers estimates that reforesting half the country could run as high as $46 billion; for comparison, restoring the Florida Everglades will cost roughly $30 billion.

Another top priority for DPRK is agroforestry. Varieties slated for mass planting include Japanese larch for timber, chestnuts, which tolerate poor soils, and aronia shrubs, which help stabilize slopes and yield chokeberries, a source of vitamin C. Other cash crops include pine nuts, mushrooms, and medicinal plants such as ginseng. Model farms now also practice intercropping: planting maize and wheat between stands of acacia grown for firewood. "They had a fine understanding of agroforestry principles and were applying them in a very understanding way to reforestation," says Peter Raven, president emeritus of Missouri Botanical Garden in St. Louis.

Bedeviling these efforts are poor survival rates of seedlings in the wild and pervasive problems with soil fertility and water, Korean scientists say. The struggle highlights the urgent need to regenerate North Korea's ailing soil. "They've virtually destroyed it by overfertilization with urea," Hardiman says. The simplest remedy, he says, would be to apply gypsum or calcium carbonate to neutralize pH, then spread compost to infuse nutrients. "They could probably deal with the problem in 10 or 15 years," he says.

A major concern in DPRK is how to adapt to climate change. In one of the more sophisticated Korean presentations, Pak Chol Jun of the Ministry of Land and Environmental Protection described how he modeled shifts in vegetation patterns on the Korean Peninsula in response to climate change over the next 30 to 50 years. Pak's analysis relied on satellite data he gathered as a visiting researcher at the China Agro-Forestry Research Institution in Kunming. Anticipating that climate change could take a toll on native species, DPRK intends to create a seed bank for endangered or threatened varieties.

More training stints like Pak's in China and similar capacity-building exercises should not be too difficult to arrange, says Liu, who has offered to host visitors and postdocs in his lab. Bowers is exploring the idea of setting up an Asia chapter of the Society for Ecological Restoration in China that could bring DPRK into the organization. And in Pyongyang, Palmer extended an offer from the University of Maryland to invite DPRK scientists to environmental workshops at her center. She is keen to help North Korean scientists come to grips with their watersheds. At present, she says, "there appears to be little or no focus on restoration of aquatic ecosystems despite extensive degradation of the water resources." Obtaining U.S. visas for DPRK scientists, however, may depend on the fallout from next month's rocket launch.

Even if the mood on the Korean Peninsula becomes more strained, participants say they are willing to give collaboration a shot. "There was a greater openness and potential for fruitful engagement than I had expected," says Dennis Ojima, an ecologist at Colorado State University, Fort Collins. The International Union for Conservation of Nature has expressed an interest in helping to catalyze landscape-restoration initiatives. One possible donor is the European Union, which has allotted €6 million for capacity building in food security and other areas in DPRK this year. If the offered money and scientific expertise aren't thwarted by politics, there may still be hope for the countryside. As Bowers notes, the nation has "the ability to mobilize thousands, possibly millions, of people to the task at hand." **–RICHARD STONE**

NEWSMAKER INTERVIEW: CHRISTOF KOCH

A Vision of How Mouse Vision Can Reveal Consciousness' Secrets

Neuroscientist Christof Koch has spent the past 25 years puzzling over the mystery of consciousness. A professor at the California Institute of Technology since 1986, Koch worked closely for years with the legendary Francis Crick exploring how the firing of neurons gives rise to perception, the experience of pleasure and pain, and other manifestations of conscious awareness.


Koch

CREDIT: KEVIN CRUFF

Now, Koch is embarking on a seemingly narrower quest at the Allen Institute for Brain Science in Seattle, Washington, one that he nonetheless hopes will ultimately lead to breakthroughs in understanding consciousness. It's a 10-year project to study vision in the mouse brain, funded by a new donation of $300 million from Microsoft co-founder Paul Allen, who had already financed the start-up of the 9-year-old Seattle research center. The project, announced publicly this week, will build on the institute's foundational work of mapping the mouse brain to study how information flows through the mouse cortex—a millimeter-thick layer of tissue—to help the animal see. Although the specific goal is to understand vision, Koch says he and his colleagues also intend to study higher-order brain functions such as perception, decision-making, and conscious awareness.

And that, for Koch, is the bridge between the project and his grander desire to understand consciousness. "Once neuroscientists know the basic mechanisms [of vision] in the mouse, they may start to understand more complex forms of perceptions in other animals, including humans," Koch and fellow neuroscientist R. Clay Reid write in a *Nature* commentary this week about the initiative.

Koch, who now spends three-quarters of his time at the Seattle institute as the project's chief scientific officer, has over the past several months described the project's vision to neuroscience labs around the country. The

goal is to hire a few hundred neuroscientists, anatomists, geneticists—as well as technicians and engineers—to work toward the initiative's goal. Koch says some scientists have told him that Allen's resources would be better spent on a diverse portfolio of projects. But he argues that the focused and systematic approach his team will undertake is a necessary experiment for neuroscience today. *Science* spoke to Koch recently about his initiation into consciousness studies, his hopes for the new venture, and how the two intersect. His remarks have been edited for clarity and brevity. **–YUDHIJIT BHATTACHARJEE**

Q: When did you seriously begin pondering consciousness as a scientific problem?

C.K.: It was sometime in the late '80s, when I had gone to the Marine Biological Laboratory at Woods Hole to teach. It was late at night and I had this terrible toothache, and it really pounded away. I was taking aspirin, and it didn't really do all that much. Then for the first time, it really hit me—this is so bizarre. How can it hurt? The infected tooth causes electrical activity in my brain that is ultimately caused by ions sloshing around in my brain—well, they are sloshing around all the time—but this actually hurts. It's really like magic; it's like a brass lamp, you rub it and a genie emerges. How do you go from the objective facts of the brain, from this biophysics, to feelings of pain or pleasure, of seeing red or feeling angry? When I described the incident to Francis Crick, he laughed and said, "Well, that's the heart of the mind-body problem."

Q: Is understanding consciousness merely a question of finding its neural correlates?

C.K.: The analogy Francis always made is with replication in DNA. You can speculate all you want about how life manages to copy my characteristics and pass them on to my children, but once you see the double structure of the DNA, it becomes all clear to you. The hope was that if we understand better which parts of the brain are involved in generating any one conscious sensation, we're much closer to understanding the heart of this problem, which is how you go from physics or from biophysics to feelings. Toward the last couple of years of Francis's life, he also evolved the realization that we need more. It's necessary but not sufficient just to track down the neural correlates. We need something more fundamental. We need a theory that tells under what condition can any system—whether it's going to be an iPhone or a mouse or my brain or a brain of a fetus—what is it about these different systems that makes them conscious or not conscious?

Q: Consciousness as we understand it is such a human experience. Can you hope to understand it using mice?

C.K.: My frustration with human work is that in humans, for ethical reasons, you're very limited in what you can do. You can see but you can't touch! In particular, it's very difficult to move from correlation to causation. For example, consider an experiment based on the magic trick of making a coin disappear in front of you. The magician manipulates your attention and your expectation so that you look at something and yet don't see it. Is any one part of your visual cortex active when you see a coin held before you? It turns out that as long as [your] eyelids are open, the retinal neurons will register whatever photons fall onto it. But later on if I don't attend [to the coin], then the light from the coin might fall on my retina, but I won't see it. Now you find another area in the brain that is active when you see the object but not when you don't pay attention to it. Once you discover this, you would then like to turn this area on or off to see whether it is necessary for generating the conscious perception of that coin. But in humans, I can't test that.

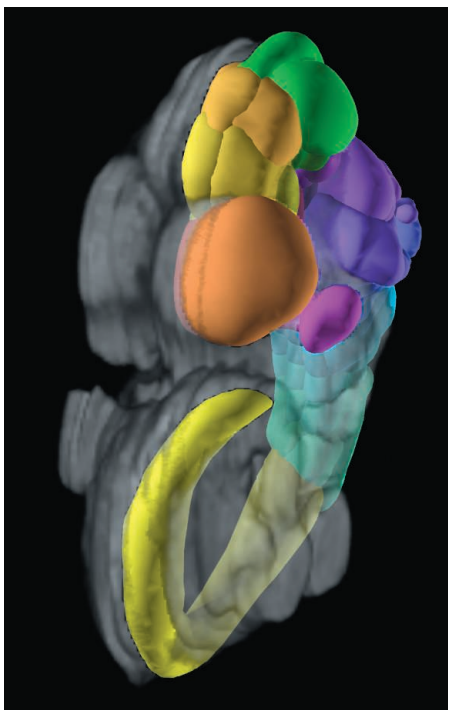

In depth. Christof Koch says a detailed study of the visual cortex in the mouse brain (above) could lead to fundamental neuroscience advances.

Q: Can you test it in mice?

C.K.: In principle, yes. I can stimulate the same neurons that I think are involved. The nerve cells are really the atoms that underlie consciousness and memory, not brain regions. In a mouse, I can then go to the individual nerve cells and with beams of blue or yellow laser light, I can activate them and inactivate them, turning them on or off with millisecond precision. So I can move from just saying, "Well, these neurons correlate with perception" to saying "No, they're actually causally involved."

Q: What specific experiments do you have in mind for the project? Are they limited to vision?

C.K.: The main emphasis is trying to understand cortex, in particular, visual cortex since I'm a visual scientist. One of the things that I'm personally going to focus on is, of course, visual consciousness, but overall we're going to pursue more tangible aspects of cortical processing such as visual behavior. How can the mouse, for example, discriminate between a rightward- and a leftward-leaning grating? There's a beautiful experiment done by David Tank, a colleague at Princeton, where you have a mouse running on a track ball. They like that, and their [visual] cortex really lights up. And then when researchers put the mouse in this video game—using the trackball to navigate a Doom-like video game with a labyrinth—the mouse has to remember to turn left to get the cheese or it has to turn right to get the cheese. This is a nontrivial behavior, and it seems to involve cortex. It's a general goal [of the project] to try to understand how does the mouse see, how does the mouse discriminate, how does the mouse make decisions.

Q: Mice don't see very well, so why study their visual system?

C.K.: They are nocturnal creatures, that's correct. They can probably survive much better being blind than we could. However, 10% of their cortex is visual. They have a perfectly functioning retina. They have perfectly decent visual behaviors. This is something that the community has realized only over the last 5 to 6 years—that mice have a pretty decent visual system and you can train them to do visual discrimination tasks.

Q: You worked with Crick right until his death in 2004. Are you channeling his consciousness in taking up this project?

C.K.: He was like a father to me. This is certainly a project he would have very much liked because he always argued that we need to do things systematically; we can't just do them haphazardly. We're very focused on what are the essential steps that you need in order to understand a particular system.

CREDIT: IMAGE COURTESY OF THE ALLEN INSTITUTE FOR BRAIN SCIENCE

Published by AAAS

IMMUNOLOGY

Gut Microbes Keep Rare Immune Cells in Line

To the dismay of mothers everywhere, the idea that exposure to microbes can be good for us—by tuning up our immune systems and preventing overreactions like asthma and autoimmune diseases—is catching. Now, a new study of this provocative notion, known as the hygiene hypothesis, suggests that microbes furnish some of their benefits in an unexpected way. Researchers have found that the typical intestinal bacteria in mice rein in a rare type of immune cell, curtailing asthma and colitis in the rodents.

Scientists following the long-running discussion over the hygiene hypothesis give the new work, reported online in *Science* (http://scim.ag/Olszak) this week, top marks. "It's one of the most rigorous and mechanistic studies in this area I've seen in a long time," says microbiologist Sarkis Mazmanian of the California Institute of Technology in Pasadena. The authors "establish the immune underpinnings for something we've observed for decades but haven't understood," says clinical immunologist Everett Meyer of Stanford University Medical School in California.

Proposed more than 20 years ago, the hygiene hypothesis posits a downside to modern society's battle against microbes. To function properly, the hypothesis suggests, the immune system needs to tangle with microbes when we are young. Without these early interactions, our immune cells later in life become more likely to promote inflammatory and autoimmune conditions such as allergies, asthma, inflammatory bowel disease, and multiple sclerosis. The hygiene hypothesis offers an explanation for observations such as the lower frequency of asthma and allergies among children who grow up on farms: They presumably encounter more germs, or a greater diversity, than do city kids. "There is a general consensus that microbial exposure protects against the development of a variety of different allergic and autoimmune diseases," says Anthony Horner, a pediatric immunologist at the University of California, San Diego.

The tricky question is how microorganisms provide this protection. Mice lacking their normal microbial partners and pathogens have now given mucosal immunologist Richard Blumberg of Brigham and Women's Hospital in Boston and colleagues an insight. Throughout their lives, these so-called germ-free mice dwell in sterile cages and nibble sterile food, so they don't acquire the intestinal denizens of normal rodents. Compared with their microbe-populated relatives, such mice are more susceptible to colitis, a type of intestinal inflammation, and to asthma, the researchers have now found. In their lungs and intestines, the germ-free mice also harbor an unusually large number of invariant natural killer T (iNKT) cells. These immune cells trigger inflammation after sensing certain microbes or particular molecules, called antigens, made by the body.

> *"It provides yet another example of how microbial exposure is important to immune development."*
>
> —ANTHONY HORNER, UNIVERSITY OF CALIFORNIA, SAN DIEGO

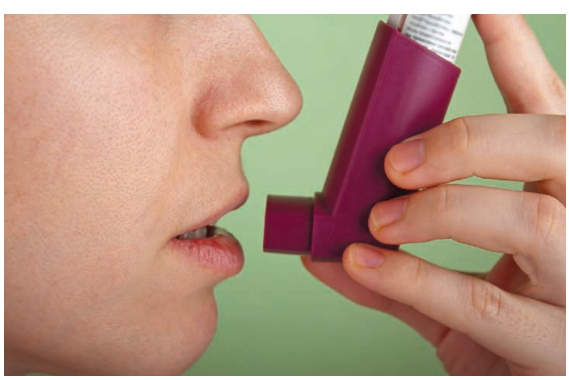

Gut reaction? A new study suggests how the lack of intestinal bacteria early in life can prompt asthma and other immune disorders.

The new study suggests that these cells are crucial for conditions such as colitis and asthma. Blumberg and colleagues discovered that genetically altered mice that lack iNKT cells are not prone to colitis, even if they are raised germ-free in sterile surroundings. Furthermore, Blumberg's team could largely prevent the development of colitis in germ-free mice that do have iNKT cells if they treated the rodents with an antibody that blocks the cells' ability to detect antigens.

By shifting germ-free mice to cages containing ordinary rodents that teem with bacteria, the researchers demonstrated the importance of early microbe exposure for the distribution of iNKT cells. Transferred mice quickly pick up intestinal bacteria from their cage mates. Moving adult germ-free animals did not reduce the number of iNKT cells in the colon. However, when the researchers rehoused pregnant germ-free mice, ensuring that their offspring would be immersed in bacteria from birth, the pups had fewer iNKT cells in the colon, even after they grew up, Blumberg and colleagues discovered. "It became clear from the study that [iNKT cells are] sensing the composition of the microbial community in the gut and responding to it," Blumberg says.

Researchers would expect that the presence of intestinal microbes would lead to more immune cells, Horner says, but the study reveals the opposite. "It's a very intriguing observation that goes against conventional wisdom of the relationship between immune system development and microbial exposure." The mechanism behind this relationship may involve an immune system signal called CXCL16. Blumberg and colleagues showed that the absence of intestinal microbes triggers a surge in production of CXCL16, which may stimulate the accumulation of iNKT cells.

"There are no germ-free humans," says immunologist Mitchell Kronenberg of the La Jolla Institute for Allergy and Immunology in California. And because we all have gut microbes, the next step for this research, he says, is to sort out which specific intestinal inhabitants benefit the immune system. Kronenberg says that today's powerful DNA-sequencing technologies might be able to identify species that would otherwise be difficult to detect. Blumberg adds that he and his colleagues are already trying to pin down the particular microbes that provide protection.

Although the results won't immediately help people with asthma breathe easier, the work does point researchers toward possible new treatments, Mazmanian says. Inflammation involves so many cells and signaling molecules that it's difficult to know which to try to block, he says. By revealing a cell that promotes inflammatory conditions, the study gives researchers a bull's-eye to aim for, he says.

In addition, researchers say, the findings offer further evidence that despite what our mothers told us, cleanliness sometimes leads to sickness. "It provides yet another example of how microbial exposure is important to immune development," Horner says.

–MITCH LESLIE

CREDIT: FOTOSEARCH

Published by AAAS

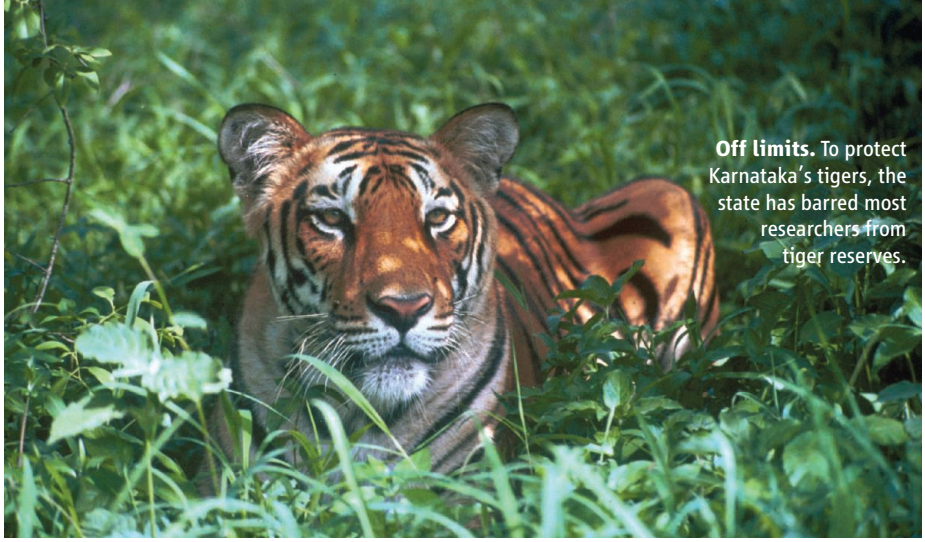

Off limits. To protect Karnataka's tigers, the state has barred most researchers from tiger reserves.

INDIA

Field Biologists Cry Foul Over Ban

NEW DELHI—For 12 years, Anindya Sinha would camp out for weeks at a stretch in Bandipur Tiger Reserve to observe social behavior in a troop of bonnet macaques, and how the monkeys responded to tourism pressure. Then in 2010, his study came to a grinding halt. The wildlife manager in southern India's Karnataka State revoked Sinha's research permit, citing a need to safeguard the reserve's tigers. It was a "high-handed, unjustified decision," charges Sinha, a primate biologist at the National Institute of Advanced Studies in Bangalore. After failing to land a new permit, Sinha recently abandoned his study.

Sinha is not the only researcher to have suffered such a setback. In the past 2 years, Karnataka has canceled 40 out of 42 research permits in four tiger reserves, shutting down studies on topics as diverse as Asian elephant migrations and long-term ecological plots. Karnataka's chief wildlife warden, Brij Kishore Singh, says he has barred most researchers from reserves to protect Karnataka's estimated 300 tigers, perhaps the single largest population in the wild. The reserves, he says, are "critical tiger habitats, and all human activity inside them has to be curtailed as it causes disturbance to the conservation of the tiger." A 2011 census found that India's adult tiger population in the wild has declined to about 1700, half the number it was a decade ago.

Scientists are perplexed by Singh's belief that their research is not compatible with conservation. After months of fruitless efforts to persuade Singh to reverse these decisions, they are now going public with their complaints. "I see no logic in this denial of permissions. Tiger reserves are natural scientific laboratories," says Raman Sukumar, an ecologist at the Indian Institute of Science in Bangalore. Last year, Singh revoked Sukumar's permit to monitor tree growth patterns and forest hydrology in Bandipur. Keeping researchers out of tiger reserves undermines conservation, Sukumar contends, because most reserve managers welcome sound scientific advice.

So far, only Karnataka has cracked down on research. But Singh is lobbying other state wildlife wardens to follow his lead and ban research in all of India's 39 tiger reserves. Singh's "discriminatory and arbitrary decisions," asserts M. D. Madhusudan, a wildlife ecologist at the Nature Conservation Foundation in Mysore, could "ruin field research in India."

At the center of the dispute is the 40-year-old Indian Wildlife Protection Act, which grants states the authority to regulate research in tiger reserves. The act spells out that tiger poachers would be subject to at least 1 year of imprisonment and a $100 fine. Those penalties were not an effective deterrent. In 2004, poachers wiped out the last of 15 tigers in Sariska Tiger Reserve in Rajasthan State. Decrying that extirpation, India's Parliament amended the wildlife act in 2006, declaring tiger reserves "inviolate" and giving the act more teeth by hiking up the punishment for poaching to a minimum of 3 years in prison and a $1000 fine.

Proper credentials. K. Ullas Karanth deplores the "draconian restriction."

Singh has invoked the "inviolate" clause in justifying his decision to bar most scientists from Karnataka's tiger reserves: Bandipur, Nagarahole, Bhadra, and Dandeli-Anshi. He points out that India's tiger habitat has shrunk to just 8% of the area it occupied a century ago, leaving tigers "very vulnerable." Singh says he doesn't want the tigers under his protection to suffer the same fate as those in Sariska.

One scientist whom Singh tolerates in his reserves is K. Ullas Karanth, a tiger biologist with the Wildlife Conservation Society in Bangalore. "Ullas is the real grandfather of all tiger research in India," Singh explains, noting that Karanth also has the endorsement of the central government to study tigers throughout India. Karanth told *Science* that research in reserves should be regulated. "I know of some cases where totally unqualified people have been given research permits to indulge in commercial photography, filmmaking, or even to release potentially dangerous hand-reared big cats," he says. But he also feels that Karnataka's policy has gone too far, calling Singh's ban of researchers en masse "a draconian restriction on the access to our natural laboratories."

Field biologists have appealed to the federal government for help. "India is still a nation of walls, fences, and permits. The policy on research permissions needs to be unambiguous and clear," says Gladwin Joseph, director of the Ashoka Trust for Research in Ecology and the Environment in Bangalore. He worries that if other states follow Karnataka's lead, then talented students may steer clear of ecology—jeopardizing the field.

Officials in New Delhi may be powerless to intervene. "Banning research is not logical, and this is a foolish move," says Rajesh Gopal, member secretary of the National Tiger Conservation Authority here, which oversees tiger protection efforts on behalf of the federal government. In a letter to Singh last year, Gopal argued that forbidding research based on the inviolate clause "was not a fair interpretation of the law." Gopal concedes that there is little he can do, because authority to grant research permits rests with the states.

Gopal plans to write a letter to the Karnataka government insisting that "the spirit of the Wildlife Protection Act is to facilitate research, not ban it." Singh intends to hold his ground. "I have to save the tiger from extinction, come what may," he says.

–PALLAVA BAGLA

CREDITS: (TOP PHOTO) PALLAVA BAGLA; (BOTTOM PHOTO) KALYAN VARMA; PROVIDED BY ULLAS KARANTH

Published by AAAS

A Flapping of Wings

Robot aircraft that fly like birds could open new vistas in maneuverability, if designers can forge a productive partnership with an old enemy: unsteady airflow

IN A PACKED CONFERENCE HALL, ALL HEADS are turned to the back of the room. The crowd murmurs as a man holds up what appears to be an enormous model of a seagull with its wings outspread. The murmurs turn to silence as the wings begin to flap while it is still in his hands. Then he tosses the bird forward … and with a whir, SmartBird takes off.

The silence gives way to applause as the bird flies once, twice, three times around the auditorium. As it glides gently to a stop, the audience gets up and gives the SmartBird a standing ovation.

More than a million and a half people have watched the video of the SmartBird flying at a TED conference in Edinburgh last July (www.youtube.com/watch?v=Fg_JcKSHUtQ). And humans aren't the only ones who find it fascinating. At the same conference, when the robotic bird flew outside, it attracted a mob of curious seagulls.

The last couple of years have been an exciting time for flapping-wing flight. Another bird-inspired aircraft, AeroVironment's Nano Hummingbird, made *Time* magazine's list of 50 top inventions of 2011 (see sidebar, p. 1433). The U.S. Defense Advanced Research Projects Agency and the Office of Naval Research are investing millions of dollars into so-called micro air vehicles and nano air vehicles, as well as basic research into how birds and insects fly.

A century after the Wright brothers, fixed-wing aircraft have become a routine part of our lives. But flapping-wing aircraft, or ornithopters, still elicit wonder. "Just about everybody gets a thrill out of seeing one for the first time," says Nathan Chronister of Rochester, New York, who makes ornithopter kits for hobbyists and science classes. At the same time, there is serious science behind them. While the theory of airflow over a flapping wing remains surprisingly rudimentary, humans are now making significant progress in understanding how to fly, control, and land flapping-wing aircraft. "It's not the physics that's the problem any more," says aeronautical engineer Wolfgang Send, the mastermind behind the SmartBird.

Online
sciencemag.org
Podcast interview (http://scim.ag/Indo_6075) with author Dana Mackenzie.

Soaring. Festo's SmartBird (*above*) and MIT's Phoenix (*left*) take robotic flapping-wing flight to new levels of grace and precision.

Dead end?

From Daedalus to Leonardo da Vinci to Otto Lilienthal, early researches in flying emphasized flapping wings. And in fact, the first rubber band–powered ornithopters, made by Alphonse Pénaud of France in 1874, predate motorized airplanes.

But after the spectacular success of the Wright brothers, flapping-wing aircraft began to look like a technological dead end. Even now, engineers struggle to understand unsteady airflow. "Not even for the simplest flight situation—level cruising flight—is there a global, recognized theory, accepted by most of the experts," says Horst Räbiger of Nuremberg, Germany, a longtime designer of ornithopters. Yet, he adds, such a theory "is necessary to compute the best lift distribution along the wingspan at every moment, the ideal airfoils at every part of the wing, the best flapping angle, best flapping frequency, and much more. Today, every expert makes his own theory—including myself."

Ornithopters also languished for many years because they are simply inferior in aerodynamic efficiency to airplanes with rotating parts. "The limit of efficiency for a flapping vehicle for thrust is when it works

CREDITS (TOP TO BOTTOM): FESTO AG & CO. KG; JASON DORFMAN

Published by AAAS

like a bad propeller," says Russ Tedrake of the Massachusetts Institute of Technology (MIT) in Cambridge. "For hovering, the limit of efficiency is when it approximates a helicopter."

However, ornithopters should have advantages, too, if they can be built. They should be more maneuverable than fixed-wing airplanes. They should be able both to hover and to fly forward. Birds, for example, direct their thrust upward at takeoff, flapping their wings at a large angle of attack to push themselves away from the ground. In cruising flight, the wings level out to a lower angle of attack, minimizing drag, generating mostly lift and only a little bit of thrust. When landing, the bird shifts once again to a high angle of attack with a lot of drag, in effect stalling out and using the wings as a parachute.

Conventional airplanes are not so versatile. Pilots scrupulously avoid high angles of attack and stalling. To take off or land, an airplane must reproduce the conditions of cruising flight—high speed, low drag, low angle of attack—while on the ground. That is why airplanes require runways. Such aerodynamic conservatism was understandable in the early days of flight, when unsteady airflow killed many pilots. (Lilienthal, for instance, died in 1896 when his glider stalled and crashed.) But does it still make sense today, with modern sensors and computers and mathematical techniques at our disposal—and no pilot on board?

An elegant pitch

For decades, a few dedicated amateurs and professional engineers doing research in their spare time have kept the dream of flapping-wing flight alive. One of the latter is Send, an engineer at the German Aerospace Center (DLR) until his retirement in 2009.

For years, Send has believed that the secret of high-efficiency flapping flight lies in two papers written by Theodore Theodorsen, an American engineer, and Hans Georg Küssner, a German engineer, in 1935 and 1936. Both researchers viewed flapping as something to be avoided; they were trying to understand the causes of wing flutter in fixed-wing aircraft. They found mathematical solutions for the aerodynamic forces on a flat plate that is both plunging (going up and down) and pitching (making an S-shaped motion). In bird flight, these two motions are typically about 90° out of phase, with the wing's highest angle of attack occurring when its vertical displacement is zero, and zero angle of attack when the vertical displacement is highest.

Send viewed the phase lag as a control variable, together with the ratio of plunging amplitude to pitching amplitude (see figure, below). In the two-dimensional control space, flutter occurs spontaneously in the blue region on the middle graph of the figure, where the pitching amplitude is low and the phase lag is about 90°. In this region, the pitching motion extracts energy from the airflow. Most ornithopters employ this "passive torsion," allowing the wind to twist the wing to a positive or negative angle of attack. However, the aerodynamic efficiency (a measure of thrust as a percentage of power input) is quite low, only about 30%, as the bottom graph shows.

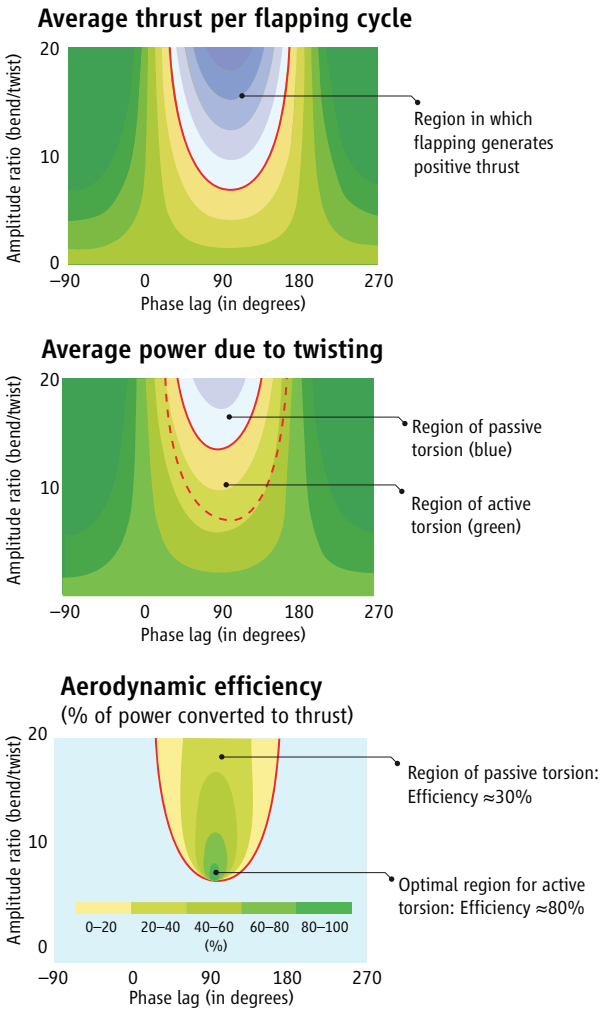

Sweet spot. SmartBird's designers used active torsion to maximize aerodynamic efficiency. In passive torsion (*center*), a wing twists spontaneously and extracts energy from the airflow. In active torsion, the twisting must be powered by a motor. Maximum efficiency occurs in a tiny "sweet spot" (*bottom*). Figures show theoretical solutions for a flat rectangular wing; SmartBird achieved an efficiency of 80% to 90%.

Send realized that a wing with active torsion—using engine power to twist the wing more than the airflow can do alone—could achieve an aerodynamic efficiency of more than 80%. This efficiency occurs in the small green "sweet spot" seen in the bottom graph, the region in which the SmartBird operates.

Send's views were definitely not shared by most of the ornithopter community. Some ornithopters had used active torsion—and Lilienthal had observed the twisting and the phase lag in bird wings in 1889—but other researchers did not consider it essential. "My colleagues were interested, but there was a skepticism," Send says.

In 2007, Send approached Festo, a company based in Esslingen, Germany, with the idea of turning his ideas on active torsion into a model. Festo was the perfect fit: a company that specializes in biomimetic automation. Its projects include robotic grippers inspired by an elephant's trunk and a helium-filled dirigible inspired by stingrays. "I asked them who is the aerodynamicist, who is the theoretician?" Send says. "They just smiled and looked at me." After retiring from DLR in October 2009, Send plunged into the SmartBird project at Festo.

Although Festo did not have an aerodynamicist, it did have a gifted team. "It was a very rare occasion in which the right people came together, from my point of view," Send says. "Rainer Mugrauer is the Mozart of model builders. Without him, that bird wouldn't ever have been constructed." Agalya Jebens and Kristof Jebens provided the control systems, which are essential to maintain the delicately controlled choreography of plunging and pitching that keeps the SmartBird in the aerodynamic "sweet spot."

SmartBird made its debut at the Hanover Trade Fair in 2011, where it drew more than 20,000 visitors. Festo will not reveal the cost of the project, which Send estimates at a couple of hundred thousand euros. At present, Festo is not planning to sell SmartBirds and denies any interest in military applications. Theme parks might be a possibility, Tedrake says: "Disney would like Tinker Bell to fly in and land on a lantern in Disney World."

CREDIT: WOLFGANG SEND

Published by AAAS

SmartBird's technological tour de force has impressed other ornithopterists. "I was totally gobsmacked by the SmartBird," says James DeLaurier of the University of Toronto in Canada, who built the first engine-powered remote-controlled ornithopter to be recognized by the Fédération Aéronautique Internationale, in 1991. Räbiger is more cautious. "Before the SmartBird, I didn't believe that a servo-controlled wing twisting is a good solution," he wrote in an e-mail. "[Now] I must say: maybe."

Finding a perch

There is one thing SmartBird still doesn't do: land like a bird. It needs conventional landing gear or a human to catch it in midair. If Tinker Bell wants to land on a lantern, she will have to learn how to perch. That is the focus of one of the newest entrants into birdlike flight, Tedrake's Robot Locomotion Group at MIT.

In 2010, Tedrake and his former Ph.D. student, Rick Cory, built a fixed-wing glider, launched from a crossbow, that successfully perched on a wire 19 times out of 20. They have also built an ornithopter, called the Phoenix, that can perch successfully but is not yet as well understood theoretically.

Surprisingly, the most novel technology behind the perching glider was mathematics. When approaching a perch, the glider has a desired trajectory that will bring it into a safe landing. However, the complicated aerodynamics of stall mean that it cannot necessarily hit that trajectory, and the actual trajectory cannot be fully anticipated. A beautiful mathematical device called Lyapunov functions makes it possible to identify a "funnel" within which all trajectories are attracted toward the desired one.

Engineers have long known of Lyapunov functions, but they were hard to compute. The difficulty lies in proving that a polynomial function of several variables is always positive, except at one point (the center of the "funnel"). That changed in 2000, when Pablo Parrilo of the California Institute of Technology (now at MIT) showed that such functions can be found in a quick and dirty way by limiting the search to functions that are sums of squares: numbers that are never negative.

With the sums of squares method, "we are now in the game of applying Lyapunov functions to very complicated tasks," Tedrake says. "A planned trajectory can be much more aggressive, like a bird darting through the forest."

Unlike Festo, Tedrake's group has funding from the military; he is the principal investigator for a $7.5 million multi-university research initiative from the Office of Naval Research. The military interest is understandable. Maneuverable robotic birds would be useful for flying through cluttered urban settings; robots that resemble actual birds would be easier to disguise; and perching robots could conduct surveillance for long periods of time without consuming energy. Such applications, however, are far off; the research is still in a conceptual phase.

"Our goal is to do maneuvering flight," Tedrake says. "I'm not convinced that flapping wings are strictly necessary for that, but it's plausible. It's just a primal belief on my part that there will be a benefit from flapping. There are some remarkable success stories in nature where they're doing things that airplanes cannot do." **–DANA MACKENZIE**

Dana Mackenzie is a writer in Santa Cruz, California.

CREDIT: AEROVIRONMENT INC.—NANO AIR VEHICLE

It's a Bird, It's a Plane, It's a … Spy?

If a hummingbird follows you into a building, one of two things is going on: Either your perfume is too strong, or the world's smallest spy plane is on your tail.

In 2011, AeroVironment, a company founded by Paul MacCready, the inventor of the first human-powered aircraft to cross the English Channel, unveiled a new crewless aircraft called the Nano Hummingbird. With a wingspan of 17 centimeters and a weight of 19 grams, the robot is hefty for a hummingbird. But it can hover in place and fly in any direction (including backward) as fast as 18 kilometers per hour. It can fly through doorways and can be steered by a remote pilot using only video from an onboard camera. All of these abilities met or exceeded the targets for a second-generation "nano air vehicle" funded by the U.S. Defense Advanced Research Projects Agency.

Very small ornithopters like the Nano Hummingbird face different challenges from their larger kin. As a flyer (animal or robot) gets smaller, flying becomes more and more like swimming. Less energy goes to lift and more to thrust. Instead of sculpted airfoils, the wings can and should be simple, rapidly beating membranes. For robots, miniaturization of components and power sources may impose the biggest constraint. A real hummingbird can fly across the Gulf of Mexico without stopping; the Nano Hummingbird can go for only 11 minutes.

The main role envisioned for nano air vehicles is military surveillance and reconnaissance. But they could also be used for civilian applications such as search and rescue or environmental monitoring (for example, inside crippled nuclear reactors).

Miniature devices have taken off in the past decade. In 2002, the dragonfly-like Mentor, developed at the University of Toronto and SRI International, demonstrated hovering flight. In 2006, the (also dragonfly-like) DelFly, developed at Delft University of Technology in the Netherlands, added a camera and forward flight; later versions have shrunk to 3 grams and a 10-centimeter wingspan.

Nano flyers aren't yet fit for duty, however. "The Hummingbird is way cool. I can't say enough good things about it," says Ephrahim Garcia, an engineer at Cornell University. "But it has a limited endurance." Eleven minutes is not much time to scan a building for insurgents or earthquake survivors. Even so, Garcia adds, "Everything doesn't have to be practical. We can learn a lot about flow-structure interaction from these devices." **–D.M.**

Published by AAAS

COMPUTATIONAL SCIENCE

Materials Scientists Look To a Data-Intensive Future

Supercomputing power now makes it possible to compute the properties of thousands of crystalline materials in a flash and is expected to guide experimentalists where to search for the next best things

When the Human Genome Project took off in 1990, the goal of sequencing all 3 billion letters of DNA in a single genome in 15 years seemed a daunting task. Ultimately, advances in sequencing technology enabled researchers to finish the job early. And today, sequencing a single genome seems almost pedestrian. Now, materials researchers are hoping that a similar technological ramp-up will help them with a Herculean task of their own: using computers to calculate the properties of a near-infinite variety of solids to identify potential materials breakthroughs for batteries, solar cells, and many other applications.

Today's machines aren't yet able to simulate all types of materials. But a broad array of researchers think steady progress in technology has now made supercomputers powerful and available enough to make the task worth starting. "The scaling of computing is really making this possible," says Gerbrand Ceder, a materials scientist at the Massachusetts Institute of Technology in Cambridge. Richard Hennig, a computational materials scientist at Cornell University, agrees. "The field of computational materials science is ready to take off," Hennig says.

To help launch it, the White House announced a new federal effort last June to promote the use of high-performance computing to cut in half the time it takes to develop a new material. Known as the Materials Genome Initiative (MGI), the effort promised $100 million just this year to drastically accelerate materials discovery—particularly in alternative energy, a field heavily reliant on advanced materials. Since then, the U.S. National Science Foundation and the Department of Energy have offered new grant programs in the area.

That initiative has been a long time coming. Ever since the advent of quantum mechanics in the early 1900s, researchers have known how to compute the properties of materials, at least in principle. But most materials are so complex that only those with a small number of electrons can be fully analyzed at the quantum level. Because complex materials have on the order of 10^{23} electrons, researchers must rely heavily on computational methods to simplify the problem. These include a wide array of simulation techniques, such as density functional theory calculations, finite-element methods, and Monte Carlo simulations, all of which have been around for years. "The codes really haven't changed that much" over time, says Sadasivan Shankar, a computational materials scientist at Intel Corp. in Santa Clara, California. "What has changed is that the computing power has caught up."

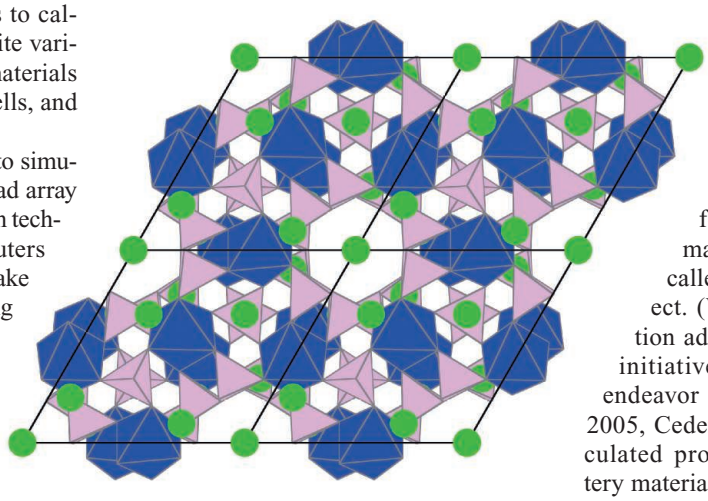

Power structure. Lithium atoms (green) nestle into a simulated crystalline framework of a vanadium-containing cathode material for advanced batteries.

CREDIT: A. JAIN *ET AL.*, *JOURNAL OF THE ELECTROCHEMICAL SOCIETY* **159** (5 MARCH 2012) © THE ELECTROCHEMICAL SOCIETY

That progress opens the door to computing the properties of a wide range of materials that once seemed unapproachably complex, Ceder says. Among the more tractable problems should be advances in catalysts, battery materials, and thermoelectrics, which convert heat to electricity. And it should be relatively straightforward to make a big impact on materials research quickly. There are between 50,000 and 100,000 known inorganic compounds, depending on whose figures you believe, Ceder notes. Crunching the numbers for all the computable properties of a single known material—including crystal structure, stability, and ionic mobility—takes the equivalent of 1 day for a standard computer chip, known as a CPU. To make that calculation for all known inorganic compounds would take between 2 million and 3 million CPU hours, a job one of the most advanced supercomputers could carry out in just a day and a half. Examining a good swath of the possible unknown materials out there would still take only half a billion CPU hours, Ceder predicts. "That's just a drop in the bucket" of the computing power available, Ceder says. "We don't know most things about most materials," he says. "Materials scientists are hungry for this data."

Computational methods won't supplant experimental synthesis of materials anytime soon, Ceder and others say. Rather, they will help focus the work. Because it's not possible to synthesize and test all possible combinations of elements, computational tools are helping experimentalists decide where best to try cooking up new winners.

That's the strategy Ceder has taken in his own lab. In 2005, Ceder's team launched an effort to compute the performance of would-be battery materials, which at the time they called the Materials Genome Project. (When the Obama Administration adopted the moniker for its own initiative, Ceder's team renamed its endeavor the Materials Project.) Since 2005, Ceder and his colleagues have calculated properties of some 80,000 battery materials and have gone on to conduct experimental screens of about 25,000. In the 5 March *Journal of the Electrochemical Society*, Ceder and his colleagues reported that a computational analysis suggested that a new vanadium-containing cathode material for lithium ion batteries had the potential to beat the energy-storage capacity of conventional lithium iron phosphate cathodes by some 10%. The material had never been synthesized before. But in February at the meeting of the American Physical Society (APS) in Boston, Ceder reported that since submitting its theoretical paper, his group had synthesized the compound and found that it behaved as predicted. In other efforts, Ceder and colleagues at Lawrence Berkley National Laboratory in California are pushing ahead with similar studies to find improved thermoelectrics and catalysts designed to absorb sunlight and use the energy to split water into oxygen and hydrogen, a potential fuel source.

Ceder's group isn't alone. In February, at

Published by AAAS

the APS meeting, Shankar reported that computational efforts are becoming increasingly important in making advances in computer chips. Over the past 50 years, chip designers have doubled the number of transistors on chips roughly every 18 months, largely by improving chip-patterning techniques to make devices with ever-smaller features. Today, Intel sells chips with 22-nanometer features and will begin manufacturing chips with 14-nanometer features in 2013. With each new generation of chips, Intel and other companies are being forced to incorporate novel materials that can perform as better conductors, insulators, and semiconductors even with less material present. That trend has put pressure on company researchers to test ever more alternatives. And one path forward has been to improve computational efforts to narrow down the range of options. In the latest generation of chip design, for example, Intel researchers used advanced computer models to simulate and predict the behavior of different materials that wound up being incorporated into the chips, Shankar says (see graph below).

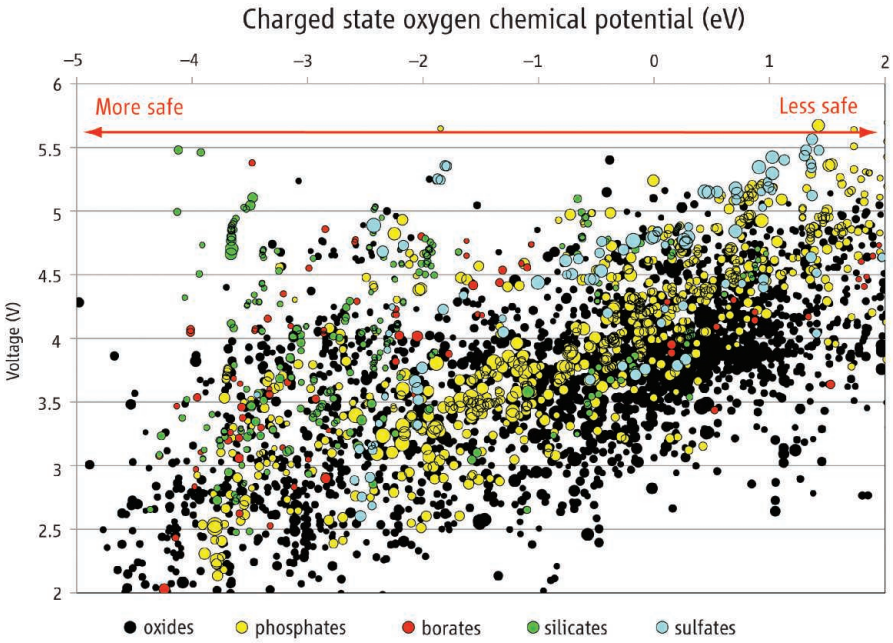

Let's compare. Computed properties of hundreds of battery materials reveal that all chemical families of battery materials (different colors) tend to be less safe when operating at higher voltages. But within each family some recipes are safer than others.

Despite such progress, Ceder and others say, some materials challenges remain out of computational reach—at least so far. Ceder cites the effort to develop new lightweight, high-strength metal alloys for construction materials. The success of such materials depends in part on the crystalline structure of their components and in part on their resistance to fracturing and ductile stretching—properties governed by how they behave on length scales far larger than the repeating unit of their crystalline lattice. "We don't even know the underlying science of how these materials work," Ceder says. In battery materials, by contrast, about 75% of the performance of the material comes from properties that can be computed. "So you've got to pick the right problems," Ceder says.

That said, Krishna Rajan, a computational materials scientist at Iowa State University, Ames, says he and colleagues are making headway on challenging materials problems with an approach that doesn't require them to compute properties from first principles. The researchers have created a machine-learning program for designing novel materials as different as piezoelectric and drug-delivery compounds. Piezoelectrics are materials that change shape when zapped with an electric field, or generate electricity when squeezed. They can also be complex, so Rajan decided that improving them would pose a good challenge for his machine-learning approach.

Rajan's team started by creating a database of 30 observations on different materials variables, such as bond distances between pairs of atoms in a would-be crystal, and the affinity of different elements for electrons. They proposed a list of relationships between different variables. They then used a program called a genetic algorithm to search through the relationships, see how well they predicted the properties of known piezoelectrics, and then refine its search to zero in on which ones are most important. They used the results to create a set of design rules that predicts a piezoelectric material's properties and then turned their computational effort loose to scan the universe of unknown compounds for better piezoelectrics.

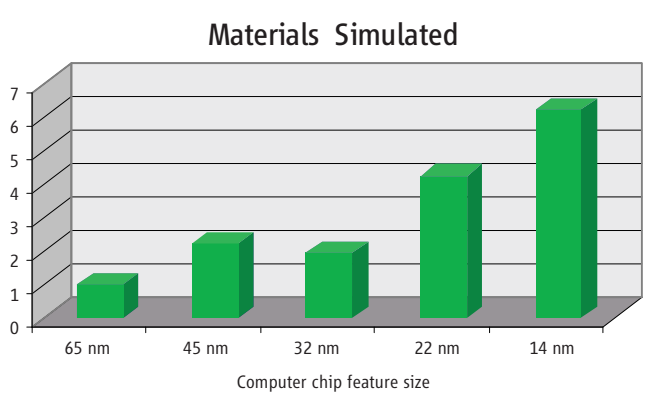

Rising tide. As feature size in computer chips has shrunk in each generation, chips have incorporated increasing numbers of materials that had initially been simulated.

Using this approach, Rajan and his colleagues reported in the 2 March 2011 issue of the *Proceedings of the Royal Society A* that they had discovered a pair of novel piezoelectrics that outperform others at high temperatures. And in the 16 December 2011 issue of *Nature*, Rajan's team reported using much the same strategy to design novel polymers capable of encapsulating a vaccine against *Yersinia pestis*, the bacterium that causes bubonic plague, and helping to activate the vaccine inside the body. "There is no theory for what makes a good vaccine-delivery material," Rajan says. But with the informatics approach, "we were able to tease that out." Rajan says he's now adapting the same tools to predict the toxicity of nanomaterials.

Rajan readily acknowledges that computational materials design still has its limits. Understanding complex interfaces between multiple materials, for example, remains a major challenge. "If we try to compute everything, it's still too complex," Rajan says. However, he adds, "there are enough discoveries to be made that it will make a huge impact."

–ROBERT F. SERVICE

SOURCE CREDITS (TOP TO BOTTOM): G. CEDER/MIT; S. SHANKAR/INTEL CORP.

Published by AAAS

Ohio rumblings. Wastewater injected at this site in Youngstown triggered jolting earthquakes that prompted injection-well shutdowns and strong new regulations.

SEISMOLOGY

Learning How to NOT Make Your Own Earthquakes

As fluid injections into Earth's crust trigger quakes across the United States, researchers are scrambling to learn how to avoid making more

First off, fracking for shale gas is not touching off the earthquakes that have been shaking previously calm regions from New Mexico to Texas, Ohio, and Arkansas. But all manner of other energy-related fluid injection—including deep disposal of fracking's wastewater, extraction of methane from coal beds, and creation of geothermal energy reservoirs—is in fact setting off disturbingly strong earthquakes. These quakes of magnitude 4 and 5 are rattling the local populace, shutting down clean energy projects, and prompting a flurry of new regulations.

Researchers have known for decades that deep, high-pressure fluid injection can trigger sizable earthquakes. But after a decades-long lull in triggered quake studies, researchers are playing catch-up with the latest round of temblors. When triggered quakes surprise drillers, "we're often in the position of ambulance chasers without the necessary science done ahead of time," says seismologist William Ellsworth of the U.S. Geological Survey (USGS) in Menlo Park, California.

As researchers link cause and effect in recent cases of triggered seismicity, they are beginning to see a way ahead: learn as you go. Thorough preinjection studies followed by close monitoring of cautiously increasing injection offer to lower, although never eliminate, the risk of triggering intolerable earthquakes.

An injection too deep

"I'm told it feels like a car running into the house," says Stephen Horton, speaking of the magnitude-4 triggered quakes he saw coming a couple of years ago in north-central Arkansas. In the current March/April issue of *Seismological Research Letters*, the University of Memphis seismologist recounts his learn-as-you-go experience with injection-triggered quakes strong enough to seriously shake up the locals.

Quake masters. USGS geophysicists Barry Raleigh (*left*) and Jack Healy are poised to open a valve and pressurize deep rock to turn on earthquakes. They could also turn them off in this 1970s study.

Fracking for natural gas, formally known as hydraulic fracturing, had come to Arkansas around 2009. Not that a seismologist in Memphis would have noticed. Injecting water into gas-bearing shale at high pressures does break the rock to free the gas—that's the point, after all. But the resulting tiny quakes rarely get above magnitude 0 (the logarithmic scale includes negative numbers), never mind to the magnitude-3 quakes that people might feel.

But shale gas drillers need to dispose of the millions of liters of water laden with natural brines and added chemicals that flow back up after a shale gas well has been fracked (*Science*, 25 June 2010, p. 1624). Injecting fracking wastewater into deep rock is a common solution, so starting in April 2009, 1- to 3-kilometer-deep disposal wells were sunk in the vicinity of Guy (population 706) and Greenbrier (population 4706), Arkansas.

That's when Horton and Scott Ausbrooks of the Arkansas Geological Survey took note of a curious cluster of earthquakes near Greenbrier. The Guy-Greenbrier area had had only one quake of magnitude 2.5 or greater in 2007 and two in 2008. But there were 10 in 2009, the first year of deep disposal, and 54 in 2010. The suspicious timing of the quake cluster—which included hundreds of small quakes with one of magnitude 3.0—and its location near the first disposal well got their attention.

Once alerted to the suspicious quakes, Horton and Ausbrooks cast a network of seismometers around two new wells that would start injecting in July and in August 2010. On 1 October of that year, Horton warned the director of the Arkansas Oil and Gas Commission, the state agency that regulates deep injection, to "watch out" for more earthquakes. Ten days later, a magnitude 4.0 struck about a kilometer northeast of the deeper of the two new wells. On 20 November, a magnitude 3.9 struck 2 kilometers farther to the northeast toward Guy. Then, in February 2011, magnitude-4.1 and -4.7 quakes struck to the southwest of the deeper well, toward Greenbrier.

By spring, nearly 1000 recorded quakes had struck the area since the wells had started up. "People were feeling a lot of earthquakes,"

CREDITS (TOP TO BOTTOM): AMY SANCETTA/AP PHOTO; C. BARRY RALEIGH

Published by AAAS

Horton says. By 4 March, the public, the Oil and Gas Commission, and the governor agreed that it was all a bad idea, and the wells were shut down. The quakes tapered away.

"I have no problem convincing scientific audiences these earthquakes were induced" by the deep wastewater disposal, Horton says. Their timing and location were certainly strongly suggestive. The quakes began only after injection began, surged when the rate of injection surged, were limited to the vicinity of the wells, and trailed off after injection was stopped.

But the data from the seismometer network also painted a detailed picture of exactly how the injected wastewater triggered the quakes. It was injected into an aquifer 3 kilometers down, where it increased the pressure of groundwater in the rock's pores and fractures. From there the increased pressure due to injection spread through a previously unknown buried fault into the underlying rock, triggering quakes on the fault as it went.

Those elevated pressures could spread far and wide. Tens of thousands of cubic meters of wastewater were injected each month, month after month; fracking usually involves far smaller volumes pressurized for hours or days. Only in the deeper rock could the added pressure of the injection trigger magnitude 4s. Burdened by far more overlying rock, the deep rock is already carrying stress that will make for larger earthquakes.

The deep rock of the Guy-Greenbrier fault is also innately stronger than the overlying aquifer's sedimentary rock. The stronger rock could therefore store the stress that plate-tectonic forces load onto the North American continent. In this setting, the widespread fluid pressures of injection could pry apart the two sides of the fault just enough to let them suddenly slip by each other and release long-stored tectonic stress as a sizable earthquake.

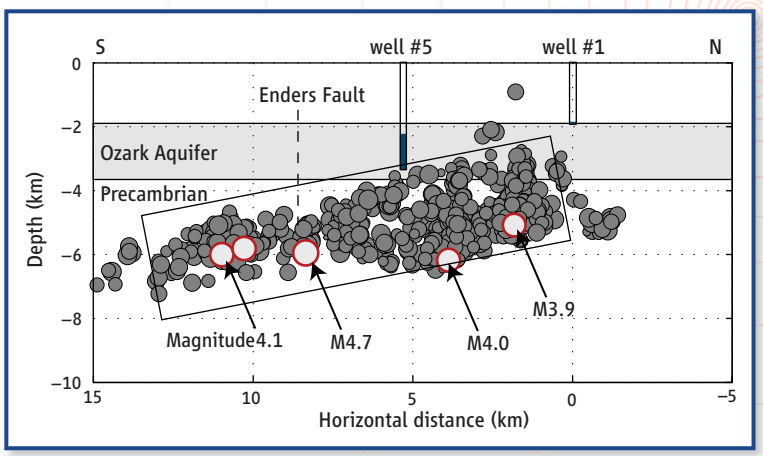

Bad leak. Wastewater injected into the Ozark aquifer of Arkansas leaked into a deeper unknown fault (roughly outlined by the rectangle in this side view). The heightened water pressure in the fault relieved just enough of the squeeze on the fault to allow earthquakes (gray and orange circles).

A trigger here, a trigger there

North-central Arkansas is not the only place where fiddling with Mother Nature has lately set off earthquakes. On 9 March, the Ohio Department of Natural Resources announced that it had evidence "strongly indicating" that wastewater injection—at least part of it from fracking—had triggered 12 magnitude-2.0-to-4.0 quakes in Youngstown (population 66,982) since March 2011. The indications were strong enough to prompt the state to order the shutdown of four injection wells in the area and issue strong new regulations. And injection of fracking wastewater under the Dallas/Fort Worth International Airport in Texas triggered a sequence of more than 180 earthquakes ranging up to magnitude 3.3 in 2008–2009. The quakes tapered off once the injection was stopped.

Other pursuits of cleaner energy can apparently also trigger earthquakes. Ellsworth and his Menlo Park USGS colleagues will report at next month's annual meeting of the Seismological Society of America that a "remarkable increase" in magnitude-3 and larger earthquakes since 2000 in the central United States is "almost certainly manmade." In addition to the Arkansas cluster, seismic activity surged along the Colorado–New Mexico border beginning in 2001. That's where drillers were injecting water to extract methane from still-buried coal beds. In central and southern Oklahoma, seismicity abruptly increased in 2009 by a factor of 20 over the rate of the previous half-century, exclusive of November's magnitude 5.6 and its aftershocks. Exactly what is causing the Oklahoma surge is still unclear, but "we're suspicious industrial activities are at the heart of what's going on" all across the central United States, Ellsworth says.

Drillers are running short of ideal waste injection sites, says geophysicist Mark Zoback of Stanford University in Palo Alto, California. There are already 144,000 wastewater injection wells in the country, he notes, but almost none trigger quakes. That's probably because they were drilled into weak, porous rock well suited to accommodating injected fluids. But some areas new to drilling are far from suitable rock formations. Deep, brittle, low-permeability rock "doesn't have a lot of capacity for taking any of these fluids," says geophysicist Barry Raleigh, who ran the Rangely, Colorado, earthquake-control experiment in the 1970s (see photo, left). "As a storage medium, they're pretty crappy."

Red light, green light

Wastewater injection "is not a mysterious process," Zoback says. "These are manageable problems. We simply have to be more careful." In his article in the April issue of *Earth*, Zoback lays out a learn-as-you-go approach to locating injection operations similar to one that geophysical modeler Jonny Rutqvist of Lawrence Berkeley National Laboratory suggested in a January *Geotechnical and Geological Engineering* article. Learn-as-you-go would likely also apply to fluid injections to create geothermal energy reservoirs (injections beneath Basel, Switzerland, touched off a project-ending magnitude-3.4 quake in 2006) or to keep the greenhouse gas carbon dioxide out of the atmosphere.

Zoback's first recommendation is to look before you leap. He believes that the seismic imaging techniques used in oil and gas exploration should easily find buried faults capable of producing damaging quakes—those above, say, magnitude 6.0.

When injection begins—and it should begin cautiously, Zoback says—seismometers should be monitoring the area. At a minimum, their data could paint a subsurface picture in real time, as in Arkansas, that could reveal smaller faults capable of magnitude 4s and 5s. But seismic data and well observations could also be fed into models of crustal rock behavior that could, with considerable uncertainties, project the potential for sizable earthquakes. If actual or projected quakes emerged, injection could be throttled back or even stopped, Zoback says. (Stopping injection has stopped significant earthquakes within days to a year.)

The new regulations in Ohio and Arkansas at least move in the direction of such a learn-as-you-go approach. Studies by the U.S. Environmental Protection Agency and by the National Research Council on the injection triggering of quakes are due out in the coming months. **–RICHARD A. KERR**

LETTERS

edited by Jennifer Sills

Finding a Good Research Question, in Theory

NEWTON NEEDED AN APPLE, FRANKLIN A FLASH, GALILEO A telescope, and Archimedes a crown. What do these people have in common? They observed a phenomenon that they could not explain, devoted their lives to investigating it, and in doing so achieved groundbreaking discoveries. From observations to hypotheses, from experiments to potential explanations, they conducted every part of the research required to answer the question they had chosen.

Nowadays, rarely—if ever—can a single scientist start at the beginning of the research process and follow it through all the way to its conclusion. Rather than a marathon, research today resembles a relay race: We focus on a small part of a larger question and then pass the baton to the next scientist. In a system where most advances are incremental, many scientists struggle to pursue original research questions. We identified and evaluated several methods that scientists use to select the subject of their research.

Some scientists approach the task by picking a theory and reading all the papers within its theoretical framework in search of a question not yet asked. However, the mere fact that some aspect has not been explored yet does not necessarily make it interesting. Others create a problem they think they can solve by applying one of the solutions their theories or methodologies have already provided to them. This may be an engaging intellectual exercise, but it usually leads to sterile research questions, unlinked to the real world. These question-generation strategies lead to smart and creative solutions to problems that do not exist—a phenomenon called Type III error: finding the right answer to the wrong question (*1*). It seems to us that too much research is based on these approaches, especially in behavioral economics and behavioral sciences.

There is another way to generate a research question: Go back to the basics. Observe the world, and when you encounter a phenomenon that intrigues you, investigate it. Theories should not be the only source of research questions or the benchmark against which we define what is right and wrong. Shall we abandon a research question when there is no theory from which we could derive our hypotheses? Should we feel compelled to conform our own results only to the mainstream theoretical framework to be accepted in the field? Should we be more concerned about the theory than about the actual problem under investigation? Research runs the risk of growing too dependent on theories, neglecting real-world problems as a result and constraining perspectives and methodologies. If Newton had been preoccupied with established theories, he might have been too busy in his office to realize how surprisingly interesting an apple falling from a tree could be.

NICOLAI BODEMER* AND AZZURRA RUGGERI

Max Planck Institute for Human Development, 14195, Berlin, Germany.

*To whom correspondence should be addressed. E-mail: bodemer@mpib-berlin.mpg.de

Reference

1. A. W. Kimball, *J. Am. Stat. Assoc.* **57**, 133 (1957).

Science in Nepal Needs Neighborly Aid

COMPARED WITH ITS NEIGHBORS, NEPAL remains sluggish in economic development as well as investments in research and development [(*1*) and "Report notes China's influence in emerging Asian science zone," News & Analysis, J. Mervis, 20 January, p. 274)]. While China and India have made substantial progress in science and technology, Nepal, sandwiched between the two countries, lags in basic science and technology infrastructure, high-quality education, retention of talented researchers, and qualified manpower.

China and India support Nepal's development primarily by providing physical infrastructure. However, military assistance has overshadowed other aid. China has promised to provide military aid of US$7.7 million and to establish a military academy in Nepal. Likewise, India has resumed military assistance and promised to provide more military supplies in the future (*2*). In contrast, support is dismal for Nepal's higher education, science and technology, and research and development. Furthermore, scientific cooperation between Nepal and its large neighbors is negligible (*3*).

Instability, corruption, and lack of technological development, as well as frequent disasters, have undermined economic development in Nepal. Because of the lack of research and development investments, about 40% of Nepalese who have master's and Ph.D. degrees are teaching instead of conducting their own research (*4*). Thousands of talented Nepalese emigrated during the

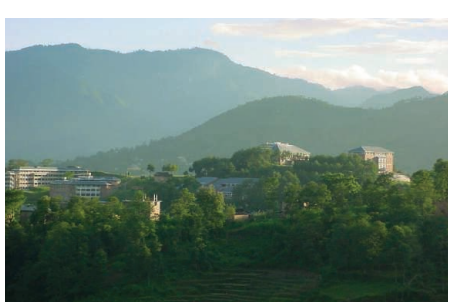

Kathmandu University. Investments in Nepal's research and development are lagging.

CREDITS (TOP TO BOTTOM): ISTOCKPHOTO.COM/WIKIMEDIA COMMONS

Published by AAAS

conflict and are now reluctant to return home because of limited opportunities.

After a decade-long conflict, Nepal is undergoing peace and a state-restructuring process. Rather than competing to provide military assistance to a country heading toward peace, China and India should foster innovation and economic prosperity by supporting Nepalese science and technology and research and development. An impoverished and uneducated Nepal is a greater threat to its neighbors than a Nepal that is enriched and educated.

UTTAM BABU SHRESTHA

Department of Biology, University of Massachusetts, Boston, MA 02125, USA. Harvard University Herbaria, Cambridge, MA 02138, USA. E-mail: ubshrestha@yahoo.com

References

1. The World Fact Book (www.cia.gov/library/publications/the-world-factbook).
2. K. R. Koirala, *Republica*, "India, China rivalry over security aid worries lawmakers," 1 February 2012, p. 3 (http://e.myrepublica.com/component/flippingbook/book/780-republica-01-feb-2012/1-republica.html).
3. UNESCO Science Report Part II (2010); unesdoc.unesco.org/images/0018/001899/189958e.pdf.
4. D. Bajracharya *et al.*, Science, Research and Technology in Nepal (UNESCO Working paper no. 10, 2006); unesdoc.unesco.org/images/0014/001461/146117e.pdf.

India Lacks Scientific Leadership

P. BAGLA'S INTERVIEW OF C. N. R. RAO ("TOP Indian chemist helps make the case for science windfall," Newsmakers interview, 13 January, p. 157) lacks some important context. In my experience, the Scientific Advisory Committee to the Prime Minister (SAC-PM) of India, which Rao chairs, has shown neither social responsibility nor genuine commitment to science. For example, in 2001, then–Education Minister Murali Manohar Joshi proposed that astrology be included along with subjects such as chemistry and economics among the first degree courses in India's universities. A colleague and I filed a petition with the Supreme Court of India against the proposal. Our petition was admitted and heard but eventually dismissed. The support of our science academies and credible scientists such as Rao could have helped our case by countering the judges' unscientific beliefs about astrology.

Rao says, "We have been short of high-level talent for some time." He lays the blame for this on our bureaucracy. I believe that the true blame lies with India's scientific leaders. The scientific leadership in the country, with notable exceptions, rewards sycophancy and punishes independence, integrity, courage, effective communication, scientific competence, and credibility.

PUSHPA M. BHARGAVA

Former Vice Chairman, National Knowledge Commission, Government of India; Former Member, National Security Advisory Board, Government of India; Former CSIR Distinguished Fellow; Former and Founder Director, Centre for Cellular and Molecular Biology, Hyderabad, 500 007, Andhra Pradesh, India. E-mail: bhargava.pm@gmail.com

Response

I AGREE WITH BHARGAVA THAT INDIA'S ACADEMIES have not provided leadership to the scientific community, but to say that they are not committed to science is inaccurate.

I do believe that having a critical mass of outstanding young people in various areas of science and engineering is crucial for the future of India. There are many reasons for the talent deficit, such as insufficient funding and an environment that is not conducive to the scientific pursuit. Bureaucracy also plays a part, as it controls everything that happens in

India. Appointments and extensions of senior scientists need to be approved by bureaucrats. Administrative procedures and financial controls are becoming increasingly oppressive.

C. N. R. RAO

National Research Professor and Honorary President and Linus Pauling Research Professor, Jawaharlal Nehru Centre for Advanced Scientific Research, Jakkur P.O., Bangalore 560 064, India. E-mail: cnrrao@jncasr.ac.in

TECHNICAL COMMENT ABSTRACTS

Comment on "Productivity Is a Poor Predictor of Plant Species Richness"

Xubin Pan, Fengqiao Liu, Mi Zhang

Adler *et al*. (Reports, 23 September 2011, p. 1750) analyzed the standardized sampling data from 48 herbaceous-dominated plant communities and concluded that "Productivity is a poor predictor of plant species richness" at fine-scale. However, their method was biased toward site-number–dominated plant communities. They also failed to provide enough data for regional analysis and detailed information for within-site analysis.

Full text at www.sciencemag.org/cgi/content/full/335/6075/1441-a

Comment on "Productivity Is a Poor Predictor of Plant Species Richness"

Jason D. Fridley, J. Philip Grime, Michael A. Huston, Simon Pierce, Simon M. Smart, Ken Thompson, Luca Börger, Rob W. Brooker, Bruno E. L. Cerabolini, Nicolas Gross, Pierre Liancourt, Richard Michalet, Yoann Le Bagousse-Pinguet

Adler *et al*. (Reports, 23 September 2011, p. 1750) reported "weak and variable" relationships between productivity and species richness and disputed the "humped-back" model (HBM) of plant diversity. We show that their analysis lacks sufficient high-productivity sites, ignores litter, and excludes anthropogenic sites. If corrected, the data set of Adler *et al*. would apparently yield strong HBM support.

Full text at www.sciencemag.org/cgi/content/full/335/6075/1441-b

Response to Comments on "Productivity Is a Poor Predictor of Plant Species Richness"

James B. Grace, Peter B. Adler, Eric W. Seabloom, Elizabeth T. Borer, Helmut Hillebrand, Yann Hautier, Andy Hector, W. Stanley Harpole, Lydia R. O'Halloran, T. Michael Anderson, Jonathan D. Bakker, Cynthia S. Brown, Yvonne M. Buckley, Scott L. Collins, Kathryn L. Cottingham, Michael J. Crawley, Ellen I. Damschen, Kendi F. Davies, Nicole M. DeCrappeo, Philip A. Fay, Jennifer Firn, Daniel S. Gruner, Nicole Hagenah, Virginia L. Jin, Kevin P. Kirkman, Johannes M. H. Knops, Kimberly J. La Pierre, John G. Lambrinos, Brett A. Melbourne, Charles E. Mitchell, Joslin L. Moore, John W. Morgan, John L. Orrock, Suzanne M. Prober, Carly J. Stevens, Peter D. Wragg, Louie H. Yang

Pan *et al*. claim that our results actually support a strong linear positive relationship between productivity and richness, whereas Fridley *et al*. contend that the data support a strong humped relationship. These responses illustrate how preoccupation with bivariate patterns distracts from a deeper understanding of the multivariate mechanisms that control these important ecosystem properties.

Full text at www.sciencemag.org/cgi/content/full/335/6075/1441-c

Letters to the Editor

Letters (~300 words) discuss material published in *Science* in the past 3 months or matters of general interest. Letters are not acknowledged upon receipt. Whether published in full or in part, Letters are subject to editing for clarity and space. Letters submitted, published, or posted elsewhere, in print or online, will be disqualified. To submit a Letter, go to www.submit2science.org.

Published by AAAS

Comment on "Productivity Is a Poor Predictor of Plant Species Richness"

Xubin Pan,[1,2]* Fengqiao Liu,[3] Mi Zhang[4]

Adler *et al*. (Reports, 23 September 2011, p. 1750) analyzed the standardized sampling data from 48 herbaceous-dominated plant communities and concluded that "Productivity is a poor predictor of plant species richness" at fine-scale. However, their method was biased toward site-number–dominated plant communities. They also failed to provide enough data for regional analysis and detailed information for within-site analysis.

Adler *et al*. (*1*) presented the results of statistical regression between live biomass and species richness at three scales: within sites, within regions, and across the globe. They adopted standardized and observational sampling methods to minimize the methodological difference in other meta-analyses, which is of particular importance in enriching the data set for the productivity–plant species richness (P-PSR) relationship. However, we challenge the statistical method they used and the conclusions they reached.

To adequately test P-PSR at global and regional scales, data from many and randomly distributed sites should be used (*2*). Although the 48 experimental sites were from five continents, the number of sites of different vegetation types varied from one to six, with only one site each for grassland, desert grassland, and mixed-grass prairie, and six sites for annual grassland. In addition, the total number of sites is only 48, making the global analysis biased toward site-number–dominated plant communities. To address this concern, using the vegetation type in the regression analysis (*3*) could reduce the statistical effect of site-number difference between different vegetation types. Thus, we used the average vegetation-type value calculated from site mean live biomass and site mean richness to conduct a global regression analysis. The managed and anthropogenic sites were excluded from this analysis to preclude the effects of human activities, and salt marsh was also excluded because of its special feature of land-ocean interfaces. Then, within 30 sites we included 12 vegetation types in total: alpine grassland, annual grassland, desert grassland, grassland, mesic grassland, mixed-grass prairie, montane meadow, savanna, semiarid grassland, shortgrass prairie, shrub steppe, and tallgrass prairie. The regression analysis results showed a significantly positively linear relationship between productivity and species richness at the global level in Fig. 1 ($P = 0.016$, $R^2 = 0.454$), which was in conformity with other studies (*2*).

We also challenge the rationality of the regional analysis in Adler *et al*. (*1*). Whether comparing the same vegetation type in different regions or different vegetation types within the same region, the authors failed to provide enough data for the analysis; in addition, 5 out of 13 sites were anthropogenic. For within-site analysis, they needed more detailed information to conduct P-PSR analysis based on case-by-case evaluation (*4*), such as considering the sampling location difference at each site and the species composition of samplings at each site.

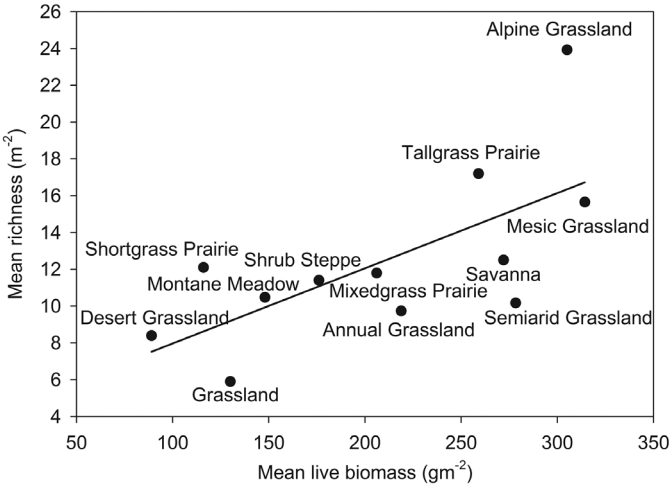

Fig. 1. Global P-PSR relationship analysis between mean live biomass and mean richness based on vegetation-type category. The solid line shows the linear relationship between productivity and biodiversity.

[1]Department of Environmental Engineering, Texas A&M University–Kingsville, 700 University Boulevard, Kingsville, TX 78363, USA. [2]School of Environment, Tsinghua University, Beijing 100084, China. [3]School of Sustainability, Arizona State University, Post Office Box 872511, Tempe, AZ 85287, USA. [4]Northwest Institute of Plateau Biology, Chinese Academy of Sciences, 23 Xining Road, Xining 81008, China.

*To whom correspondence should be addressed. E-mail: xubin.hu.pan@gmail.com

References and Notes

1. P. B. Adler *et al*., *Science* **333**, 1750 (2011).
2. L. N. Gillman, S. D. Wright, *Ecology* **87**, 1234 (2006).
3. Y. F. Bai *et al*., *J. Appl. Ecol.* **44**, 1023 (2007).
4. R. J. Whittaker, *Ecology* **91**, 2522 (2010).

Acknowledgments: This work was supported by the Green Design and Planning, Chinese Government Award for Outstanding Self-Financed Students Abroad and Texas A&M University–Kingsville.

3 October 2011; accepted 15 February 2012
10.1126/science.1214786

Comment on "Productivity Is a Poor Predictor of Plant Species Richness"

Jason D. Fridley,[1]* J. Philip Grime,[2] Michael A. Huston,[3] Simon Pierce,[4] Simon M. Smart,[5] Ken Thompson,[2] Luca Börger,[6] Rob W. Brooker,[7] Bruno E.L. Cerabolini,[8] Nicolas Gross,[6] Pierre Liancourt,[9] Richard Michalet,[10] Yoann Le Bagousse-Pinguet[10]

Adler *et al*. (Reports, 23 September 2011, p. 1750) reported "weak and variable" relationships between productivity and species richness and dispute the "humped-back" model (HBM) of plant diversity. We show that their analysis lacks sufficient high-productivity sites, ignores litter, and excludes anthropogenic sites. If corrected, the data set of Adler *et al*. would apparently yield strong HBM support.

The humped-back model (HBM) of plant diversity, describing a unimodal relationship between annual production (standing biomass and litter) and maximum species richness for herbaceous vegetation, was proposed nearly four decades ago (*1*) and is among the preeminent theories of plant community organization (*2*–*5*). The conclusion of Adler *et al*. (*6*) that relationships between productivity and richness are "weak and variable," based on an analysis of a global-scale data set, casts doubt on the utility of this model. However, even cursory examination of the data and methods of Adler *et al*. reveals that it is an inadequate basis for rejecting the HBM for several reasons.

First, it is deficient in its range of productivity values, including only a handful of sites above 500 g/m^2. In one of the earliest extensive descriptions of the HBM, Al-Mufti *et al*. (*7*) found consistently low species richness at productivity levels of 800 g/m^2 or higher, which is broadly consistent with subsequent studies conducted at this scale (*8*–*11*). With so few high-productivity sites, Adler *et al*. have no statistical basis for expecting a maximal unimodal curve to emerge from their data, an artifact of a limited range of productivity values that has been acknowledged repeatedly in the literature (*4*, *5*, *12*).

Second, although never clearly stated, Adler *et al*. apparently did not include litter in their productivity measurements. (Statistical testing involved "live biomass," although the methods refer to the collection of "recently senescent material"; whether this would include production from early phenological species is unclear, but presumably it ignores accumulated litter.) Data collected to evaluate the HBM have routinely included plant litter along with standing biomass in estimates of productivity, because dead plant material is an important component of productivity and has an important role as a mechanism of competitive suppression (*13*). This means that plots shown by Adler *et al*. as being of intermediate productivity are likely much higher, which would likely shift the peak of maximum species richness found by Adler *et al*. from 300 to 400 g/m^2 closer to the 500 to 600 g/m^2 range observed by Al-Mufti *et al*. (*7*).

Third, the statistical inadequacy of the data set at high levels of productivity is compounded when the authors dismiss "anthropogenic" sites without sufficient scientific basis. The authors treat anthropogenicity as if it were a categorical factor, either human-derived or not. This may provide a basis for them to then delete anthropogenic sites, but this assignment is not justified in their paper and is not logical given the continuum of variation in productivity and the gradual way natural ecosystem productivity is augmented by human inputs. Due to eutrophication associated with agricultural activities, anthropogenic sites are often of high productivity, and, as the HBM predicts, are typically of low richness due to dominance by large plants of high competitive ability (*14*). It is unfortunate that Adler *et al*. dismiss such sites, because one of the main applications of the HBM is to show how eutrophication reduces local richness in terrestrial communities, which has been of much import to the conservation community (*5*, *15*). Had the data set been gathered with the intent of addressing local production-richness relationships across a broad productivity gradient, we have no doubt that "natural" herbaceous assemblages of high production—such as salt marshes, meadows of rich substrate, and herbaceous floodplains, all of which are characterized by high dominance and low species richness—would reveal the classic HBM pattern of declining richness at high levels of productivity. Adler *et al*. also omit one (high biomass, low richness) wetland site, without explanation.

Finally, despite the clear deficiencies in the data for testing the HBM, it is remarkable that the data in their figures 2, 3, and S3 show a clear peak of maximum species richness that comes close to both the production and richness values at the peak (30 to 40 species at about 400 g/m^2) found by Al-Mufti *et al*. (*7*). If these data were to include litter and a larger sample of high productivity sites, regardless of their anthropogenic influence, it is reasonable to conclude that a clear HBM would emerge.

The HBM is a cornerstone of plant ecology, backed by decades of careful mechanistic analysis and used extensively by plant conservationists and restoration ecologists, as well as by theoretical ecologists. It would be imprudent to abandon this important concept on the basis of one unsuitable data set.

[1]Department of Biology, Syracuse University, Syracuse, NY 13244, USA. [2]Department of Animal and Plant Sciences, University of Sheffield, Sheffield, S10 2TN, UK. [3]Department of Biology, Texas State University, San Marcos, TX 78666, USA. [4]Department of Plant Production, University of Milan, Via Celoria 2, Milan, Italy. [5]Centre for Ecology and Hydrology, Lancaster Environment Centre, Lancaster, LA1 4AP, UK. [6]Centre d'Etudes Biologiques de Chizé, CNRS (UPR1934) and INRA (USC1339), 79360 Beauvoir sur Niort, France. [7]The James Hutton Institute, Craigiebuckler, Aberdeen, AB15 8QH, UK. [8]Department of Structural and Functional Biology, University of Insubria–Varese, via Dunant 3, I-21100 Varese, Italy. [9]Department of Biology, University of Pennsylvania, Philadelphia, PA 19104, USA. [10]Université Bordeaux 1, UMR 5805 EPOC, Avenue des Facultés, 33405 Talence, France.

*To whom correspondence should be addressed. E-mail: fridley@syr.edu

References

1. J. P. Grime, *Nature* **242**, 344 (1973).
2. M. A. Huston, *Am. Nat.* **113**, 81 (1979).
3. D. Tilman, *Resource Competition and Community Structure* (Princeton Univ. Press, Princeton, NJ, 1982).
4. J. B. Grace, *Perspect. Plant Ecol. Evol. Syst.* **2**, 1 (1999).
5. P. A. Keddy, *Ann. Bot.* **96**, 177 (2005).
6. P. B. Adler *et al*., *Science* **333**, 1750 (2011).
7. M. M. Al-Mufti, C. L. Sydes, S. B. Furness, J. P. Grime, S. R. Band, *J. Ecol.* **65**, 759 (1977).
8. D. R. J. Moore, P. A. Keddy, *Vegetatio.* **79**, 99 (1989).
9. B. D. Wheeler, S. C. Shaw, *J. Ecol.* **79**, 285 (1991).
10. L. Gough, J. B. Grace, K. L. Taylor, *Oikos* **70**, 271 (1994).
11. O. Kull, A. Aan, *Ecography* **20**, 146 (1997).
12. M. L. Rosenzweig, *Species Diversity in Space and Time* (Cambridge Univ. Press, Cambridge, 1995).
13. J. M. Facelli, S. T. A. Pickett, *Bot. Rev.* **57**, 1 (1991).
14. S. M. Smart *et al*., *J. Appl. Ecol.* **43**, 1128 (2006).
15. D. R. J. Moore, P. A. Keddy, C. L. Gaudet, I. C. Wisheu, *Biol. Conserv.* **47**, 203 (1989).

10 October 2011; accepted 15 February 2012
10.1126/science.1215042

Response to Comments on "Productivity Is a Poor Predictor of Plant Species Richness"

James B. Grace,[1]* Peter B. Adler,[2] Eric W. Seabloom,[3] Elizabeth T. Borer,[3] Helmut Hillebrand,[4] Yann Hautier,[5] Andy Hector,[5,6] W. Stanley Harpole,[7] Lydia R. O'Halloran,[8] T. Michael Anderson,[9] Jonathan D. Bakker,[10] Cynthia S. Brown,[11] Yvonne M. Buckley,[12] Scott L. Collins,[13] Kathryn L. Cottingham,[14] Michael J. Crawley,[15] Ellen I. Damschen,[16] Kendi F. Davies,[17] Nicole M. DeCrappeo,[18] Philip A. Fay,[19] Jennifer Firn,[20] Daniel S. Gruner,[21] Nicole Hagenah,[22,23] Virginia L. Jin,[24] Kevin P. Kirkman,[22] Johannes M. H. Knops,[25] Kimberly J. La Pierre,[23] John G. Lambrinos,[26] Brett A. Melbourne,[17] Charles E. Mitchell,[27] Joslin L. Moore,[28] John W. Morgan,[29] John L. Orrock,[16] Suzanne M. Prober,[30] Carly J. Stevens,[31,32] Peter D. Wragg,[3] Louie H. Yang[33]

Pan *et al*. claim that our results actually support a strong linear positive relationship between productivity and richness, whereas Fridley *et al*. contend that the data support a strong humped relationship. These responses illustrate how preoccupation with bivariate patterns distracts from a deeper understanding of the multivariate mechanisms that control these important ecosystem properties.

Debate over the productivity-richness relationship (PRR) has been strongly influenced by the way that scientific motives influence how theories are evaluated. Analyses of how scientists participate in the process of theory maturation (*1*) point out that attachment to particular explanations can result in a tendency to overlook inadequacies and contradictions. Such attachment can lead to a reliance on "theory demonstrations," which selectively sift through data to find supporting evidence. "Theory investigations," in contrast, have a different motivation: to evaluate the explanatory adequacy and limitations of theories so as to improve them. Theory investigations are challenged to be either exhaustive in their examination of evidence (e.g., through complete meta-analyses) or to rely on unfiltered samples that represent the variation nature has to offer. Generally, demonstrations seek qualitative (yes/no) support, whereas theory investigations seek to quantify the relative importance of different processes.

In our study (*2*), we investigated the PRR at the local, regional, and global scale and reported the patterns found with all sites included or with sites of anthropogenic origin (e.g., old fields and restored prairies) excluded. Along with the mean responses, we evaluated boundaries using nonlinear quantile regression. We emphasized that for all these different analyses, there was a great deal of unexplained variance.

Pan *et al*. (*3*) argue that our study provides clear and strong support for a positive linear relationship between productivity and richness. They selected one subset where we found a weak, positive linear PRR among site means (the straight dotted line in Adler *et al*., figure 3), culled additional sites, and then averaged across similar sites, boosting the apparent strength of the relationship. Pan *et al*. (*3*) claim that we were biased in our investigation of the PRR because of unbalanced replication of samples across the bins in the community classification scheme they used to post-process the data. Counter to their claim, there is no requirement for equal representation in bins unless one seeks homogeneity of variance across the relationship. Averaging across similar sites so as to create a single value for each bin, however, reduces unexplained variance by eliminating within-bin variance and exaggerates predictive capacity. The use of bins defined by an informal community classification scheme also confounds productivity with the classification scheme.

In sharp contrast to Pan *et al*., Fridley *et al*. (*4*) contend that our data show strong support for the humped-back model (HBM). Original support for the HBM comes from theory demonstrations, such as the Al-Mufti (*5*) study where data were hand-selected to represent a humped-back line. Theory investigations based on unfiltered samples and rigorous quantitative analyses since that time have consistently found PRR patterns to be weak and variable (*6*–*8*), consistent with our findings [although analyses that have filtered studies have produced more consistent results, with the form of relationship depending on the filtering applied (*9*, *10*)].

Fridley *et al*.'s specific claims are that we (i) filtered data by eliminating anthropogenic sites; (ii) failed to properly test the HBM by not including litter; (iii) failed to include enough high-productivity sites to detect a hump; and, inconsistent with that point, (iv) claim the data show a humped relationship. We dispute their implication that we presented biased results and disagree with their conclusions as described here:

(i) We performed many analyses and summarized the full range of patterns found. One of the analyses prominently presented was across all sites (Adler *et al*., figure 3, solid line) and showed a weak but significant humped relationship. Another analysis excluded anthropogenic sites (Adler *et al*., figure 3, dotted line), anticipating that some might object to inclusion of highly altered sites (which Pan *et al*. did). This analysis showed a (weak) linear positive relationship. Within-site analyses of small-scale richness patterns showed very weak and highly variable patterns (Adler *et al*., figure 2).

[1]U.S. Geological Survey, National Wetlands Research Center, 700 Cajundome Boulevard, Lafayette, LA 70506, USA. [2]Department of Wildland Resources and the Ecology Center, Utah State University, 5230 Old Main, Logan, UT 84322, USA. [3]Ecology, Evolution, and Behavior, University of Minnesota, 1987 Upper Buford Circle, St. Paul, MN 55108, USA. [4]Institute for Chemistry and Biology of the Marine Environment, University of Oldenburg, Schleusenstrasse 1, Wilhelmshaven, D-26381, Germany. [5]Institute of Evolutionary Biology and Environmental Studies, University of Zurich, Winterthurerstrasse 190, Zurich, 8057, Switzerland. [6]Microsoft Research, 7 J. J. Thomson Avenue, Cambridge, CB3 0FB, UK. [7]Ecology, Evolution and Organismal Biology, Iowa State University, 133 Bessey Hall, Ames, IA 50011, USA. [8]Department of Zoology, Oregon State University, 3029 Cordley Hall, Corvallis, OR 97331, USA. [9]Department of Biology, 206 Winston Hall, Wake Forest University, Winston-Salem, NC 27109, USA. [10]School of Environmental and Forest Sciences, Box 354115, University of Washington, Seattle, WA 98195–4115, USA. [11]Bioagricultural Sciences and Pest Management, Colorado State University, 1177 Campus Delivery, Fort Collins, CO 80523–1177, USA. [12]School of Biological Sciences, The University of Queensland, St. Lucia, Queensland, 4072, Australia. [13]Department of Biology, MSC03-2020, University of New Mexico, Albuquerque, NM 87131, USA. [14]Biological Sciences, Dartmouth College, Hanover, NH 03755, USA. [15]Department of Biological Sciences, Imperial College London, Silwood Park, Ascot, Berks, SL5 7PY, UK. [16]Department of Zoology, University of Wisconsin, 430 Lincoln Drive, Madison, WI 53706, USA. [17]Ecology and Evolutionary Biology, UCB 334, University of Colorado, Boulder, CO 80309, USA. [18]U.S. Geological Survey, Forest and Rangeland Ecosystem Science Center, 3200 Southwest Jefferson Way, Corvallis, OR 97331, USA. [19]Grassland Soil and Water Research Lab, USDA ARS, 808 East Blackland Road, Temple, TX 76502, USA. [20]Queensland University of Technology, School of Biogeosciences, Brisbane QLD, 4001 Australia. [21]Department of Entomology, University of Maryland, College Park, 4112 Plant Sciences, College Park, MD 20742, USA. [22]School of Biological and Conservation Sciences, University of KwaZulu-Natal, Pietermaritzburg, KwaZulu-Natal, 3209, South Africa. [23]Department of Ecology and Evolutionary Biology, Yale University, New Haven, CT 06520, USA. [24]Agroecosystem Management Research Unit, 137 Keim Hall, USDA ARS, Lincoln, NE 68583–0937, USA. [25]School of Biological Sciences, 348 Manter Hall, University of Nebraska, Lincoln, NE 68588, USA. [26]Department of Horticulture, Oregon State University, 4017 Agricultural and Life Sciences Building, Corvallis, OR 97331, USA. [27]Department of Biology, 411 Coker Hall, University of North Carolina at Chapel Hill, Chapel Hill, NC 27599–3280, USA. [28]School of Botany, University of Melbourne, Parkville, Victoria, 3010, Australia. [29]Department of Botany, La Trobe University, Bundoora, Victoria, 3086, Australia. [30]Commonwealth Scientific and Industrial Research Organisation Ecosystem Sciences, Private Bag 5, Wembley, Western Australia, 6913, Australia. [31]Department of Life Sciences, The Open University, Walton Hall, Milton Keynes, Buckinghamshire, MK7 6AA, UK. [32]Lancaster Environment Centre, Lancaster University, Lancaster, LA1 4YQ, UK. [33]Department of Entomology, University of California, Davis, One Shields Avenue, Davis, CA 95616, USA.

*To whom correspondence should be addressed. E-mail: gracej@usgs.gov

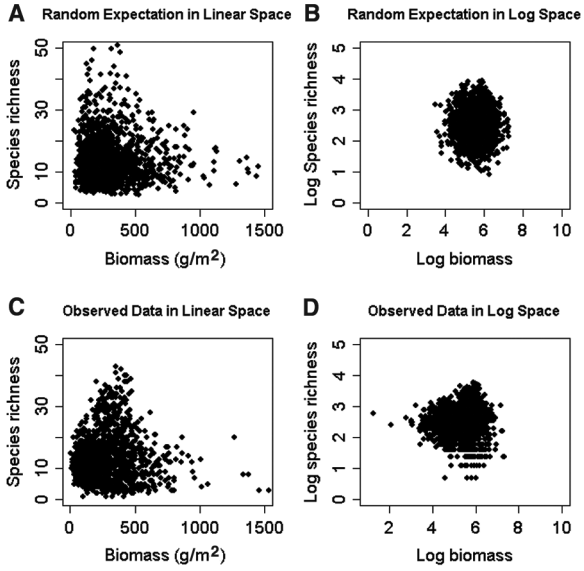

Fig. 1. (**A**) Random expectations for plot-level data, based on data characteristics in figure 2 in Adler *et al*. (*2*). Note the apparent hump produced by log-normal distributions of both biomass and species richness. (**B**) Random expectations for Adler *et al*. data in log-log space. (**C**) Observed data in linear space. (**D**) Observed data in log space.

(ii) The majority of studies of the PRR have described productivity as the variable of theoretical interest rather than accumulated biomass, including Fridley *et al*. themselves at times [(*9*), p. 127]. To be comparable with previous theory investigations, we analyzed productivity without including litter accumulated from previous years.

(iii) Sites were selected without filtering and represent the variance encountered when ecologists are asked to sample natural grasslands. Selectively including sites with high productivity, as suggested by Fridley *et al*., would bias the sample, leaving us with no estimate of the predictive adequacy of the PRR. That said, 20 of the 48 sites included in our study contained individual plots with productivity levels greater than 500 g/m^2 and 8 had levels greater than 800 g/m^2 (and ranged over 1500 g/m^2), counter to the impression given by Fridley *et al*.

(iv) Fridley *et al*. suggest, based on visual examination and no formal analysis, that there is a clear modal PRR relationship, contradicting their own claim that more high-productivity sites are needed to detect a humped relationship. However, production and richness data are log-normally distributed in this case (Adler *et al*., figure 2), and a random bivariate sample from a log-normal distribution will necessarily have a humped appearance in linear space (Fig. 1A). Plotting data from a bivariate log-normal distribution in log-log space (Fig. 1B) reveals the randomness. The observed data (Fig. 1, C and D) show only modest deviations from random expectations, illustrating why quantitative analyses failed to detect strong patterns.

We note that even if productivity and richness were strongly correlated, we still would be unable to resolve underlying mechanisms. There have been well over 100 theories proposed to explain diversity patterns (*11*). A linear positive relationship is predicted by many different possible mechanisms (*12*), and the HBM likewise represents a large collection of conflicting theories (*7*).

We reiterate that it is past time to develop the multivariate expectations for our multiprocess theories and to evaluate those expectations quantitatively (*13*). Insights into the mechanisms controlling diversity cannot be achieved by continued fixation on bivariate patterns such as the PRR.

References and Notes

1. C. Loehle, *Q. Rev. Biol.* **62**, 397 (1987).
2. P. B. Adler *et al*., *Science* **333**, 1750 (2011).
3. X. Pan, F. Liu, M. Zhang, *Science* **335**, 1441 (2012); www.sciencemag.org/cgi/content/full/335/6075/1441-a.
4. J. D. Fridley *et al*., *Science* **335**, 1441 (2012); www.sciencemag.org/cgi/content/full/335/6075/1441-b.
5. M. M. Al-Mufti, C. L. Sydes, S. B. Furness, J. P. Grime, S. R. Band, *J. Ecol.* **65**, 759 (1977).
6. G. G. Mittelbach *et al*., *Ecology* **82**, 2381 (2001).
7. J. B. Grace, *Perspect. Plant Ecol. Evol. Syst.* **2**, 1 (1999).
8. K. L. Gross, M. R. Willig, L. Gough, R. Inouye, S. B. Cox, *Oikos* **89**, 417 (2000).
9. M. A. Huston, *Biological Diversity* (Cambridge Univ. Press, Cambridge, 1994)
10. L. N. Gillman, S. D. Wright, *Ecology* **87**, 1234 (2006).
11. M. W. Palmer, *Folia Geobot. Phytotaxon.* **29**, 511 (1994).
12. J. Carnicer, L. Brotons, D. Sol, M. de Caceres, *Glob. Ecol. Biogeogr.* **17**, 352 (2008).
13. J. B. Grace, *Structural Equation Modeling and Natural Systems* (Cambridge University Press, Cambridge, 2006), chap. 12.

Acknowledgments: This work was generated using data from the Nutrient Network collaborative experiment, funded at the site scale by individual researchers and coordinated through Research Coordination Network funding from NSF to E.T.B. and E.W.S. (grant DEB-0741952). We thank the Minnesota Supercomputing Institute for hosting project data and the Institute on the Environment for hosting network meetings. The authors declare no competing interests. The data used in the primary analyses are available in the supporting online material of our original paper. We thank G. Guntenspergen, K. McKee, and J. Powell for review of an earlier draft of the manuscript.

28 October 2011; accepted 15 February 2012
10.1126/science.1214939

SCIENCE AND RELIGION

New Light on a Continuing Clash

Thomas Burnett

So much ink has been spilled over the Scopes "Monkey Trial" of 1925 that one might conclude no additional original insights could emerge from it. Jeffrey Moran's *American Genesis* proves otherwise. Moran, a historian at the University of Kansas, analyzes the evolution controversies by paying particular attention to issues of gender, race, and regional identity in the United States. In his account, the seemingly straightforward case of science versus faith takes on surprising historical dimensions.

American Genesis
The Antievolution Controversies from Scopes to Creation Science
by Jeffrey P. Moran
Oxford University Press, Oxford, 2012. 212 pp. $29.95, £19.99. ISBN 9780195183498.

Teaching evolution in the classroom had not been an important public issue in the late 19th century, when less than 5% of children attended high school. But by 1920, attendance had reached nearly 2 million students per year, and public schools began to generate great political and social concern. Evolution was certainly not the sole focus of critique—major controversies also broke out over sex education, teacher radicalism, and the portrayal of patriotism in history textbooks.

In 1925, the Tennessee state legislature passed the Butler Act, a law that prohibited schools that receive state funding from teaching "any theory that denies the story of the Divine Creation of man as taught in the Bible, and to teach instead that man has descended from a lower order of animals." Looking for an opportunity to challenge the law, the American Civil Liberties Union offered to defend anyone accused of violating it. Dayton high school teacher John Scopes volunteered and was arrested. His subsequent trial—featuring William Jennings Bryan and Clarence Darrow—took on mythical proportions after it was popularized in the 1955 Broadway play *Inherit the Wind*, then remade into a 1960 Hollywood blockbuster. Although numerous historians have pointed out the gross inaccuracies of this portrayal [e.g., (*1*)], popular myths don't die so easily. However, instead of returning to the details of the trial itself, Moran focuses on the societal context in which the event unfolded.

One might expect that the earliest evolution debates were primarily found in southern states and rural areas. But in fact, as Moran points out, until the 1920s southern Americans paid scant attention to Darwinism. When potential jurors were questioned for the Scopes trial, most confessed that they had not heard of any controversy over evolution and the Bible until after Scopes had been arrested. Before that time, the conflict was largely confined to the Northeast, where modernist views were rapidly advancing and sectarian groups were emerging to combat them.

Exploring the racial dimensions of the Scopes trial, Moran notes that teaching evolution in public schools was not a major issue for the African American community at the time. In the South, relatively few black students attended high school; for those who did, the segregated schools emphasized agriculture and practical trades. A general acceptance of evolution represented a no-win situation for African Americans. Although some black intellectuals hoped that scientific advancement would undermine the South's oppressive social structure, it was evident evolution could be marshaled to further justify black inferiority. In fact, George Hunter's *Civic Biology*—Tennessee's official biology text, used by Scopes—explicitly described a hierarchy of races. The lowest was the "Ethiopian or negro type," and it culminated with "the highest type of all, the Caucasians, [are] represented by the civilized white inhabitants of Europe and America" (*2*).

Beyond race and regional identity, the most surprising insights in *American Genesis* concern the role of gender. Moran persuasively argues that in the 1920s antievolutionism was primarily a female-led reform movement that sought political support against threats to children's moral and religious development. Women had recently secured the right to vote, and given their high visibility in the prohibition movement, politicians felt obliged to heed their concerns. During debate over the Butler bill, the speaker of the Tennessee Senate "proclaimed he had been petitioned to support the bill by 'the women of the state and the teachers association.'" At the time of the Scopes trial, nearly all letters to newspapers in support of the Butler bill were written by women, whereas dissenting letters more often came from men.

In the decades that followed—particularly after the 1961 publication of *The Genesis Flood* (*3*)—the antievolution movement

Fueling the opposition. Antievolution books for sale in Dayton, Tennessee, after the Scopes trial (July 1925).

CREDIT: TOPICAL PRESS AGENCY/GETTY IMAGES

The reviewer is at the Biologos Foundation, 6549 Mission Gorge Road, Box 251, San Diego, CA 92120, USA. E-mail: tburnett@alumni.rice.edu

Published by AAAS

shifted in emphasis from moral arguments to more "scientific" rebuttals. This transition toward natural science has galvanized greater male participation. Nevertheless, the female voice remains strong. In a 2005 Kansas survey (*4*) on whether evolution should be taught in the public schools, 74% of men answered yes while only 58% of women agreed. Asked whether it was "possible to believe in both God and evolution," 73% of men agreed, whereas only 57% of women did so.

Looking back at the U.S. controversies over evolution in the past hundred years, *American Genesis* makes it clear that the conflict is largely fueled by the perception that evolutionary theory undermines morality. When scientific issues morph into ethical and theological conundrums, we shouldn't be surprised if the ensuing discussions continue not just for decades but centuries. A debate that exasperates both scientists and the public will continue to generate mountains of data for historians far into the future.

References

1. E. J. Larson, *Summer for the Gods: The Scopes Trial and America's Continuing Debate over Science and Religion* (Basic Books, New York, 1997).
2. G. W. Hunter, *A Civic Biology: Presented in Problems* (American Book, New York, 1914).
3. J. C. Whitcomb, H. M. Morris, *The Genesis Flood: The Biblical Record and Its Scientific Implications* (Presbyterian and Reformed Publishing, Philadelphia, 1961).
4. http://www2.ljworld.com/news/2005/oct/09/can_god_evolution_coexist/?evolution.

10.1126/science.1221218

HISTORY

Objectifying Our Past

Neil MacGregor's book *A History of the World in 100 Objects* is not unlike some of the artifacts described in its pages—a thing of flawed beauty whose purpose isn't completely clear even though its provenance is.

To start with the provenance: In 2010, BBC Radio 4 broadcast a 100-part series of programs under the same title. Hosted and narrated by MacGregor, the director of the British Museum, each 15-minute episode described one object taken from the museum's collection. The radio series had the overall aim of describing the broad trajectory of human history from the first stone tools to present-day credit cards.

The series begins on a near-disastrous misstep. Smitten by the mummies in the Egyptian section of the museum as a child, MacGregor starts there, on the pretext of introducing the modus operandi of the series. But in fact the distinct impression left by this first episode (and the book's opening chapter) is that we are about to be condemned to a context-free, rudderless trawl through the vaults of a fusty old museum.

It is the second program (and second chapter in the book), on a circa-1.9-million-year-old stone chopping tool from Olduvai, where the history and the series really begin. And from there on in you'll be hooked, as the roughly chronological journey weaves back and forth across the globe and touches on many of the major events in human history. Some of the objects are iconic: the Rosetta stone (of course). Some are utterly mysterious and achingly beautiful: the Mold Cape (a finely worked gold garment, from 1900 to 1600 BCE, found in north Wales). Some are surprising: a solar-powered lamp and charger manufactured in Guandong, China (the 100th object). And some are prosaic (or so at first glance it might seem): a handful of thousand-year-old pottery shards picked up on an East African beach in 1948. Each provides grounds for an interesting tale, and the stories are well told. But where MacGregor and the series excel is in understanding the tension that exists in trying to place an object in the context of its own time as well as our own time.

Why then flawed beauty? A radio series on historical objects sets itself the challenge of bringing those objects to life for the listener. MacGregor succeeds, through description (often bringing in other opinions—experts in the field and cleverly selected "famous voices") and occasional interaction with the objects themselves. Still, you'd have thought a picture is worth a thousand words. Not so here: The illustrations in the book are disappointing in their mere adequacy. Restricted in size by the 15 cm–by–23 cm dimensions of the pages, they are very often limited to one view and are printed on the same paper stock as the text (limiting color density and vividness of detail). In addition, the text itself is merely a transcript (one irritatingly different in minor details) of the radio programs. Opportunities to showcase some of the fabulous art—such as the 2500-year-old bronze flagons from Basse-Yutz, northeastern France; the 15th-century brass Ife head from Nigeria; and the gilded mechanical model galleon (1585) from Germany—and illustrate pertinent details or to expand in the text on the history of the objects were missed. That is doubly regrettable, because the BBC website (www.bbc.co.uk/ahistoryoftheworld) associated with the series (where all 100 radio programs are freely available) is cluttered and difficult to navigate. Thus, although it includes multiple high-resolution images of each object, these are not as easily located as they could be

What, then, of the book's purpose? Imagine for a moment a MacGregor from the distant future, revisiting the series. He dusts off a fading copy of the book, pondering on the present-day MacGregor's "necessary poetry of things" (or, more prosaically, using inspiration to divine an object's meaning). I suspect our future MacGregor might cheekily imagine the book partly an act of vanity (the British Museum glancing enviously across the English Channel at the Louvre, that much more famous museum in Paris). But he might also see it as an artifact trapped uncomfortably in the juncture between two great ages, the analog and the digital. Would a future MacGregor puzzle over why—instead of a soon-to-be-outdated book on paper—a digital incarnation of the series had not combined audio, images, video, and text together with the still-considerable resources of an admittedly fledgling Internet and been delivered to the then ubiquitous computer and related tablet platforms? The truth is, we will never know.

–Guy Riddihough

10.1126/science.1221217

A closer look. Three hounds and a duck decorate the spout of one of the Basse-Yutz flagons.

A History of the World in 100 Objects
From the Handaxe to the Credit Card
by Neil MacGregor
Viking (Penguin), New York, 2011. 733 pp. $45. ISBN 9780670022700. Allen Lane (Penguin), London, 2010. £30. ISBN 9781846144134. Penguin, London, 2012. Paper, £12.99. ISBN 9780241951774.

EDUCATION

Entrepreneurship Training for the Developing World

Education focused on commercial dynamism, not just policy and bureaucracy, can contribute to economic growth in low-income countries and the world.

Iqbal Z. Quadir

Developing countries, once economically marginal, are now a critical part of the world's economy. Non-OECD (Organisation for Economic Co-operation and Development) countries account for three-quarters of the world's population, three-quarters of real gross domestic product growth over the last decade and nearly two-thirds of the world's energy, steel, and copper consumption (*1*). China and India constitute a sizable part of this development, but many other countries are showing impressive economic growth; Bangladesh and sub-Saharan Africa are projected to grow at around 6% this year (*2*).

Entrepreneurs have driven much of this progress. Universities in the West, however, largely offer programs to prepare students for entrepreneurial careers in the developed world with little focus on developing countries. Western universities offer programs focused on developing countries, but these are commonly for economic planning and policy design and intervention. Such curricula prepare students for bureaucratic careers in corporations, governments, or multilateral organizations such as the United Nations (UN) or World Bank. A mind-set that low-income countries need help exclusively in policy design and bureaucracy, not in commercial dynamism, maintains an imbalance in education that is increasingly diverging from real-world conditions.

Home-Field Advantage + Western Training

Yet Western universities could better train developing-country nationals for entrepreneurial careers in these countries. Although young college dropouts, such as Steve Jobs and Mark Zuckerberg, have gotten the media limelight, the majority of high-tech entrepreneurs are "middle-aged with 16 years of work experience" (*3*), and there is a good correlation between higher education and successful entrepreneurship (*4*). Although it may be impossible to train people to come up with "breakthrough innovations" (*5*), education can provide components of the entrepreneurial skill set that affect success. Western universities draw people from all over the world, and university neighborhoods like the Silicon Valley are often high-tech entrepreneurial hubs, which make these universities uniquely qualified to promote entrepreneurship globally. Many developing countries' enterprises—especially those in high tech—are global collaborations, or "micro-multinationals" (*6*), that have originated in university settings.

Western-trained. Mo Ibrahim brought mobile phones into 14 African countries.

Even in the absence of specialized programs, many high-tech entrepreneurs from low-income countries have already benefited from Western education: e.g., Robin Li (China, founded Baidu), Ayisi Makatiani (Kenya, founded Africa Online), and Azim Premji (India, founded Wipro). These entrepreneurs established businesses that are globally recognized, creating jobs, products, services, and increasing capacity to import Western goods. Key to such successes were both "home-field advantage" (*7*) in their native countries and the benefits of educational experiences in Western countries. Programs designed especially for potential entrepreneurs in developing countries may facilitate similar successes on a large scale.

Schumpeter argued that economic growth requires entrepreneurs who combine assets (including new technologies) in new ways, creating new opportunities, new markets, new economic value, and effectively, new supply-and-demand curves (*8*). The aforementioned entrepreneurs succeeded by combining technologies developed by others [utilizing decades of research and development (R&D)], capital accumulated by others, equipment manufactured by other businesses, and the eagerness of millions of people as consumers seeking to improve their lives.

The Cycle of Aid and Central Planning

The last half-century of economic history sheds light on both the mind-set behind the current lack of entrepreneurship programs focused on developing countries at Western universities and the opportunity that exists today. As expected from Schumpeter's theory, countries that did not experience entrepreneurial dynamism stayed poor. Inherited colonial administrative machineries, extractive industries, and foreign aid bolstered pervasive central control and planning in the last several decades. "[G]overnment interventions [were] frequently all-embracing" (*9*), and state-owned monopolies hindered entrepreneurial entry. The cycle of aid to central governments, the consequent expanded state (*10*), and more poverty, which further justified aid, ensued; the discussion about entrepreneurship nearly disappeared from development literature by the 1970s (*11*). As a result, growth of economic output per worker in developing countries slowed from 3% in the 1960s to negative growth by the 1990s (*12*).

Entrepreneurs struggled to build enterprises, despite central control and planning, but overall progress was either slow or nonexistent. In the last two decades, however, international travel, education abroad, and the dramatically favorable economics of digital technologies) have enabled entrepreneurial success and consequent economic progress in low-income countries.

For instance, entrepreneurs like Western-educated Mo Ibrahim (Sudan, founded Cel-Tel) and Miko Rwayitare (Rwanda, founded Telacel International) have made mobile communications pervasive and affordable in the poorest countries (*13*). An easily affordable phone call might save a day of travel that can be used instead in earning, giving rise to immediate benefits, overcoming the problem of low purchasing power, and contributing to economic growth. Other such technologies that enhance productivity and purchasing power for the user and commercial opportunities for entrepreneurs are on the horizon in energy, agriculture, medicine, and other

Director, Legatum Center for Development and Entrepreneurship, Massachusetts Institute of Technology, Cambridge, MA 02142 USA. E-mail: iqbalquadir@mit.edu

Published by AAAS

fields. Furthermore, a new technology can give an edge to a knowledgeable entrepreneur over established powerful players and so disperse power. Such entrepreneurial development would create jobs, addressing the chronic problem of unemployed educated people in the developing world.

Although a great deal of educational resources have been dedicated to creating better governments in low-income countries, entrepreneurial progress naturally contributes to this end. Historically, economic progress and good governance often emerged as an unintended consequence of commerce and innovations driven by entrepreneurs. Many recent entrepreneurial successes have been realized under less-than-good governance, systems of checks and balances, and other infrastructures. Entrepreneurial innovation can overcome hindrances to some extent; mainland Chinese entrepreneurs in the 1980s registered companies in Hong Kong to do business in mainland China (*14*). In short, innovations, as in the case of digital technologies, can set off entrepreneurial virtuous cycles as they have in recent decades, and Western universities can accelerate the process.

The potential for entrepreneurship has been noticed and encouraged by organizations more directly involved in global affairs and development. The U.S. President convened a summit on entrepreneurship in 2010; the Department of State subsequently announced its Global Entrepreneurship Program to support entrepreneurs in Muslim countries. Several organizations have produced extensive reports on entrepreneurship, including the UN Development Programme (UNDP), Global Entrepreneurship Monitor, the European Commission (EC), and the World Economic Forum (*15*–*17*). The World Bank series *Doing Business* (rru.worldbank.org) lays out the economic, political, and legal terrain of specific developing countries. Nonprofit organizations such as Endeavor and The Indus Entrepreneurs provide mentoring, strategic advice, and network support to entrepreneurs.

Gaining an Edge Through Engagement

Major Western universities can pursue deeper, more continuous engagement. In the process, they stand to maintain their edge in research. They can draw on existing faculty with extensive understanding of emerging technologies, economic historians knowledgeable of entrepreneurship's proven benefits, and established business school curricula relevant to new ventures. Universities can exploit their convening power to bring together potential and successful entrepreneurs. Further, these institutions hold the potential to partner with universities in developing countries to better connect with local contexts.

Six components can be taught and facilitated by professors of entrepreneurship, case writers, experienced entrepreneurs, and professors of economic history: (i) curricula on technologies on the horizon and their potential economic and social ramifications, especially in developing countries; (ii) case studies of entrepreneurship in developing countries, e.g., how setbacks were overcome; (iii) interactions with successful entrepreneurs from developed and developing countries, as effective mentorship can triple the success rates of entrepreneurs (*18*); (iv) basic business education such as accounting, marketing, and finance; (v) exposure to angel investors, seed fund investors, and potential partners or employees; and (vi) history of entrepreneurial progress in the West, demonstrating how individual entrepreneurial efforts can give rise to the larger good.

A number of Western universities have recognized the need to establish programs addressing business approaches to international social problems, such as Cornell's Center for Sustainable Global Enterprise. A few university programs specifically focus on educating entrepreneurs, including the Skoll Centre for Social Entrepreneurship at Oxford (which promotes both nonprofit and for-profit entrepreneurship) and the recently launched Stanford Institute for Innovation in Developing Economies. At the Legatum Center for Development and Entrepreneurship at the Massachusetts Institute of Technology, we help about 35 students a year prepare for commercial entrepreneurial careers in low-income countries. The Legatum Center fosters both theoretical knowledge and practical skills for creating for-profit ventures, and it exposes students to a rich entrepreneurship ecology for essential networking and support, including extensive interactions with successful entrepreneurs.

Successful programs for entrepreneurship in developing countries can be established at major Western universities that have business, engineering, and economic history curricula and the involvement of practitioners in developing countries. Universities should seek collaboration with universities in low-income countries that can identify and help recruit would-be entrepreneurs; arrange for successful entrepreneurs from developing countries to give visiting lectures and interact with students; and, when possible, host entrepreneurs-in-residence to coach students.

In engaging entrepreneurs from developing countries, Western researchers stand to gain knowledge about innovations originating from low-income countries (*19*). Universities can learn from the experience of General Electric, which recently began selling in the United States low-priced handheld electrocardiogram devices, originally designed for a rural Indian market (*20*). Economic growth spurred by entrepreneurship education can create richer two-way traffic of students and researchers between developing countries and Western universities.

Although promotion of entrepreneurship may appear to be of peripheral importance to universities committed to advancing science and humanities, entrepreneurs can anchor intellectual endeavors in reality by deploying the practical output of knowledge. Given the role of entrepreneurship in economic growth and social progress, the training of entrepreneurs can be deeply connected to public service, central to the mission of universities.

References and Notes

1. Why the tail wags the dog, *Economist*, 6 April 2011, www.economist.com/node/21525373.
2. International Monetary Fund (IMF), World Economic Outlook, September 2011: Slowing Growth, Rising Risks (World Economic Survey, IMF, Washington, DC, 2011).
3. V. Wadhwa, R. Freeman, B. Rissing, *Innovations* **5**(2), 141 (2010).
4. A. Basu, in *Oxford Handbook for Entrepreneurship*, M. Casson, B. Yeung, N. Wadeson, Eds. (Oxford Univ. Press, New York, 2006), pp. 580–600.
5. W. Baumol, Education for innovation: Entrepreneurial breakthroughs vs. corporate incremental improvements (NBER Working Paper 10578, National Bureau of Economic Research (NBER), Cambridge, MA, 2004).
6. R. Guest, *Borderless Economics* (Palgrave McMillan, New York, 2011).
7. S. Lacy, *Brilliant, Crazy, Cocky* (Wiley, Hoboken, NJ, 2011), p. 8.
8. J. Schumpeter, *The Theory of Economic Development* [original German version was published in 1911] (Harvard Univ. Press, Cambridge, MA, 1951).
9. A. O. Krueger, *Am. Econ. Rev.* **64**, 291 (1974).
10. K. L. Remmer, *Am. J. Pol. Sci.* **48**, 77 (2004).
11. N. Leff, *J. Econ. Lit.* **17**, 51 (1979).
12. W. Easterly, *The Elusive Quest for Growth* (MIT Press, Cambridge, MA, 2001), p. 74.
13. Mobile marvels: A special report on telecoms in emerging markets, *Economist*, 26 September 2009; www.economist.com/node/14483896.
14. Y. Huang, *Capitalism with Chinese Characteristics* (Cambridge Univ. Press, Cambridge, 2008), pp. 1-49.
15. Commission on the Private Sector and Development, UNDP, *Unleashing Entrepreneurship: Making Business Work for the Poor* (UNDP, New York, 2004); http://web.undp.org/cpsd/report/index.html.
16. EC, *Entrepreneurship and Higher Education, Especially Within Non-Business Studies* (EC, Brussels, 2008)
17. C. Volkmann *et al.*, *Educating the Next Wave of Entrepreneurs: Unlocking Entrepreneurial Capabilities to Meet the Global Challenges of the 21st Century* (Global Education Initiative, World Economic Forum, 2011).
18. C. J. Schramm, *The Entrepreneurial Imperative* (Harper-Collins, New York, 2006), p. 174.
19. The world turned upside down: A special report on innovation in emerging markets. *Economist*, 17 April 2010; www.economist.com/node/15879369.
20. J. R. Immelt, V. Govindarajan, C. Trimble, *Harv. Bus. Rev.* **87**, 56 (2009).

10.1126/science.1217790

MEDICINE

Old Drug, New Hope for Alzheimer's Disease

A nuclear receptor agonist increases the clearance of beta-amyloid and improves cognitive skills in a mouse model of Alzheimer's disease.

Warren J. Strittmatter

Alzheimer's disease insidiously robs patients of the ability to remember, reason, and make informed judgments. Despite decades of research, no therapeutics are available that slow disease progression, and to date no "disease-modifying" drug has succeeded to show therapeutic benefit and to be safe. On page 1503 of this issue, Cramer *et al*. (*1*) show that a drug called bexarotene reverses the effects of neurodegeneration in a mouse model of Alzheimer's disease. The study provides new hope that decades of research examining the molecular and cellular pathways in Alzheimer's disease may soon yield disease-modifying therapies.

The neuritic plaques and neurofibrillary tangles observed in the brains of Alzheimer's disease patients have led to numerous hypotheses of pathogenesis and informed decades of research elucidating the molecular mechanism of this disease. Neuritic plaque results from the aggregation of a peptide, β-amyloid (Aβ), which is generated by proteolytic cleavage of a transmembrane protein, amyloid precursor protein (APP). A complex of proteins that includes the protease γ-secretase is necessary for cleaving APP to produce the Aβ peptide. Mutations in three genes encoding APP, presenilin-1, and presenilin-2 (needed for γ-secretase activity) cause uncommon autosomal-dominant Alzheimer's disease (*2*). Although these mutations account for less than 10% of the patients with this disease, they provide compelling evidence that the proteolytic processing of APP to produce Aβ peptide can result in clinical disease. Aggregates of Aβ peptide have been postulated to cause dementia, perhaps by physically disrupting synaptic connections. Alternatively, smaller, soluble oligomers of Aβ may directly initiate the events leading to neuronal dysfunction. Despite these insights, potential therapeutic strategies to either inhibit the proteolytic processing of APP, or to directly bind the Aβ peptide once formed, have resulted in a series of failed or ongoing clinical trials.

Departments of Medicine (Neurology) and Neurobiology, Duke University Medical Center, Durham, NC 27710, USA. warren@neuro.duke.edu

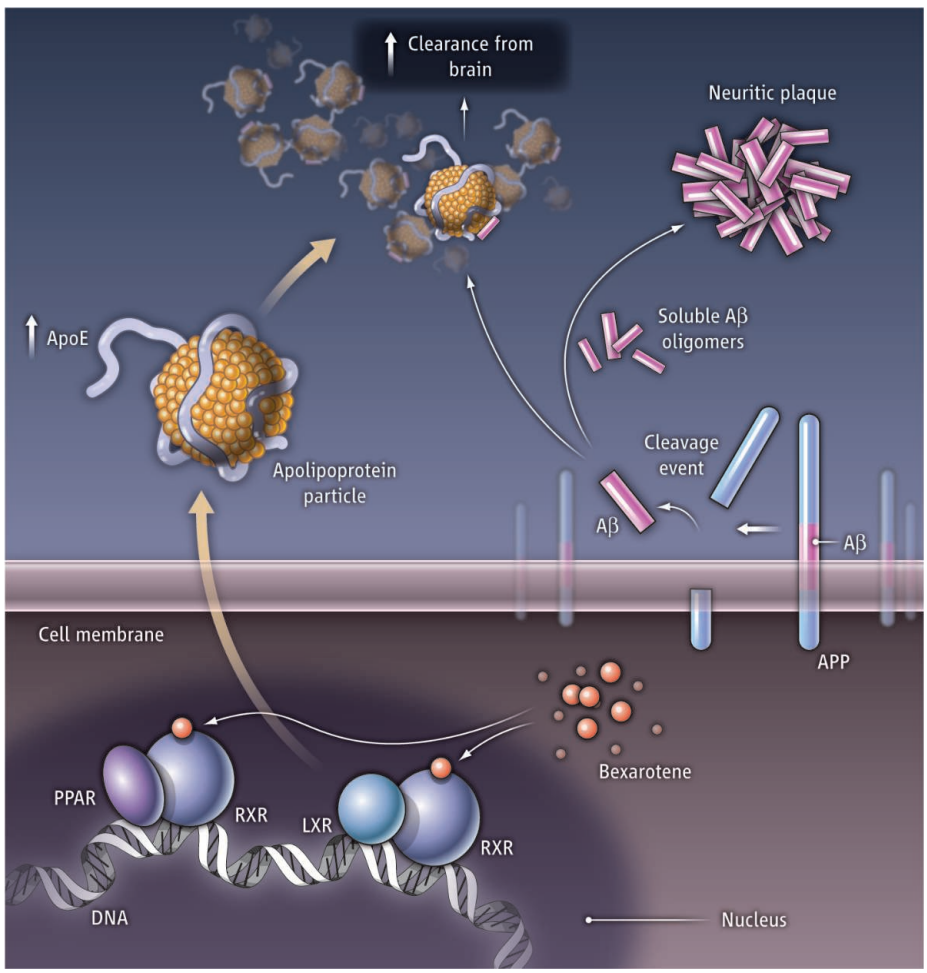

All clear. Stimulating nuclear receptors increases apoE expression and the clearance of Aβ from the brain by a mechanism requiring apoE.

The various alleles of the apolipoprotein E gene (*APOE*) determine the major genetic risk of developing Alzheimer's disease (*3*). The most common allele, *APOE3*, is considered "neutral" for disease, whereas the rare *APOE2* allele decreases the probability of disease. *APOE4* markedly increases the risk of disease, but is not necessary for Alzheimer's disease, nor is it sufficient to produce disease. Individuals with one copy of the *APOE4* allele have a 5-fold increased chance of disease, whereas individuals with two copies have an approximate 20-fold increased risk. Despite 20 years of research, the mechanism by which the various apoE isoforms differentially affect risk of developing this disease has remained elusive. Two primary hypotheses propose that apoE4 either accelerates the disease through a "toxic" mechanism, or fails to slow the disease process as effectively as apoE2 and apoE3. These alternative views have direct implications in devising therapeutic strategies, because one approach would inhibit a "toxic pathway" mediated by apoE4, whereas the other would potentiate or mimic apoE3. Cramer *et al*. partially resolve this question, but more importantly, demonstrate that pharmacologic manipulation by a drug that is already approved by the U.S. Food and Drug Administration for another disease dramatically increases

Published by AAAS

expression of apoE, accelerates Aβ clearance from the brain and, moreover, reverses abnormal behaviors in mouse models of Alzheimer's disease.

Expression of the *APOE* gene and the lipid transporter genes *ABCA1* and *ABCG1* (which facilitate the formation of apoE-associated lipoprotein particles) are increased by agonists of the nuclear receptors peroxisome proliferator–activated receptor gamma (PPARγ) and liver X receptor (LXR). These receptors form obligate heterodimers with the nuclear receptor retinoid X receptor (RXR) (*4*). LXR or PPARγ agonists can reduce the production of Aβ, as well as improve cognition, in mouse models of Alzheimer's disease. Cramer *et al*. tested whether the RXR agonist bexarotene, which activates both the PPAR-RXR and LXR-RXR receptors, would rapidly alter the amount of Aβ, and diminish behavioral abnormalities, in mice genetically engineered to express a mutant form of the *APP* gene. The authors observed rapid clearance of soluble Aβ from the brain, reduction in neuritic plaque burden, and reversal of behavioral deficits. The effects of bexarotene on Aβ metabolism required apoE expression, because they were not observed when the drug was administered to mice lacking the *APOE* gene. These observations strongly support the hypothesis that apoE plays a critical role in reducing Aβ amounts in the brain by enhancing Aβ clearance, and that strategies increasing apoE expression in patients might be truly disease modifying (see the figure).

Although Cramer *et al*. rigorously demonstrate that bexarotene clears Aβ by a mechanism dependent on apoE, the drug may enhance behavioral responses (in this mouse model of Alzheimer's disease) through an additional mechanism. Patients with Alzheimer's disease or type 2 diabetes show insulin resistance, and a small clinical trial demonstrated that the intranasal inhalation of insulin by Alzheimer's patients improved memory (*5*). PPARγ agonists and RXR agonists both have been developed as therapeutics for type 2 diabetes as "insulin sensitizers." The RXR agonist bexarotene, examined by Cramer *et al*., also reduces fasting glucose concentrations in mouse models of non–insulin-dependent diabetes (*6*). Thus, disturbance in the molecular pathway resulting in type 2 diabetes may also be critical in the mechanism of Alzheimer's disease

Although the study by Cramer *et al*. provides strong motivation for clinical trials, observations in mouse models of disease might not necessarily extrapolate to humans. The amino acid sequence of mouse apoE is not identical to any of the human apoE isoforms, and the transgenic mouse models in their study do not recapitulate the neurofibrillary tangle neuropathology of Alzheimer's disease. The rapid clearance of Aβ from the brains of mice may have unintended consequences in compromising blood-brain barrier integrity. Only carefully constructed clinical trials will determine whether this drug, or related drugs, benefits patients with Alzheimer's disease.

References

1. P. E. Cramer *et al*., *Science* **335**, 1503 (2012); 10.1126/science.1217697.
2. M. Citron, *Nat. Rev. Drug Discov.* **9**, 387 (2010).
3. E. H. Corder *et al*., *Science* **261**, 921 (1993).
4. A. Chawla *et al*., *Mol. Cell* **7**, 161 (2001).
5. S. Craft *et al*., *Arch. Neurol.* **69**, 29 (2012).
6. R. Mukherjee *et al*., *Nature* **386**, 407 (1997).

10.1126/science.1220725

GEOPHYSICS

At the Bottom of the Oceanic Plate

High-resolution seismic maps are providing a better picture of the processes involved in plate tectonics.

Hitoshi Kawakatsu

According to the theory of plate tectonics, huge plates below the Pacific Ocean are moving laterally at a speed of ~10 cm/year above a weak layer called the asthenosphere. Considering that the horizontal scale of a plate can be as large as 10,000 km (the thickness is ~100 km), how such a thin plate maintains its rigidity, while sometimes causing mega-earthquakes at the edge, is rather puzzling. Understanding what is happening at the bottom of the oceanic plate remains an open question even after some 40 years of success of plate tectonics. In the past few years, seismologists have reported sharp shallow seismic boundaries beneath oceanic basins that may define the bottom of the plate (*1*–*3*). On page 1480 of this issue, Schmerr (*4*) reports observations indicating the laterally varying nature of the bottom boundary of the oceanic plate.

The asthenosphere, named after a Greek word meaning "weak," is a viscous layer just below the lithosphere ("rock") that facilitates horizontal movement of the solid plate. The word existed before the birth of plate tectonics to explain the long-term ground deformation associated with removal of the ancient glacier. A continental lithosphere underlain by the weak viscous asthenosphere is uplifted after thousands of years from the deglaciation because of the slow deformation taking place in the asthenosphere. Compared to the continental plates, which are complicated in structure because of their long tectonic history, oceanic plates are young and their history should be much simpler.

Considering that the inside of the Earth is warmer, it is natural to assume that deep-mantle rocks are softer owing to the higher temperature. However, the high pressure at depth makes rocks harder, so there must be a minimum value of the softness. Theoretical estimates of how mantle rocks behave with depth indicate that this minimum occurs around 100 to 150 km beneath the ocean, the same depth range known for the seis-

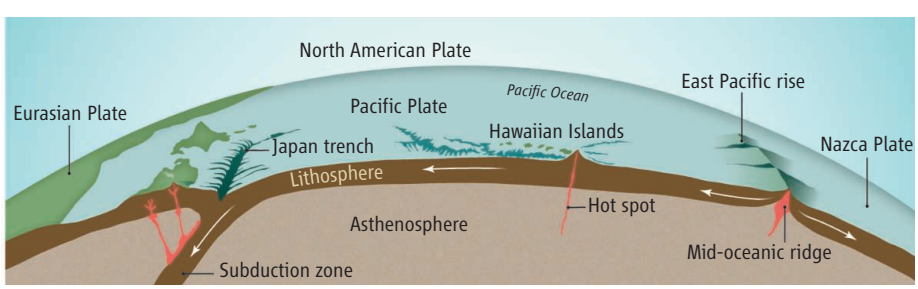

Plate tectonics in the ocean. The depth of the G discontinuity is around 50 to 100 km, and may vary with the age of the plate. The thickness of the transition region, the lithosphere-asthenosphere boundary, may be less than ~20 km.

Earthquake Research Institute, University of Tokyo, Tokyo, 113-0032 Japan. E-mail: hitosi@eri.u-tokyo.ac.jp

mic low-velocity zone (LVZ) (*5*). The question is whether this LVZ is weak or viscous enough to be consistent with the geodynamical property required for the asthenosphere (*6*). A further question is how the gradual change in temperature and pressure with depth can cause the observed large seismic-velocity reduction near the base of the lithosphere. This observed sudden drop in the seismic velocity around a depth of 50 to 100 km beneath the ocean is called the Gutenberg (or simply G) discontinuity, named after Beno Gutenberg who discovered the presence of the LVZ. The G separates the high-velocity oceanic lid from the LVZ; it is sometimes referred to as the lithosphere-asthenosphere boundary (LAB) because it invokes the idea that it is the boundary between strong lithosphere and weak asthenosphere (see the figure).

There are several ingredients that can make mantle rocks weaker: a small amount of melting (*7*) or water (*8*), and the size reduction of mineral grains. Among them, partial melting is the most effective for producing a sharp and large velocity drop at the G discontinuity, although the presence of water itself enhances melting. As the presence of a small amount of melt also lubricates the boundary (*9*), some argue that it even defines the LAB. In finding an intermittent G discontinuity beneath the Pacific, as distinct from the conventional view of a ubiquitous LVZ, Schmerr argues that a large amount of melt may exist in regions of the LAB where recent volcanism or melt production is known. As few G discontinuities have been observed where no volcanism exists, additional mechanisms are invoked—small-scale convections or mantle upwelling—that regionally enhance the discontinuity. However, as the reported properties of the G discontinuity show large scatter (*1*–*4*), further investigation is required. If we could map the G discontinuity beneath the entire ocean with accuracy, then we might be able to understand the enigmatic asthenosphere.

One of the key properties of the asthenosphere that is not well elucidated from both observational and theoretical standpoints is the strong seismic anisotropy known to exist in the LVZ (*10*, *11*). Seismic anisotropy is a polarization-direction dependence of seismic wave propagation that reflects the deformation history of mantle rocks. At present, we have neither a model of the asthenosphere that fully accounts for the observed properties of seismic anisotropy, nor do we have a well-constrained anisotropy structure of the LVZ. Thus, new seafloor observations and new analysis techniques combined with a large amount of seismic data from global land-based networks will be important to refine our understanding of the asthenosphere.

Plate tectonics started as a theory to explain the origins of the oceanic basin by investigating its shallowest part, leaving the deeper part of the lithosphere or lithosphere-asthenosphere system behind. Geophysical exploration of the ocean in the past several decades has focused on tectonically active areas, such as subduction zones, hot spots, and mid-oceanic ridges. Although these studies have elucidated the active part of the Earth's processes, the importance of normal, or tectonically inactive, oceanic areas, where the underlying structure may offer a textbook view of the deep mantle, might have been underestimated. Planned multidisciplinary ocean-bottom geophysical observations of the normal Pacific Ocean may finally shed light on the enigma of plate tectonics.

References

1. B. Bagley, J. Revenaugh, *J. Geophys. Res.* **113**, B12301 (2008).
2. H. Kawakatsu *et al.*, *Science* **324**, 499 (2009).
3. C. A. Rychert, P. M. Shearer, *J. Geophys. Res.* **116**, B07307 (2011).
4. N. Schmerr *et al.*, *Science* **335**, 1480 (2012).
5. L. Stixrude, C. Lithgow-Bertelloni, *J. Geophys. Res.* **110**, (B3), B03204 (2005).
6. M. A. Richards, W. S. Yang, J. R. Baumgardner, H. P. Bunge, *Geochem. Geophys. Geosyst.* **2**, 1026 (2001).
7. D. Anderson, C. Sammis, *Phys. Earth Planet. Inter.* **3**, 41 (1970).
8. S. Karato, H. Jung, *Earth Planet. Sci. Lett.* **157**, 193 (1998).
9. Y. Takei, B. K. Holtzman, *J. Geophys. Res.* **114**, B06205 (2009).
10. M. Nettles, A. M. Dziewonski, *J. Geophys. Res.* **113**, B02303 (2008).
11. A. Maggi, E. Debayle, K. Priestley, G. Barruol, *Earth Planet. Sci. Lett.* **250**, 53 (2006).

10.1126/science.1219658

ECOLOGY

Keystones in a Tangled Bank

Thomas M. Lewinsohn[1] and Luciano Cagnolo[2]

Ecological network studies highlight the importance of individual species to community conservation.

In the past decade, ecologists have increasingly applied complex network theory (*1*, *2*) to ecological interactions, both in entire food webs (*3*) and in networks representing ecological interactions, especially those between plants and their animal pollinators or seed dispersers (*4*). How important are individual species to the maintenance of such ecological networks? On page 1489 of this issue, Stouffer *et al*. (*5*) analyze terrestrial, freshwater, and marine food webs to infer the contributions of individual species to network stability. In a related field study on page 1486 of this issue, Aizen *et al*. (*6*) explore plant and pollinator webs on a landscape scale. Using a different field study design, Pocock *et al*. (*7*) recently focused on a local community in which several webs of different kinds of interactions and organisms form a composite network.

Stouffer *et al*. decomposed previously studied food webs into groups of three species linked by interactions (see the figure, panel A). Such species triads can form 13 different configurations or motifs that may be differentially represented in networks (*8*). Each species can belong to several motifs in a food web. The authors propose that most species tend to preferentially occupy certain motifs, giving them distinctive "motif profiles."

Previous simulation studies have shown that each trophic motif contributes to either an increase or a decrease in the probability of community persistence (*9*). Combining their findings with these previous observations, Stouffer *et al*. find that each species or entity can be assigned a probability of increasing or decreasing the persistence of a community to which it belongs. Families or higher taxonomic entities tend to occupy similar motifs across different communities, which suggests that they also have invariant effects on the future persistence of a community.

Aizen *et al*. analyzed flower visitation webs in 12 isolated hills of varying size in the Argentinian Pampas, 400 km south of Buenos Aires. They recorded 268 species of plants and insect flower visitors in standardized field surveys. The number of interactions decreased from larger to smaller hills, at a higher rate than expected from the well-established species-area relation (*10*). What could cause these interaction losses?

[1]Department of Animal Biology, State University of Campinas–UNICAMP, 13083-970 Campinas SP, Brazil. [2]Instituto Multidisciplinario de Biología Vegetal, Universidad Nacional de Córdoba, X5016 GCA Córdoba, Argentina. E-mail: thomasl@unicamp.br; lcagnolo@efn.uncor.edu

To address this question, the authors related two attributes of an interaction within each hill—the local frequency of a plant-visitor interaction, and the degree of generality of the partnered species—to the ubiquity of that interaction across all hills. As the networks shrink, visitation links tend to concentrate more and more on the interaction core of highly connected generalistic species, a "master hub" of species links (see the figure, panel B). However, a further result was unexpected. Several interactions that did persist on smaller hills shifted away from the core to a peripheral position in the network. Species partnered in those interactions have fewer interactors in depauperate communities.

Pocock *et al*. assembled a "network of networks" from several studies within a mixed-use 125-ha organic farm in southwest England. The farm mainly comprises fields cultivated with pastures and several crops in rotation; less than 10% of the area consists of noncultivated habitats, including small woods, hedgerows, and field margins. The authors inventoried local species including all native and cultivated plants, samples for a suite of vertebrates and insects, and their parasites and parasitoids. They linked 101 plant species, including six crops, to 459 animal species in 11 networks, whose interactions were either observed or inferred from published records.

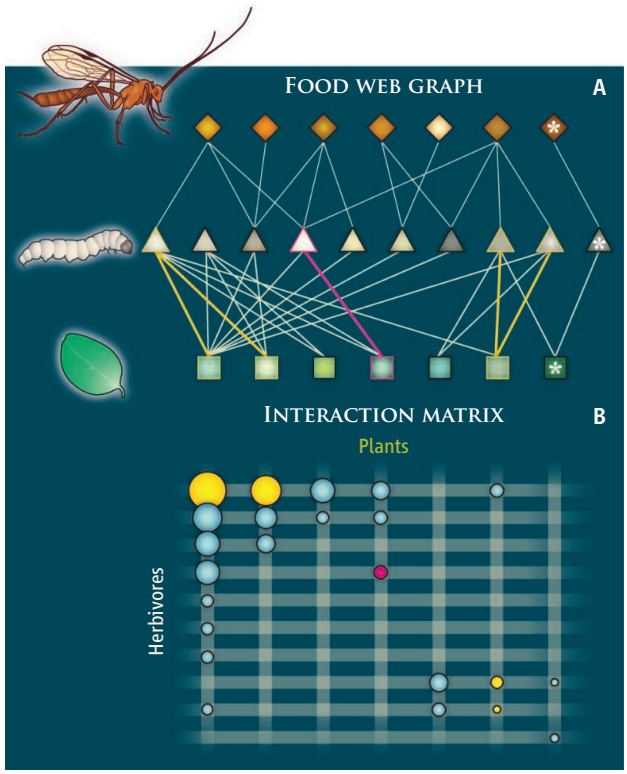

Species interaction networks. (**A**) A food web graph (*14*) with three trophic levels (plants, herbivorous animals, and parasites or parasitoids). Generalist species have more connections than specialists (from left to right), and this web has a nested structure. Stouffer *et al*. decompose entire food web networks into three-species motifs; two example motifs are highlighted in yellow. Pocock *et al*. simulate potential extinction cascades, provoked by the loss of a plant, as illustrated by the starred species on the right. (**B**) Plants and herbivores from panel A are shown as a matrix (*14*). Occupied cells are interaction links; the red ball corresponds to the red link in panel A, and the yellow balls to the example motifs highlighted in yellow in panel A. In this representation, symbol sizes can have different meanings; in Aizen *et al*. they represent the ubiquity of each interaction across all hills. As Aizen *et al*. show, some core interactions (top left corner) from the largest communities lose importance in depauperate communities, being shifted downward and/or to the right in the interaction matrix.

In contrast to other studies, the networks assembled in this agricultural ecosystem not only comprise different kinds of organisms but also span several interaction modes, such as herbivory and parasitism (which are antagonistic), and floral visitation and granivory (which are mostly mutualistic). Pocock *et al*. evaluated the vulnerability of each network to disturbance. Simulating the removal of plant species in many different sequences, they evaluated their cumulative effect in each network by the extent of ensuing animal loss (starred species in panel A of the figure). Flower visitors and insect plant feeders were most sensitive to plant species loss; vertebrate seed feeders and parasitoids suffered far less. Furthermore, different networks did not covary substantially in their dependence on plants, except for sets of parasites and parasitoids and their respective hosts, which channel the effect of plant removal to the higher trophic level. In each network, different sets of plants were most important; however, some plants—keystone species (*11*)—are critical to the maintenance of animals in several networks.

The three studies all strive to assess the importance of individual species to the maintenance of a community, but use different approaches to do so. Pocock *et al*., assuming the primacy of bottom-up effects, projected the domino effects of the loss of each plant species on associated animals. Stouffer *et al*. appraised the value of every species or entity in complete webs by a more elaborate route, which relies on correlating membership and position in particular motifs with the effect of including that motif in model communities. Their simulations enabled the projection of dynamic consequences of removal or addition of each network component. Aizen *et al*. compared sites and communities of different sizes to assess network changes directly, without the need to simulate species removals. By focusing on interactions rather than species, they evaluated changes in community integrity either by loss of interactions or by their displacement from the core of highly connected species to more peripheral positions.

The keystone components—those critically important to the organization and maintenance of communities (*11*)—identified by Pocock *et al*. are plants; in Stouffer *et al*. they are certain taxa according to their preferred positions in networks; and in Aizen *et al*. they are interactions rather than organisms. In focusing on these different entities, practical recommendations derived from these studies will accordingly emphasize distinct aspects of community organization.

Are these results readily applicable to the conservation and management of ecosystems? Although the authors endeavor to provide advice, these are early steps. For instance, as Pocock *et al*. note, farmers are unlikely to adopt enthusiastically the conservation of farm weeds for their keystone conservation value, unless ecosystem services (such as crop pollination or enhanced control of crop pests) are shown to be improved by these measures. The spatial scale for management of keystone components must also be considered; conservation measures are unlikely to be effective at scales smaller than the landscape or regional level.

More broadly, if Stouffer *et al*.'s results are validated by further studies, they raise hopes of foretelling a community's capacity of persistence from its taxonomic profile alone—a triple jump indeed in ecological prediction. However, other recent results suggest otherwise. A regional study in Finland (*12*) showed that network attributes were far more resilient to habitat isolation and fragmentation than was species composition itself. It would be interesting to find out whether motif profiles were also preserved in this case.

The rich variety of results from different approaches shows their individual and complementary value. However, detailed and comprehensive data sets are certainly the scarcest and most critical resource for quantum advances in understanding the dynamics of ecological networks. Pocock *et al*. were able to resort to the large store of recorded infor-

CREDIT: P. HUEY/SCIENCE

Published by AAAS

mation in the United Kingdom to build several networks. In most places, however, these have to be built from scratch, as was done by Aizen *et al*. This requires sound design and planning and is resource-intensive, but it is feasible even in the most difficult conditions, such as lowland tropical rainforests (*13*), and the returns are highly rewarding. Indeed, such data are essential for building a sound bridge between species lists and ecosystem functions—a key priority in ecology.

References

1. D. J. Watts, S. H. Strogatz, *Nature* **393**, 440 (1998).
2. M. Buchanan, *Nexus: Small Worlds and the Groundbreaking Science of Networks* (Norton, New York, 2002).
3. M. Pascual, J. A. Dunne, Eds., *Ecological Networks: Linking Structure to Dynamics in Food Webs* (Oxford Univ. Press, New York, 2006).
4. N. M. Waser, J. Ollerton, Eds., *Plant-Pollinator Interactions: From Specialization to Generalization* (Univ. of Chicago Press, Chicago, 2006).
5. D. B. Stouffer, M. Sales-Pardo, M. I. Sirer, J. Bascompte, *Science* **335**, 1489 (2012).
6. M. A. Aizen, M. Sabatino, J. M. Tylianakis, *Science* **335**, 1486 (2012).
7. M. J. O. Pocock, D. M. Evans, J. Memmott, *Science* **335**, 973 (2012).
8. R. Milo *et al*., *Science* **298**, 824 (2002).
9. D. B. Stouffer, J. Bascompte, *Ecol. Lett.* **13**, 154 (2010).
10. M. Sabatino, N. Maceira, M. A. Aizen, *Ecol. Appl.* **20**, 1491 (2010).
11. R. T. Paine, *Am. Nat.* **103**, 91 (1969).
12. R. Kaartinen, T. Roslin, *J. Anim. Ecol.* **80**, 622 (2011).
13. V. Novotny *et al*., *J. Anim. Ecol.* **79**, 1193 (2010).
14. T. M. Lewinsohn, P. I. Prado, P. Jordano, J. Bascompte, J. M. Olesen, *Oikos* **113**, 174 (2006).

10.1126/science.1220138

PLANT SCIENCE

How Plants See the Invisible

Plants can sense ultraviolet light with a photoreceptor that only contains standard amino acid side chains.

Kevin H. Gardner and Fernando Correa

Light is a key stimulus for biological function, controlling movement, gene expression, development, circadian clocks, and many other activities across virtually every form of life. This regulation is achieved by families of photosensory receptor proteins, each of which converts light of different wavelengths into biochemical signals that can control biological function. This conversion is well understood for photosensors sensitive to visible light (wavelengths λ = 400 to 700 nm), but far less is known about photoreception outside this range. On page 1492 of this issue, Christie *et al*. (*1*) elucidate the mechanism by which plant receptors detect light in the middle of the ultraviolet (UV) portion of the electromagnetic spectrum.

Visible-light photosensors must use small-molecule chromophores such as flavins, retinals, and linear tetrapyrroles as integral parts of their sensory function (*2*). Unlike the 20 natural amino acids, these molecules can efficiently use visible light to undergo photochemical changes, including bond isomerization and addition. These configurational changes trigger allosteric changes in the surrounding protein structure, often affecting interactions between the photosensor and downstream effector domains.

However, plants also use other parts of the electromagnetic spectrum. Forty years ago, Hahlbrock and Grisebach showed that plants irradiated with UV light produce sunscreen-type protective compounds, among other responses (*3*). The discovery of components in a plant signaling pathway triggered by UV-B (λ = 280 to 320 nm) (*4*, *5*) showed that the response is not a result of a general trigger such as DNA damage, but rather is specific to UV irradiation.

How do plants use these proteins to "see the invisible" (*6*)? Christie *et al*. provide an elegant answer to this question. They study UVR8, a component of the UV-B response pathway in *Arabidopsis thaliana*. UVR8 was previously identified as an essential component of the plant UV-B response (*4*, *7*) and exhibits several hallmarks of typical photoreceptors, including a light-dependent interaction with another protein partner (COP1) in the same signaling pathway (*7*).

The central role of UVR8 as the long-sought UV-B photoreceptor was cemented last year when Rizzini *et al*. (*8*) showed that UVR8 undergoes a light-dependent conversion from a dark-state dimer to a lit-state monomer that can interact with COP1. In contrast to all other known photoreceptors, UVR8 was found without any exogenous chromophore. Noting that UVR8 was enriched in aromatic residues with UV-absorbing side chains, the authors hypothesized that several tryptophan residues, predicted to be adjacent to each other in a UVR8 model, might play a critical role in photosensing. Mutating several of these residues to phenylalanine led to defects in light-dependent UVR8 signaling; however, key aspects of the mechanism remained unclear.

Plant UV-B photosensing. UVR8 is a doughnut-shaped molecule that forms a stable dimer in the dark state through a network of salt bridges and aromatic side-chain interactions. Christie *et al*. (*1*) show that excitation of tryptophan residues by UV-B radiation results in the donation of electrons from the aromatic clusters to nearby arginine residue(s), leading to charge neutralization and concomitant dimer dissociation. Once monomeric, UVR8 binds to the partner protein COP1, continuing the signaling pathway.

Department of Biochemistry, University of Texas Southwestern Medical Center, Dallas, TX 75390–8816, USA. E-mail: kevin.gardner@utsouthwestern.edu

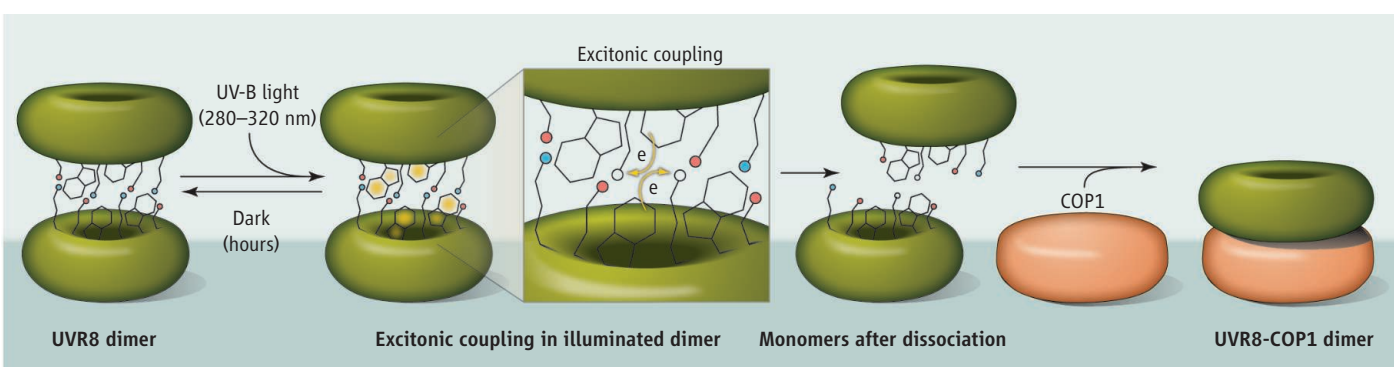

CREDIT: P. HUEY/*SCIENCE*

Published by AAAS

To address these issues, Christie *et al*. combined x-ray diffraction and other biophysical approaches to characterize UVR8 structure and function. The crystal structure of UVR8 showed that in the dark-state dimer of this protein, two seven-bladed β-propeller monomers are packed face-to-face onto each other. This arrangement, validated in solution with x-ray scattering, orients loops from each monomer into the dimeric interface. A number of aromatic side chains point from these loops into the interface, including several of the tryptophan residues implicated in UV-B sensing (*8*). The rest of the interface involves multiple salt bridges, with charged residues instead of the hydrophobic contacts among side chains typically found between protein subunits (*9*). These salt bridges are essential for stabilizing the dark-state dimer; their disruption by point mutation leads to constitutive UVR8 monomerization.

How does the detection of a UV-B photon switch UVR8 from dimer to monomer? Christie *et al*. propose an excitonic coupling mechanism (see the figure) like that used by plants in photosynthetic light harvesting (*10*). In this case, the close packing of multiple aromatic residues at the dimer interface (termed a tryptophan pyramid by the authors) facilitates orbital overlap among these chromophores, producing a distinct signature in the far-UV circular dichroism spectrum of wild-type UVR8 (*11*). Mutating residues in the pyramid affects both excitonic coupling and light-dependent conformational changes, reinforcing the linkage between photon absorption and structure change. Replacement of one member of the tryptophan pyramid (Trp 285) with phenylalanine sensitizes UVR8 to shorter-wavelength UV-C irradiation, consistent with the change in absorption characteristics of these two residue types.

Christie *et al*. note that the pyramid does not stand alone: Several salt-bridged residues are within or adjacent to it, including a critical arginine. The authors hypothesize that electron transfer from the excitonically coupled tryptophan pyramid to these salt-bridged residues is essential for the photosignaling process (see the figure).

UVR8 is fundamentally different from other photoreceptors in its use of standard amino acid side chains instead of specialized chromophores for the initial photochemical event. However, this critical difference belies several similarities, including the spontaneous (albeit slow) recovery of the dimeric form with extended dark-state incubation after illumination. Furthermore, UVR8 allosterically converts photosensing to control protein-protein interactions, as seen among the flavin-based blue light photoreceptors (*12*), among others.

Coupled with similar structure/function studies of UVR8 by Wu *et al*. (*13*), the studies by Rizzini *et al*. (*8*) and Christie *et al*. (*1*) address key questions of UV-B photosensing while opening up new directions for research. Based on homologies with other β-propeller proteins, there are clear predictions as to how COP1 (or other partners) will bind the newly freed UVR8 monomer that await testing. Further mechanistic studies of the UVR8 photochemistry and dark state reversion are needed to understand how the sensitivity and timing of the system are set. Finally, the simplicity of UVR8 light-controlled partner switching may also enable this new photochemistry to be harnessed for new biotechnological applications (*14*).

References and Notes

1. J. M. Christie *et al*., *Science* **335**, 1492 (2012).
2. A. Möglich *et al*., *Annu. Rev. Plant Biol.* **61**, 21 (2010).
3. K. Hahlbrock, H. Grisebach, *Annu. Rev. Plant Physiol.* **30**, 105 (1979).
4. B. A. Brown *et al*., *Proc. Natl. Acad. Sci. U.S.A.* **102**, 18225 (2005).
5. R. Ulm *et al*., *Proc. Natl. Acad. Sci. U.S.A.* **101**, 1397 (2004).
6. P. Vallurupalli *et al*., *J. Am. Chem. Soc.* **130**, 2734 (2008).
7. J. J. Favory *et al*., *EMBO J.* **28**, 591 (2009).
8. L. Rizzini *et al*., *Science* **332**, 103 (2011).
9. Y. Ofran, B. Rost, *J. Mol. Biol.* **325**, 377 (2003).
10. G. D. Scholes, G. R. Fleming, A. Olaya-Castro, R. van Grondelle, *Nat. Chem.* **3**, 763 (2011).
11. I. B. Grishina, R. W. Woody, *Faraday Discuss.* **99**, 245 (1994).
12. B. D. Zoltowski, K. H. Gardner, *Biochemistry* **50**, 4 (2011).
13. D. Wu *et al*., *Nature*; 10.1038/nature10931 (29 February 2012).
14. J. E. Toettcher *et al*., *Nat. Methods* **8**, 35 (2011).

15. We thank W. Briggs and J. Deisenhofer for helpful discussions. This work was supported by grants from NIH (R01 GM081875) and the Robert A. Welch Foundation (I-1424).

10.1126/science.1220248

PALEONTOLOGY

The Hunters Did It

Matt McGlone

Human hunting was responsible for the extinction of large mammal species in tropical Australia.

In the past 100,000 years, many of the largest animals on Earth became extinct. The reasons for these megafaunal extinctions remain contentious (*1*, *2*). In 1967, Martin suggested that within a few hundred years of their arrival, fast-moving bands of hunters eliminated the big game by overkill (*3*). Similarly, Flannery claimed in the 1990s that the current fire-swept Australian landscape with its impoverished soils was created by human elimination of massive marsupial browsers and grazers (*4*, *5*). However, a diverse array of counter-hypotheses has been proposed; the leading argument is that habitat loss through climate change or fire was the critical blow to many large animals (*6*). The loss of 55 large mammal species in Australia (see the figure), shortly after humans arrived ~45,000 years ago (*7*), provides a key test case. On page 1483 of this issue, Rule *et al*. (*8*) present new results from tropical Australia supporting the idea that hunting alone was responsible.

The sparse distribution and poor dating of megafaunal sites have been the greatest obstacles to resolving the late Pleistocene extinction controversy. In recent years, the problem of how to track megaherbivore change has been addressed by use of the coprophilous fungus *Sporormiella*. These fungi grow in herbivore dung; high percentages of their spores in lake or peat deposits show that megaherbivores are abundant nearby (*9*).

Rule *et al*. have generated a 130,000-year record of *Sporormiella* spores, pollen, and charcoal from Lynch's Crater, a volcanic maar in Queensland, Australia, that was surrounded by tropical rainforest until European settlement. From 130,000 to 41,000 years ago, rainforest and sclerophyll forest dominated, with a steady input of *Sporormiella* spores and very low charcoal levels. About 41,000 years ago, *Sporormiella* dropped abruptly to low values, indicating the absence of megaherbivores. At the same time, incidence of fire increased, as evidenced by a steep rise in charcoal fragments. The pollen record shows that these changes were followed by expansion of grassy, eucalypt-dominant sclerophyll forest and eventual loss of rainforest conifers.

Habitat change cannot have been responsible for the loss of the large marsupsials, because the grassy sclerophyll forest expanded only after the *Sporormiella* decline. Furthermore, both climate and veg-

Landcare Research, Lincoln, 7640 New Zealand. E-mail: mcglonem@landcareresearch.co.nz

Extinct after human arrival. Australia once had a diverse range of large marsupial browsers, such as this 150-kg kangaroo *Sthenurus*. Along with 54 other mammal species 10 kg or more in weight, it became extinct shortly after the arrival of humans ~45,000 years ago. Rule *et al*. show that these extinctions can be attributed to human hunting alone.

CREDIT: PETER MURRAY; WITH PERMISSION BY CHRIS JOHNSON/UNIVERSITY OF TASMANIA

etation had been stable for the previous five millennia. It is thus difficult to argue, as some have (*2*), that progressive drying of the climate was largely responsible for the megaherbivore collapse.

The argument can, however, be made that the initial hunting of large, keystone herbivores increased the fuel load, thus permitting more severe fires and leading to extinctions through habitat loss. Did megaherbivore decline lead to more fire in Queensland as Rule *et al*. suggest?

The best evidence for fire and megaherbivore interactions comes from savannah ecosystems, where the loss of elephants, rhinoceroses, and other large browsers and grazers leads to elimination of forest glades and spread of tall, fire-promoting grasslands (*10*). In a dense tropical forest like that in Queensland, it is unlikely that a similar sequence of events could follow megaherbivore elimination. Such forests have little leaf biomass within terrestrial herbivore reach, and thus regrowth of the understory would have little effect on fire potential (*7*). Similar rainforests in Fiji and other Pacific islands that had no megaherbivores persisted even under low rainfall until the arrival of humans (*11*). The documented extinction of a rainforest conifer and the severe restriction of conifer-dominated rainforest after human arrival suggests that the Queensland forests were hypersensitive to fire and had been little exposed to it until then (*12*). Human-lit fires, which are often targeted in space and time to have the greatest effect on vegetation, were most likely the key factor in the subsequent switch to sclerophyll.

The Australasian megafaunal extinction story now seems clear. Shortly after their arrival, small bands of hunters had a devastating effect on large animals, whether it was ~41,000 years ago in Australia or ~750 years ago in New Zealand (*13*). Any climate change at those times was modest and highly unlikely to affect the outcome. Fire and massive biome disruption followed human arrival in regions where there had previously been little or no fire, such as wet tropical Queensland and eastern New Zealand. But large animals were eliminated just as efficiently from regions with dense, untouched rainforests, such as New Guinea and western Tasmania (*7*). Human hunting was a new, more intense form of predation that was particularly dangerous for large, slow-breeding animals. Human-lit fire, deliberately targeted in space and time and an order of magnitude more frequent than natural lightning ignitions, had a devastating effect on plants hitherto protected by climate and location.

What happened in Australia and adjacent island groups has implications for North America and Eurasia. No fewer than 13 separate hypotheses have been distinguished for the North American extinctions (*14*). Most current work has been cautiously interpreted to allow a role for climate change or ecosystem change in the extinction of megaherbivores (*6*, *15*). A recent modeling study of global megafaunal extinctions follows this trend by arguing for near equivalence of climate and human factors (*16*). However, the coarse resolution of the study and lack of local climate or vegetation factors make it of questionable relevance. The Australasian records clearly show that human hunting alone, on a continental scale at a time of only slight climate and vegetation change, is sufficient to eliminate megaherbivores. Contemporaneous substantial climate and vegetation changes could have sped up or slowed the rate at which the megaherbivores were eliminated in other regions, but are unlikely to have altered the final outcome.

The central question now shifts to the ecosystem effects of eliminating large herbivores while increasing targeted, more frequent fire (*17*). Large herbivores are more efficient than fire at recycling nutrients. They encourage some fast-growing or well-defended plants and disadvantage others. They disperse seeds and spores. To what extent were these functions picked up by other, smaller herbivores? Do global ecosystems function differently now that megaherbivores are gone and human-lit fires are common? New results strongly suggest that they do. Human-lit fires removed drought-adapted Australian woodlands and grasslands, replacing them with fire-adapted chenopod/desert scrub and grassland (*18*). In North America, broadleaf forests of a composition not seen before, and not matched in the present-day vegetation, sprang up shortly after the megafaunal decline, and reduced herbivory has been implicated in this change (*15*). More results are needed from South America, Asia, and Europe to elucidate the effects of megaherbivore declines in different settings and at different times.

References

1. D. K. Grayson, *J. Anthropol. Res.* **63**, 185 (2007).
2. S. Wroe, J. Field, *Quat. Sci. Rev.* **25**, 2692 (2006).
3. P. S. Martin, in *Pleistocene Extinctions: The Search for a Cause*, P. S. Martin, H. E. J. Wright, Eds. (Yale Univ. Press, New Haven, CT, 1967), pp. 75–120.
4. T. F. Flannery, *Archaeol. Oceania* **25**, 45 (1990).
5. T. Flannery, *The Future Eaters* (Reed Books, Melbourne, 1994).
6. E. D. Lorenzen *et al*., *Nature* **479**, 359 (2011).
7. C. Johnson, *Australia's Mammal Extinctions: A 50,000 Year History* (Cambridge Univ. Press, Cambridge, 2006).
8. S. Rule *et al*., *Science* **335**, 1483 (2012).
9. R. S. Feranec, N. G. Miller, J. C. Lothrop, R. W. Graham, *Quat. Int.* **245**, 333 (2011).
10. N. Owen-Smith, *Paleobiology* **13**, 351 (1987).
11. G. Keppel, M. V. Tuiwawa, *N.Z. J. Bot.* **45**, 545 (2007).
12. A. P. Kershaw, S. C. Bretherton, S. van der Kaars, *Palaeogeogr. Palaeoclimatol. Palaeoecol.* **251**, 23 (2007).
13. D. B. McWethy *et al*., *Proc. Natl. Acad. Sci. U.S.A.* **107**, 21343 (2010).
14. G. S. Robinson, L. Pigott, D. A. Burney, Burney, *Ecol. Monogr.* **75**, 295 (2005).
15. J. L. Gill, J. W. Williams, S. T. Jackson, K. B. Lininger, G. S. Robinson, *Science* **326**, 1100 (2009).
16. G. W. Prescott, D. R. Williams, A. Balmford, R. E. Green, A. Manica, *Proc. Natl. Acad. Sci. U.S.A.*; 10.1073/pnas.1113875109 (2012).
17. D. A. Burney, T. F. Flannery, *Trends Ecol. Evol.* **20**, 395 (2005).
18. G. H. Miller *et al*., *Science* **309**, 287 (2005).

10.1126/science.1220176

ENGINEERING

Searching for a Better Thermal Battery

Improved materials for storing heat could save energy in applications such as heating and cooling and could enhance generation from solar thermal plants.

Ilan Gur,[1,2] Karma Sawyer,[1] Ravi Prasher[1,3]

Energy storage has mainly focused on electrochemical systems (*1*). However, more than 90% of the world's primary energy generation is consumed or wasted thermally. Thermal energy storage has a broad and critical role to play in making energy use more sustainable for heating and cooling, solar energy harvesting, and other applications. Thermal storage technologies are still based on solutions developed decades ago, such as molten salt, ice, and paraffin phase-change systems, whose performance and cost do not merit wider-scale adoption. Progress in materials science, chemistry, and engineering may lead to dramatic breakthroughs in thermal energy storage that could improve the efficiency with which we produce, distribute, and consume energy.

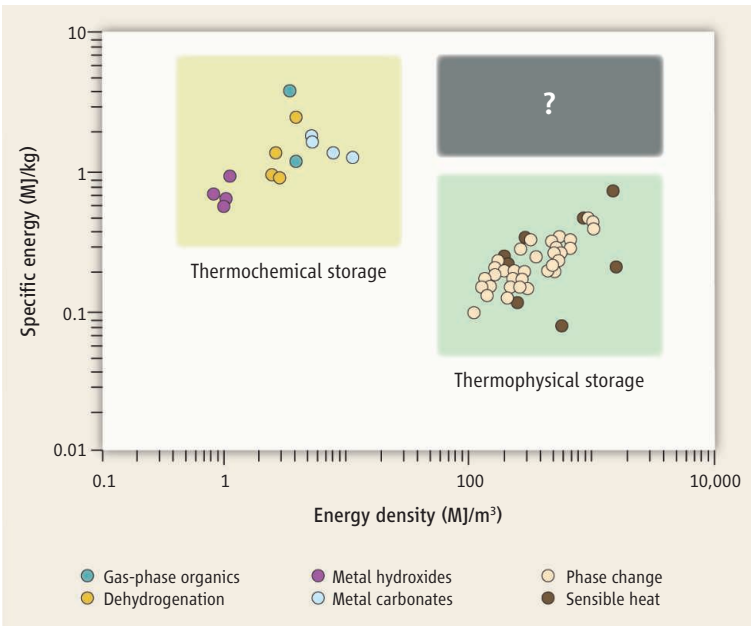

Energy density of various thermal batteries. Theoretical volumetric and gravimetric energy densities for leading thermal storage materials are plotted, illustrating the distinct advantages of thermochemical and thermophysical approaches. The energy densities have been calculated for a wide range of temperatures. As a point of reference, the active materials in a state-of-the-art lithium ion battery have volumetric and gravimetric energy density of roughly 5000 MJ/m^3 and 1.3 MJ/kg, respectively; no existing thermal energy storage material has comparable performance. New materials and system designs that achieve performance metrics in the gray region at the upper right could enable wider adoption of thermal batteries.

Thermal storage materials can be broadly grouped into two classes, thermophysical and thermochemical. Thermophysical approaches rely on changes in a system's physical state and use sensible heat (by increasing the temperature of the storage material), latent heat (absorbed at a constant temperature, as in a phase change), or both. For example, storing solar energy by heating molten salts is currently used to extend output and reduce production cost of solar thermal power plants (*2*). In thermophysical systems, thermal insulation is needed to minimize heat losses to the environment. In thermochemical approaches, chemical reactions reversibly store energy without a need for insulation. Despite the advantages of enabling high energy density and insulation-free long-term storage, thermochemical technologies have yet to be widely used.

One key performance metric for any energy storage technology is energy density. In the figure, we plot the theoretical volumetric and gravimetric energy densities for approximately 50 thermal storage materials. The data illustrate the limitations of each of the two classes of thermal storage. Thermophysical storage relies primarily on liquids and solids and offers high volumetric energy density but low gravimetric energy density. Thermochemical systems generally contain at least one gas-phase component, affording light weight but requiring large volume in the absence of mechanical compression. If mechanical compression is used, it can reduce the system-level gravimetric energy density and also the round-trip efficiency of storage. An example of a reaction that is often suggested for thermochemical storage is $CaCO_3 \leftrightarrow CaO + CO_2$.

The recently developed ARPA-E High Energy Advanced Thermal Storage (HEATS) program (*3*) illustrates that new thermal storage materials that achieve best-in-class gravimetric and volumetric performance simultaneously could enable several new energy applications. In buildings, modular on-demand heating and cooling could reduce or eliminate the use of inefficient centralized air conditioning. Advanced high-temperature solar thermal plants could integrate thermal storage directly into concentrating dishes. This approach offers a low-cost solution to solar intermittency while increasing the capacity factor of the power block and thus reducing the levelized ("break-even") cost of electricity.

Electric vehicles, which today can draw as much as 35 to 40% of their electrical battery capacity for cabin heating and cooling, could dramatically increase their driving range by using a separate thermal battery, charged from the grid or waste-heat sources, for cabin conditioning (*4*). Even conventional combustion-engine vehicles could use thermal storage to avoid cold-engine starts, which can temporarily reduce fuel efficiency by 10% or more, depending on the ambient temperature (*5*). When connected to the electricity grid, thermal storage would offer the added benefit of load shifting for applications such as air conditioning or refrigeration (*6*), or it could be used directly to store electricity from the grid (*7*).

[1]Advanced Research Projects Agency, U.S. Department of Energy, 1000 Independence Avenue SW, Washington, DC 20585, USA. [2]Energy Institute, Haas School of Business, University of California, Berkeley, CA 94720, USA. [3]School for Engineering of Matter, Transport and Energy, Arizona State University, Tempe, AZ 85287, USA. E-mail: ilan.gur@hq.doe.gov; karma.sawyer@hq.doe.gov; ravi.prasher@hq.doe.gov

Published by AAAS

Irrespective of the storage mechanism, a breakthrough will depend on finding a reversible phenomenon with a high enthalpy change based on components with low molecular weight and high volumetric density. Recent advances in flexible design and synthesis of new materials offer an exciting set of possibilities. For example, the versatility of metal-organic frameworks and ionic liquids is now being exploited to modulate binding energies and adsorptivity of adsorbents (*8*, *9*). Condensed-phase chemical reactions can store thermal energy in covalent bonds or through the entropy of mixing of condensed phases. One possible approach could be the exploration of entirely condensed phase reactions of relatively small organic molecules (*10*). High-density isomerization reactions may show renewed potential for thermal storage; a recent calculation on the photoisomerization of azobenzene suggests that stored volumetric energy density could be enhanced by nearly four orders of magnitude (approaching the energy density of lithium ion batteries) by anchoring the molecules on carbon nanotube templates (*11*). Lastly, binary mixtures of fluids have shown anomalous enhancements in heat capacity near the critical point (*12*), which, in combination with recent advances in high-strength materials, may enable the use of supercritical fluids as a storage medium.

Practical thermal storage solutions not only need high energy density but must operate in the appropriate temperature range and provide sufficient power, cycle life, and efficiency for a given application. Optimization of these factors requires that new materials be coupled with advanced engineering designs and system-level innovations, such as novel direct-contact heat exchangers or thermally conductive nanoscale binders for efficient thermal power delivery. Despite these challenges, a key metric for commercial viability—cost—is one area where thermal systems may have an inherent advantage over electrochemical or mechanical energy storage, given the potential for solutions based on simple active chemistries and purely thermal systems with no moving parts.

References and Notes

1. M. Armand, J. M. Tarascon, *Nature* **451**, 652 (2008).
2. E. Cartlidge, *Science* **334**, 922 (2011).
3. http://arpa-e.energy.gov/ProgramsProjects/HEATS.aspx
4. R. Farrington, J. Rugh, *Impact of Vehicle Air-Conditioning on Fuel Economy, Tailpipe Emissions, and Electric Vehicle Range* (NREL/CP-540-28960, 2000; www.nrel.gov/docs/fy00osti/28960.pdf).
5. K. Kunze, S. Wolff, I. Lade, J. Tonhauser, *A Systematic Analysis of CO_2-Reduction by an Optimized Heat Supply During Vehicle Warm-Up* (SAE paper 2006-01-1450, 2006; http://papers.sae.org/2006-01-1450).
6. J. Taneja *et al.*, *Toward Cooperative Grids: Sensor/Actuator Networks for Renewables Integration* (Proceedings of IEEE SmartGridComm, 2010; http://ieeexplore.ieee.org/xpl/freeabs_all.jsp?arnumber=5621992).
7. R. Laughlin, *Powering the Future* (Basic Books, New York, 2011), pp. 94–98.
8. R. Bannerjeei *et al.*, *Science* **319**, 939 (2008).
9. B. E. Gurkan *et al.*, *J. Am. Chem. Soc.* **132**, 2116 (2010).
10. H. Kwart, K. King, *Chem. Rev.* **68**, 415 (1968).
11. A. M. Kolpak, J. C. Grossman, *Nano Lett.* **11**, 3156 (2011).
12. P. Losada-Perez *et al.*, *J. Chem. Phys.* **132**, 154509 (2010).

Acknowledgments: We thank A. Gidwani for help with the figure.

10.1126/science.1218761

NEUROSCIENCE

The Imaginary Mind of a Mouse

Can the brain combine a previous memory into a current situation, creating the memory of an imaginary experience?

Richard G. M. Morris and Tomonori Takeuchi

It is commonplace to say teasingly of others that they live in an imaginary world. They go about their daily life much as others, but their thoughts and recollections have a surreal air—as if they lived in a world that is some combination of their imagination and the objective events of the physical world around them. Consider an experiment that deliberately creates this scenario, in which memories formed reflect not only the objective physical context of the study, but also imaginary "internal" stimuli that have somehow been artificially induced in the subject. Such a study could provide insights into the subtle interactions in cognition that occur between representations of the physical world and our internal thoughts. On page 1513 of this issue, Garner *et al*. (*1*) use elegant chemical and genetic engineering technology to peer into this aspect of the mind of a mouse.

Garner *et al*. exploited the natural neural activity of a mouse's brain that induces expression of the immediate early gene *c-fos* (one that responds rapidly to different stimuli). Mice were genetically engineered such that neurons with activated *c-fos* (which encodes a transcription factor) express a G protein–coupled receptor called hM_3D_q in brain cells, thereby labeling the cells with the receptor. Given later, the drug clozapine-*N*-oxide (CNO) can activate this receptor in neurons, causing membrane depolarization and cell firing (*2*). Over a short period of time, the neurons artificially activated by CNO will reflect the patterns of *c-fos* activation that occurred earlier in those neurons expressing hM_3D_q receptors. These patterns will, in some sense, reflect a memory of past experience as the mouse goes about its behavior in a test chamber where this part of the study is conducted. In such a scenario, giving CNO later in a different place will reactivate the same neurons in which hM_3D_q receptor expression had previously been induced.

The advantage of CNO-driven hM_3D_q receptor activation is the ability to activate specific spatial patterns of neurons. By contrast, intracranial electrical stimulation nonspecifically activates all neurons in the vicinity of the tips of the wire. Optogenetic stimulation, in which neural activity is controlled by light, can be cell type–specific (*3*) but produces no spatial pattern. Although it is possible that CNO may activate additional cells that do not express hM_3D_q receptors, the mouse should nonetheless imagine that it is somewhere other than where it is currently located.

Garner *et al*. subjected mice to fear conditioning, a standard test in which animals first explore a test chamber for a period of time, become familiar with it, and then later receive one or more mild electric shocks. Typically rodents display a "freezing" reaction when they are put back into this same context for a memory retrieval test, reflecting the fear that has been conditioned to the box earlier. This type of learning involves both the amygdala and the hippocampus. The procedure involved first exposing animals to a test chamber (context A) to label active neurons with hM_3D_q receptors (see the figure). After a day, the mice were treated with CNO and then put into a physically different test chamber (context B) for the learning trial. This sequence of events juxtaposes the animal's "internal remembrances" about one context (the CNO-induced neural activation; context A) with its internal sen-

Centre for Cognitive and Neural Systems, University. of Edinburgh, Edinburgh EH8 9JZ, Scotland, UK. E-mail: r.g.m.morris@ed.ac.uk; tomonori.takeuchi@ed.ac.uk

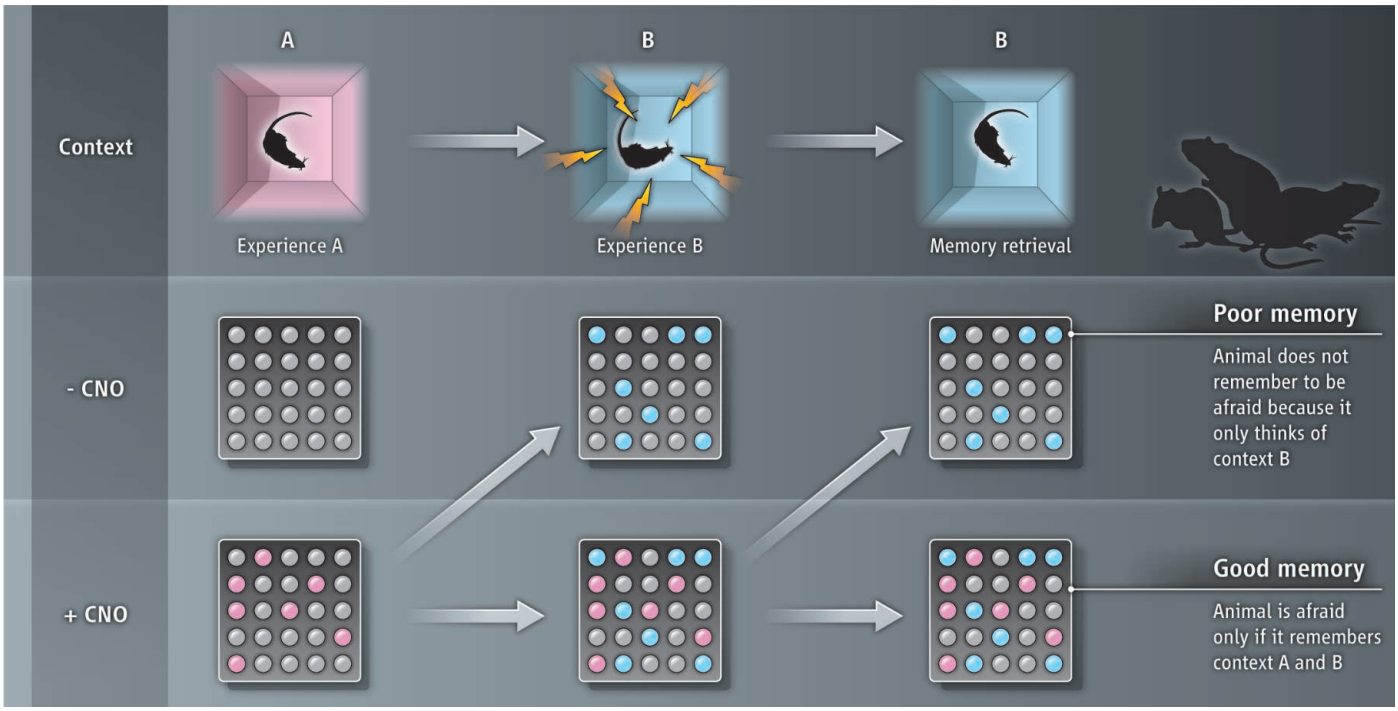

Hybrid memory. The memory of context A is first marked in a chemically genetic manner (pink neurons). This memory is then activated using the drug CNO while the animal is in a different place—context B (blue neurons)—and subject to fear conditioning. Later memory retrieval is only successful if the animal remembers both contexts A and B (pink and blue neurons). Had CNO not been present at retrieval, the pattern of neuronal firing would have been different.

sory representations of the objective context in which the fear conditioning actually takes place (context B). An intriguing result emerged: Fear conditioning occurred to the combined cue of the second test chamber and the animals' imaginary representations of the first chamber. Either cue alone did not elicit freezing, but both together did do so. This could be because only the combined cue entered into associative learning, or because neural representation of either test chamber flickered rapidly back and forth (*4*).

To narrow down the possible interpretations of this observation, Garner *et al*. established that activation of a remembrance of a prior test chamber can also interfere with other conditioned memories, as well as operate synergistically. The authors also examined whether CNO activation of hM_3D_q receptors operates like a "diffuse" internal state akin to the manner in which an emotion such as sadness can modulate memory (*5*). In these cases, the internal state serves only to "modulate" or set the occasion for the expression of other memories but does not enter directly into an association. This was ruled out by conditioning the mice in test chamber B with a co-occurrent CNO-induced pattern of neural activation of an earlier test chamber A, then allowing the hM_3D_q receptor expression pattern for chamber A to degrade over time, inducing a new pattern of hM_3D_q expression in a further test chamber C, and finally attempting to retrieve the fear-conditioned memory of B + A in the presence of a potentially different internal pattern—namely that of B + C. The "state dependence" idea predicts effective retrieval, because cue states A and C would be similar and merely modulate the retrieval of the memory of test chamber B, whereas the "specificity" hypothesis predicts a blockade of retrieval. The latter result was observed. These and other control studies point to an apparently exquisite neural ensemble specificity induced by the technique of CNO-mediated activation of hM_3D_q in a spatially and temporally restricted manner.

The study of Garner *et al*. shows how chemical and genetic engineering techniques are addressing questions of systems neuroscience. Considerable excitement has long surrounded the use of new techniques from another discipline (e.g., medical physics) to help address key questions in neuroscience (such as using human brain imaging). Less well known is when techniques at one level of analysis—molecular, cellular, network, or whole brain—can help to answer questions at another level [such as work on pattern completion and pattern separation in distributed networks (*6*)]. And every new technique has its advantages and its drawbacks—the limitation with the approach of Garner *et al*. being the apparent preservation of the spatial pattern of neural activation at the cost of losing the temporal dynamics. But if this is taken into account, there may still be the opportunity to use the approach of Garner *et al*. to address some fundamental questions about neural representations in cognitive processing that have hitherto proven elusive. For example, new research on the role of schemas in memory encoding, assimilation, and consolidation (*7*) indicate that existing network activity is important for relevant new learning. This concept might be taken further using CNO-driven hM_3D_q receptor activation to distinguish, in a subset of cortical cells, between the mere presence of a trained but silent schema and the presence of a neurally activated schema. Human memory studies suggest that only the latter enables effective learning of new information (*8*). Investigating schema activation in animal studies may no longer be as difficult.

References

1. A. R. Garner *et al*., *Science* **335**, 1513 (2012).
2. G. M. Alexander *et al*., *Neuron* **63**, 27 (2009).
3. L. E. Fenno, O. Yizhar, K. Deisseroth, *Annu. Rev. Neurosci.* **34**, 389 (2011).
4. K. Jezek, E. J. Henriksen, A. Treves, E. I. Moser, M. B. Moser, *Nature* **478**, 246 (2011).
5. G. H. Bower, K. P. Monteiro, S. G. Gilligan, *J. Verbal Learn. Verbal Behav.* **17**, 573 (1978).
6. T. Nakashiba *et al*., *Cell*; 10.1016/j.cell.2012.01.046 (2012).
7. D. Tse *et al*., *Science* **333**, 891 (2011).
8. J. D. Bransford, *Human Cognition: Learning, Understanding and Remembering* (Wadsworth, Belmont, CA, 1979).

10.1126/science.1220824

CREDIT: C. BICKEL/*SCIENCE*

RETROSPECTIVE

Oscar Miller (1925–2012)

An unconventional molecular biologist used the electron microscope to take snapshots of active genes.

Steven McKnight,[1] Ann Beyer,[2] Joseph Gall[3]

Oscar Lee Miller Jr. died on 28 January 2012 in Charlottesville, Virginia, at the age of 86. He was a "magician" of molecular cytology, whose stunning views of active genes provided new insights into gene expression. His important glimpses opened the doors for exploring numerous fundamental questions about chromosomes.

Oscar was born in 1925 in Gastonia, North Carolina. His path to scientific research was unusual. After serving 3 years in the U.S. Navy during World War II, he earned a bachelor's and master's degree in agronomy at North Carolina State University. He then became a tobacco farmer in North Carolina for 6 years. Unsatisfied with this life, he enrolled at the University of Minnesota, where he earned a doctoral degree in plant genetics (focusing on corn). His postdoctoral work included research with one of us (J.G.) in the Zoology Department at Minnesota where he was interested in chromosome structure. Because we were nearly the same age, we were not so much mentor and student as enthusiastic collaborators. In 1961, at the age of 36, Oscar took his first independent position at Oak Ridge National Laboratory. In the ensuing decade, he wove his magic, perfecting a technique that allowed visualization of active genes with the electron microscope. His most famous paper was coauthored with his technician, Barbara Beatty, in 1969. The phrase "a picture is worth a thousand words" aptly describes the electron micrograph of ribosomal RNA (rRNA) genes that graced the cover of *Science* 43 years ago.

In the 1960s, it was known that DNA was the genetic material, and the central dogma had become, "DNA makes RNA makes protein." What was not known, particularly for eukaryotes, was the size of the genes, whether they had distinct beginning and end points, and how they engaged RNA polymerase molecules. Oscar's technique clarified all these issues. Simple inspection of active rRNA genes immediately revealed that they had discrete starting and stopping points—the tips and bases of the serially repeated "Christmas trees." The existence of nontranscribed spacers between genes was evident, and a ruler could be put to the micrograph to measure the size of genes. One could count the number of genes along the chromosome. One could see that the rRNA genes were all in the same orientation and that each gene was simultaneously transcribed by hundreds of RNA polymerases. Remarkably, these watershed observations were made four decades before the dawn of genomics. In one fell swoop, Oscar Miller revealed the anatomy of a gene.

What else was learned from this technique—the "Miller Chromatin Spread"—in which a cell's DNA is spread out for viewing by an electron microscope? Oscar's laboratory soon discovered that transcription and translation are coupled in bacterial operons, regions of DNA containing a cluster of genes controlled by a single regulatory apparatus. Ada and Donald Olins described "Nu bodies," beads on a string that turned out to be the fundamental structural units of chromatin, now called nucleosomes. Yvonne Osheim visualized amplified chorion genes in the oocytes of the fruit fly *Drosophila melanogaster*, supporting the "onion skin" model of gene amplification predicted by Allan Spradling (the re-replication of a gene occurs in a single cell cycle). The list of discoveries coming from Oscar's technique goes on and on, providing a lasting legacy—our shared mental image of active genes. Textbooks need not include schematics of these beautiful micrographs because the real thing is so crystal clear.

How did Miller invent the technique? First, he held the passionate belief that it should be possible to see genes up close and personal, an idea that was wildly unconventional a half-century ago. Although he employed technically sophisticated methods of electron microscopy (EM), it was his treatment of the cell nucleus that was the magic of his success; he simply dissolved it in distilled water. The nuclear contents were then centrifuged directly onto the EM grid, dried, stained, and visualized. Simple, yes, but the trial and error required to accomplish the feat took skill, fortitude, and creative thinking. Had Miller not made this discovery, how much longer would it have taken for another scientist to do so—or would we never have had these remarkable images?

Oscar Miller was recognized in many ways, including election to the U.S. National Academy of Sciences. Fittingly, this scientific adventurer held the Lewis and Clark chair at the University of Virginia (UVA), an endowment named for the two most celebrated adventurers in U.S. history. Miller chaired the Department of Biology at UVA and mentored many graduate students, postdoctoral fellows, and young faculty members. Those of us so fortunate as to have worked under his guidance learned how to think freely, yet rigorously, and how to dream big and gamble on new adventures. We learned from Oscar how to free ourselves from convention, yet abide by the principles of science as crafted by its most honorable pillars. We remember two pieces of advice given by Oscar: "Don't believe everything you read in the scientific literature" and "There are a thousand Ph.D. thesis projects in a mound of dung." The latter brings to mind the famous phrase of Vannevar Bush that science is an "endless frontier." Oscar Miller was comfortable on the frontier of the unknown; he taught us that it is only on the frontier that discoveries of significance can be made. Our community of science will miss Oscar, as will all his dear friends and family. A good man has passed.

10.1126/science.1220681

[1]Department of Biochemistry, University of Texas Southwestern Medical Center, Dallas, TX 75390, USA. [2]Department of Microbiology, University of Virginia, Charlottesville, VA 22904, USA. [3]Department of Embryology, Carnegie Institution for Science, Baltimore, MD 21218, USA. E-mail: steven.mcknight@utsouthwestern.edu

CREDIT (TOP TO BOTTOM): DAVID SKINNER/UNIVERSITY OF VIRGINIA; OSCAR MILLER AND BARBARA BEATTY/OAK RIDGE NATIONAL LABORATORY

Photoacoustic Tomography: In Vivo Imaging from Organelles to Organs

Lihong V. Wang* and Song Hu

Photoacoustic tomography (PAT) can create multiscale multicontrast images of living biological structures ranging from organelles to organs. This emerging technology overcomes the high degree of scattering of optical photons in biological tissue by making use of the photoacoustic effect. Light absorption by molecules creates a thermally induced pressure jump that launches ultrasonic waves, which are received by acoustic detectors to form images. Different implementations of PAT allow the spatial resolution to be scaled with the desired imaging depth in tissue while a high depth-to-resolution ratio is maintained. As a rule of thumb, the achievable spatial resolution is on the order of 1/200 of the desired imaging depth, which can reach up to 7 centimeters. PAT provides anatomical, functional, metabolic, molecular, and genetic contrasts of vasculature, hemodynamics, oxygen metabolism, biomarkers, and gene expression. We review the state of the art of PAT for both biological and clinical studies and discuss future prospects.

Optical imaging of tissue offers potential advantages in distinguishing different structures according to their chemical composition. Because tissue is a highly scattering medium for electromagnetic waves in the optical spectral range, methods that attempt to form images from light passing through tissue fall into two categories—ballistic (minimally scattered) optical microscopy and diffuse (multiscattered) optical tomography. The former provides fine resolution but with a low imaging depth in tissue—up to ~1 mm, as defined by the optical diffusion limit (*1*, *2*). When incident photons reach this limit, most of them have undergone tens of scattering events, which scramble the photon paths and inhibit effective optical focusing. In contrast, diffuse optical tomography can probe centimeters into tissue but with poor spatial resolution—equal to about one-third of the imaging depth (*3*). Randomized paths of the diffuse photons render the image reconstruction mathematically ill-posed. It remains a challenge for pure optical imaging to attain fine spatial resolution at depths beyond the optical diffusion limit.

Fortunately, photons in tissue can be converted into ultrasonic waves, which are scattered much less. Absorption of photons by biomolecules thermoelastically induces pressure waves through the photoacoustic effect. Photoacoustic tomography (PAT) forms images by detecting the induced pressure waves. The conversion from optical to ultrasonic energy immediately brings several advantages: (i) PAT breaks through the optical diffusion limit (*4*) by capitalizing on the low acoustic scattering in tissue—about three orders of magnitude less than optical scattering in tissue per unit path length. (ii) PAT enables multiscale high-resolution imaging of biological structures, ranging in size from organelles to organs, using the same contrast. (iii) By exciting different molecules at different optical wavelengths, PAT reveals rich optical contrasts according to chemical composition. (iv) PAT images optical absorption with 100% sensitivity (*5*), two orders of magnitude greater than those of confocal microscopy and optical coherence tomography (*6*). (v) PAT provides inherently background-free detection because the photoacoustic amplitude is proportional to the optical absorption; nonabsorbing tissue components present no background. (vi) Unlike fluorescence imaging, PAT ensures no leakage of excitation photons into detectors. (vii) Unlike optical coherence tomography and ultrasonography, PAT is speckle-free (*7*). (viii) All molecules are optically absorbing at some wavelengths and can potentially be imaged by PAT, whereas far fewer molecules are fluorescent. Although both conventional ultrasound imaging and PAT are based on ultrasonic detection, the former measures only mechanical contrasts and the latter optical and thermoelastic contrasts.

PAT has been developed rapidly in the past decade, with applications explored in vascular biology (*8*, *9*), oncology (*10*, *11*), neurology (*12*–*14*), ophthalmology (*15*, *16*), dermatology (*17*, *18*), gastroenterology (*19*, *20*), and cardiology (*21*, *22*). Here, we first introduce the fundamentals and three state-of-the-art embodiments of PAT. Next, we highlight the scalability of PAT over four major length scales in biology—covering organelles, cells, tissues, and organs—and show rich photoacoustic contrasts for tissue anatomies and functions as well as for metabolic, molecular, and genetic processes. To conclude, we envision high-impact applications in biomedicine and point out remaining major challenges in PAT.

Fundamentals and Major Implementations

PAT is based on optical excitation and ultrasonic detection. The biological tissue to be imaged is irradiated usually by a nanosecond-pulsed laser beam to engender thermal and acoustic impulse responses. The temporally confined optical absorption induces a temperature rise ΔT and consequently an initial pressure rise p_0 due to thermoelastic expansion: $p_0 = \beta \cdot \Delta T / \kappa$, where β is the thermal expansion coefficient and κ is the isothermal compressibility. Approximately, a temperature rise of 1 mK results in a pressure rise of 800 Pa, which is above the noise level of a typical ultrasonic transducer. As β and κ are beyond our control, it is fortunate that PAT can provide a high signal-to-noise ratio without thermally damaging the tissue. After propagating through the tissue, the pressure wave is detected by an ultrasonic transducer (or a set of transducers) to form a high-resolution tomographic image of optical absorption. Although pulsed lasers are most commonly used, intensity-modulated light sources may be used alternatively (*23*). Currently, PAT has three major implementations: focused-scanning photoacoustic microscopy (PAM), photoacoustic computed tomography (PACT), and photoacoustic endoscopy (PAE). Whereas PAM and PAE usually aim to image millimeters deep at micrometer-scale resolution, PACT can be implemented for both microscopic and macroscopic imaging.

In PAM, both the optical excitation and ultrasonic detection are focused, and the dual foci are usually configured confocally to maximize sensitivity. Each laser pulse produces a one-dimensional (1D) depth-resolved image without mechanical scanning, and 2D transverse scanning generates a 3D image. The axial resolution is determined by the acoustic time of flight, whereas the lateral resolution is determined by the overlap of the dual foci. Quantitatively, the axial and lateral resolutions are defined as the corresponding full widths at half maximum of the system response to a point target. Depending on whether the optical or ultrasonic focus is finer, PAM is further classified into optical-resolution PAM (OR-PAM) (*24*, *25*) and acoustic-resolution PAM (AR-PAM) (*26*).

OR-PAM provides lateral resolution at the subcellular or cellular scale ranging from a few hundred nanometers to a few micrometers (Fig. 1A). If such resolution were to be achieved acoustically, the center frequency of the acoustic signal would have to be at least 300 MHz. At such a high frequency, ultrasonic waves sustain severe propagation loss and can penetrate only a few hundred micrometers in tissue. Fortunately, optical focusing can readily confine the photoacoustic excitation for high lateral resolution while maintaining substantial imaging depth; in addition, acoustic focusing can improve detection sensitivity. This system enables in vivo label-free functional imaging of hemoglobin oxygen saturation (sO_2) in vessels down to single capillaries (Fig. 1A). However, the imaging depth is limited by optical diffusion to 1.2 mm in vivo (*24*).

In OR-PAM (Fig. 1A), the laser beam is focused by a microscope objective to a diffraction-limited spot for excitation in the tissue. An optical-acoustic beam combiner, consisting of two prisms sandwiching a thin layer of silicone oil, is positioned beneath the objective to align the optical

Optical Imaging Laboratory, Department of Biomedical Engineering, Washington University, St. Louis, MO 63130, USA.

*To whom correspondence should be addressed. E-mail: lhwang@wustl.edu

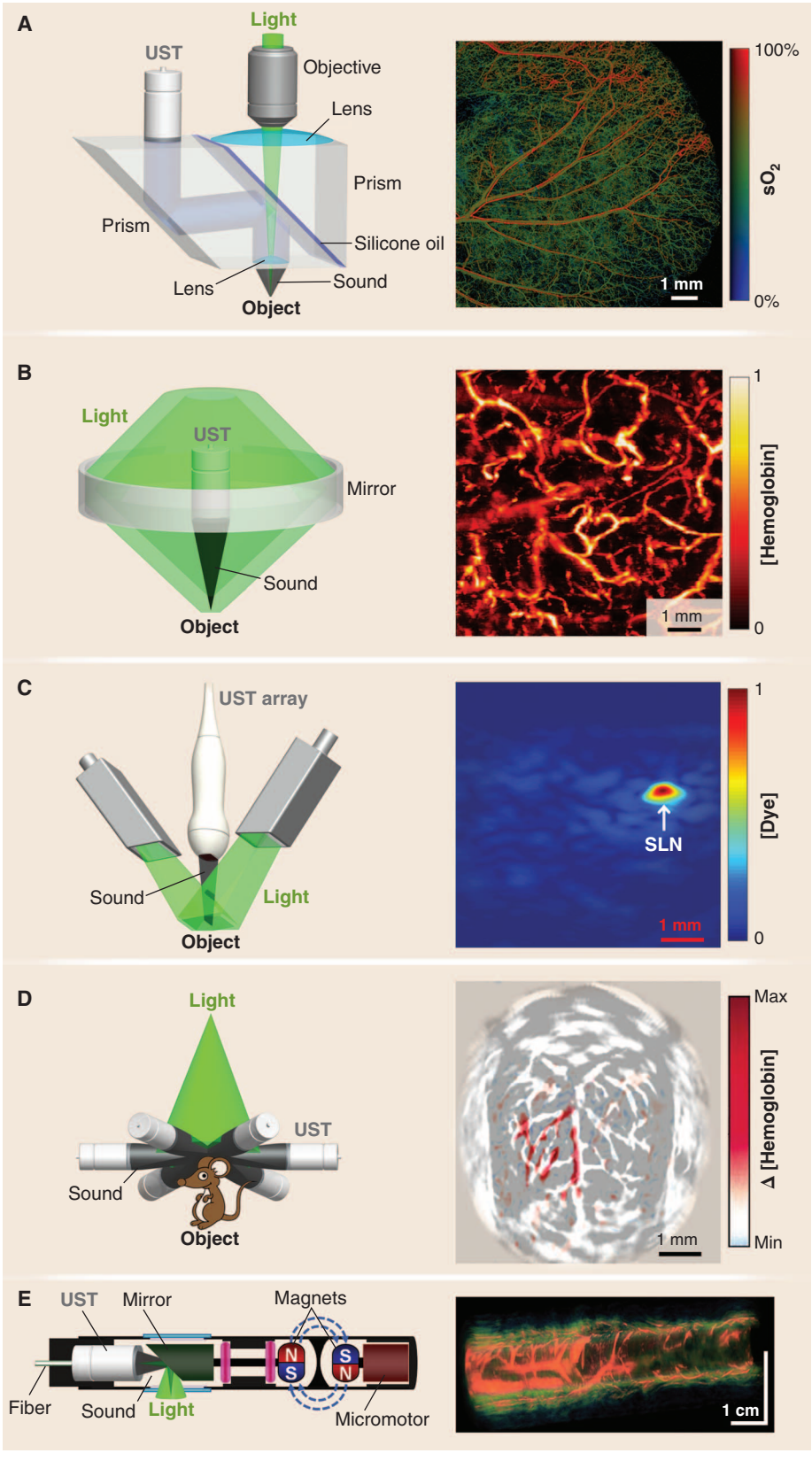

Fig. 1. Major embodiments of PAT, with representative in vivo images. (**A**) OR-PAM of sO_2 in a mouse ear. (**B**) AR-PAM of normalized total hemoglobin concentration, [hemoglobin], in a human palm. (**C**) Linear-array PACT of normalized Methylene Blue concentration, [dye], in a rat sentinel lymph node (SLN). (**D**) Circular-array PACT of cerebral hemodynamic changes, Δ[hemoglobin], in response to one-sided whisker stimulation in a rat. (**E**) PAE of a rabbit esophagus and adjacent internal organs, including the trachea and lung. UST, ultrasonic transducer.

excitation and acoustic detection coaxially and confocally. The matched optical refractive indices but mismatched acoustic impedances between the prism glass and silicone oil provide optical transmission but acoustic reflection. The optical aberration created by the optical transmission through the beam combiner is offset by a correction lens attached to the top surface of the right-angle prism. To focus acoustic detection, a concave acoustic lens is ground into the bottom of the rhomboid prism. An unfocused ultrasonic transducer with a broad bandwidth matching that of the received acoustic waves is attached to the top of the rhomboid prism. Although ideal for light transmission, the solid-liquid interface adversely transforms 85% of the incident acoustic energy from longitudinal waves to shear waves. Because shear waves are not detected with high sensitivity, the rhomboid prism is used to regain the longitudinal wave at the second inclined surface.

At depths beyond the optical diffusion limit and up to a few millimeters, AR-PAM achieves high resolution by taking advantage of the much lower acoustic scattering. Despite diffuse optical excitation, lateral resolution of tens of micrometers is achieved by diffraction-limited acoustic detection. In AR-PAM, optical excitation is implemented through dark-field illumination, as shown in Fig. 1B, for two critical reasons: First, the donut-shaped illumination eliminates otherwise dominant interference signals from the tissue surface. Second, the donut hole is ideal for positioning the ultrasonic transducer coaxially and confocally with respect to the optical excitation. The system provides a 45-μm lateral resolution in vivo with a 3-mm imaging depth. Anatomical images of the human cutaneous microvasculature in both the superficial epidermis and deep dermis have been acquired by detecting hemoglobin (Fig. 1B) (*18*). However, further advancement of the imaging depth to centimeters for macroscopic imaging requires the use of more energetic lasers at low pulse repetition rates. As a result, the transverse scanning becomes too slow for many clinical applications.

To accelerate data acquisition, state-of-the-art ultrasonic array detectors have been used for PACT. The entire region of interest (ROI) is excited by an expanded optical beam, and the photoacoustic waves are simultaneously detected by an ultrasonic array. Then, an inverse algorithm—essentially a method for sophisticated triangulation of photoacoustic sources from the time-resolved acoustic signals—is used to reconstruct a high-resolution image (*27*–*30*). As most ultrasonic arrays are 1D, the 2D resolutions in the imaging plane are derived from reconstruction, whereas the orthogonal resolution comes from cylindrical acoustic focusing. The imaging plane can be further translated along the orthogonal dimension for 3D imaging. According to the anatomy of the organ of interest, the ultrasonic array may be configured linearly (*31*) or circularly (*32*–*34*).

In linear-array PACT (Fig. 1C), a multimode optical fiber bundle is bifurcated to flank the handheld

ultrasonic array for dark-field optical illumination, as in AR-PAM. A single laser pulse—with a safe exposure to the tissue (≤20 mJ/cm^2 in the visible spectral range)—yields a 2D image. A clinical ultrasound imaging system has been adapted for concurrent imaging with PACT. This system, with an axial resolution of 400 μm and a lateral resolution of ~1 mm (*35*), has been used for noninvasive in vivo functional imaging of Methylene Blue–labeled sentinel lymph nodes in small animals (Fig. 1C) (*10*), and more recently in human breast cancer patients (*36*).

Circular-array PACT (Fig. 1D) is designed to accommodate round objects, such as the brain, a peripheral joint, and even the whole body of a small animal. The ROI is encircled by the array to detect photoacoustic waves propagating along all in-plane directions; unlike the partial-view detection (i.e., the angle subtended by the ultrasound detectors with respect to the object is less than 360°) in linear-array PACT, full-view detection provides high-quality images without missing boundaries (*37*). The principle of circular-array PACT was originally demonstrated by circularly scanning a single-element ultrasonic transducer in the first functional PAT system, which imaged the cerebral vascular response to one-sided whisker stimulation in an adult rat through intact scalp and skull with an in-plane resolution of ~200 μm (Fig. 1D) (*14*).

PAE has been intensively investigated in recent years (*19*–*22*, *38*) as a means of imaging internal organs such as the esophagus and colon. In a representative PAE design (Fig. 1E) (*19*), light from a high-repetition-rate laser is delivered by a multimode optical fiber placed in the central hole of a ring transducer. An optically and acoustically reflective mirror, driven by a micromotor through coupled magnets, rotates both the optical illumination and the acoustic detection for circumferential cross-sectional scanning. Further, a linear motor pulls back the entire probe for volumetric imaging. In contrast to conventional optical endoscopy, which has an imaging depth within the optical diffusion limit, PAE has shown a 7-mm imaging depth in the dorsal region of a rat colon ex vivo (Fig. 1E) (*20*).

Multiscale PAT in Vivo: Organelles, Cells, Tissues, and Organs

The elegant marriage between light and sound endows PAT with the unique capability of scaling its spatial resolution and imaging depth across both optical and ultrasonic dimensions. The lateral resolution of OR-PAM is given by $R_{L,OR} = 0.51 \cdot \lambda/NA$, where λ denotes the optical wavelength and NA is the numerical aperture of the microscope objective. Varying the NA can scale the lateral resolution from subwavelength to a few wavelengths, with the imaging depth varied accordingly. With NA = 1.23 and λ = 532 nm, a 220-nm lateral resolution has been achieved with an imaging depth of 100 μm, enabling in vivo subcellular imaging of individual melanosomes (Fig. 2A) (*39*). Halving the NA to 0.63 quadruples the imaging depth while the lateral resolution is still maintained at 500 nm (*40*). Reducing the NA to 0.1 further triples the imaging depth to the optical diffusion limit and relaxes the lateral resolution to 2.6 μm, enabling in vivo label-free functional imaging of individual red blood cells flowing in capillaries (Fig. 2B) (*24*). As in conventional optical microscopes, it is possible to combine multiple optical objectives of different NAs in a single OR-PAM system, which would allow convenient adjustment of the magnification. Further, OR-PAM and AR-PAM systems can be integrated to extend the range of scalability of a single device.

The lateral resolution of AR-PAM or partial-view PACT is given by $R_{L,AR} = 0.71 \cdot v_s/(NA \cdot f_0)$, where v_s is the speed of sound, NA is the acoustic numerical aperture, and f_0 is the photoacoustic center frequency. The center frequency f_0 is determined by the laser pulse width, the targeted tissue depth, and the ultrasonic transducer's frequency response. With f_0 = 50 MHz and NA = 0.44, AR-PAM has achieved a lateral resolution of 45 μm and an imaging depth of 3 mm (*26*). Such a system is adequate to see through human skin lesions in vivo, as required for accurate diagnosis and staging (Fig. 2C) (*18*). Reducing the center frequency to 5 MHz extends the imaging depth to 4 cm and relaxes the lateral resolution to 560 μm (*41*). Because the resolution is now within the resolving power of human eyes, such an instrument is called a photoacoustic macroscope (PAMac). A PACT system based on a clinical linear ultrasound array operating with a frequency band of 4 to 8 MHz has extended the imaging depth to 7 cm, with a submillimeter lateral resolution (720 μm) (*36*). Figure 2D shows a representative in vivo PACT image of the breast vasculature in a human volunteer (*33*). PACT can also perform microscopic imaging when operating at high ultrasonic frequencies (*42*).

The axial resolution of PAM or partial-view PACT always originates from the time of arrival of the acoustic signal. It can be estimated as $R_A = 0.88 \cdot v_s/\Delta f$, where Δf is the photoacoustic bandwidth (approximately proportional to f_0). So far, axial resolutions ranging from 15 to 640 μm have been achieved in PAT systems of various targeted imaging depths (*25*, *36*). The 2D in-plane resolutions of full-view PACT can be similarly estimated with Δf.

Figure 2E summarizes the scalability of PAT. Within the optical diffusion limit, the imaging depth of OR-PAM is approximately proportional to the chosen lateral resolution. Beyond the limit, the imaging depth is primarily determined by the frequency-dependent acoustic attenuation. As both f_0 and Δf are inversely proportional to the desired imaging depth, the lateral and axial resolutions are proportional to the imaging depth. For both

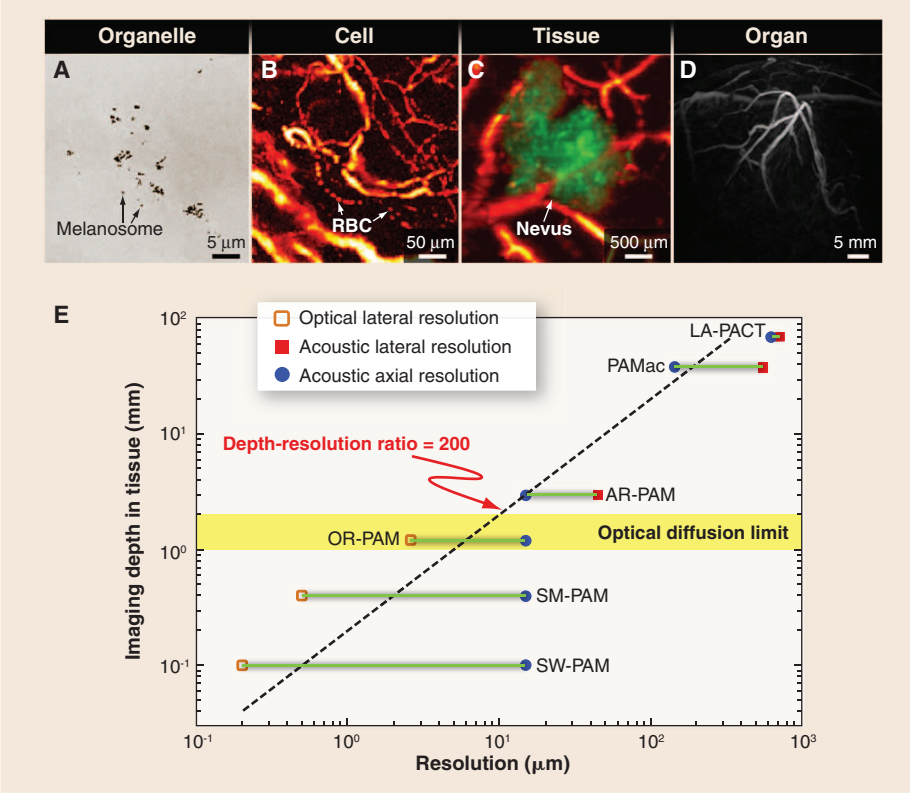

Fig. 2. Multiscale PAT of organelles, cells, tissues, and organs in vivo. (**A**) Subwavelength (SW) PAM of melanosomes in the ear of a black mouse. (**B**) OR-PAM of individual red blood cells traveling along a capillary in a mouse ear. (**C**) AR-PAM of a nevus on a human forearm. (**D**) PACT of a human breast. (**E**) Imaging depth versus spatial resolution in PAT. SM, submicrometer; LA, linear array.

regimes, the ratio of the imaging depth to the best spatial resolution is roughly a constant of 200 (as shown by the slope of the dashed line in Fig. 2E), making PAT a high-resolution modality across all four length scales. The optimal tradeoff between spatial resolution and imaging depth depends on the application.

Multicontrast PAT in Vivo: Anatomy, Function, Metabolism, and Molecular/Genetic Processes

With selected optical wavelengths, PAT can probe a wide variety of endogenous or exogenous absorbers to reveal the anatomy, function, metabolism, and molecular/genetic processes in biological systems in vivo. Endogenously, DNA/RNA, hemoglobin, melanin, water, and lipid are important anatomical and functional contrast agents. Using the strong ultraviolet absorption of DNA and RNA, OR-PAM recently achieved noninvasive imaging of individual cell nuclei (Fig. 3A), which can provide an in vivo label-free substitute for ex vivo hematoxylin and eosin staining histology (*43*). Because malfunction of DNA replication induces abnormal nuclear morphology in cancer, this technology can potentially provide early detection and intraoperative demarcation of cancer. Hemoglobin, as a primary oxygen carrier, is essential to tissue metabolism. Using hemoglobin's predominant optical absorption in the visible range over other absorbers, PAT provides comprehensive anatomical and functional imaging of the blood circulation system (*8*, *44*). Abnormal concentrations of water and lipid can be important disease indicators. Their relatively strong optical absorption in the near-infrared range allows PAT to map their distributions at substantial depths in vivo (*45*, *46*). Melanin, a major pigment in the skin and most melanomas, has broadband optical absorption from the ultraviolet to the near-infrared range, which can be spectroscopically distinguished from hemoglobin absorption by PAT. Simultaneous imaging of the melanoma anatomy and the surrounding vascular function provides an unprecedented opportunity for understanding the interactions between a tumor and its microenvironment and for noninvasively detecting and staging melanoma (Fig. 3B) (*26*).

Exogenous contrast agents further extend PAT to molecular and genetic imaging. Nanoparticles, organic dyes, and reporter gene products can be excellent photoacoustic contrast agents. The primary advantage of gold nanoparticles lies in their large absorption cross section tuned to the optical window (~730 nm), minimizing endogenous absorption and maximizing imaging depth. Moreover, the bioconjugation capability of nanoparticles enables effective biomarker targeting for both molecular imaging (Fig. 3, C and D) (*11*, *47*) and drug delivery. Recently, the use of iron oxide and gold-coupled core-shell nanoparticles as a photoacoustic contrast agent has led to the development of magnetomotive PAT (Fig. 3E) (*48*), which markedly improves the contrast and specificity of PAT by suppressing the nonmagnetomotive background. Depending on the application, the relatively slow tissue clearance of nanoparticles can be either an advantage or a disadvantage.

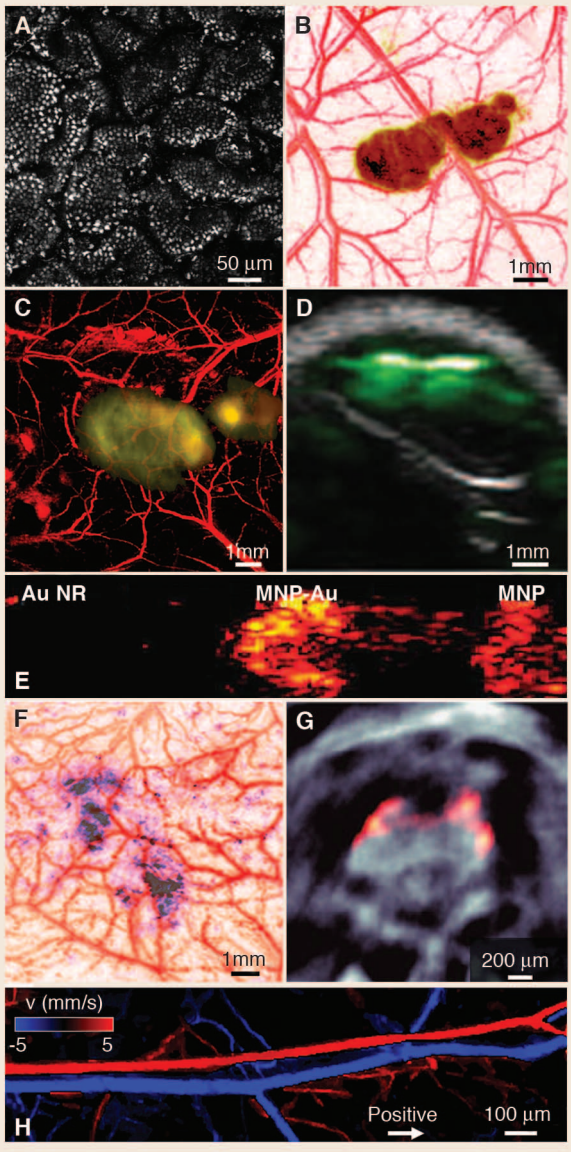

Fig. 3. Multicontrast PAT of tissue anatomy, function, molecular biomarkers, and gene expression. (**A**) OR-PAM of epithelial cell nuclei in the intestinal villi of a mouse ex vivo by excitation of DNA and RNA. (**B**) AR-PAM of a subcutaneously inoculated B16 melanoma and the surrounding vasculature on the back of a living mouse. (**C**) AR-PAM of a subcutaneously inoculated B16 melanoma labeled with targeted gold nanocages on the back of a living mouse. (**D**) Dual-contrast ultrasound (gray) and photoacoustic (green) imaging of a tumor labeled with single-walled carbon nanotubes in a living mouse. (**E**) Magnetomotive PAT of a polyvinyl alcohol phantom with three inclusions, each 2 mm in diameter. The left inclusion contains gold nanorods (Au NR) with absorption comparable to the 3 nM magnetic-gold hybrid nanoparticles (MNP-Au) placed in the center inclusion, and the right inclusion contains 3 nM magnetic nanoparticles (MNP). (**F**) AR-PAM of a lacZ-marked 9L gliosarcoma and the surrounding vasculature under the scalp of a living rat. (**G**) PACT of the brain of a 6-month-old mCherry-expressing transgenic zebrafish. (**H**) OR-PAM of blood flow velocity and direction in the ear of a living mouse.

Although the clinical translation of most nanoparticles is still awaiting FDA approval, many organic dyes have been approved for human use. Organic dyes clear rapidly from the body because of their small molecular size (typically ~1 nm), and some can penetrate the blood-brain barrier. Reporter gene products can be detected for PAT of biological processes at the genetic level, as was demonstrated using the *LacZ* gene—a common reporter encoding the protein β-galactosidase (*49*). Gliosarcoma cells transfected with *LacZ* genes were inoculated into a Sprague-Dawley rat. As the tumor grew, *LacZ* genes were expressed to β-galactosidase, which metabolized the locally injected lactose-like substrate into highly absorbing blue products, thereby providing contrast for genetic PAT in vivo (Fig. 3F) (*49*). Even fluorescent proteins from reporter genes have been imaged in vivo by PAT (Fig. 3G) (*50*).

All molecules can potentially be imaged by PAT at appropriate wavelengths, whereas only a small subset of molecules is fluorescent. Even fluorophores can serve as absorbing contrast agents for PAT (*13*, *50*, *51*). Optical excitation of fluorophores, in the absence of photochemical relaxation, relaxes via either fluorescence or thermal emission. Because most fluorophores have imperfect fluorescence quantum yields, PAT can rely on the thermal relaxation for high-resolution deep imaging of fluorophores.

Besides the aforementioned static contrasts, PAT can also image two important dynamic contrasts: blood flow (hemodynamic contrast) and temperature variation (thermodynamic contrast). The recently discovered photoacoustic Doppler effect laid the foundation for PAT of flow (*52*). Figure 3H shows a functional PAT image of both blood flow velocity and direction in a living

mouse (*53*). With excellent scalability, Doppler PAT bridges the spatial gap between scattering-based optical and ultrasonic technologies. More important, the high optical absorption contrast between the intravascular blood and extravascular background greatly increases detection sensitivity.

Tissue temperature monitoring is essential for thermal therapy. Because the initial photoacoustic pressure depends on the equilibrium temperature, PAT provides a potential means for high-resolution temperature imaging deep in tissue (*54*, *55*). Recent tissue phantom experiments showed that the initial photoacoustic pressure increases with the equilibrium temperature by ~5% per degree, which enables a sensitivity of the order of 0.1°C (*54*).

Combining both static and dynamic contrasts from PAT enables metabolic imaging. Indeed, PAT is the only modality that uses endogenous contrasts to measure all the parameters—including vessel diameter, total hemoglobin concentration, sO_2, tissue volume of interest, and blood flow velocity—required to compute the metabolic rate of oxygen (MRO_2). Recently, label-free absolute quantification of the MRO_2 in a living mouse was demonstrated (*44*).

Outlook

PAT is expected to find broad applications in biology and medicine. Major preclinical applications include imaging of angiogenesis, microcirculation, tumor microenvironments, drug response, brain functions, biomarkers, and gene activities. Initial clinical applications include melanoma cancer imaging, gastrointestinal tract endoscopy, intravascular catheter imaging, neonatal brain imaging, breast cancer detection, prostate cancer detection, guided sentinel lymph node needle biopsy for cancer staging, early chemotherapeutic response imaging, dosimetry in thermal therapy, in vivo label-free histology, blood perfusion imaging, blood oxygenation imaging, and tissue metabolism imaging. Although preclinical PAT systems have been commercialized, clinical systems need to pass rigorous validation and arduous regulatory approval.

PAT is distinctly capable of in vivo metabolic imaging based only on endogenous contrast. Upscaling metabolic PAT from small animals (*44*) to humans is expected to revolutionize the screening, diagnosis, and treatment of metabolic diseases, particularly cancers and cerebral disorders. Downscaling metabolic PAT to cells provides a tool for understanding metabolic pathways. Because hypermetabolism is a quintessential hallmark of cancer, metabolic PAT may enable in vivo cancer screening at the earliest stage without using exogenous contrast agents.

The scalability of PAT provides an unprecedented opportunity to link a complex biological system at multiple length scales through consistent optical absorption contrasts. In current practice, microscopic biological structures (including organelles and cells) are usually imaged by optical microscopy, whereas macroscopic structures (including tissues and organs) are imaged using nonoptical modalities such as x-ray computed tomography. Correlation of microscopic and macroscopic images can be challenging because of their vastly different contrast mechanisms. Imaging with the same contrast enables PAT to bridge this gap between the microscopic and macroscopic domains. Therefore, experimental observations from multiscale PAT are expected to facilitate the development of theoretical models for systems biology that explain and even predict biological phenomena at multiple scales. Moreover, PAT will likely accelerate the translation of microscopic laboratory discoveries to macroscopic clinical practice.

PAT still must overcome multiple technical challenges to maximize its impact in biomedicine. For high-speed multicontrast PAM or PAE based on spectroscopy, high-repetition lasers with fast wavelength-tuning at each scan position must be developed. PAE probes require further miniaturization to fit within generic endoscopes or even intravascular catheters. For deep-penetrating PACT, high-energy lasers with video-rate pulse repetition are needed. The required laser energy, however, can potentially be lowered by using time-reversed ultrasonically encoded (TRUE) optical focusing to improve light penetration (*56*). Also needed are sophisticated algorithms to perfect molecular quantification and to suppress skull-induced artifacts. It is anticipated that further advancement of this fast-growing imaging technology will revolutionize both fundamental life sciences and clinical patient care.

References and Notes

1. L. V. Wang, H. Wu, *Biomedical Optics: Principles and Imaging* (Wiley, Hoboken, NJ, 2007).
2. The optical diffusion limit represents the depth of the quasi-ballistic regime in biological tissue beyond which light propagating along the predefined linear trajectory becomes too weak to be detected in practice. It is usually equated with the transport mean free path (i.e., the mean distance between two consecutive equivalent isotropic scattering events).
3. J. P. Culver, V. Ntziachristos, M. J. Holboke, A. G. Yodh, *Opt. Lett.* **26**, 701 (2001).
4. L. V. Wang, *Nat. Photonics* **3**, 503 (2009).
5. The sensitivity is defined here as the ratio of the fractional change in the photoacoustic signal to the fractional change in the optical absorption coefficient.
6. L. V. Wang, *IEEE J. Sel. Top. Quantum Electron.* **14**, 171 (2008).
7. Z. Guo, L. Li, L. V. Wang, *Med. Phys.* **36**, 4084 (2009).
8. S. Oladipupo *et al.*, *Proc. Natl. Acad. Sci. U.S.A.* **108**, 13264 (2011).
9. S. S. Oladipupo *et al.*, *Blood* **117**, 4142 (2011).
10. T. N. Erpelding *et al.*, *Radiology* **256**, 102 (2010).
11. C. Kim *et al.*, *ACS Nano* **4**, 4559 (2010).
12. S. Hu, L. V. Wang, *Front. Neuroenerg.* **2**, (2010).
13. S. Hu, P. Yan, K. Maslov, J.-M. Lee, L. V. Wang, *Opt. Lett.* **34**, 3899 (2009).
14. X. Wang *et al.*, *Nat. Biotechnol.* **21**, 803 (2003).
15. S. Hu, B. Rao, K. Maslov, L. V. Wang, *Opt. Lett.* **35**, 1 (2010).
16. S. Jiao *et al.*, *Opt. Express* **18**, 3967 (2010).
17. E. Z. Zhang *et al.*, *Biomed. Opt. Express* **2**, 2202 (2011).
18. C. P. Favazza, O. Jassim, L. A. Cornelius, L. V. Wang, *J. Biomed. Opt.* **16**, 016015 (2011).
19. J.-M. Yang *et al.*, *Opt. Lett.* **34**, 1591 (2009).
20. J.-M. Yang *et al.*, *Proc. SPIE* **8223**, 822316 (2012).
21. K. Jansen, A. F. W. van der Steen, H. M. M. van Beusekom, J. W. Oosterhuis, G. van Soest, *Opt. Lett.* **36**, 597 (2011).
22. B. Wang *et al.*, *Nano Lett.* **9**, 2212 (2008).
23. K. Maslov, L. V. Wang, *J. Biomed. Opt.* **13**, 024006 (2008).
24. S. Hu, K. Maslov, L. V. Wang, *Opt. Lett.* **36**, 1134 (2011).
25. K. Maslov, H. F. Zhang, S. Hu, L. V. Wang, *Opt. Lett.* **33**, 929 (2008).
26. H. F. Zhang, K. Maslov, G. Stoica, L. V. Wang, *Nat. Biotechnol.* **24**, 848 (2006).
27. K. P. Kostli *et al.*, *IEEE J. Sel. Top. Quantum Electron.* **7**, 918 (2001).
28. M. Xu, L. V. Wang, *IEEE Trans. Med. Imaging* **21**, 814 (2002).
29. D. Finch, S. K. Patch, *SIAM J. Math. Anal.* **35**, 1213 (2003).
30. M. Xu, L. V. Wang, *Phys. Rev. E* **71**, 016706 (2005).
31. R. J. Zemp *et al.*, *J. Biomed. Opt.* **12**, 010501 (2007).
32. H. P. Brecht *et al.*, *J. Biomed. Opt.* **14**, 064007 (2009).
33. R. A. Kruger, R. B. Lam, D. R. Reinecke, S. P. Del Rio, R. P. Doyle, *Med. Phys.* **37**, 6096 (2010).
34. C. Li *et al.*, *J. Biomed. Opt.* **15**, 010509 (2010).
35. C. Kim, T. N. Erpelding, L. Jankovic, M. D. Pashley, L. V. Wang, *Biomed. Opt. Express* **1**, 278 (2010).
36. L. V. Wang, seminar presented at the Isaac Newton Institute for Mathematical Sciences: Inverse Problems, Cambridge, 23 August 2011; www.newton.ac.uk/programmes/INV/seminars/082314051.html.
37. Y. Xu, L. V. Wang, G. Ambartsoumian, P. Kuchment, *Med. Phys.* **31**, 724 (2004).
38. Y. Yang *et al.*, *Biomed. Opt. Express* **2**, 2551 (2011).
39. C. Zhang, K. Maslov, L. V. Wang, *Opt. Lett.* **35**, 3195 (2010).
40. C. Zhang *et al.*, *J. Biomed. Opt.* **17**, 020501 (2012).
41. K. H. Song, L. V. Wang, *J. Biomed. Opt.* **12**, 060503 (2007).
42. L. Song, K. Maslov, L. V. Wang, *Opt. Lett.* **36**, 1236 (2011).
43. D. K. Yao, K. Maslov, K. K. Shung, Q. Zhou, L. V. Wang, *Opt. Lett.* **35**, 4139 (2010).
44. J. Yao, K. I. Maslov, Y. Zhang, Y. Xia, L. V. Wang, *J. Biomed. Opt.* **16**, 076003 (2011).
45. Z. Xu, Q. Zhu, L. V. Wang, *J. Biomed. Opt.* **16**, 066020 (2011).
46. H. W. Wang *et al.*, *Phys. Rev. Lett.* **106**, 238106 (2011).
47. A. De la Zerda *et al.*, *Nat. Nanotechnol.* **3**, 557 (2008).
48. Y. Jin, C. Jia, S. W. Huang, M. O'Donnell, X. Gao, *Nat. Commun.* **1**, 41 (2010).
49. L. Li, H. F. Zhang, R. J. Zemp, K. Maslov, L. V. Wang, *J. Innov. Opt. Health Sci.* **1**, 207 (2008).
50. D. Razansky *et al.*, *Nat. Photonics* **3**, 412 (2009).
51. D. Razansky, C. Vinegoni, V. Ntziachristos, *Opt. Lett.* **32**, 2891 (2007).
52. H. Fang, K. Maslov, L. V. Wang, *Phys. Rev. Lett.* **99**, 184501 (2007).
53. J. Yao, K. I. Maslov, Y. Shi, L. A. Taber, L. V. Wang, *Opt. Lett.* **35**, 1419 (2010).
54. M. Pramanik, L. V. Wang, *J. Biomed. Opt.* **14**, 054024 (2009).
55. J. Shah *et al.*, *J. Biomed. Opt.* **13**, 034024 (2008).
56. X. Xu, H. Liu, L. V. Wang, *Nat. Photonics* **5**, 154 (2011).

Acknowledgments: We thank J. Ballard for close reading of the manuscript, and J. Yao for providing Fig. 3H. Supported by NIH grants R01 EB000712, R01 EB008085, R01 CA134539, U54 CA136398, R01 CA157277, R01 EB010049, and R01 CA159959. L.V.W. has financial interests in Microphotoacoustics Inc. and Endra Inc., which, however, did not support this work.

10.1126/science.1216210

Seroevidence for H5N1 Influenza Infections in Humans: Meta-Analysis

Taia T. Wang,[1] Michael K. Parides,[2] Peter Palese[1,3]*

Since 2003, there have been 573 World Health Organization (WHO)–documented cases of avian H5N1 influenza infections in humans reported from 15 countries (*1*). Of the WHO-confirmed cases, 58.6% have resulted in death (as of 15 December 2011) (*1*, *2*). These severe H5N1 infections were diagnosed by using criteria developed by the WHO that are specific for H5N1 disease but that lack the sensitivity to identify the total number of human infections (table S1) (*3*).

Given the fact that most H5N1 infections in poultry and in humans occur in resource-poor areas where access to health care is often arduous and expensive to obtain, we hypothesized that many people with H5N1 virus infection would not have been examined by a health provider to allow formal H5N1 disease confirmation. In addition, persons who are seropositive for H5N1 infection often report no history of influenza-like illness, and subclinical or mild H5N1 infections are not recognized under the WHO criteria for confirmed cases (*4*–*8*).

We conducted a meta-analysis of studies that evaluated the serological evidence of H5N1 infections in humans (table S2). The study participants, by and large, reported no recent respiratory and/or febrile illness. Variation between studies was taken into account by using a random effects approach (*9*). We included in our primary analysis only studies that assessed serum samples on the basis of modified WHO guidelines (N = 19 study groups) or that presented data in such a way that modified WHO guidelines for H5N1 seropositivity could be applied [for modified WHO guidelines, see (*10*)]. In a secondary analysis, we compiled data from the remaining manuscripts on the basis of the authors' criteria for positivity (N = 10). Study participants with confirmed H5N1 infection were excluded to allow an analysis of seroprevalence in the persons without WHO-documented infection; exposure to poultry or humans with confirmed or suspected H5N1 infection was not a criterion for exclusion.

The primary analysis using WHO criteria had its basis in 7304 study participants. All studies reported rates of seropositivity ranging from 0 to 5.3%, with the exception of one study reporting 11.7% positivity among household contacts of infected individuals (*5*). By using WHO criteria, meta-analysis revealed an overall seropositivity rate of 1.2% with a 95% confidence interval of 0.6 to 2.1% (Fig. 1A). Analysis of studies that could not be interpreted by WHO guidelines [(*10*), table S2, and references therein] included 6774 participants and yielded a seropositivity rate of 1.9% with a 95% confidence interval of 0.5 to 3.4% (Fig. 1B). With either criterion, the rate of human H5N1 infections within the study populations was about 1 to 2% (*10*).

With WHO criteria, we performed subanalyses of study participants who were specifically employed as poultry workers (N = 2729) (*4*) (table S2). This analysis revealed a seropositivity rate of about 1.4%. If reports from the 1997 outbreak in Hong Kong are considered separately, the rate of seropositivity is about 3.2% (*4*, *5*, *7*). Studies after 1997 that use WHO criteria show an overall seropositivity rate of about 0.5% (*8*) (table S2).

The data were compiled from 12,677 study participants in 20 studies. They show that avian H5N1 viruses can cause a rate of mild or subclinical infections in humans that is not currently accounted for; thus, the true fatality rate for H5N1 influenza viruses is likely to be less than the frequently reported rate of more than 50%. Although it is not possible to determine an accurate fatality rate for H5N1 infections on the basis of the data presented here, if one assumes a 1 to 2% infection rate in exposed populations, this would likely translate into a large number of missed infections worldwide. It is possible that deaths caused by H5N1 infection, as documented by the WHO, are also underestimated. We suggest that further investigation, on a large scale and by a standardized approach, is warranted to better estimate the total number of H5N1 infections that have occurred in humans. This information is critical for calculation of a real fatality rate that is not solely based on hospitalized patients.

[1]Department of Microbiology, Mount Sinai School of Medicine, New York, NY 10029, USA. [2]Mount Sinai Center for Biostatistics and Department of Health Evidence and Policy, Mount Sinai School of Medicine, New York, NY 10029, USA. [3]Department of Medicine, Mount Sinai School of Medicine, New York, NY 10029, USA.

*To whom correspondence should be addressed. E-mail: peter.palese@mssm.edu

References and Notes

1. WHO, Cumulative number of confirmed human cases for avian influenza A(H5N1) reported to WHO (2011), www.who.int/influenza/human_animal_interface/H5N1_cumulative_table_archives/en/index.html.
2. A. N. Abdel-Ghafar *et al.*, *N. Engl. J. Med.* **358**, 261 (2008).
3. WHO, WHO case definitions for human infections with influenza A(H5N1) virus (2006), www.who.int/influenza/resources/documents/case_definition2006_08_29/en/.
4. C. B. Bridges *et al.*, *J. Infect. Dis.* **185**, 1005 (2002).
5. J. M. Katz *et al.*, *J. Infect. Dis.* **180**, 1763 (1999).
6. P. Buchy *et al.*, *PLoS ONE* **5**, e10864 (2010).
7. C. Buxton Bridges *et al.*, *J. Infect. Dis.* **181**, 344 (2000).
8. P. Cavailler *et al.*, *J. Clin. Virol.* **48**, 123 (2010).
9. R. DerSimonian, N. Laird, *Control. Clin. Trials* **7**, 177 (1986).
10. Materials and methods in supporting material on *Science* Online.

Acknowledgments: The authors thank N. Pica for generous assistance in the preparation of this manuscript and H. Jia for statistical analysis. This work was partially supported by NIH grants U54 AI057158-04 and HHSN2662000700010C. T.T.W. was supported by NIH training grant T32 AI007647 and Mount Sinai medical scientists training grant T32 GM007280.

Supporting Online Material

www.sciencemag.org/cgi/content/full/science.1218888/DC1
Materials and Methods
Tables S1 and S2
References (*11*–*40*)

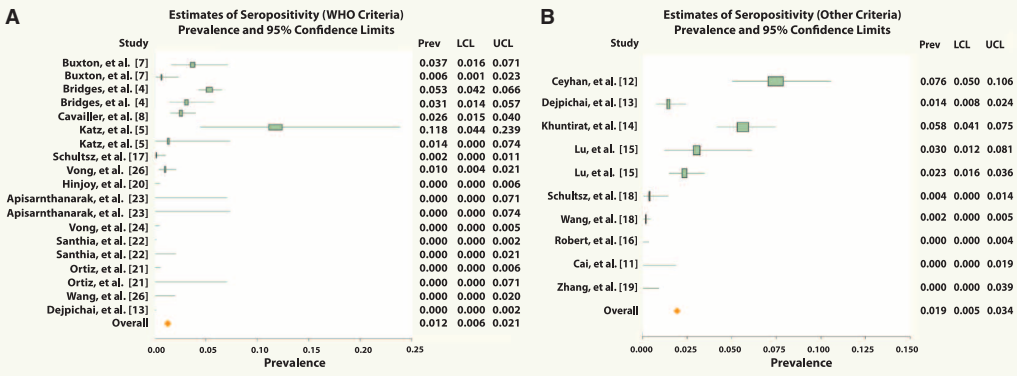

Fig. 1. Forest plots of overall and study-specific seroprevalence estimates with 95% confidence limits. Analyses used WHO criteria (**A**) or other criteria (*10*) (**B**) for seropositivity. Individual values for prevalence (seropositivity); lower and upper confidence limits are shown at the right of each plot.

9 January 2012; accepted 15 February 2012
Published online 23 February 2012;
10.1126/science.1218888

Actinide Topological Insulator Materials with Strong Interaction

Xiao Zhang,[1] Haijun Zhang,[1] Jing Wang,[1] Claudia Felser,[2] Shou-Cheng Zhang[1]*

Topological band insulators have recently been discovered in spin-orbit coupled two-and three-dimensional systems. We theoretically predict a class of topological insulators where interaction effects play a dominant role. In actinide elements, simple rocksalt compounds formed by Pu and Am lie on the boundary between metals and insulators. We show that interaction drives a quantum phase transition to a topological insulator phase with a single Dirac cone on the surface. These putative topological insulators may provide a setting for both applied and fundamental investigation.

Topological insulators (TIs) are new states of quantum matter with a full insulating gap in the bulk of the material and gapless Dirac fermion states on the surface (*1*–*3*). The compounds identified so far to be TIs, such as HgTe, $Bi_{1-x}Sb_x$, and Bi_2Te_3, are band insulators with band inversion driven by spin-orbit coupling (*4*). Soon after the discovery of topological band insulators, the concept of a topological Mott insulator was proposed (*5*); there the electron-electron interaction effects are responsible for TI behavior. Such materials are interesting because the interplay between electron interaction and spin-orbit coupling could enhance the bulk insulating gap, which is important for device applications. In addition, magnetic and superconducting order driven by interactions could coexist with topological order and give rise to exotic excitations such as magnetic monopole (*6*), Majorana fermion (*7*), and dynamic axion field (*8*).

We theoretically predict a new class of topological Mott insulators in actinide compounds with electrons in the 5f valence orbitals. In this work, we refer to Mott insulators as systems whose energy gap are opened up through interactions rather than band structure effects. Interaction and spin-orbit coupling energy scales are comparable in these compounds, making them ideal material systems to investigate the interplay between these two important effects. Simple rocksalt compounds formed by Pu and Am lie on the boundary between metals and insulators, where the 5f electrons change character from itinerant to localized (*9*). The predicted actinide TIs, such as AmN, are binary compounds with a simple rocksalt crystal structure and reasonably large energy gaps, providing an ideal platform to investigate interacting TIs. In comparison to standard TIs such as Bi_2Te_3, the actinide compounds predicted in this work have stronger three-dimensional ionic bonds. As a result, they may have fewer bulk defects; in fact, earlier photoemission experiments indicate vanishing density of states at the Fermi level (*10*).

Americium and plutonium are actinide elements with electron configurations of $5f^7 6d^0 7s^2$ and $5f^6 6d^0 7s^2$. Many of the Am monopnictides AmX (X can be N, P, Sb, and Bi) and Pu monochalcogenides PuY (Y is Se and Te) are known to be nonmagnetic and narrow-gap semiconductors (*10*–*15*). At ambient conditions, they crystallize in the rocksalt structure. The rocksalt structure has face-centered cubic (FCC) symmetry with the $Fm\bar{3}m$ space group (Fig. 1A, with AmN as an example). It can be represented as two interpenetrating FCC lattices with a two-atom basis. The first atom (Am) is located at each lattice point, and the second atom (N) is located halfway between lattice points along the FCC unit cell edge. The Bravais lattice vectors are $\mathbf{a}_1 = (0, a/2, a/2)$, $\mathbf{a}_2 = (a/2, 0, a/2)$, and $\mathbf{a}_3 = (a/2, a/2, 0)$. Its Brillouin zone (BZ) has three independent time-reversal-invariant-momentum (TRIM) points: $\Gamma(000)$, $X(\pi\pi0)$, and $L(\pi00)$ (Fig. 1B).

In order to study the electronic structure of these materials, ab initio calculations are carried out in the framework of local density functional approximation (LDA) supported by BSTATE package (*16*) within the plane-wave pseudopotential method. The ultrasoft pseudopotential (*17*) is used for localized orbitals, that is, Am (Pu) 5f and N 2p orbitals. The **k**-point grid is taken as 16 by 16 by 16, and the kinetic energy cutoff is fixed to 340 eV for all the self-consistent calculations. The spin-orbit coupling (SOC) interaction is taken into account because both Am and Pu have very heavy nuclei. LDA+U method (*18*, *19*) is used to deal with strong correlations in these compounds with empirical values of Hubbard interaction U = 2.5 eV for Am 5f orbitals (*11*) and U = 3.0 eV for Pu 5f orbitals (*13*). There is an transition from metal to insulator by tuning U from zero to these empirical values. If U is taken to be much larger, such as 4 eV, AmN becomes semimetal again, which is not consistent with the experimental results (*10*). We used experimentally measured lattice constants in our calculations (*20*).

Because all the AmX and PuY have similar electronic structures, AmN was used as an example. The band structures for AmN with U = 0 eV and U = 2.5 eV are shown in Fig. 2, A and B, respectively. The strong interaction U is responsible for the metal-to-insulator transition. If we ignore the effect of U in the calculation, there are residual 5f states at the Fermi level (E_F), indicating metallic behavior (Fig. 2A). Only by using finite U = 2.5 eV were those residual 5f states lifted away from E_F, and we can correctly predict AmN to be an insulator (Fig. 2B), consistent with experimental findings (*10*). The following energy band analysis elucidates the effect. Let us consider the Am-X (Pu-Y) bonding. One f and two s electrons of Am bond with the three p electrons of pnictides, whereas two s electrons of Pu bond with the four p electrons of chalcogenides. As a result, there are six f electrons left in the ground states for both AmX and PuY before we consider the hybridization between 5f and 6d states in Am or Pu. Because the strong Am-X (Pu-Y) bonding states are further away from E_F than the low-energy Am-Am and Pu-Pu bonding states, we ignore them in our band structure analysis in Fig. 3. In the following, we will just consider the Am-Am (Pu-Pu) d and f low-energy bonding states. The

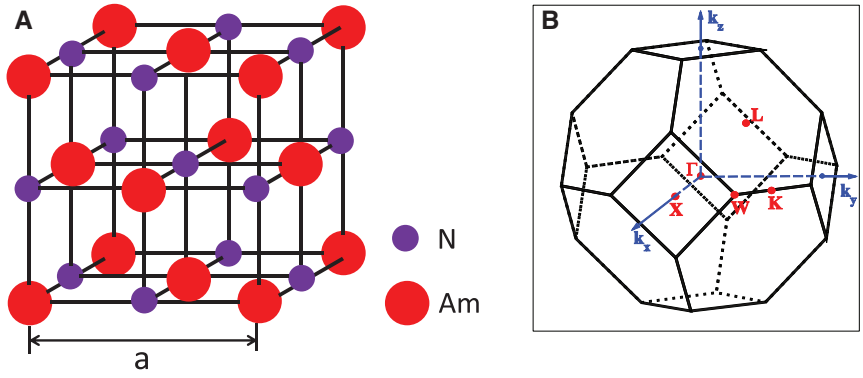

Fig. 1. (**A**) Rocksalt crystal structure of AmN with $Fm\bar{3}m$ space group. Am and N separately form a FCC sublattice, and these two sublattices are separated by a distance $a/2$ along one cubic edge. (**B**) BZ for AmN of rocksalt structure. Three independent time-reversal-invariant points are $\Gamma(000)$, $L(\pi00)$, and $X(\pi\pi0)$.

[1]Department of Physics, Stanford University, Stanford, CA 94305, USA. [2]Institute for Inorganic and Analytical Chemistry, Johannes Gutenberg University of Mainz, D-55099 Mainz, Germany and Max Planck Institute for Chemical Physics of Solids, Dresden, Germany.

*To whom correspondence should be addressed. E-mail: sczhang@stanford.edu

6d orbital first splits into e_g and t_{2g} states because of the large crystal-field splitting (CFS) and then splits again into Γ_7^+ and Γ_8^+ subbands as a consequence of a small SOC (Fig. 3) (*21*). The f states split into $5f^{5/2}$ and $5f^{7/2}$ states with total angular momentum of 5/2 and 7/2 because of the strong SOC interaction. For the $U = 2.5$ eV case, the Coulomb interaction U additionally shifts the $5f^{7/2}$ states away from E_F (*11*), leading to the metal-to-insulator transition (Fig. 2, A and B). Therefore, only the $5f^{5/2}$ states are fully occupied with the six f electrons with a nonmagnetic ground state. Before hybridizing with d orbital, CFS further splits the $5f^{5/2}$ states into Γ_8^- and Γ_7^- (*22*).

At E_F, the most important feature is the downward dispersion of the Γ_8^+ subband of Am's d band, which crosses the Γ_8^- subband of the $5f^{5/2}$ bands along the Γ-*X* direction, leading to a band inversion near *X* point in the BZ (Fig. 3). An energy gap is formed at the crossing point because of f-d hybridization. Because the d and f orbitals have "even" and "odd" parities at three *X* points, respectively, this inversion of bands with opposite parities determines the nontrivial topology of these materials. This d-f band inversion phenomenon leads these materials to be TIs, just as the band inversion between the s and p bands in HgTe quantum wells (*4*) and between p bands of opposite parities in the Bi_2Te_3 class of materials (*23*). We calculated the parity at all TRIM points (*24*) and predicted that AmN and all other AmX materials in this family are TIs with their band gaps shown in Table 1. The LDA+U method cannot obtain the energy gap for PuTe and PuSe, which was measured experimentally to be 0.178 eV for PuTe at ambient pressure and 0.4 eV with pressure up to 5 GPa (*13*, *14*). The dynamical mean-field theory (DMFT) method successfully reproduces the energy gap for PuSe and PuTe (*13*, *15*) (Table 1). With the same low-energy physics as AmN, we can conclude that PuSe and PuTe are TIs.

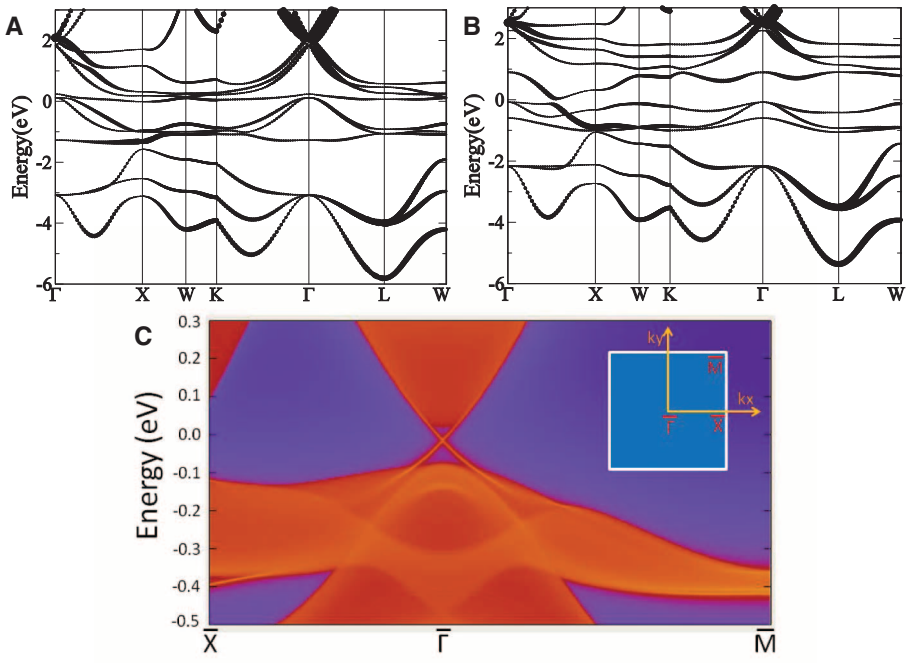

Fig. 2. Band structures for AmN at (**A**) $U = 0$ eV and (**B**) $U = 2.5$ eV. The line width in these fat band structures corresponds to the projected weight of Am's d orbitals on Bloch states. The f states are divided into two parts with angular momentum 5/2 and 7/2 resulting from the SOC interaction. The part with angular momentum 5/2 is occupied, and the other part with angular momentum 7/2 is partially occupied with $U = 0$ eV. For the $U = 2.5$ eV case, these partially occupied f states of angular momentum 7/2 move up further toward high energy and become completely unoccupied. (**C**) Energy spectrum of the ab initio calculation-based TB Hamiltonian with the open boundary condition along "+*z*" direction. One surface Dirac cone is seen at $\bar{\Gamma}$ point as red lines dispersing in the bulk gap on the AmN [001] surface. (Inset) The projected two-dimension BZ is shown.

According to the ab initio calculation, the two low-energy $\Gamma_8^{\pm}$ bands can capture the salient topological features of these materials. Therefore, we propose the following 8 × 8 Hamiltonian:

$$\mathcal{H} = \begin{pmatrix} H_d & H_{df} \\ H_{df}^{+} & H_f \end{pmatrix} \quad (1)$$

H_d and H_f are 4 × 4 Hamiltonians for Γ_8^+ and Γ_8^- representations with an effective angular momentum $j = 3/2$. We write down the $\mathbf{k}\cdot\mathbf{p}$ Hamiltonian near the Γ point of the BZ from symmetry analysis and extend it to a tight binding (TB) model for the full BZ (*25*). The effective Hamiltonian for $\Gamma_8^{\pm}$ bands is the Luttinger model (*26*):

$$H_{d(f)} = C_{d(f)} + A_{d(f)}\mathbf{k}^2 + B_{d(f)}(\mathbf{k}\cdot\mathbf{J}_{3/2})^2 + D_{d(f)}$$
$$[k_x^2(J_{3/2}^x)^2 + k_y^2(J_{3/2}^y)^2 + k_z^2(J_{3/2}^z)^2] \quad (2)$$

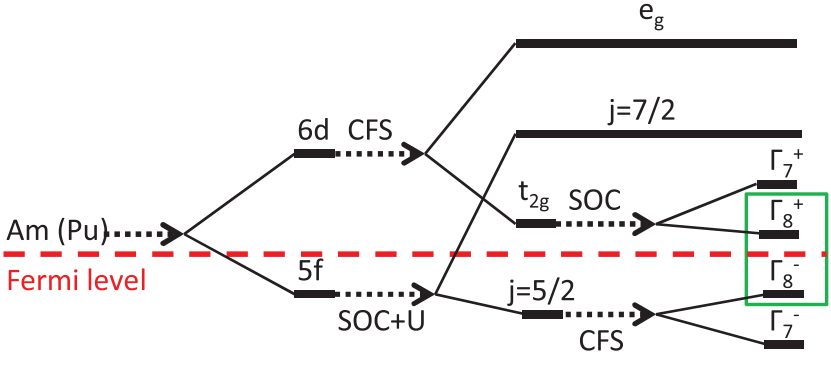

Fig. 3. Band sequence. Diagram of the evolution from the atomic d and f orbitals of Am or Pu into the conduction and valence bands of AmX or PuY at the Γ point. The black dashed arrows represent the effect of turning on chemical bonding, CFS, SOC, and *U*. The red dashed line represents the Fermi energy. In the green box, there are two low-energy bands, Γ_8^+ and Γ_8^-. The inversion of them at *X* points of the BZ makes these materials to be TIs.

Table 1. Energy gap and parity eigenvalue. E_g indicates the energy gap. The band gaps of PuTe and PuSe are taken from (*13*), in which the band gap of PuSe is theoretically predicted and the band gap of PuTe is the experimental value that agrees well with theoretical prediction. Γ, *X* and *L* are the TRIM points in BZ. – and + indicate the odd and even parity product for all the occupied bands. "Tot." means the total parity product of all TRIM points. All those materials have paramagnetic ground state, except for AmAs, which has a possible antiferromagnetic ground state with Neel temperature $T_N = 13$ K (*29*). The band gap of AmAs that we list is the value of its paramagnetic phase.

	E_g	Γ	3*X*	4*L*	Tot.
AmN	0.100eV	–	+	–	–
AmP	0.085eV	–	+	–	–
AmAs	0.080eV	–	+	–	–
AmSb	0.055eV	–	+	–	–
AmBi	0.040eV	–	+	–	–
PuSe	0.2eV	–	+	–	–
PuTe	0.178eV	–	+	–	–

$A_{d(f)}$, $B_{d(f)}$, $C_{d(f)}$, and $D_{d(f)}$ are parameters, and $\mathbf{J}_{3/2}$ are spin matrices for angular momentum 3/2. The first three terms have continuous rotational symmetry; the last term breaks continuous rotational symmetry while preserving cubic symmetry, which is responsible for the band inversion only along Γ-X direction rather than other directions in the BZ (*25*). The off-diagonal Hamiltonian H_{df} connects d and f bands of opposite parities; therefore, the first-order term can be written as

$$H_{df} = iF(k_x\{J_{3/2}{}^y, J_{3/2}{}^z\} + k_y\{J_{3/2}{}^z, J_{3/2}{}^x\} + k_z\{J_{3/2}{}^x, J_{3/2}{}^y\}) \quad (3)$$

F is a parameter, and the notation $\{A, B\} = (AB + BA)/2$ denotes the symmetrized product of its arguments. The above effective model preserves time-reversal and inversion symmetry.

Because the 5f and 6d orbitals are localized, we only consider the nearest neighborhood hopping of Am-Am and Pu-Pu atoms. Each Am (Pu) atom has 12 nearest neighbors located at $\pm\mathbf{a}_1$, $\pm\mathbf{a}_2$, $\pm\mathbf{a}_3$, $\pm(\mathbf{a}_2 - \mathbf{a}_1)$, $\pm(\mathbf{a}_2 - \mathbf{a}_3)$, and $\pm(\mathbf{a}_3 - \mathbf{a}_1)$. So we can extend the above continuum model to the TB lattice model and reproduce the low-energy bands of these materials well, with AmN as an example (*25*). Two important effects of the U interaction are to renormalize the SOC parameters between $5f^{5/2}$ and $5f^{7/2}$states and to induce a metal-insulator transition. On the insulator side, we can effectively fit our eight-by-eight Hamiltonian in the single-particle picture with parameters renormalized by U to the LDA+U first-principle calculations.

To identify the surface states, we perform an ab initio calculation for the semi-infinite AmN system with open boundary condition in the "+z" direction on the basis of maximally localized Wannier functions (MLWFs) (*27*, *28*). We can obtain the surface Green's function of the semi-infinite system iteratively. Lastly, the local density of states (LDOS) can be calculated with the imaginary part of these Green's functions. From these LDOS, we can obtain the dispersion of the surface states, (Fig. 2C). A single Dirac cone at $\bar{\Gamma}$ shows up in the energy gap, which demonstrates the nontrivial Z_2 topology of the material in addition to the parity analysis. The Fermi velocity for the Dirac cone is $v_F \cong 1.3 \times 10^5$ m/s, a little smaller than Bi_2Se_3 (*23*). To confirm this result, we also take the open boundary condition in z direction in the analytical TB model (*25*), which yields the same single Dirac cone surface state at Γ point of the BZ as in the ab initio calculation.

This work could lead to the discovery of more interacting TI materials in the actinide family. The topological surface states in actinide materials would offer better ways to optimize electrical and thermal transport properties, leading to novel designs for nuclear energy applications.

References and Notes

1. X. L. Qi, S. C. Zhang, *Phys. Today* **63**, 33 (2010).
2. X. L. Qi, S. C. Zhang, *Rev. Mod. Phys.* **83**, 1057 (2011).
3. M. Z. Hasan, C. L. Kane, *Rev. Mod. Phys.* **82**, 3045 (2010).
4. B. A. Bernevig, T. L. Hughes, S. C. Zhang, *Science* **314**, 1757 (2006).
5. S. Raghu, X. L. Qi, C. Honerkamp, S. C. Zhang, *Phys. Rev. Lett.* **100**, 156401 (2008).
6. X. L. Qi, R. D. Li, J. D. Zang, S. C. Zhang, *Science* **323**, 1184 (2009); 10.1126/science.1167747.
7. L. Fu, C. L. Kane, *Phys. Rev. Lett.* **100**, 096407 (2008).
8. R. D. Li, J. Wang, X. L. Qi, S. C. Zhang, *Nat. Phys.* **6**, 284 (2010).
9. K. T. Moore, G. van der Laan, *Rev. Mod. Phys.* **81**, 235 (2009).
10. T. Gouder, P. M. Oppeneer, F. Huber, F. Wastin, J. Rebizant, *Phys. Rev. B* **72**, 115122 (2005).
11. D. B. Ghosh, S. K. De, P. M. Oppeneer, M. S. S. Brooks, *Phys. Rev. B* **72**, 115123 (2005).
12. S. Suzuki, T. Ariizumi, *J. Phys. Soc. Jpn.* **76**, 024707 (2007).
13. M.-T. Suzuki, P. M. Oppeneer, *Phys. Rev. B* **80**, 161103 (2009).
14. V. Ichas, J. C. Griveau, J. Rebizant, J. C. Spirlet, *Phys. Rev. B* **63**, 045109 (2001).
15. M. S. S. Brooks, *J. Magn. Magn. Mater.* **63-64**, 649 (1987).
16. Z. Fang, K. Terakura, *J. Phys. Condens. Matter* **14**, 3001 (2002).
17. D. Vanderbilt, *Phys. Rev. B* **41**, 7892 (1990).
18. V. I. Anisimov, I. V. Solovyev, M. A. Korotin, *Phys. Rev. B* **48**, 16929 (1993).
19. V. I. Anisimov, J. Zaanen, O. K. Andersen, *Phys. Rev. B* **44**, 943 (1991).
20. F. Wastin, J. C. Spirlet, J. Rebizant, *J. Alloy. Comp.* **219**, 232 (1995).
21. M. S. Dresselhaus, G. Dresselhaus, A. Jorio, *Group Theory Application to the Physics of Condensed Matter* (Springer, Berlin, 2008).
22. M. Dzero, K. Sun, P. Coleman, V. Galitski, *Phys. Rev. B* **85**, 045130 (2012).
23. H. J. Zhang *et al.*, *Nat. Phys.* **5**, 438 (2009).
24. L. Fu, C. L. Kane, *Phys. Rev. B* **76**, 045302 (2007).
25. Materials and methods are available as supporting material on *Science* Online.
26. J. M. Luttinger, *Phys. Rev.* **102**, 1030 (1956).
27. N. Marzari, D. Vanderbilt, *Phys. Rev. B* **56**, 12847 (1997).
28. I. Souza, N. Marzari, D. Vanderbilt, *Phys. Rev. B* **65**, 035109 (2001).
29. B. Kanellakopulos, J. P. Charvillat, F. Maino, W. Muller, *Transplutonium 1975* (North-Holland, Amsterdam, 1976).

Acknowledgments: We thank S. Raghu for useful discussions. This work is supported by the U.S. Department of Energy, Office of Basic Energy Sciences, Division of Materials Sciences and Engineering, under contract DE-AC02-76SF00515 and in part by the Army Research Office under the grant number W911NF-09-1-0508.

Supporting Online Material

www.sciencemag.org/cgi/content/full/335/6075/1464/DC1
Materials and Methods
SOM Text
Fig. S1
Tables S1 and S2
References (*30*, *31*)

3 November 2011; accepted 17 February 2012
10.1126/science.1216184

Experimental Realization of a Magnetic Cloak

Fedor Gömöry,[1] Mykola Solovyov,[1] Ján Šouc,[1] Carles Navau,[2] Jordi Prat-Camps,[2] Alvaro Sanchez[2]*

Invisibility to electromagnetic fields has become an exciting theoretical possibility. However, the experimental realization of electromagnetic cloaks has only been achieved starting from simplified approaches (for instance, based on ray approximation, canceling only some terms of the scattering fields, or hiding a bulge in a plane instead of an object in free space). Here, we demonstrate, directly from Maxwell equations, that a specially designed cylindrical superconductor-ferromagnetic bilayer can exactly cloak uniform static magnetic fields, and we experimentally confirmed this effect in an actual setup.

Rendering an object in free space invisible has important scientific and technological implications. Invisibility at several frequencies, including visible light, has started to be an actual possibility (*1*–*4*). Most cloak designs, however, require extreme (anisotropic, spatially inhomogeneous, and even singular) values of magnetic permeability μ and electric permittivity ε. They also involve other more fundamental problems, such as superluminal phase velocities and extremely narrow bandwidths (*5*, *6*). Whereas cloaks based on plasmonics are free from some of these limitations, they are achieved at the price of giving up exact invisibility by canceling only some scattering terms (*4*).

Some experimental works have attempted to achieve cloaking, albeit in reduced schemes; that is, giving up exactness for the sake of feasibility. In recent work by Schurig *et al*. (*7*), the goal was not to render a full cloak but a reduced scheme, with some reflection and shadowing. Resonant metamaterials in the microwave frequency were used, which had a narrow frequency band with a relatively large loss (*8*). A plasmonic approach was also experimentally demonstrated (*9*) in which the scattering of a particular dielectric object was decreased but not eliminated. Another strategy to reduce a full cloaking scheme into something more practical is the carpet cloak (*10*, *11*), with several experimental realizations, even in the optical range (*12*–*14*), although they attempt to hide

[1]Institute of Electrical Engineering, Slovak Academy of Sciences, Slovakia. [2]Grup d'Electromagnetisme, Departament de Física, Universitat Autònoma de Barcelona, 08193 Bellaterra, Barcelona, Catalonia, Spain.

*To whom correspondence should be addressed. E-mail: alvar.sanchez@uab.cat

a bulge instead of a three-dimensional object in free space (*12*).

The definitive confirmation of cloaking requires finding a system that (i) can be theoretically derived as an exact cloak from first principles (not a reduced scheme) and (ii) can be experimentally realized with existing materials; for example, those made only of nonsingular, homogeneous, and isotropic materials.

We show in this work that for static magnetic fields one can design a scheme fulfilling (i) and (ii), as mentioned above. Our scheme consists of a long cylinder with two concentric layers made of homogeneous isotropic materials: an inner superconducting (SC) one, which expels magnetic fields (ideally considered as a zero-permeability material), and an outer ferromagnetic (FM) one. An exact cloak behavior of uniform static magnetic fields for such a bilayer will be analytically demonstrated directly based on Maxwell equations. Cloaking static magnetic fields has the important advantage that the magnetic and electric effects decouple and only the magnetic permeabilities need to be considered. A scheme to cloak static magnetic fields was proposed (*15*–*17*) based on transformation optics (*1*) [note that the scheme in (*2*) is valid only on scales much larger than the wavelength, so is not applicable to dc cloaking], but it required extreme values of permeabilities. An approximate design based on discrete layers has recently been presented (*18*).

Based on Maxwell equations, we show [see supporting online material (SOM) text] that a bilayer consisting of an infinitely long cylindrical superconducting shell of interior and exterior radii R_0 and R_1, respectively, surrounded by another cylindrical magnetic shell (with constant permeability μ_2) of interior and exterior radii R_1 and R_2, respectively (Fig. 1C), exactly cloaks a uniform magnetic field when the permeability of the outer layer follows

$$\mu_2 = \frac{R_2^2 + R_1^2}{R_2^2 - R_1^2} \qquad (1)$$

Equation 1 represents a whole family of solutions, depending on μ_2 and the ratio R_2/R_1. A similar bilayer structure also exactly cloaks static uniform magnetic fields in a sphere (SOM text). Moreover, when the applied field is nonuniform, the field distortion outside the bilayer is relatively small and can be reduced by adjusting the thickness of the layers (SOM text).

For nonzero frequency electromagnetic waves, the interaction between electric and magnetic fields complicates the control of light. Controlling static magnetic fields is simpler: Materials exist in nature with permeabilities $\mu > 1$ and $\mu < 1$ that attract and repel magnetic flux lines, respectively (Fig. 1, A and B). Our bilayer (Fig. 1C) is based on the existence of an exact solution that provides the right combination of repelling (inner SC layer) and attracting (outer FM layer) magnetic field lines so as to cancel any external distortion.

An important property of our bilayer is that placing a superconductor as the inner layer ensures that an external field does not penetrate inside the cylinder (*18*, *19*) and that the field of a magnetic source inside the cloak will not leak outside (*18*). So the challenging task is to experimentally demonstrate the zero external-field distortion.

We fabricated a SC-FM bilayer (Fig. 2A). Instead of uniform superconducting and ferromagnetic cylinders proposed in the ideal bilayer, the inner superconducting shell consisted of a few turns of high-temperature superconductor tape (*20*), and the outer layer was composed of a few turns of a thick FeNiCr commercial alloy sheet (*21*). The magnetic response of the bilayer in a uniform applied field of 40 mT generated by a split pair of race-track electromagnets was measured using an existing experimental setup, utilized before for measuring superconducting tapes (*22*), which provided the required accuracy and calibration in magnetic and position measurements but did not allow for measuring of long cylinders. We obtained good cloaking results, even though the cylindrical bilayer was relatively short. We mapped the vertical component of magnetic field (y component) with a Hall probe in the median plane of the bilayer along the lines transversal to its axial length (green dotted lines in Fig. 1). Such an experiment was performed in three different cases: (i) FM only at room temperature (i.e., superconducting tape over the critical temperature, thus electromagnetically inactive); (ii) SC only at 77 K, after unwinding the outer FM shell, to see the reference case of only the inner superconducting shell; and (iii) SC-FM bilayer at 77 K, the anticipated operating condition for magnetic invisibility.

The calculated vertical component of the magnetic field along the dotted lines in Fig. 1 corresponding to the three cases is plotted in Fig. 3A, assuming an exact bilayer with ideal parameters and the dimensions used in the experiments. The superconductor and the ferromagnet repel and attract field lines so the vertical component of the magnetic field in the central region tends to be smaller and larger than the applied field, respectively. For our bilayer, the combined response yields only the vertical component of the applied field (no field distortion).

The results of our experiments (Fig. 3, B and C) show that the magnetic signature of our bilayer cloak practically leaves the applied field of 40 mT unaffected and is weaker than the cases of only the SC or only the FM layer. Some small deviations appear in the experiments, possibly resulting from the short length of the bilayer (comparable to its diameter), so that the magnetic flux can also avoid the object in more directions, as well as the nonideal behavior of the SC and FM layers (*21*). Experimental results did not change with the rotation of the bilayer around its longitudinal axis. The observed suppression of magnetic signature was also substantial at some distance

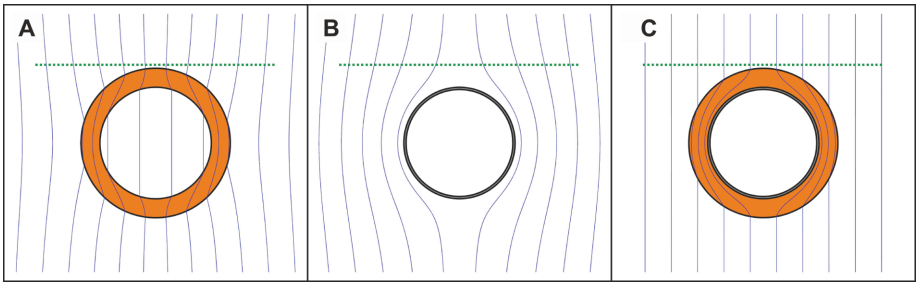

Fig. 1. Calculated field lines for (**A**) a single cylindrical magnetic shell with $\mu = 3.54$, attracting fields and having some field penetration in its interior; (**B**) a single cylindrical superconducting shell with $\mu = 0$ repelling field lines; and (**C**) a cylindrical bilayer with an inner superconducting layer ($\mu = 0$) of interior (exterior) radius of $R_0 = 0.96\ R_1$ (R_1) and an outer magnetic layer with $R_2/R_1 = 1.34$ with $\mu_2 = 3.54$, fulfilling Eq. 1. These values are chosen to approximate those used in the experiments. Green dotted lines denote the measuring lines in the experiments.

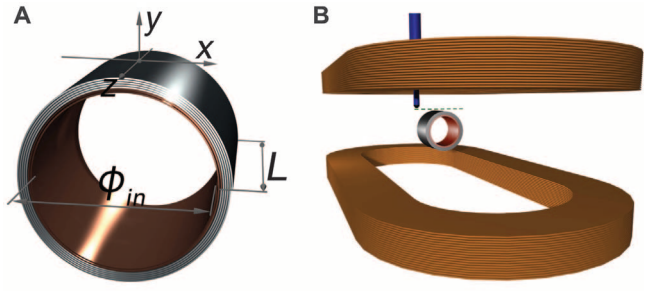

Fig. 2. (**A**) Scheme of the experimental magnetic cloak consisting of two shells: The inner one (brown) is made of several turns of superconducting tape, and several turns of tape with ferromagnetic properties create the outer shell (gray). In our case, length $L = 12$ mm and diameter $\phi_{in} = 12.5$ mm. Preparation of such structure requires a cylindrical former (not shown in the image). (**B**) Experimental setup for mapping the magnetic field in the vicinity of the magnetic cloak. The magnetic field is generated by a pair of race-track coils wound from Cu wire (brown). The Hall probe is mounted on the bottom of the holder rod (blue).

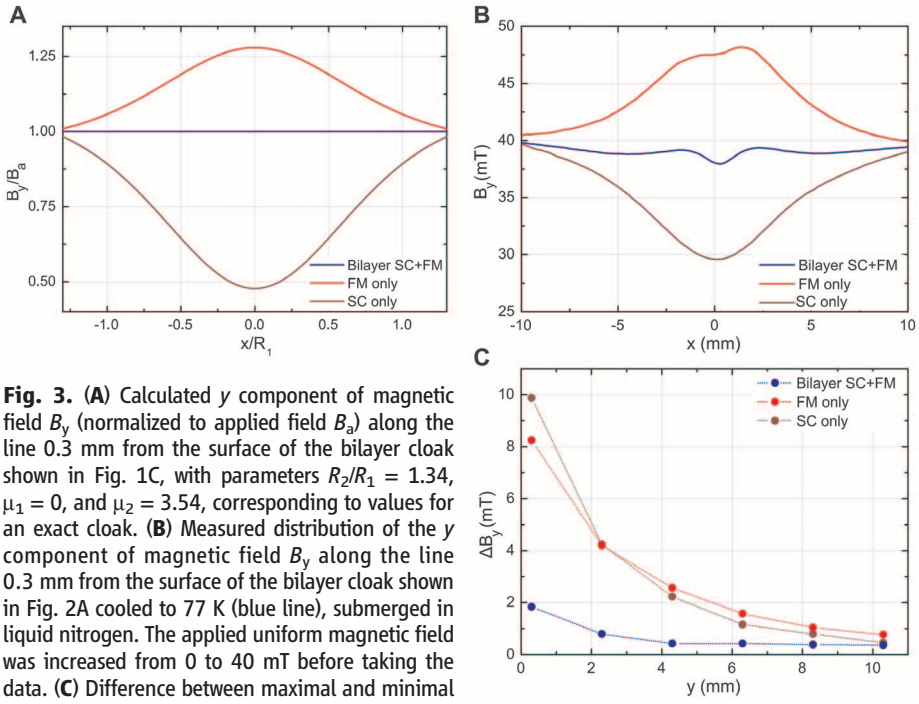

Fig. 3. (**A**) Calculated *y* component of magnetic field B_y (normalized to applied field B_a) along the line 0.3 mm from the surface of the bilayer cloak shown in Fig. 1C, with parameters $R_2/R_1 = 1.34$, $\mu_1 = 0$, and $\mu_2 = 3.54$, corresponding to values for an exact cloak. (**B**) Measured distribution of the *y* component of magnetic field B_y along the line 0.3 mm from the surface of the bilayer cloak shown in Fig. 2A cooled to 77 K (blue line), submerged in liquid nitrogen. The applied uniform magnetic field was increased from 0 to 40 mT before taking the data. (**C**) Difference between maximal and minimal values of the *y* component of magnetic field B_y for scans taken from $x = -10$ to 10 mm at various heights *y*. (A to C) Red line, FM only (in experiments obtained at room temperature; i.e., superconductor inactive); deep red line, SC only (experimentally, after removing the ferromagnetic layers); blue line, data for the SC-FM bilayer.

from the object, as seen from mapping at different vertical heights above the surface (Fig. 3C).

Both the SC and FM layers have been widely used independently of one another for magnetic shielding (*23*); our results show that the right combination of them yields shielding with no external-field distortion. Because in our static case there is no wavelength limiting the size of the objects, which differs from cloaks at other frequencies, our results can be naturally scaled up or down to any size of interest.

Because our cloak design for uniform magnetic field does not rely on transformation optics (*24*, *25*), problems present in previous cloaking proposals, such as superluminial velocity and singular parameters (*6*, *24*, *26*), are avoided. Also, the starting exact cloak means that scattering fields are zero and not only the dominant orders as in the scattering-cancellation technique based on plasmonics (*4*). Thus, our magnetic bilayer in a uniform magnetic field is an ideal case for full confirmation of cloaking ideas. Because the imperfection in the cloaking results not from intrinsic reasons but from the simplicity of the experiments, further experimental refinements will better approach the theoretical exact-field cancellation. Finally, our results were obtained using only commercially available materials, for fields as large as 40 mT, and at liquid-nitrogen temperatures, indicating that our ideas may be readily applied to technology.

References and Notes

1. J. B. Pendry, D. Schurig, D. R. Smith, *Science* **312**, 1780 (2006).
2. U. Leonhardt, *Science* **312**, 1777 (2006).
3. A. Greenleaf, M. Lassas, G. Uhlmann, *Physiol. Meas.* **24**, 413 (2003).
4. A. Alù, N. Engheta, *J. Opt. A Pure Appl. Opt.* **10**, 093002 (2008).
5. J. Perczel, T. Tyc, U. Leonhardt, *N. J. Phys.* **13**, 083007 (2011).
6. P. Alitalo, F. Bongard, J.-F. Zürcher, J. Mosig, S. Tretyakov, *Appl. Phys. Lett.* **94**, 014103 (2009).
7. D. Schurig *et al.*, *Science* **314**, 977 (2006).
8. H. F. Ma, T. J. Cui, *Nat. Commun.* **1**, article 21 (2010).
9. B. Edwards, A. Alù, M. Silveirinha, N. Engheta, *Phys. Rev. Lett.* **103**, 153901 (2009).
10. J. Li, J. B. Pendry, *Phys. Rev. Lett.* **101**, 203901 (2008).
11. R. Liu *et al.*, *Science* **323**, 366 (2009).
12. X. Chen *et al.*, *Nat. Commun.* **2**, article 176 (2011).
13. T. Ergin, N. Stenger, P. Brenner, J. B. Pendry, M. Wegener, *Science* **328**, 337 (2010).
14. B. Zhang, Y. Luo, X. Liu, G. Barbastathis, *Phys. Rev. Lett.* **106**, 033901 (2011).
15. B. Wood, J. B. Pendry, *J. Phys. Condens. Matter* **19**, 076208 (2007).
16. F. Magnus *et al.*, *Nat. Mater.* **7**, 295 (2008).
17. C. Navau, D.-X. Chen, A. Sanchez, N. Del-Valle, *Appl. Phys. Lett.* **94**, 242501 (2009).
18. A. Sanchez, C. Navau, J. Prat-Camps, D.-X. Chen, *New J. Phys.* **13**, 093034 (2011).
19. J. J. Rabbers, M. P. Oomen, E. Bassani, G. Ripamonti, G. Giunchi, *Supercond. Sci. Technol.* **23**, 125003 (2010).
20. Y. Xie, K. Tekletsadik, D. Hazelton, V. Selvamanickam, *IEEE Trans. Appl. Supercond.* **17**, 1981 (2007).
21. Materials and methods are available as supporting material on *Science* Online.
22. M. Solovyov, F. Gömöry, *IEEE Trans. Appl. Supercond.* **21**, 3277 (2011).
23. J. Vrba, S. E. Robinson, *Methods* **25**, 249 (2001).
24. H. Chen, C. T. Chan, P. Sheng, *Nat. Mater.* **9**, 387 (2010).
25. V. M. Shalaev, *Science* **322**, 384 (2008).
26. U. Leonhardt, *Nature* **471**, 292 (2011).

Acknowledgments: We thank D.-X. Chen for valuable comments and Consolider Project NANOSELECT (CSD2007-00041) and VEGA 2/0172/09 for financial support.

Supporting Online Material

www.sciencemag.org/cgi/content/full/335/6075/1466/DC1
Materials and Methods
SOM Text
Figs. S1 to S4
References (*27*–*33*)

22 December 2011; accepted 8 February 2012
10.1126/science.1218316

Renewable Cathode Materials from Biopolymer/Conjugated Polymer Interpenetrating Networks

Grzegorz Milczarek[1] and Olle Inganäs[2]*

Renewable and cheap materials in electrodes could meet the need for low-cost, intermittent electrical energy storage in a renewable energy system if sufficient charge density is obtained. Brown liquor, the waste product from paper processing, contains lignin derivatives. Polymer cathodes can be prepared by electrochemical oxidation of pyrrole to polypyrrole in solutions of lignin derivatives. The quinone group in lignin is used for electron and proton storage and exchange during redox cycling, thus combining charge storage in lignin and polypyrrole in an interpenetrating polypyrrole/lignin composite.

Renewable energy systems based on intermittent sources require methods for power balancing over time, and thus some means of storage. Charge storage in organic polymers rarely gives energy and power densities, gravimetric or volumetric, that match the needs for secondary batteries and supercapacitors. This was one reason for the abandonment of efforts to make polymer batteries from conjugated polymers two decades ago (*1*), because inorganic insertion electrodes are superior. Widespread application of electrical power storage may require more abundant materials than those available in inorganics (which often require rare metals), and

at a lower cost. Materials for charge storage are desired from easily accessible and renewable sources (*2*). Combining cellulose materials and conjugated polymers for charge storage (*3*, *4*) has again attracted attention (*5*).

Biopolymers with redox functions are used in energy conversion processes in plants. The highly sophisticated structures designed to split water to oxygen and protons, in photosystem II in green plants, are made from protein structures combined with a manganese complex and use temporary proton storage on amino acid residues to accomplish this four-electron oxidation step (*6*). Electron and proton storage is found in the metabolism of plants and bacteria, where quinones are used as soluble electron/proton transport agents. With hydroquinone (Q/QH_2), two electrons and protons are stored in a structure of 6 carbon and 2 oxygen atoms, an electronic charge density of 2 Faraday per 108 g, 1787 C/g, or 496 mAh/g. This is a favorable number compared with standard electrochemical systems; in lithiated carbon materials, a maximum doping level is 6 carbons per lithium, equivalent to 344 mAh/g and, in the olivine $FePO_4$ system, 170 mAh/g (*7*). It is desirable to use the quinone redox function in electroactive materials to enhance charge-storage capacity.

Conjugated polymers with added quinone groups within the conjugation path on the main chain give improved charge storage (*8*–*10*). The inclusion of anionic redox species as the counter ion, also incorporating quinones, in doped conjugated polymers is well demonstrated (*11*–*14*). The combined redox processes of polymer and redox anion contribute to charge capacity in these materials.

Phenol and quinones are found in plants and wood. A by-product of paper processing is brown liquor, also called spent sulfite liquor, an abundant and cheap residue mainly used as a surfactant. Brown liquor incorporates derivatized lignins rich in phenol groups, which can be further converted to quinones through oxidation processes.

We report synthesis and characterization of a class of materials based on the combination of polypyrrole and lignin derivatives with redox functions. Among biopolymers, lignin is second only to cellulose in biosynthesis and makes up some 20 to 28% of wood. The lignin polymer (*15*) is chemically variable and electronically insulating. The electrochemistry of lignins has been studied in thin layers (*16*) and evaluated for electrocatalysis (*17*, *18*). If lignin is incorporated into an electrode material with sufficient electronic and ionic conductivity to allow charge transport to and from the quinone site, it is possible to use this redox function for charge storage. We show that polypyrrole is suitable and that quinone electrochemistry and polypyrrole conductivity combine to create an electroactive conjugated polymer/biopolymer composite. Previous reports of electrical properties of composites of polypyrrole with lignin derivatives (*19*, *20*) did not report the use of the redox capacity in lignin.

Electrochemical polymerization of pyrrole at Au electrodes in aqueous lignosulfonate solutions (*21*), using a three-electrode system, generates a solid, black conducting product [Ppy(Lig)] that adheres to the substrate. Growth of this material (fig. S1) can continue unabated for more than 2 hours, giving a film of thickness 3 μm. The conductivity of these materials is ~1 S/cm. From elemental analysis (*21*), we deduce the characteristic N:S ratio, which indicates a mass fraction of ~50% doped polypyrrole and 50% lignosulphonate.

Cyclic voltammetry (CV) of Ppy(Lig) electrodes in 0.1 M aqueous $HClO_4$ reveals two redox waves, one very well defined and narrow at ~0.5 V versus Ag/AgCl and one less well pronounced in the potential range where oxidation/reduction of polypyrrole is typically found (Fig. 1 and fig. S2). The redox process of the Ppy(Lig) electrode in aqueous electrolytes with pH buffers shows a systematic dependence of the redox potential with pH, with 58 mV/pH unit, close to the 59 mV/pH unit expected for a 1-electron/1-proton process (fig. S3).

Discharge under galvanostatic conditions in 0.1 M $HClO_4$ probe the available charge of these materials (Fig. 2) and the rate at which this charge can be extracted. We note that for the thinner film, almost no dependence of the discharge rate is observed, but the thicker film shows clear limitation of capacity and rate within the interval of 1 to 17 A/g. We note from the discharge curves two different slopes of voltage versus charge capacity, with a transition at 0.35 to 0.55 V (depending on the film thickness and the discharge current), which should be a reflection of the two contributing materials with different redox potentials. The transition is where the quinone system should be reduced from its Q form to its QH_2 form, with remaining capacity due to the polypyrrole. For the thinner film, with little dependence on the discharge rate and therefore reflecting a situation of minor diffusion limitations, we find the quinone charge capacity to be ~40 mAh/g and the polypyrrole charge to be 30 to 35 mAh/g.

Capacitance analysis was done with the experiments reported in Fig. 2. The two slopes found in these discharge curves are interpreted as due to the two electrode mechanisms of quinone and polypyrrole electrochemistry. The capacitance values calculated from the inverse of the slopes are plotted in Fig. 3 and span from 1000 F/g

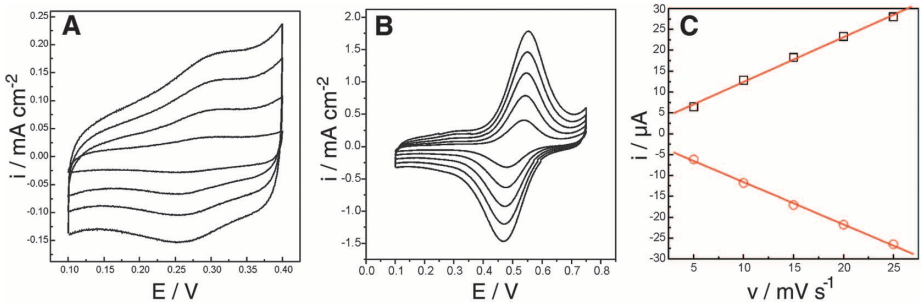

Fig. 1. CV of the Ppy(Lig) composite electrode. (**A**) Voltammograms recorded between 0.1 and 0.4 V. (**B**) Voltammograms recorded between 0.1 and 0.75 V versus Ag/AgCl, scan rates 5 to 25 mV s^{-1} (inner to outer). (**C**) Dependence of the redox peak currents on scan rate. Film thickness, 0.5 μm.

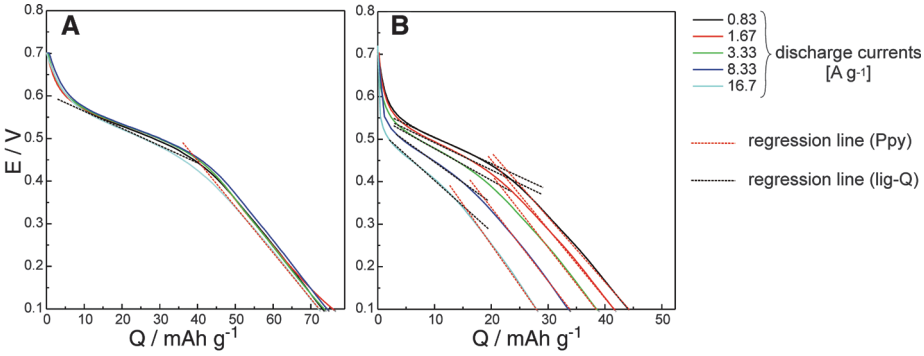

Fig. 2. Galvanostatic discharge curves for (**A**) thinner (0.5 μm) and (**B**) thicker (1.9 μm) Ppy(Lig) composite film. Two regions are visible, assigned to electrochemical activity of Ppy and lignin-derived quinones, along with linear regression lines used for capacitance analysis. For clarity, in (A) the regression lines are shown for the highest discharge current only; the other ones nearly overlap with each other.

[1]Institute of Chemistry and Technical Electrochemistry, Poznan University of Technology, Piotrowo 3, 60-965 Poznan, Poland. [2]Biomolecular and Organic Electronics, Department of Physics, Chemistry, and Biology, Linköping University, S-581 83 Linköping, Sweden.

*To whom correspondence should be addressed. E-mail: ois@ifm.liu.se

for the thin-film electrode quinone system at low discharge rates to 350 F/g for the thick electrode at high discharge rates, with diffusion limitations. The overall capacitance in the composite material, a combination of both processes, is lower.

We have studied the mass change of the electrode, both during the synthesis process and during oxidation and reduction, using a quartz crystal microbalance with dissipation monitoring (*21*). The synthesis of the polymer material under galvanostatic conditions leads to a mass that grows linearly with charge (fig. S1).

During redox cycling of the electrode material in 0.1 M aqueous $HClO_4$, mass changes are small and indicative of a mixed anion and cation exchange with the electrolyte (figs. S4 and S5). By comparison with standard polypyrrole (ClO_4^-), we note smaller mass change and suppressed variation of the mechanical modulus of the material during redox.

The presence of two distinct redox waves in the CV of composite electrodes further illustrates the difference between the Ppy(Lig) material and standard forms of polypyrrole. The location and shape of the second redox wave shows that the quinone groups of the lignosulfonate are responsible for this charge. The wave can be deconvoluted into two redox peaks 0.3 V apart when measured by differential pulse polarography (fig. S2C). The different monolignols in the lignosulfonate material show different chemical structures adjacent to the quinone groups, and the sinapyl element—with a methoxy group near the quinone group—is plausibly the one found at lower potential, as the methoxy group injects electrons into the phenyl ring (*18*).

Integration of the charge in the CV in Fig. 1B indicates that the ratio of charge in the redox of polypyrrole and the quinone groups is ~1:1.4. Because the fraction of polypyrrole to lignosulfonate is almost 1:1 in the composite material, as deduced from elemental analysis, we conclude that the major charge storage is within the quinone system. This is true also for thick films and indicates that the quinone redox site is readily accessible. The redox process requires both ion and electron transport, and the redox peak amplitude is linear in sweep rate for thin electrodes (0.5 μm), indicating a surface-bound electroactive species. As we go to thicker films (1.9 μm), we transit to a diffusion-limited redox peak for the quinone group (fig. S2B).

We propose that the redox activity in the composite electrode is due to anion insertion in the first wave and a proton release in the second wave (Fig. 4).

$$Ppy^0(Lig\text{-}QH_2) \rightarrow Ppy^+(ClO_4^-)(Lig\text{-}QH_2) + e^-$$

$$Ppy^+(ClO_4^-)(Lig\text{-}QH_2) \rightarrow Ppy^+(ClO_4^-)(Lig\text{-}Q) + 2e^- + 2H^+$$

The net reaction (if completed) is

$$Ppy^0(Lig\text{-}QH_2) \rightarrow Ppy^+(ClO_4^-)(Lig\text{-}Q) + 3e^- + 2H^+$$

Water can be the proton donor/acceptor in quinone electrochemistry and is a most probable site where the proton is stored. This is why the

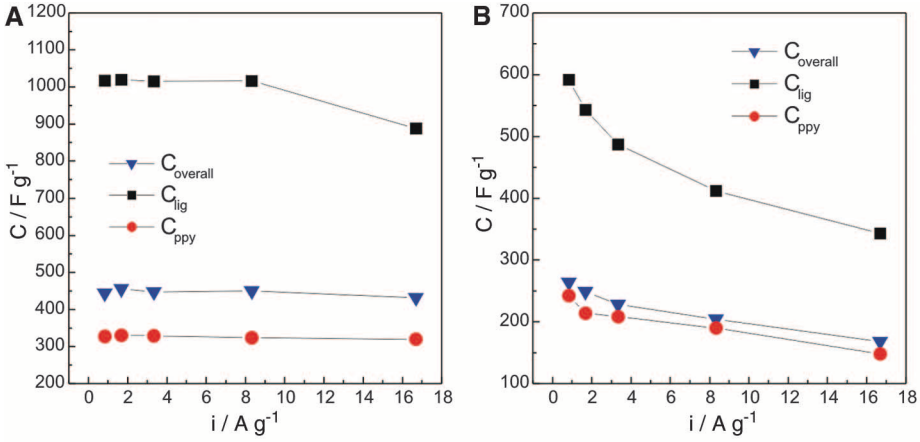

Fig. 3. Capacitance versus discharge current of Ppy(Lig) electrodes, as evaluated in terms of two contributing capacitances due to the quinone (C_{lig}) and the polypyrrole (C_{ppy}) redox processes. The data are extracted from the slopes of the linear parts of the discharge curves shown in Fig. 2. The overall capacitance ($C_{overall}$) was calculated from the charge stored and the voltage change. The thinner electrode (**A**) (0.5 μm) shows only a minor dependence of the three variables (C_{lig}, C_{ppy}, and $C_{overall}$) on the discharge current, whereas the thicker electrode (**B**) (1.9 μm) is strongly influenced by diffusion limitations.

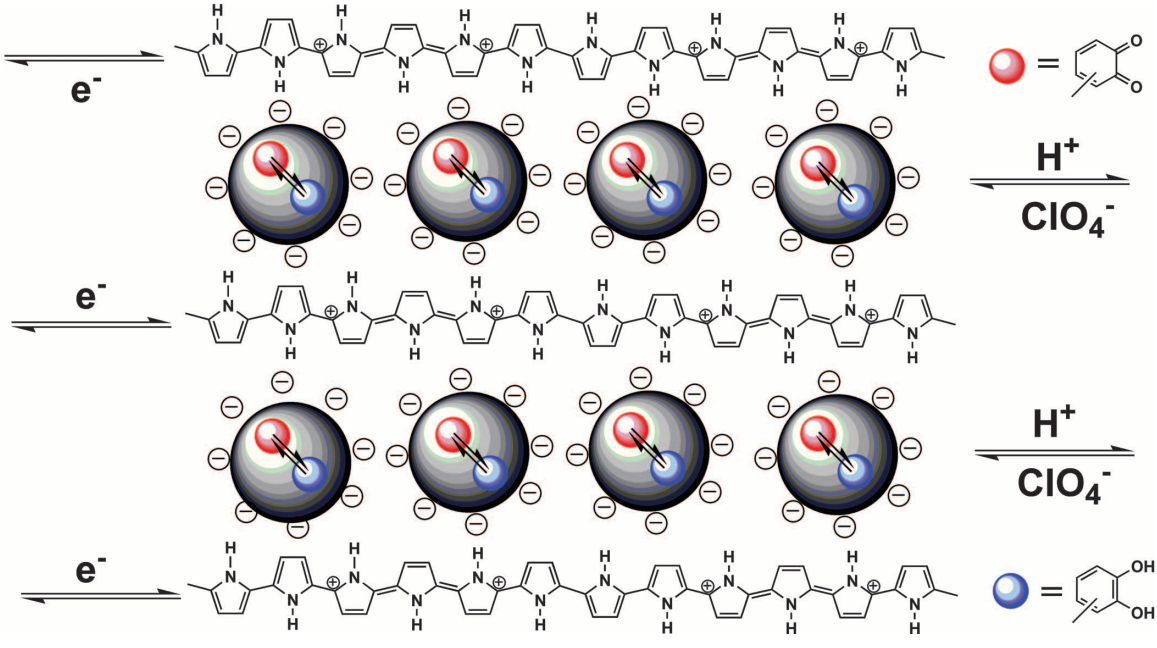

Fig. 4. A simplified reaction of oxidative electrochemical redox of quinone functions in a lignosulfonate biopolymer within a polypyrrole matrix.

use of nonaqueous solutions almost completely suppresses electroactivity (*21*). However, polypyrrole has acid-base properties leading to marked pH sensitivity of conductivity (*22*, *23*). It is a conceivable proton acceptor, but within this pH range conductivity is retained.

Polypyrrole may thus be a site for proton storage after oxidation and for retrieval upon reduction of the quinone group.

We know the mass fraction of –OH groups in the lignosulfonate material and can calculate the fraction of phenol groups in the composite electrode (*21*). In the lignosulfonate used, two of the monomers (sinapyl and coniferyl alcohol) dominate, and we neglect the contribution from the p-coumaryl alcohol group. These monomers could each contribute one quinone group, giving a maximum of 7% by weight of quinone in the composite electrode. This gives us a value of 69 mAh/g. For the polypyrrole fraction, elemental analysis indicates a low amount of anionic dopant species due to ClO_4^-, and we can estimate a upper limit to this charge capacity of 40 mAh/g, based on anion exchange only. Assuming that polypyrrole can be charged to one charge per four monomers (with some fixed counterions carried on the lignosulfonate) and that cation exchange accounts for the ion flow, we obtain values of 90 mAh/g. We did not observe mass loss during oxidation of the electrode, so the cation insertion mechanism must be a minor one. The 50/50% composite material could therefore store ~80 mAh/g, based on the 1:1 stoichiometry. In measurements, we find charge densities at lower but comparable numbers, 70 to 75 mAh/g, for the thin-film electrode.

The theoretical ratio between charge capacity in the lignosulfonate and in polypyrrole is between 1.75 and 0.8, depending on the method of estimating polypyrrole capacity. Our experimental value is 1.4. However, as we must assume that the charge capacity in polypyrrole is higher than that of the oxidized lignosulfonate in order to explain our experimental results, we must also conclude that we used a large fraction of all quinone groups incorporated in the polymer film. The observation that a large fraction of the redox capacity of the lignosulfonate is accessible for electrochemistry is consistent with the almost molecular miscibility of polypyrrole and lignosulfonate, as also proven by the absence of nanostructure in electron microscopy (*21*). The density of the material is 1.4 g/cm^3, which leads to a volumetric charge density of 100 mAh/cm^3.

Self discharge (*21*) is a problem with these electrodes and will need further study. However, we observe considerable differences of performance between different lignosulfonate compounds. The fraction of phenolic groups varies widely in lignosulfonates, depending on origin and processing of lignin. This means that there is room for optimization of the Ppy(Lig) materials using different sources of processed lignins with varying loading, with varying charge densities, and with a possibility to improve upon present results.

We compare the charge capacity and the capacitance per mass of these materials to those for polypyrrole/carbon composites [table 1 in (*24*)]—as analyzed for the three-electrode situation, which does not take counter electrode and electrolyte into account—and find that the charge density and capacitance of Ppy(Lig) are higher than reported for most of these materials. Only polypyrrole combined with nanostructured carbons is close to the values reported here.

We have demonstrated interpenetrating networks of lignosulfonate and polypyrrole that can be used for charge and energy storage. The use of the renewable biopolymer should lead to low-cost electrodes with improved safety and nontoxicity, operating in water. There is ample room for further developments to improve charge density and capacitance by searching through the universe of lignins.

References and Notes

1. P. Novák, K. Müller, K. S. V. Santhanam, O. Haas, *Chem. Rev.* **97**, 207 (1997).
2. M. Armand, J. M. Tarascon, *Nature* **451**, 652 (2008).
3. R. B. Bjorklund, B. Liedberg, *J. Chem. Soc. Chem. Commun.* **1986**(16), 1293 (1986).
4. P. Novák, O. Inganäs, R. Bjorklund, *J. Electrochem. Soc.* **134**, 1341 (1987).
5. G. Nyström, A. Razaq, M. Strømme, L. Nyholm, A. Mihranyan, *Nano Lett.* **9**, 3635 (2009).
6. T. J. Meyer, M. H. V. Huynh, H. H. Thorp, *Angew. Chem.* **46**, 5284 (2007).
7. Y. H. Huang, J. B. Goodenough, *Chem. Mater.* **20**, 7237 (2008).
8. B. Piro *et al*., *J. Chim. Phys.* **95**, 1522 (1998).
9. D. Haringer, P. Novák, O. Haas, B. Piro, M. C. Pham, *J. Electrochem. Soc.* **146**, 2393 (1999).
10. K. Naoi, S. Suematsu, A. Manago, *J. Electrochem. Soc.* **147**, 420 (2000).
11. B. Zinger, *Synth. Met.* **30**, 209 (1989).
12. H. Yoneyama, Y. Ii, S. Kuwabata, *J. Electrochem. Soc.* **139**, 28 (1992).
13. S. A. Hashmi, S. Suematsu, K. Naoi, *J. Power Sources* **137**, 145 (2004).
14. H. K. Song, G. T. R. Palmore, *Adv. Mater.* **18**, 1764 (2006).
15. C. Heitner, D. R. Dimmel, J. A. Schmidt, *Lignin and Lignans: Advances in Chemistry* (CRC Press, Boca Raton, FL, 2010).
16. G. Milczarek, *Electroanalysis* **19**, 1411 (2007).
17. G. Milczarek, *Electroanalysis* **20**, 211 (2008).
18. G. Milczarek, *Langmuir* **25**, 10345 (2009).
19. C. Sasso, M. Fenoll, O. Stephan, D. Beneventi, *Bioresources* **3**, 1187 (2008).
20. C. Yang, P. Liu, *Ind. Eng. Chem. Res.* **48**, 9498 (2009).
21. Materials and methods are available as supporting material on *Science* Online.
22. O. Inganäs, R. Erlandsson, C. Nylander, I. Lundstrom, *J. Phys. Chem. Solids* **45**, 427 (1984).
23. Q. Pei, R. Qian, *Synth. Met.* **45**, 35 (1991).
24. L. Nyholm, G. Nyström, A. Mihranyan, M. Strømme, *Adv. Mater.* **23**, 3751 (2011).

Acknowledgments: This work was supported by the Knut and Alice Wallenberg Foundation, and O.I. is a Wallenberg Scholar. We thank R. Gabrielsson, N. Solin, A. Elfving, and V. Andersson for experimental support and discussion. The kind donation of lignosulfonate samples from Borregaard LignoTech AS is gratefully acknowledged. The authors have applied for a Swedish patent on the class of materials reported here.

Supporting Online Material

www.sciencemag.org/cgi/content/full/335/6075/1468/DC1
Materials and Methods
Figs. S1 to S9
References (*25*–*29*)

11 October 2011; accepted 15 February 2012
10.1126/science.1215159

Iron-Catalyzed Cyclopropanation in 6 M KOH with in Situ Generation of Diazomethane

Bill Morandi and Erick M. Carreira*

Diazomethane is a common and versatile reagent in organic synthesis whose broader use is generally impeded by its explosiveness and toxicity. Here we report that a simple iron porphyrin complex catalyzes the cyclopropanation of styrenes, enynes, and dienes under the demanding conditions [aqueous 6 molar potassium hydroxide (KOH) solution, open to air] necessary for the in situ generation of diazomethane from a water-soluble diazald derivative. A biphasic reaction medium arising from the immiscibility of the olefin substrates with water appears essential to the overall efficiency of the process. The work we describe highlights an approach to catalysis with untoward reactive intermediates, in which the conditions for their generation under operationally safe regimes dictate catalyst selection.

In general, chemical processes requiring the use of reactive intermediates, such as diazoalkanes, azides, and arene diazoniums, experience limitations as a consequence of the inherent risk associated with the use of these reaction partners because of their explosive and toxic nature, despite the fact that in many instances these intermediates are readily accessible and inexpensive. A particularly useful example is diazomethane, CH_2N_2, a valuable reagent available to the synthetic chemist (*1*): It may be used in esterification, dipolar cycloaddition, epoxidation, aziridination, cyclopropanation, and carbonyl

Laboratory of Organic Chemistry, HCI H335, Wolfgang-Pauli-Strasse 10, 8093 Zürich, Switzerland.

*To whom correspondence should be addressed. E-mail: carreira@org.chem.ethz.ch

homologation (*1*). However, the hazardous nature of this reagent is well appreciated (*2*–*5*). The untoward properties of diazomethane, combined with its versatility, make the identification of safe protocols for its use an important task. The development of user-friendly reaction conditions for its generation in substoichiometric quantities as part of a continuous process and subsequent use in catalytic transformations would be a welcome development in synthesis. In this report, we disclose results toward that goal achieved by conducting an iron-catalyzed cyclopropanation reaction under demanding conditions (aqueous 6 M KOH) that permit safer use of diazomethane, obviating its isolation, purification, and handling.

More than 100 years ago, von Pechman discovered that the treatment of nitrosamides with alkali produces diazomethane as a yellow gas (*6*, *7*). Since this seminal report, many precursors of diazomethane have been developed that rely on base-mediated decomposition of nitrosamide derivatives in organic solvents, mostly diethyl ether (*1*). The diazomethane formed in this way is typically co-distilled with the diethyl ether with the use of a special apparatus (a diazald kit) (*8*), requiring great care because of the explosion risk during this manipulation. Historically, *N*-nitroso-*N*-methylurea was one of the most commonly used reagents for the generation of diazomethane (*9*, *10*). Unfortunately, this reagent itself was later recognized as being explosive (*11*) and highly carcinogenic (*12*), and its use was therefore discouraged. This led to the development of a class of more-stable, low-toxicity *N*-methyl-*N*-nitrososulfonamide reagents. Among them, *N*-methyl-*N*-nitroso-*p*-toluenesulfonamide (diazald), a stable, commercially available compound, shows low toxicity (median lethal dose 2.7 g per kilogram of body weight) as compared to other diazomethane precursors (*13*). This search for safer diazomethane precursors contrasts with the scant research efforts dedicated to the development of safer protocols for the use of the generated diazomethane itself (*14*). A notable exception is the recent development of approaches involving continuous-flow chemistry (*15*–*17*).

We have recently become interested in the generation and use of trifluoromethyl diazomethane in metal-carbene transfer processes (*18*–*20*), which has led in turn to the development of a safer strategy for the use of diazomethane in catalytic reactions. The approach we describe combines base-mediated generation of diazomethane over time from water-soluble diazald with an in situ metal-catalyzed carbene transfer process in a tandem manner (Fig. 1) (*21*, *22*). We reasoned that slow addition of the nitrosamide **1** to a mixture of base, catalyst, and substrate in water would avoid buildup of any appreciable concentration of in situ–generated diazomethane, which would instead be rapidly consumed by the metal catalyst. Implementation of such a protocol would minimize human exposure to the reagent as well as considerably reduce the risk of uncontrollable decomposition. In this respect, chemical processes are considered to be inherently safer in water (*23*) as a consequence of its high specific heat capacity and nonflammability. However, the identification of a catalyst compatible with aqueous 6 M KOH would be key to the successful development of such a procedure.

The protocols for the generation of diazomethane define the boundary conditions under which a catalyst would have to perform cyclopropanation reactions (Fig. 1). Any such catalyst must be compatible with strongly oxidizing (diazald) and strongly alkaline conditions (6 M KOH) and water. Moreover, it was our goal at the outset to conduct the reaction open to air. The set of excessive demands placed on any catalyst that is compatible defines a distinct approach to catalysis, in which untoward reactive intermediates are generated and used in situ, and in which the conditions for their generation under operationally safe regimes dictate catalyst selection and development. In an attempt to address the challenge, we screened a range of common metal complexes known for their ability to mediate carbene transfer with diazocompounds. We selected the cyclopropanation of *p*-methoxy styrene to test the catalytic activity of these complexes under the demanding conditions required for the decomposition of **1** (*24*), a water-soluble diazald analog.

We started our investigations with the following reaction conditions (Fig. 2): Catalyst [5 mole % (mol %); 2.5 mol % in the case of rhodium dimers], *p*-MeO-styrene [1 equivalent (equiv.), limiting reagent], and 6 M KOH (*25*) were vigorously stirred in an open vial, and an aqueous solution of reagent **1** (3 equiv.) was added slowly over 4 hours to avoid any substantial buildup of diazomethane, which could be directly consumed in a tandem manner in the cyclopropanation reaction. The two most commonly used transition

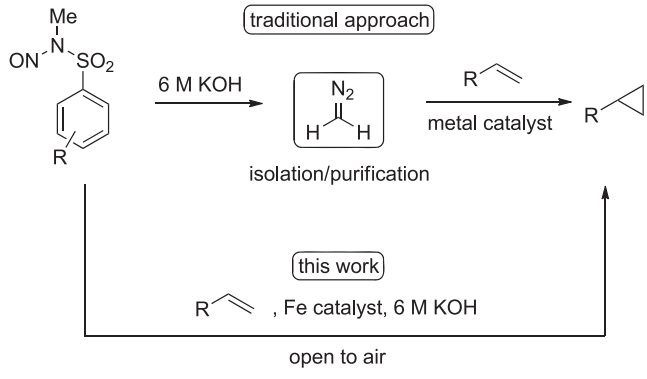

Fig. 1. Tandem diazomethane generation/iron-catalyzed cyclopropanation avoids the hazards of diazomethane isolation. R, organic group.

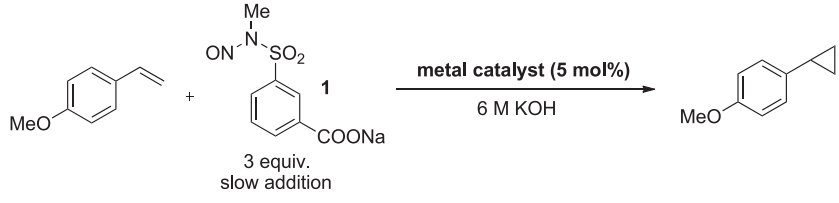

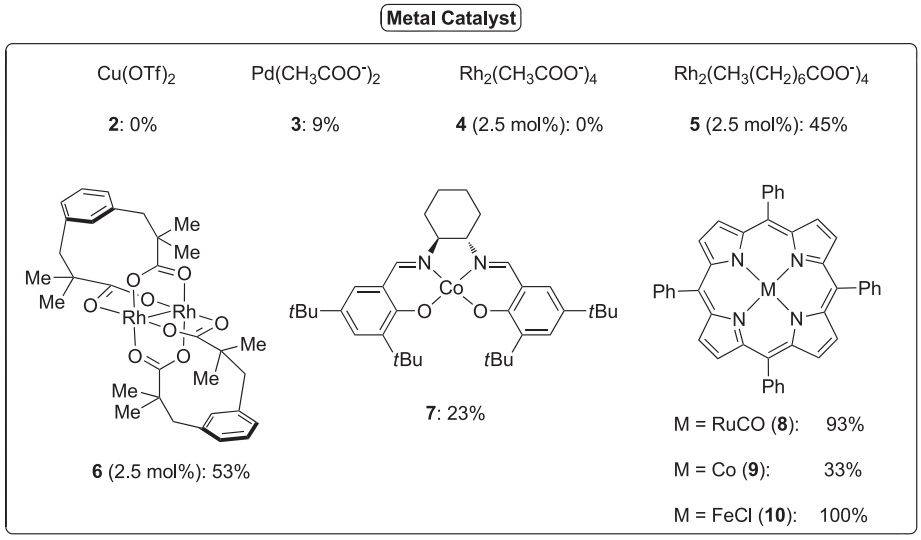

Fig. 2. Catalyst screening for the cyclopropanation reaction. OTf, trifluoromethanesulfonate.

metals in catalytic cyclopropanation with diazomethane, copper (catalyst **2**) and palladium (catalyst **3**) (*26*), were inactive under the conditions required for the diazomethane generation. To our delight, a range of other transition metals (Fe, Co, Rh, and Ru) proved suitable, giving the product cyclopropane as observed by ^{1}H nuclear magnetic resonance analysis of the crude mixture. Fe(TPP)Cl (TPP = 5,10,15,20-tetraphenyl-21H,23H-porphine) (**10**) (*27*) gave the highest conversion, which is particularly gratifying in light of the recent interest in this inexpensive and nontoxic metal (Fe) as an alternative to noble metal catalysts (*28*, *29*). A turnover number of 600 was measured using 0.1 mol % of the complex, attesting to the ability of this complex to resist decomposition under these basic conditions. We conducted the reaction of *p*-methoxystyrene at a 2-mmol scale to furnish product (Table 1, entry 2) in 91% yield.

Having a safe and practical protocol in hand, we examined the scope of olefins that could be used under these conditions (Table 1) (*30*). Terminal aromatic cyclopropanes are important motifs in drug discovery (*31*). Styrene derivatives bearing both electron-withdrawing and -donating substituents gave the corresponding products in good yields. Disubstitution was tolerated (Table 1, entry 6), and the chemistry could be extended to the preparation of versatile vinyl (entries 9 and 10) and alkynyl cyclopropanes (entries 11 and 12) (*32*, *33*). In the case where a solid substrate was used (entry 7), the addition of toluene (100 μl) was needed to dissolve the substrate and catalyst. Overall, the transformation shows broad scope and affords useful products.

This transformation overcomes many potential incompatibility concerns, such as catalyst deactivation or degradation by 6 M KOH, irreversible oxidation of the metal catalyst by strongly oxidizing diazald, or OH insertion of the metal-carbene intermediate, involving diazomethane generation and the catalytic carbene transfer reaction in a single reaction vessel. We therefore performed some preliminary experiments to gain information about the exact nature of this tandem process (Fig. 3A). First, a water-soluble substrate (**11**) was probed under the standard reaction conditions and gave no product formation. This indicates that the substrate needs to be immiscible with water, creating a biphasic reaction mixture. Second, $Rh_2(CH_3COO^-)_4$, a water-soluble catalyst, gave no conversion, whereas $Rh_2(CH_3(CH_2)_6COO^-)_4$, a lipophilic analog, gave 45% conversion. This demonstrates that the catalyst needs to be dissolved in the organic phase to induce reaction of the metal-carbene intermediate with the substrate. Third, the addition of EtOH as cosolvent led to very low conversion. Formation of a homogeneous reaction mixture is thus deleterious to the process, illustrating the importance of the phase separation. Based on these observations, we believe that the biphasic nature is responsible for the efficiency of the reaction. The following working model is proposed (Fig. 3B): The aqueous phase contains the base and water-soluble reagent **1**, whereas the catalyst is dissolved in the substrate phase (organic). Upon formation, diazomethane migrates from the aqueous phase into the lipophilic substrate phase (organic), where it reacts with the catalyst to form a metal-carbene intermediate that is trapped by the surrounding substrate that is locally present in excess. This model explains the insensitivity of the catalytic reaction to the strong base and the strong oxidizing reagent that are localized in the aqueous phase. It also provides a rationale for the preferred reaction of the metal-carbene intermediate with the substrate over OH insertion with the water present in excess.

The unexpected compatibility of metal-carbene catalysis with the strong alkaline conditions necessary for diazomethane generation illustrates the power of this approach to catalysis. Given the number of other noxious reagents that are inexpensively prepared in aqueous media (diazoniums, azides, and diazocompounds), we believe that these results will have broader implications for their use in catalysis, enabling the development of safer protocols for the preparation of valuable molecules for materials science, biology, and drug discovery.

Table 1. Scope of the tandem diazomethane generation/iron-catalyzed cyclopropanation.

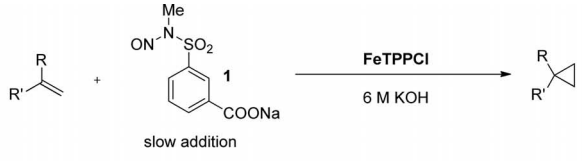

Entry	Alkene	Cyclopropane	Yield‡ (%)
1*			80
2*	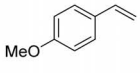	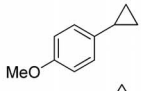	89
3*	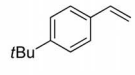	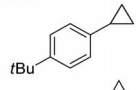	78
4*	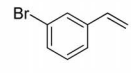	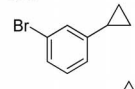	81
5*	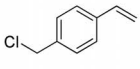	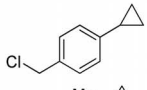	76
6*	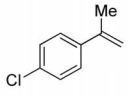	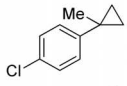	74
7†	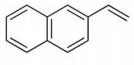	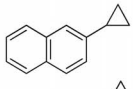	70
8†	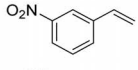	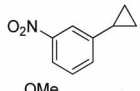	64
9†	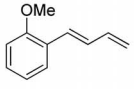	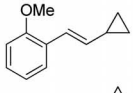	78
10†	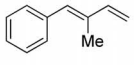	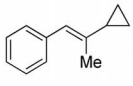	72
11†	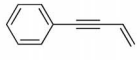	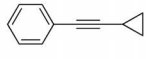	74
12†	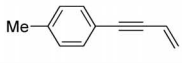	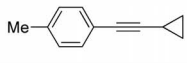	76

*Conditions: FeTPPCl (2 mol%), **1** (3 equiv. added over 4 hours), substrate (0.22 mmol), 2 ml of 6 M KOH. †Conditions: FeTPPCl (3 mol%), **1** (5 equiv. added over 7 hours), substrate (0.22 mmol), 3 ml of 6 M KOH. ‡Isolated yield of pure product.

References and Notes

1. T. H. Black, *Aldrichim. Acta* **16**, 3 (1983).
2. R. Schoental, *Nature* **188**, 420 (1960).
3. C. E. Lewis, *J. Occup. Med.* **6**, 91 (1964).

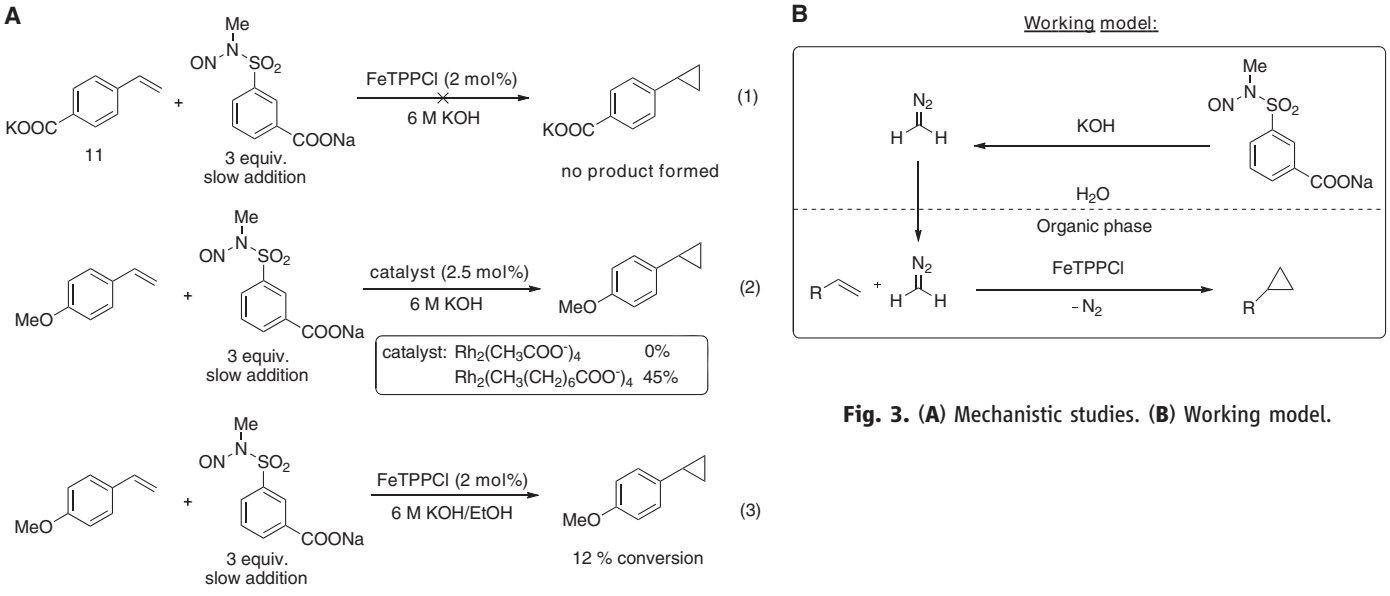

Fig. 3. (**A**) Mechanistic studies. (**B**) Working model.

4. E. B. Lewinn, *Am. J. Med. Sci.* **218**, 556 (1949).
5. T. J. de Boer, H. J. Backer, *Org. Synth. Coll.* **4**, 250 (1963).
6. H. von Pechman, *Chem. Ber.* **27**, 1888 (1894).
7. H. von Pechman, *Chem. Ber.* **28**, 855 (1895).
8. Aldrich Technical Bulletin No. AL-180 (Aldrich Chemical Company, Milwaukee, WI, 2004).
9. B. Eistert, *Angew. Chem.* **54**, 99 (1941).
10. O. M. Nefedov, Y. V. Tomilov, A. B. Kostitsyn, U. M. Dzhemilev, V. A. Dokitchev, *Mendeleev Commun.* **2**, 13 (1992).
11. In our preliminary studies, we experienced explosions when concentrated base was added to this reagent, and its use was therefore abandoned because of serious safety concerns. For a discussion about the explosive properties of *N*-nitrosomethylurea, see (*9*).
12. U.S. Department of Health and Human Services, Public Health Service, National Toxicology Program, *Report on Carcinogens* (U.S. Department of Health and Human Services, Washington, DC, ed. 12, 2011), p. 316.
13. Material Data Safety Sheet for *N*-methyl-*N*-nitroso-*p*-toluenesulfonamide (Sigma-Aldrich Chemical Company, Switzerland, 2011).
14. K.-T. Yip, D. Yang, *Chem. Asian J.* **6**, 2166 (2011).
15. R. A. Maurya, C. P. Park, J. H. Lee, D.-P. Kim, *Angew. Chem. Int. Ed.* **50**, 5952 (2011).
16. L. D. Proctor, A. J. Warr, *Org. Process Res. Dev.* **6**, 884 (2002).
17. M. Struempel, B. Ondruschka, A. Stark, *Org. Process Res. Dev.* **13**, 1014 (2009).
18. B. Morandi, E. M. Carreira, *Angew. Chem. Int. Ed.* **49**, 938 (2010).
19. B. Morandi, E. M. Carreira, *Angew. Chem. Int. Ed.* **49**, 4294 (2010).
20. B. Morandi, B. Mariampillai, E. M. Carreira, *Angew. Chem. Int. Ed.* **50**, 1101 (2011).
21. J. R. Fulton, V. K. Aggarwal, J. de Vicente, *Eur. J. Org. Chem.* **2005**, 1479 (2005).
22. R. P. Wurz, A. B. Charette, *Org. Lett.* **4**, 4531 (2002).
23. Health and Safety Executive, *Designing and Operating Safe Chemical Reaction Processes* (HSE Books, UK, 2000), p. 16.
24. D. Moody, international patent WO/2008/040947 (2008).
25. The reaction using Fe(TPP)Cl was performed with 0.5 M KOH under otherwise identical reaction conditions and afforded only 20% conversion. Strongly basic medium is thus required for the process.
26. G. Maas, *Top. Curr. Chem.* **137**, 75 (1987).
27. J. R. Wolf, C. G. Hamaker, J.-P. Djukic, T. Kodadek, L. K. Woo, *J. Am. Chem. Soc.* **117**, 9194 (1995).
28. *Iron Catalysis in Organic Synthesis, Reactions and Applications*, B. Pliekter, Ed. (Wiley-VCH, Weinheim, Germany, 2008).
29. S. Enthaler, K. Junge, M. Beller, *Angew. Chem. Int. Ed.* **47**, 3317 (2008).
30. Materials and methods are available as supporting material on *Science* Online.
31. J. Salaün, *Top. Curr. Chem.* **207**, 1 (2000).
32. M. Rubin, M. Rubina, V. Gevorgyan, *Chem. Rev.* **107**, 3117 (2007).
33. B. Morandi, J. Cheang, E. M. Carreira, *Org. Lett.* **13**, 3080 (2011).

Acknowledgments: We are grateful to Stipendienfonds der Schweizerischen Chemischen Industrie (SSCI) for a fellowship to B.M. and to ETH-Zurich for generous support through grant 0-20744-11.

Supporting Online Material

www.sciencemag.org/cgi/content/full/335/6075/1471/DC1
Materials and Methods
Figs. S1 to S16
References (*34*, *35*)

5 January 2012; accepted 14 February 2012
10.1126/science.1218781

Energy Capture from Thermolytic Solutions in Microbial Reverse-Electrodialysis Cells

Roland D. Cusick, Younggy Kim, Bruce E. Logan*

Reverse electrodialysis allows for the capture of energy from salinity gradients between salt and fresh waters, but potential applications are currently limited to coastal areas and the need for a large number of membrane pairs. Using salt solutions that could be continuously regenerated with waste heat (≥40°C) and conventional technologies would allow much wider applications of salinity-gradient power production. We used reverse electrodialysis ion-exchange membrane stacks in microbial reverse-electrodialysis cells to efficiently capture salinity-gradient energy from ammonium bicarbonate salt solutions. The maximum power density using acetate reached 5.6 watts per square meter of cathode surface area, which was five times that produced without the dialysis stack, and 3.0 ± 0.05 watts per square meter with domestic wastewater. Maximum energy recovery with acetate reached 30 ± 0.5%.

Microbial fuel cell (MFC)–based technologies are promising methods for direct electrical power production from waste organic matter, wastewater treatment, and the capture of salinity gradients in salt- and freshwater sources (*1*–*3*). Exoelectrogenic microorganisms can oxidize soluble organic matter, such as that present in wastewater (*4*, *5*), and release electrons to an electrode. Power densities with air-cathode MFCs have reached 2.7 W/m^2 by using optimized solutions with equally sized electrodes (*6*) but are lower when using complex organics or solutions (0.26 to 0.45 W/m^2) with ionic conductivities typical of domestic wastewater (~1 mS/cm) (*7*–*9*).

Reverse electrodialysis (RED) is a process for direct electricity production from salinity-gradient

Department of Civil and Environmental Engineering, 212 Sackett Building, Pennsylvania State University, University Park, PA 16802, USA.

*To whom correspondence should be addressed. E-mail: blogan@psu.edu

energy, obtained from seawater and freshwater sources, based on the use of many pairs of anion and cation exchange membranes situated between two electrodes. Many membrane pairs are needed for effective harnessing of salinity gradients as electricity, resulting in high costs for standalone RED systems (*10*, *11*). The use of natural waters in RED can result in membrane fouling without extensive pretreatment of fresh and salt water. In principle, salinity-gradient energy can be effectively captured within a microbial reverse-electrodialysis cell (MRC) by using only a small number of membrane pairs (Fig. 1). Bacterial oxidation of organic matter and oxygen reduction provide favorable electrode reactions, resulting in efficient capture of energy in the RED stack (*12*). However, RED and MRC applications are currently limited to estuarine or coastal areas because of the need for both fresh- and saltwater solutions (*12*).

Thermolytic solutions such as ammonium bicarbonate (NH_4HCO_3), which can be concentrated with low-grade thermal energy (*13*), theoretically may be able to provide the salinity-gradient energy source for a RED stack. When combined with a favorable reaction at the electrodes in an MFC, or used in a microbial electrolysis cell (MEC) for hydrogen gas production (*12*, *14*), an MRC using NH_4HCO_3 could result in more efficient capture of energy from wastewaters and other sources of biomass than could an MFC. The capture of waste heat (>40°C) energy with NH_4HCO_3 is possible with conventional and well-proven technologies, such as vacuum distillation (*15*), that can produce high-concentrate (HC) and low-concentrate (LC) salt solutions. The resulting energy difference between 1 M and 0.01 M NH_4HCO_3 HC and LC solutions is equivalent to 370 m of hydraulic head, which is even greater than that of typical ocean and river water (270 m) (*11*). NH_4HCO_3 is relatively distinct among many different chemicals that have been proposed for capturing energy through pressure differences, in a process called pressure-retarded osmosis (PRO), because of the easily volatilized ionic species (*16*). PRO requires the flow of water through specific types of membranes, distillation of larger volumes of water than would be needed for a RED stack, and mechanical conversion of pressure into electrical power. This is different than the MRC process, in which electricity is directly generated by bacteria, voltages are increased by the salinity gradient, conventional ion exchange membranes are used, and there is no direct contact of the fresh water and salt solutions.

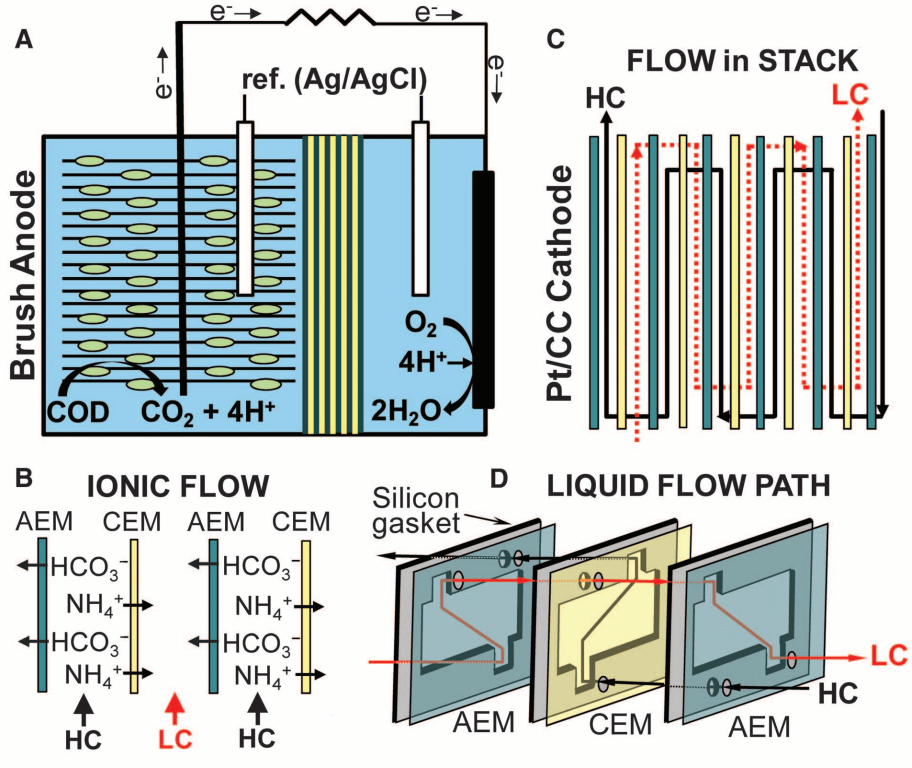

Fig. 1. (**A**) Main components of the MRC, showing the membrane stack between the electrodes, the reference electrodes, and the circuit containing a load (resistor). (**B**) Example of how the anion-exchange membranes (AEMs) and cation-exchange membranes (CEMs) are used to selectively drive the flow of positive ions to the right (toward the cathode) and the negatively charged ions to the left (toward the anode). The flow of these charged ions adds potential to the current produced by the microbes on the anode and maintains electroneutrality at the electrodes. (**C**) Expanded view of the membrane stack showing flow path of the HC and LC solutions of NH_4HCO_3. (**D**) Construction of the gaskets used to direct the flow from one LC chamber to the next LC chamber, avoiding the HC chamber through a short flow path through the membrane and gasket.

To test the utility of NH_4HCO_3 solutions for energy production, we examined four different salinity ratios (SRs) with a single HC solution (0.95 M NH_4HCO_3, conductivity of 65.5 mS/cm) in an MRC (58.4 mL) containing five membrane pairs (Fig. 1) at a fixed-solution flow rate (1.6 mL/min). The maximum power (normalized to projected cathode area of 7 cm^2) was 5.4 W/m^2 (SR = 100) with 1 g/L of sodium acetate. For these conditions, the RED stack contributed 2.1 ± 0.01 W/m^2 (39%) of the produced power, compared with 3.3 ± 0.04 W/m^2 (61%) from the oxidation of the substrate (Fig. 2A). The cell obtained peak power at a total cell voltage of 0.75 V and current density of 0.72 mA/cm^2. Lowering the flow rate (fig. S2) from 1.6 to 0.85 mL/min (4.9 ± 0.1 W/m^2) reduced power by an amount equivalent to using an SR of 50 (4.7 ± 0.1 W/m^2). The use of the RED stack and a saline catholyte alone increased power, as shown by an MRC power density of 1.7 ± 0.05 W/m^2 with membranes all containing the same saline solution (SR = 1), relative to that of a single-chamber MFC (no membranes; 1.08 ± 0.03 W/m^2). This improved performance of the MRC could be due to a number of factors, including improved charge transfer at the cathode (65.5 mS/cm), a salinity gradient between the stack and the anode, and the flow of bicarbonate ions through the anion exchange membrane, which helps to maintain anode pH at 6.9 ± 0.1 compared with a decrease in pH to 5.5 by using NaCl salt solutions (*12*).

We further examined power production using different concentrations of HC and LC solutions at a fixed salinity ratio (SR = 100). MRC power density reached a maximum of 5.6 ± 0.04 W/m^2 for the 1.1 M HC solution (Fig. 2B). This was 20% higher than that produced with an artificial seawater (NaCl) and freshwater (*12*). Internal resistances, obtained from the slope of the polarization curves (fig. S6), ranged from 170 ohms (HC = 0.5 M) to 138 ohms (HC = 1.8 M).

The most substantial impact of the RED stack on MRC performance was that it increased maximum power production using organic matter. Electrode reactions in the MRC produced up to 3.2 ± 0.2 W/m^2, which is three times the power produced in the absence of the stack in a single-chamber MFC (1.08 ± 0.03 W/m^2) (Fig. 2). The contribution of the electrodes to total power generation did not appreciably vary for HCs between 0.5 and 1.1 M (SR = 100), although power was reduced at the highest HC (1.8 M) (Fig. 2B). The use of the RED stack produced a very stable cell voltage with increasing current, with electrode potentials maintained very close to their open circuit values as current density increased (Fig. 3). In contrast, MFC electrode potentials substantially changed with increasing current. High salt concentrations (1.1 and 1.8 M) adversely affected the anode biofilm at the highest current densities, as shown by a rapid increase in the electrode potential (Fig. 3). This rapid change in electrode potential resulted in substantially reduced power densities in subsequent cycles, indicating damage

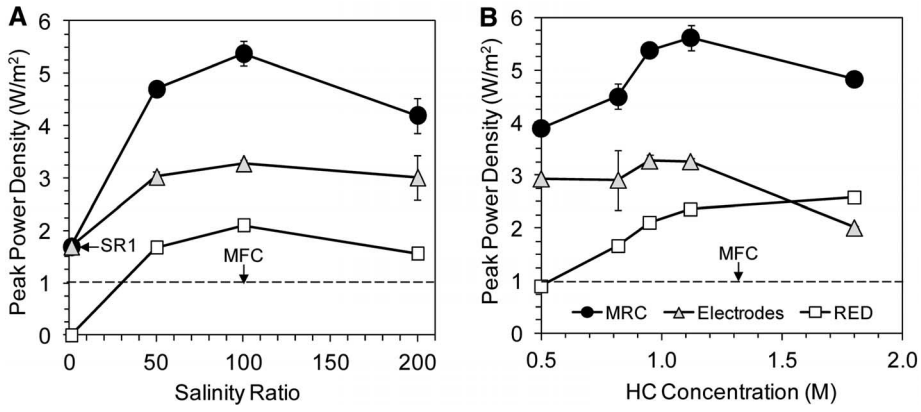

Fig. 2. Peak power densities obtained from polarization curves, apportioned to power from the RED (salinity-gradient power) compared with the electrodes (organic matter power). (**A**) Effect of SR on peak power density with a fixed HC solution (0.95 M). (**B**) Effects of HC concentrations on power with a fixed SR of 100. The dashed line represents peak power density of the same electrodes in a single chamber.

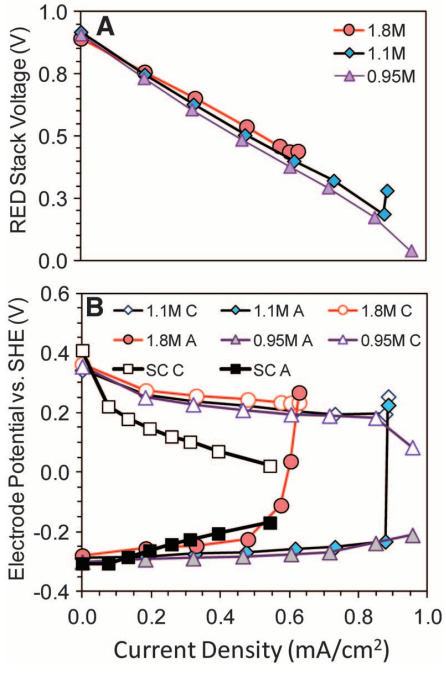

Fig. 3. (**A**) RED stack voltage and (**B**) anode (A) and cathode (C) potentials versus current density for the MRC by using different HC solutions (0.95, 1.1, and 1.8 M). The stability of the anode potential at higher current densities was the primary reason for the increased power density.

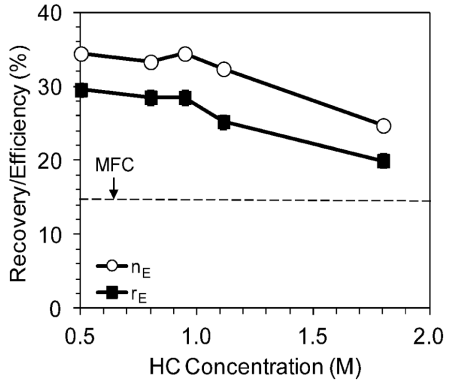

Fig. 4. Energy recovery (r_E) and energy efficiency (η_E) for the MRC in batch recycle experiments, using different HC solutions. Energy recovery is defined by the ratio of energy produced by the MRC reactor and the energy input as substrate and salinity gradient. Energy efficiency was calculated as the ratio of energy produced to the energy consumed based on the substrate used and the salinity gradient. The dashed line indicates energy recovery and efficiency using the same electrodes in a single chamber MFC reactor (no membranes).

to the anode biofilm. Several additional cycles were needed at low current densities (high resistances) to restore performance.

Energy recoveries (r_E, based on total energy entering) and energy efficiencies (η_E, energy-in minus energy going out) were higher for the MRC than a MFC. Energy recoveries for the MRC, at a fixed salinity ratio (SR = 100), ranged from 30 ± 0.5% (HC = 0.5 M) to 20 ± 0.0% (HC = 1.8 M), with energy efficiencies of 34 ± 0.5% (HC = 0.5 M) to 25 ± 0.0% (HC = 1.8 M) (Fig. 4). Maximum energy recovery in the MFC was only 14 ± 2%, with a slightly larger energy efficiency of 16 ± 2%. Coulombic efficiencies, or the percentage recovery of electrons from the substrate, were higher in the MRC (66 ± 4%) than in the MFC (35 ± 4%) because the membrane stack reduced oxygen crossover from the cathode to the anode (*12*, *17*).

The use of a salinity-gradient power source in the MRC also resulted in very high power production from domestic wastewater, with up to 2.9 ± 0.05 W/m^2 (fig. S6) produced at a HC concentration of 0.95 M (SR = 100, 1.6 mL/min flow rate). The power derived from the electrode reactions was 2.0 ± 0.05 W/m^2, which is a 740% increase in power production as compared with that achieved with wastewater in a single-chamber MFC (0.27 ± 0.05 W/m^2). This power production by the electrode reactions is 50% larger than that achieved with carbon nanotube–coated electrodes in the absence of a RED stack (*18*). Power production from wastewater dropped off after only 2 hours, indicating rapid treatment of easily degraded organic matter (fig. S7). The percentage of organic matter removal based on chemical oxygen demand (COD) was 35 ± 2%, with an energy production of 0.94 kWh/kg COD. In contrast, conventional wastewater treatment using activated sludge processes can consume 1.2 kWh/kg COD (*19*). The relatively low COD removal with wastewater, compared with essentially complete removal with acetate, is typical for biofilm processes used in wastewater treatment (*20*). Soluble COD (that passing a 0.45-μm-pore-diameter filter) can easily be removed by the biofilm in a trickling filter, for example, with particulate COD removed in a secondary solids contact process (*21*) that can be used to generate methane (*19*).

One limitation in a MRC stack arrangement with NH_4HCO_3 is nitrogen crossover from the stack into the anode chamber. The predominant nitrogen forms in the ammonium carbonate solution are ammonium (NH_4^+), ammonia (NH_3), and carbamate ($NH_4CO_3^-$). Negatively charged carbamate ions crossed the anion exchange membrane and moved into the anode chamber to balance charge (protons released by the bioanode). Total ammonia nitrogen concentrations in the anode chamber after a fed-batch cycle ranged from 263 ± 32 mg/L (HC = 0.5 M) to 590 ± 36 mg/L (HC = 1.8 M) (fig. S8). For the observed values of effluent anode pH (6.8 to 7.1), free ammonia nitrogen concentrations in the anode chamber ranged from 1.0 ± 0.2 mg/L to 2.6 ± 0.03 mg/L. Total ammonia nitrogen concentrations above 500 mg/L and free ammonia nitrogen concentrations above 11 mg/L are known to inhibit power production in MFCs (*22*). However, the main concerns of nitrogen crossover are contamination of the anode solution with ammonia and loss of the salt solution. These losses can be minimized in future designs through the use of bipolar membranes or a low-salt solution in the membrane stack nearest the anode.

The use of thermolytic solutions in RED stacks could substantially change the energy balance for wastewater treatment, enable sanitation in energy-poor areas, and allow for energy capture from renewable energy sources such as solar thermal and waste heat. Three types of wastewaters (food processing, animal, and domestic) contain nearly as much energy (17 GW) as that used for the whole water infrastructure in the United States (*23*). There is approximately nine times more energy in domestic wastewater than that required to treat it by using conventional methods (*24*). In energy-poor areas, production of electrical power from wastewater creates incentive for a community to operate a treatment plant, and therefore accomplish water sanitation. Other biomass and heat sources could also be harvested in MRCs. For example, cellulose and end products from cellulose fermentation can be used in these bioelectrochemical systems (*25*–*27*), and as much as

1.34 billion tons of biomass could be produced annually in the United States without affecting food production (*28*). Industrial applications offer a good opportunity to recover the 7 to 17% of energy used in the United States that is lost as waste heat (*29*), but solar or geothermal heat sources could also be used. All of these renewable energy sources provide opportunities for producing electricity, or alternatively hydrogen gas (*14*), from salinity gradients and biomass sources.

References and Notes

1. Intergovernmental Panel on Climate Change (IPCC), *Climate Change 2007: Synthesis Report* (IPCC, Geneva, 2007).
2. H. Liu, R. Ramnarayanan, B. E. Logan, *Environ. Sci. Technol.* **38**, 2281 (2004).
3. R. D. Cusick, P. D. Kiely, B. E. Logan, *Int. J. Hydrogen Energy* **35**, 8855 (2010).
4. B. E. Logan *et al.*, *Environ. Sci. Technol.* **40**, 5181 (2006).
5. B. E. Logan, *Nat. Rev. Microbiol.* **7**, 375 (2009).
6. Y. Fan, H. Hu, H. Liu, *Environ. Sci. Technol.* **41**, 8154 (2007).
7. Y. Ahn, B. E. Logan, *Bioresour. Technol.* **101**, 469 (2010).
8. H. Liu, B. E. Logan, *Environ. Sci. Technol.* **38**, 4040 (2004).
9. S. Cheng, H. Liu, B. E. Logan, *Environ. Sci. Technol.* **40**, 2426 (2006).
10. G. L. Wick, *Energy* **3**, 95 (1978).
11. G. Z. Ramon, B. J. Feinberg, E. M. V. Hoek, *Environ. Sci.* **4**, 4423 (2011).
12. Y. Kim, B. E. Logan, *Environ. Sci. Technol.* **45**, 5834 (2011).
13. J. R. McCutcheon, R. L. McGinnis, M. Elimelech, *Desalination* **174**, 1 (2005).
14. Y. Kim, B. E. Logan, *Proc. Natl. Acad. Sci. U.S.A.* **108**, 16176 (2011).
15. R. L. McGinnis, J. R. McCutcheon, M. Elimelech, *J. Membr. Sci.* **305**, 13 (2007).
16. T. Kim *et al.*, *Desalination* **284**, 253 (2012).
17. J. R. Kim, S. Cheng, S.-E. Oh, B. E. Logan, *Environ. Sci. Technol.* **41**, 1004 (2007).
18. X. Xie *et al.*, *Environ. Sci.* **5**, 5265 (2012).
19. P. L. McCarty, J. Bae, J. Kim, *Environ. Sci. Technol.* **45**, 7100 (2011).
20. B. E. Logan, S. W. Hermanowicz, D. S. Parker, *J. Water Pollut. Control Fed.* **59**, 1029 (1987).
21. D. Parker, J. Bratby, *J. Environ. Eng.* **127**, 380 (2001).
22. J. Y. Nam, H. W. Kim, H. S. Shin, *J. Power Sources* **195**, 6428 (2010).
23. B. E. Logan, *Environ. Sci. Technol.* **38**, 160A (2004).
24. I. Shizas, D. M. Bagley, *J. Energy Eng.* **130**, 45 (2004).
25. E. Lalaurette, S. Thammannagowda, A. Mohagheghi, P.-C. Maness, B. E. Logan, *Int. J. Hydrogen Energy* **34**, 6201 (2009).
26. F. Rezaei *et al.*, *Appl. Environ. Microbiol.* **192**, 304 (2009).
27. A. Wang *et al.*, *Bioresour. Technol.* **102**, 4137 (2011).
28. U.S. Department of Energy, Biomass as feedstock for a bioenergy and bioproducts industry: The technical feasibility of a billion-ton annual supply. *DOE/GO-102005-2135* (2005).
29. U.S. Energy Information Administration (EIA), *Annual Energy Review 2010 DOE/EIA-0384* (DOE, Washington, DC, 2010).

Acknowledgments: This research was supported by award KUS-I1-003-13 from the King Abdullah University of Science and Technology (KAUST). The data are presented in the figures and supporting online material.

Supporting Online Material

www.sciencemag.org/cgi/content/full/science.1219330/DC1
Materials and Methods
Figs. S1 to S7
References (*30*–*36*)

18 January 2012; accepted 16 February 2012
Published online 1 March 2012;
10.1126/science.1219330

Silicon Isotope Evidence Against an Enstatite Chondrite Earth

Caroline Fitoussi[1,2]* and Bernard Bourdon[1,2]

The compositions of Earth materials are strikingly similar to those of enstatite chondrite meteorites in many isotope systems. Although this suggests that Earth largely accreted from enstatite chondrites, definitive proof of this model has been lacking. By comparing the silicon (Si) isotope signatures of several extraterrestrial materials with terrestrial samples, we show that they cannot be explained by core-formation scenarios involving a bulk Earth of enstatite chondrite composition. Si isotope similarities between the bulk silicate Earth and the Moon preclude the existence of a hidden reservoir in the lower mantle, a necessary condition of the enstatite chondrite model, and require an equilibrium process after the Moon-forming impact. A three–end-member chondritic mixing model for Earth reconciles the Si isotope similarities between enstatite chondrites and Earth.

Most models of Earth's bulk composition consider that its accreting material was compositionally similar to chondritic meteorites. For example, the simplest approach for establishing Earth composition models is to consider that Earth is similar to CI carbonaceous chondrites, based on the fact that this class of meteorites is closest to the solar composition (*1*, *2*). One important issue with this approach is that, although it succeeds in matching the relative abundances of refractory lithophile elements (such as Al, Ca, and Sc), it fails to explain isotope variations. Notably, for several isotope systems such as oxygen (*3*), chromium (*4*), and nickel (*5*), the isotope composition of Earth is identical to that of enstatite chondrites. Because oxygen is a major constituent of Earth (up to 50% in mass), models that invoke a bulk Earth (a solid having the mean composition of the total Earth) of enstatite chondrite bulk composition have also been proposed (*6*, *7*). However, enstatite chondrites are undifferentiated meteorites indicating an environment more reducing than that of Earth (*8*) such that (i) the iron content is extremely small in the silicate phase and (ii) sulfides of elements that are otherwise lithophile (such as MgS or MnS) are present. Another major obstacle to an enstatite chondrite model is that the Mg/Si ratio of the upper mantle found in the most fertile peridotites (*9*, *10*) differs considerably from that of enstatite chondrites. Therefore, if the bulk Earth has a bulk enstatite chondrite composition, a correspondingly large difference of the Si abundance, which influences Mg/Si ratios, between the upper mantle and the bulk Earth must be accounted for (*11*).

Silicon isotopes, which can reveal fractionation during metal-silicate equilibrium reactions (the silicate phase gets enriched in heavy Si isotopes relative to the metal), may help resolve these discrepancies. For example, in models calling on a "solar" bulk Earth composition, Si isotopes explain how the superchondritic Mg/Si ratio of the bulk silicate Earth [(BSE), a solid having the mean composition of the terrestrial crust and mantle] resulted from the incorporation of Si into the core (*12*). If one assumes 7 weight percent (wt %) Si in the core (*2*) and metal-silicate equilibrium temperatures derived from core-formation models (*13*, *14*), the calculated δ^{30}Si value for the BSE is consistent with the measured $\delta^{30}Si_{BSE}$ (*12*). Studies using the mean of all chondrites for the bulk Earth composition also concluded that the Si isotope difference between the BSE and chondrites was due to the incorporation of Si into Earth's core (*15*, *16*). A bulk Earth with an enstatite chondrite composition (EH), however, requires a core containing 28 wt % Si, which would yield a density deficit much higher than that deduced from seismic velocities (*17*). To circumvent this issue, it was proposed that a hidden lower mantle had a higher Si content compared with the upper mantle (*7*).

To further examine the enstatite chondrite model, we analyzed the Si isotope composition of enstatite chondrites, enstatite mineral separates of enstatite chondrites and aubrites that would represent the composition of material accreting to Earth, and compared them with previously analyzed terrestrial samples and new data for lunar samples. Preparation and mass spectrometric analysis of the samples have been carried out similarly to (*12*) with only minor changes (*11*). A salient feature of this data set is that the δ^{30}Si values of enstatite chondrites are systematically lower than those of other chondrites (table S1), which confirms the suggestions from previous studies (*12*, *15*, *16*).

The Si isotope composition of the BSE (measured in terrestrial basalts and peridotites) was first reported to be $\delta^{30}Si_{BSE} = -0.38 \pm 0.04$ per mil (‰) (2 SE) (*15*). Subsequently, we measured

[1]Laboratoire de Géologie de Lyon, ENS Lyon, CNRS and Université Claude Bernard de Lyon, 46 allée d'Italie, 69364 Lyon Cedex 07, France. [2]Institute of Geochemistry and Petrology, ETH Zurich, Clausiusstrasse 25, 8092, Zurich, Switzerland.

*To whom correspondence should be addressed. E-mail: caroline.fitoussi@ens-lyon.fr

a heavier value of $\delta^{30}Si_{BSE} = -0.28 \pm 0.02‰$ (2 SE) (*12*), which was later confirmed by several studies (Fig. 1) (*16*, *18*–*21*). The one study (*22*) that differs from all others in $\delta^{30}Si_{BSE}$ value also reported a different Si isotope composition for the terrestrial standard BHVO-1 (Fig. 1). The bulk silicate Moon (BSM), which we infer from high- and low-Ti lunar basalts (Fig. 1 and table S2), has a Si isotope composition of $\delta^{30}Si_{BSM} = -0.29 \pm 0.02‰$ (2 SE), which is indistinguishable from our BSE value, a result that differs from previously reported data (*11*, *15*).

The similarity of the BSE and the BSM in Si isotopes has far-reaching implications for understanding the BSE composition, as well as the Moon-forming impact. Numerical simulations of the giant impact suggest that the Moon composition should mainly reflect the silicate phase of the impactor rather than that of Earth (*23*, *24*). However, because the BSM has a terrestrial Si isotope composition, it seems highly unlikely that the impactor fortuitously had a terrestrial $\delta^{30}Si$ value that falls outside the range defined by chondrites and achondrites (*12*, *16*, *18*). In contrast, in all other isotope systems for which the BSE and the BSM are identical [O (*25*), Cr (*26*), W (*27*), Ti (*28*)], the isotope composition of the terrestrial and lunar mantles falls in the chondritic range or can be explained by mixtures of (a)chondritic compositions. Therefore, the identical Si isotope composition for the BSE and the BSM is evidence for the existence of an equilibrium process between Earth and the protolunar disk after the impact. A corresponding physical scenario has been proposed (*29*). Given that the energy provided by the Moon-forming impact was sufficient to generate a global magma ocean on Earth (*23*), this result also implies that the Si isotope composition of terrestrial samples derived from the upper mantle is indeed representative of the entire mantle. Even if magma ocean crystallization subsequently produced chemical layering in the mantle, these layers should have the same $\delta^{30}Si$ value as the upper mantle and the Moon.

Together with this key implication about the BSE, we modeled two end-member scenarios testing that the bulk Earth has the composition of enstatite chondrites [taking the mean value measured in bulk enstatite chondrites of $\delta^{30}Si = -0.62 \pm 0.04‰$ (2 SE); table S1], assuming that Earth's core contains 7 wt % Si, as in (*7*), and that the $\delta^{30}Si$ of the BSE is best explained by incorporation of Si in Earth's core, as shown in (*12*, *15*, *16*). We first tested the enstatite chondrite model considering that Earth's core formation occurred with full metal-silicate equilibration during a magma ocean stage [fig. S1, scenario 1]. In this case, the accreting material (assumed to be of enstatite chondrite composition) is entirely mixed and equilibrates with the proto-Earth's mantle before the liquid metal fraction sinks to the proto-core. A single-stage core-formation model would imply a metal-silicate equilibrium temperature of ~1500 K (Fig. 2), based on the Si isotope difference between the BSE and bulk Earth and assuming any of the recently reported fractionation factors between metal and silicate for Si isotopes (*18*, *30*, *31*). This temperature is far below those derived from core-formation models of ~3000 K for a single-stage model (*13*) or more realistic multistage models (*14*), as it is below the peridotite liquidus, even at low pressure (*32*). Deriving a Si

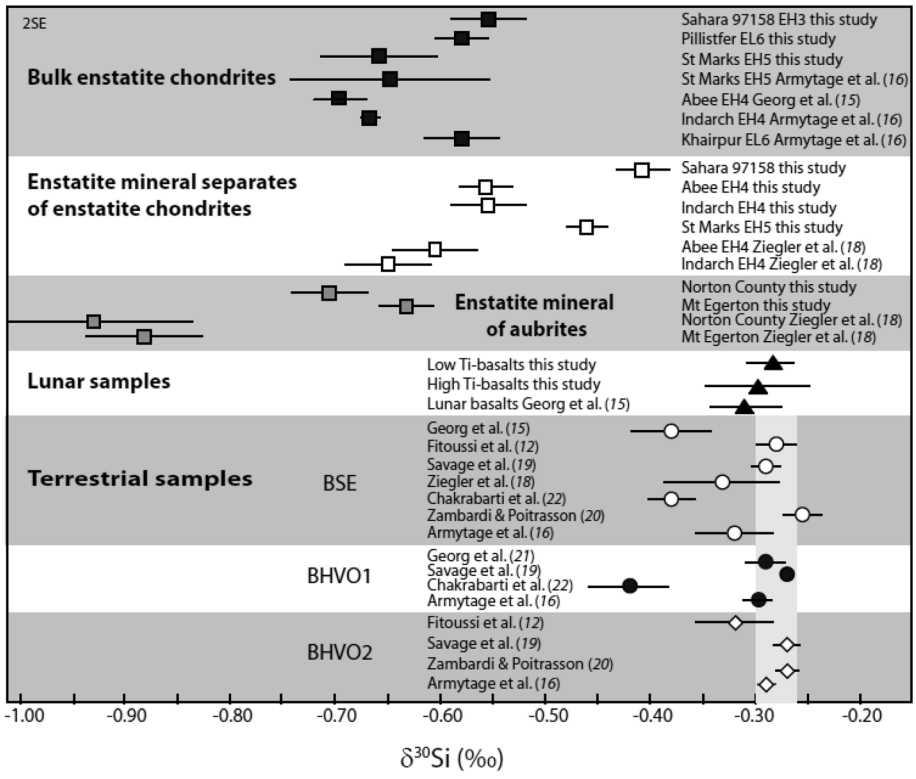

Fig. 1. Silicon isotope composition of bulk enstatite chondrites, enstatite mineral separates extracted from enstatite chondrites and aubrites, lunar samples, and terrestrial samples. The vertical band shows the mean BSE value from (*12*), which is consistent with all other studies except for (*15*) and (*22*) (see text).

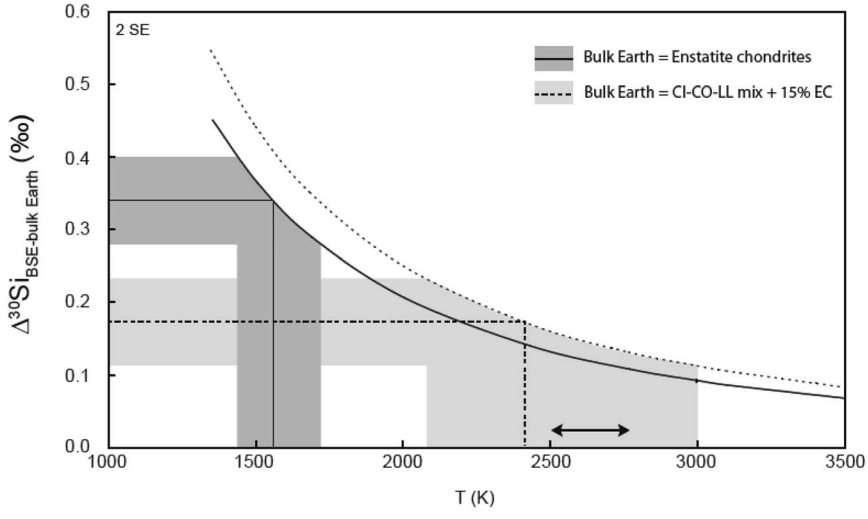

Fig. 2. Predicted difference in $\delta^{30}Si$ values between the bulk silicate Earth ($\delta^{30}Si = -0.28‰$) and the bulk Earth as a function of metal-silicate equilibrium temperature, using the fractionation factor given in (*30*) and assuming 7 wt % silicon in Earth's core. If the bulk Earth composition is assumed to be equal to that of enstatite chondrites, with $\delta^{30}Si = -0.62‰$ (solid lines), this yields an equilibrium temperature of 1500 K, well below the peridotite liquidus. If the bulk Earth is assumed to be a mixture of CI-CO-LL + 15% enstatite chondrite (EC), with $\delta^{30}Si = -0.45‰$, (dashed lines), the predicted equilibrium temperature is consistent with the range of metal-silicate equilibrium temperatures inferred from siderophile elements (see text). For reference, the temperature interval between the liquidus and solidus of peridotite at 30 GPa is marked with a double horizontal arrow.

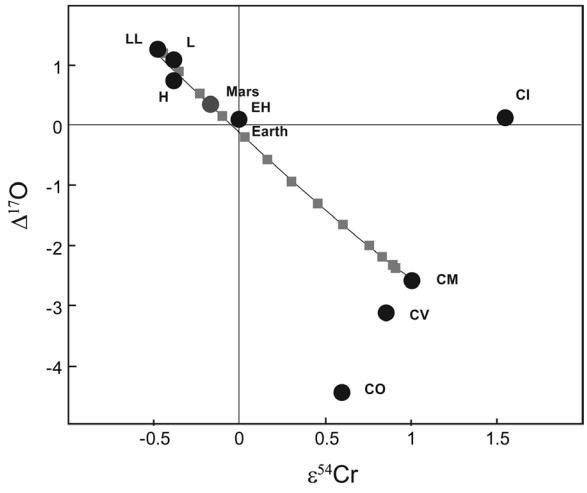

Fig. 3. A diagram of $\Delta^{17}O$ versus $\varepsilon^{54}Cr$ for a range of ordinary, carbonaceous, and enstatite chondrites [data from (*4*, *36*–*39*)], where $\Delta^{17}O = \delta^{17}O - 0.52*\delta^{18}O$, with $\delta^{i}O$ using the standard delta notation and $\varepsilon^{54}Cr = [(^{54}Cr/^{52}Cr)_{sample}/(^{54}Cr/^{52}Cr)_{std} - 1]*10^4$. The terrestrial composition plots at the origin (0,0), and the mean composition of SNC meteorites is also shown as Mars. The mean oxygen isotope composition was used to plot each meteorite group (*36*–*39*). The line with squares represents a possible mixing line between an ordinary chondrite component and a mixture of various carbonaceous chondrites (here a mixture between CO and CI chondrites). The terrestrial and martian compositions both plot on this mixing line, which indicates that the inner planets could have formed from mixtures of the same components. The similarity of Mars and Earth in their mixing relationships, while representing most of the mass in this region of the solar system, shows that there is no argument to select a single meteorite group to make the terrestrial planets.

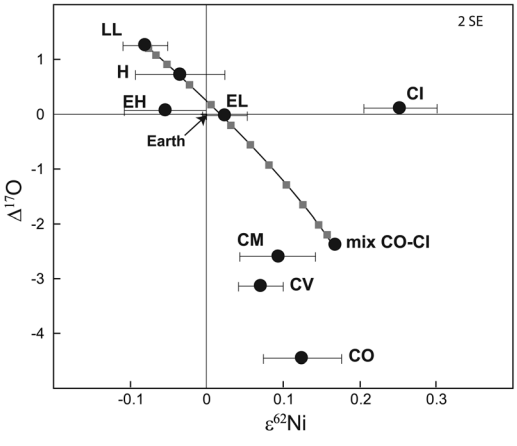

Fig. 4. A diagram of $\Delta^{17}O$ versus $\varepsilon^{62}Ni$ for a range of ordinary, carbonaceous, and enstatite chondrites [data from (*5*, *36*–*39*)]. The terrestrial composition plots at the origin (0,0). The mean oxygen isotope composition was used to plot each meteorite group (*36*–*39*). The mixing line uses the same end-member components as in Fig. 3, and again the terrestrial composition can be explained by a mixture of three components.

isotope fractionation factor from our measurements in bulk enstatite chondrites and their silicate phase (Fig. 1 and tables S1 and S3), assuming again that metal-silicate equilibration induced the observed silicon isotope difference (SOM text), also suggests that this end-member scenario is not feasible. On the other hand, if we assume that temperature of metal-silicate equilibration was 3000 K, the difference of −0.34‰ in $\delta^{30}Si$ between BSE and enstatite chondrites must be explained by a core composition of 26 wt % Si, which is well above geophysical estimates (*17*).

The other end-member scenario assumes that there is no equilibrium between newly accreted metal and silicate, as has been advocated in a number of studies [e.g., (*14*, *33*)] [fig. S1, scenario 2]. This corresponds to a core-merging scenario in which the core of the impactor directly merges with that of the proto-Earth. In this case, the Si isotope composition of the BSE is controlled by the composition of the silicate mantle in the accreting material. The silicate phase of aubrites is a reasonable candidate for estimating an upper limit of mantle composition in the context of an enstatite model (SOM text). Thus, to test this scenario with Si isotopes, we used the $\delta^{30}Si$ values of enstatite mineral separates in aubrites which, based on this work and similar earlier measurements (*18*), range from −0.93 to −0.63‰ (Fig. 1 and table S3). In this case, the Si isotope composition of the mantle would again fall well below the measured $\delta^{30}Si$ value (−0.28‰) of the BSE. Therefore, this second end-member scenario also fails to explain the Si isotope composition of the BSE.

Our end-member models based on Si isotopes support the conclusion that Earth was not built solely from enstatite chondrites. However, the marked similarity of other isotope systems (for instance, O, Cr, Ni) between Earth and enstatite chondrites still requires an explanation. Using a simple mixing calculation (*11*, *34*), three chondritic components (LL, CI, and CO chondrites in the proportions 0.63:0.16:0.21) reproduce the terrestrial composition relatively well. Although this calculation is merely illustrative as other end-member compositions could have been chosen, the mixing proportions that match the Cr and O isotopes (Fig. 3) also match the terrestrial composition in a Ni–versus–O-isotope binary mixing diagram within error (Fig. 4). This model shows that the narrow feeding zones resulting from numerical simulations of terrestrial planet accretion (*35*) would not be restricted to a unique type of chondritic material. From this perspective, the terrestrial composition may only represent the mean composition of various materials that have accreted to form Earth, similarly to Mars, whose composition plots close to that of Earth in the Cr-O isotope diagram (Fig. 3). This heterogeneous accretion model is also consistent with Si isotope observations and does not preclude that Earth could have included a fraction of enstatite chondrites. Using the same relative proportions of LL, CI, and CO as above while accounting for the Si isotope composition of the BSE (Fig. 2 and SOM text), a maximum of 15% enstatite chondrites can be present in the mixture of chondrites that would form Earth.

References and Notes

1. E. Anders, N. Grevesse, *Geochim. Cosmochim. Acta* **53**, 197 (1989).
2. C. J. Allègre, J.-P. Poirier, E. Humler, A. W. Hofmann, *Earth Planet. Sci. Lett.* **134**, 515 (1995).
3. R. N. Clayton, T. K. Mayeda, A. E. Rubin, *J. Geophys. Res.* **89**, C245 (1984).
4. A. Trinquier, J.-L. Birck, C. J. Allègre, *Astrophys. J.* **655**, 1179 (2007).
5. M. Regelous, T. Elliott, C. D. Coath, *Earth Planet. Sci. Lett.* **272**, 330 (2008).
6. M. Javoy, *Geophys. Res. Lett.* **22**, 2219 (1995).
7. M. Javoy *et al.*, *Earth Planet. Sci. Lett.* **293**, 259 (2010).
8. B. Mason, *Geochim. Cosmochim. Acta* **30**, 23 (1966).
9. E. Jagoutz *et al.*, *Proc. Lunar Planet. Sci. Conf.* **2**, 2031 (1979).
10. H. Palme, H. St. C. O'Neill, in *Treatise on Geochemistry*, vol. 2, R. W. Carlson, Ed. (Elsevier, Amsterdam, 2003), pp. 1–38.
11. Materials and methods are available as supporting material on *Science* Online.
12. C. Fitoussi, B. Bourdon, T. Kleine, F. Oberli, B. Reynolds, *Earth Planet. Sci. Lett.* **287**, 77 (2009).
13. A. Corgne, S. Keshav, B. J. Wood, W. F. McDonough, Y. Fei, *Geochim. Cosmochim. Acta* **72**, 574 (2008).
14. D. C. Rubie *et al.*, *Earth Planet. Sci. Lett.* **301**, 31 (2011).
15. R. B. Georg, A. N. Halliday, E. A. Schauble, B. C. Reynolds, *Nature* **447**, 1102 (2007).
16. R. M. G. Armytage, R. B. Georg, P. S. Savage, H. M. Williams, A. N. Halliday, *Geochim. Cosmochim. Acta* **75**, 3662 (2011).
17. J. Badro *et al.*, *Earth Planet. Sci. Lett.* **254**, 233 (2007).
18. K. Ziegler, E. D. Young, E. A. Schauble, J. T. Wasson, *Earth Planet. Sci. Lett.* **295**, 487 (2010).
19. P. S. Savage, R. B. Georg, R. M. G. Armytage, H. M. Williams, A. N. Halliday, *Earth Planet. Sci. Lett.* **295**, 139 (2010).
20. T. Zambardi, F. Poitrasson, *Geost. Geoanal. Res.* **35**, 89 (2011).
21. R. B. Georg, A. J. West, A. R. Basu, A. N. Halliday, *Earth Planet. Sci. Lett.* **283**, 67 (2009).
22. R. Chakrabarti, S. B. Jacobsen, *Geochim. Cosmochim. Acta* **74**, 6921 (2010).
23. R. M. Canup, *Philos. Trans. R. Soc. London Ser. A* **366**, 4061 (2008).
24. R. M. Canup, A. C. Barr, *Lunar Planet. Sci. Conf.* **41**, 2488 (abstr.) (2010).
25. U. Wiechert *et al.*, *Science* **294**, 345 (2001).
26. G. Lugmair, A. Shukolyukov, *Geochim. Cosmochim. Acta* **62**, 2863 (1998).

27. M. Touboul, T. Kleine, B. Bourdon, H. Palme, R. Wieler, *Nature* **450**, 1206 (2007).
28. A. Trinquier *et al.*, *Science* **324**, 374 (2009).
29. K. Pahlevan, D. J. Stevenson, *Earth Planet. Sci. Lett.* **262**, 438 (2007).
30. A. Shahar *et al.*, *Earth Planet. Sci. Lett.* **288**, 228 (2009).
31. A. Shahar *et al.*, *Geochim. Cosmochim. Acta* **75**, 7688 (2011).
32. J. Wade, B. J. Wood, *Earth Planet. Sci. Lett.* **236**, 78 (2005).
33. J. F. Rudge, T. Kleine, B. Bourdon, *Nat. Geosci.* **3**, 439 (2010).
34. K. Lodders, *Space Sci. Rev.* **92**, 341 (2000).
35. K. J. Walsh, A. Morbidelli, S. N. Raymond, D. P. O'Brien, A. M. Mandell, *Nature* **475**, 206 (2011).
36. R. N. Clayton, T. K. Mayeda, *Geochim. Cosmochim. Acta* **60**, 1999 (1996).
37. R. N. Clayton, T. K. Mayeda, *Geochim. Cosmochim. Acta* **63**, 2089 (1999).
38. R. N. Clayton, T. K. Mayeda, A. E. Rubin, *Proc. Lunar Planet. Sci. Conf.* **89**, C245 (1984).
39. R. N. Clayton, T. K. Mayeda, J. N. Goswami, E. J. Olsen, *Geochim. Cosmochim. Acta* **55**, 2317 (1991).

Acknowledgments: We thank R. Wieler, the Curation and Analysis Planning Team for Extraterrestrial Materials, NASA curatorial staff, and G. Lofgren for giving us access to the Apollo lunar samples; the reviewers for their very helpful comments; and W. Bottke and S. Labrosse for insightful discussions. Silicon isotope data have been included in the SOM.

Supporting Online Material
www.sciencemag.org/cgi/content/full/science.1219509/DC1
Materials and Methods
SOM Text
Fig. S1
Tables S1 to S3
References (*40*–*48*)

3 October 2011; accepted 14 February 2012
Published online 1 March 2012;
10.1126/science.1219509

The Gutenberg Discontinuity: Melt at the Lithosphere-Asthenosphere Boundary

Nicholas Schmerr*

The lithosphere-asthenosphere boundary (LAB) beneath ocean basins separates the upper thermal boundary layer of rigid, conductively cooling plates from the underlying ductile, convecting mantle. The origin of a seismic discontinuity associated with this interface, known as the Gutenberg discontinuity (G), remains enigmatic. High-frequency *SS* precursors sampling below the Pacific plate intermittently detect the G as a sharp, negative velocity contrast at 40- to 75-kilometer depth. These observations lie near the depth of the LAB in regions associated with recent surface volcanism and mantle melt production and are consistent with an intermittent layer of asthenospheric partial melt residing at the lithospheric base. I propose that the G reflectivity is regionally enhanced by dynamical processes that produce melt, including hot mantle upwellings, small-scale convection, and fluid release during subduction.

Seismological surface wave studies of the upper mantle reveal a high-velocity lithospheric "lid" of varying thickness that gradually transitions into the low-velocity zone (LVZ) or asthenosphere of the upper mantle [e.g., (*1*, *2*)]. Rheological investigations of the LAB using glacial rebound and gravitational constraints require a one- to two-order-of-magnitude decrease in mantle viscosity across the interface (*3*). Numerous hypotheses have been proposed to explain the origin of the LVZ and associated lowered viscosities, ranging from temperature (*2*), hydration (*4*), compositional variations (*5*), grain size (*6*), and anisotropy (*7*) to the presence of melt (*8*). Some have speculated that the low viscosity of the asthenosphere enables plate tectonics on Earth (*9*); therefore, understanding the origin of asthenospheric properties is a key constraint for the evolution of plate tectonics and mantle convection within terrestrial planets.

Regional seismological techniques that use refracted, reflected, and converted seismic waves have produced evidence for a sharp seismic discontinuity in the depth range of 35 to 120 km beneath the ocean basins, representing a velocity reduction of 5 to 10% across a sharp boundary no more than 20 km thick [e.g., (*5*, *10*–*13*)]. This interface is often labeled the "Gutenberg discontinuity" or more simply the "G" after Beno Gutenberg, who first detected the feature beneath the oceans nearly a century ago (*14*). In many studies, the G is roughly coincident with the expected depth of the LAB and potentially provides important constraints on the seismic properties of the lithosphere and asthenosphere (*15*). Only partial information about the G beneath oceanic settings is available, owing to the limitation of seismic sampling to island stations, narrow seismic corridors, and ocean-bottom seismometers. Complete oceanic coverage of the G is provided by underside reflections arriving as precursors to the seismic phase *SS* (*16*), sampling structure halfway between an earthquake and receiver (Fig. 1). However, using this technique to directly investigate seismic discontinuities less than 100 km deep is challenging, owing to the obfuscation of shallow reflectors by the long-period waveform of *SS*. Past approaches overcame this difficulty using a modeling and cross-correlation approach to detect shallow discontinuities beneath the Pacific (*17*), but a direct imaging technique is

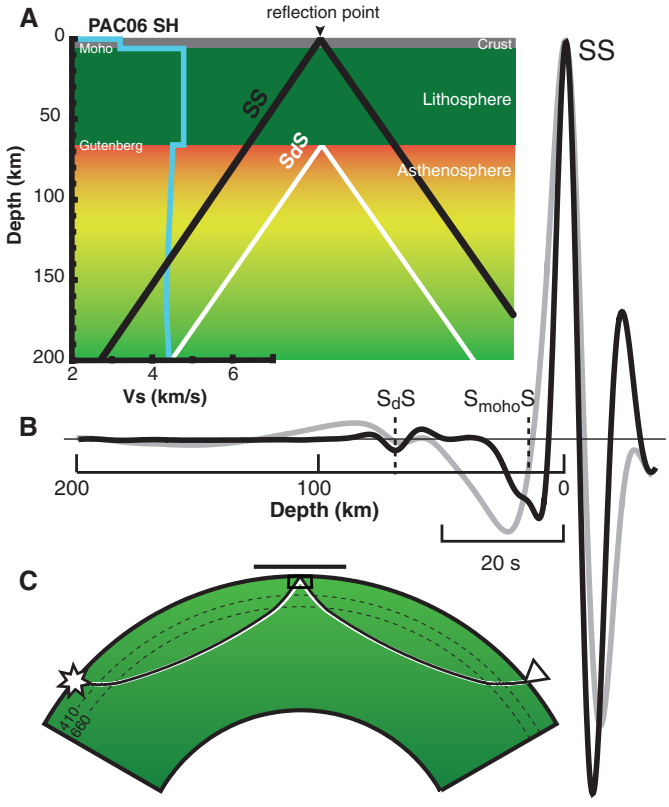

Fig. 1. Seismic ray path and theoretical waveforms of underside reflections from the G. (**A**) Reference velocity model (*10*) of oceanic lithosphere (blue) and reflection point geometry of the *SS* precursory seismic phase (*SdS*). (**B**) Synthetic acceleration (black) and displacement (gray) seismograms generated for PAC06SH (*10*) at an epicentral distance of 125° and low-pass filtered to a corner of 10 s (*18*). (**C**) Global seismic ray path of *SS* (black) and *SdS* (white). The small box outlines the location of (A), found halfway between the earthquake (star) and seismometer (inverted triangle). The horizontal line indicates the sampling size of a 1000-km-radius bin.

Department of Terrestrial Magnetism, 5241 Broad Branch Road, NW, Washington, DC 20015, USA. E-mail: nschmerr@dtm.ciw.edu

*Present address: NASA Goddard Space Flight Center Planetary Geodynamics Laboratory, Code 698, Greenbelt, MD 20771, USA.

desirable, especially in regions where complex structure is present and not captured by earlier approaches.

Here the detailed G structure beneath the Pacific Ocean basin was directly imaged by stacking a large data set of *SS* precursors (*18*). Previous studies used low-frequency displacement data to detect the G (*17*), whereas this study uses higher frequencies and differentiates each displacement seismogram twice to obtain acceleration seismograms that distinctly separate the *SS* precursor from the long-period waveform of *SS* (Fig. 1). The *SS* precursor data set includes a comprehensive set of records from broadband seismic stations around the globe. Selecting only shallow (<75 km) earthquake sources with magnitudes $M_w \geq 5.8$ and using a stringent set of data selection criteria resulted in a data set of 30,423 high-quality acceleration seismograms that sample beneath the Pacific plate (*18*).

Negative *SS* precursors with travel times and amplitudes consistent with underside reflections from a ~6% decrease in shear velocity at 40- to 100-km depth were detected in about 20% of the stacks across the Pacific region (Fig. 2, figs. S1 and S2, and table S1). To be considered robust, the negative *SS* precursor must be the highest-amplitude arrival preceding the *SS* sidelobe with an amplitude above the 95% (2σ) confidence interval (*18*). Stacks not meeting these criteria are well populated by seismic records but do not form coherent precursory arrivals distinguishable from the background noise. Laterally continuous stacks sampling near subduction zones often exhibit an underside reflection; however, given the long wavelength (>1000 km) of the *SS* Fresnel zone and potential for aliasing of considerable complexity in subduction zones, these stacks are categorized separately in this analysis (Fig. 2A, crosses). Another set of weaker negative precursors are detected from reflectors at 120- to 180-km depth, though the deeper underside reflections are found in only 16% of the stacks (Fig. 2B and figs. S1 and S2). These deeper mantle interfaces originate from the base of the LVZ and are described in more detail in the SOM text. Seismic waveform modeling of discontinuity structure and reflectivity (fig. S3) indicates that the discontinuity has a relatively sharp velocity gradient (≤20 km). Furthermore, modeling shows that the *SS* precursors are sensitive to negative velocity contrasts >2 to 3%, though the discontinuity must be very sharp (<5 km). For *SS* precursor amplitudes below the detection threshold, it is difficult to distinguish between regions characterized by a broad velocity gradient and/or a weak velocity contrast from regions with no discontinuity (Fig. 2A, squares). Other seismic approaches are more sensitive to weaker discontinuities; a detailed technical comparison of the G structure presented here to past work in the Pacific is available online (SOM text and figs. S1 and S2).

Several different mechanisms for the origin of the G have been proposed. One hypothesis states that if the G corresponds to the LAB, it should deepen with increasing age of the overlying plate

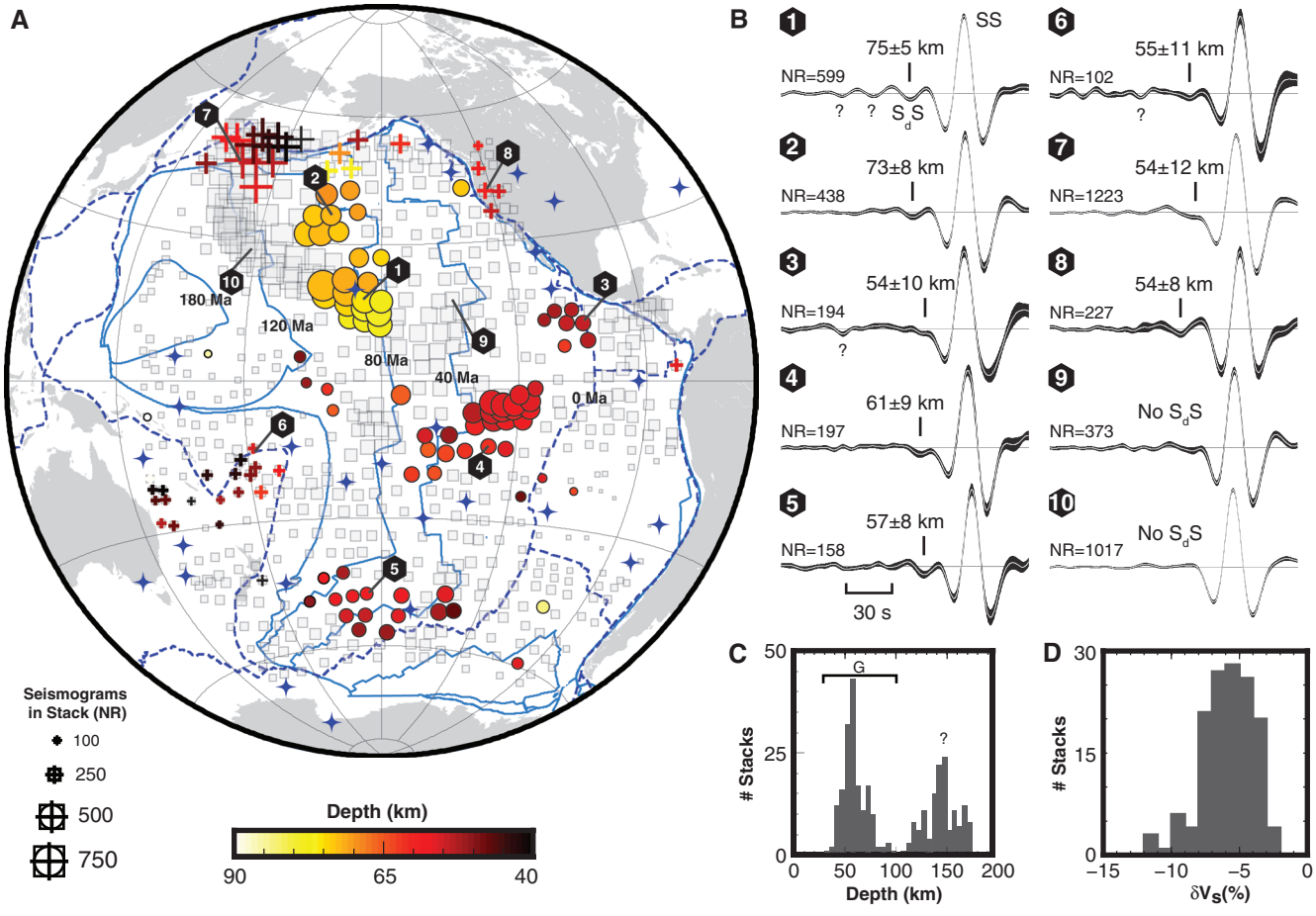

Fig. 2. Detections of enhanced G reflectivity beneath the Pacific. (**A**) Geographic distribution of stacks without an underside reflection (squares), shallow *SS* precursors near subduction zones (crosses), and all other *SS* precursors (circles) <100 km in depth. Symbols are scaled to the number of seismic records (NR) in the stack. Plate boundaries (blue dashed lines), hotspots (blue stars), and isochrons (blue solid lines) designate tectonic and volcanic features [fig. S1 (*18*)]. (**B**) Example stacks from the Pacific study region; locations are indicated in (A). The uncertainty in depth is obtained from the bootstrap-resampling algorithm (*18*). Error envelopes (black shading) indicate the ±2σ confidence bounds of stacked amplitudes. The maximum amplitude of each stack is normalized to unity; amplitudes are displayed relative to the zero line. (**C**) Histogram of the depth of the G and a deeper discontinuity related to the base of the LVZ. (**D**) Histogram of shear-wave velocity (V_S) contrasts at the G obtained from *SS* precursor amplitudes. Discontinuity depths, errors, location of deeper interfaces, and modeled velocity contrasts are available online (figs. S1 and S2 and table S1).

(*11*, *17*), owing to cooling and subsequent thickening of the lithosphere over time. Another hypothesis poses the G as a constant-depth interface related to the depth of melting at the mid-ocean ridges that represents a compositional transition from depleted, dehydrated lithosphere to underlying fertile, hydrous mantle (*4*, *5*, *19*). Surface-wave tomography models show a high-velocity lid thickening with crustal age (*2*, *20*), though some models require a reheating of the lithosphere older than 80 million years to explain the observed oceanic bathymetry, heat flow, and seismic velocities (*1*, *21*). Where the G is detected by the *SS* precursors, the boundary deepens slightly with increasing overlying crustal age (Fig. 3) and coincides with the depth of the negative velocity gradient between the lithosphere and underlying LVZ [e.g., (*2*, *20*)]. A crustal age relationship has also been detected by other studies (*11*, *17*), though for fewer observations across the Pacific (fig. S2). The presence of age dependence does not necessarily rule out the depletion hypothesis; a similar pattern might arise from variations in the depth of melting at the ridge over geological time scales [e.g., (*22*)]. Alternatively, the overprinting of a depletion boundary by the cooling and thickening lithosphere may locally enhance a weak seismic discontinuity (*15*). In any case, both the depletion and thermal cooling hypotheses fail to predict the highly regionalized variations in the reflectivity of the G observed by the *SS* precursors. Moreover, interpreting age relationships is not straightforward, as many G observations underlie or are associated with areas of recent volcanism (Fig. 2 and fig. S4). Thermal perturbations from an upwelling plume will reset the apparent thermal age of the lithosphere and move the LAB to shallower depths (*23*).

The numerous high-reflectivity G observations underlying recent surface volcanism suggest high homologous mantle temperature [e.g., (*2*)], volatiles (*19*), and/or the presence of localized partial melt at the base of the lithosphere [e.g., (*8*)]. Melt at the LAB is used to explain ocean-bottom receiver function observations of a sharp, negative discontinuity beneath the Philippine Plate and Pacific Ocean offshore of Japan (*11*). Small melt fractions (<0.1%) are stabilized by

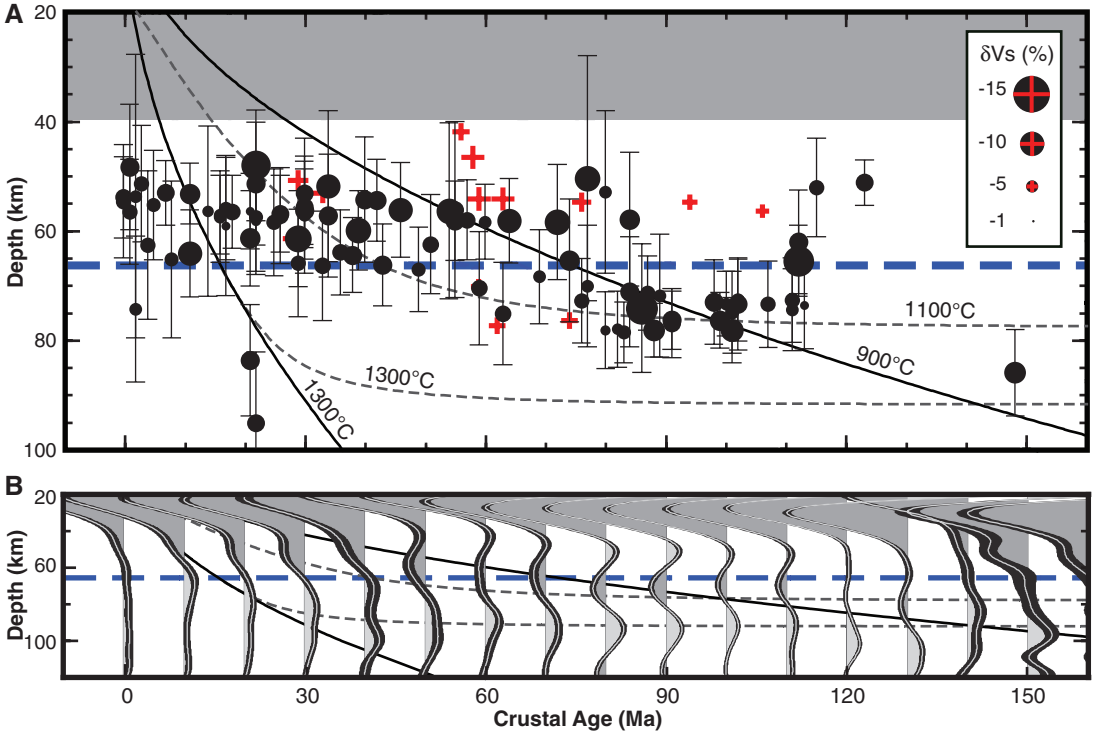

Fig. 3. Relationship of the G observations to the age of the overlying plate. (**A**) Correlation of discontinuity depth and velocity contrast to crustal age. Symbols are the same as in Fig. 2A; error bars specify the uncertainty in each depth measurement obtained from the bootstrap-resampling algorithm (*18*). The shaded region indicates depths outside the sensitivity of the *SS* precursor technique. (**B**) Stacks of regions with a shallow *SS* precursor by crustal age. Error envelopes (black shading) are the same as in Fig. 2B; negative (dark gray) and positive (light gray) shading signifies amplitudes ≥2σ. Both panels indicate the predicted depths for isotherms from a half-space cooling model (solid lines), a plate model (gray dashed lines), and a depletion boundary (blue dashed lines). The half-space cooling and plate models assume a ΔT = 1350°C, a plate thickness of 95 km, an average plate velocity of 80 mm/year, and a thermal diffusivity of 1 mm^2/s (*21*).

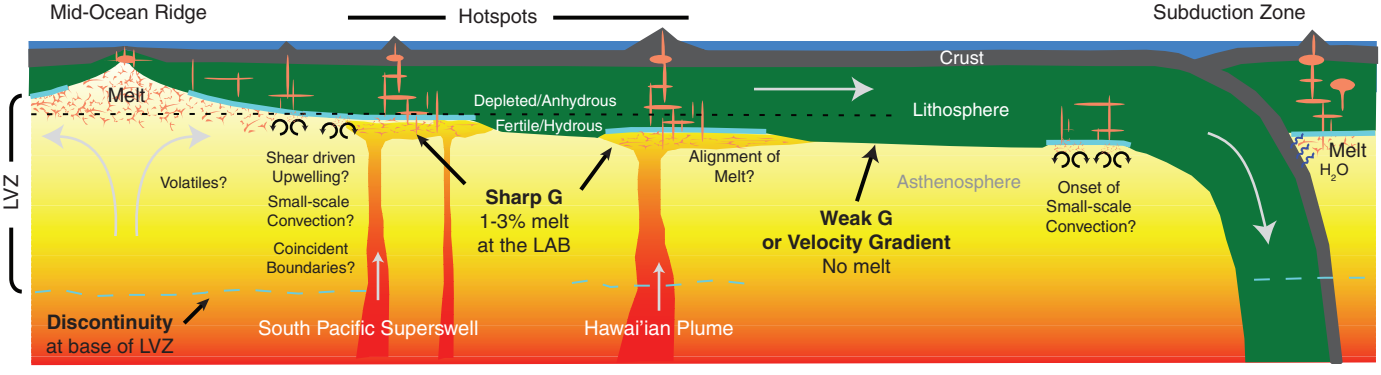

Fig. 4. Cross-sectional portrayal of proposed mechanisms (see text) for the origin of a high-reflectivity G beneath the Pacific. The reflectivity of the G is enhanced by the stagnation of partial melt at the base of the lithosphere (blue lines). Another deeper discontinuity (blue dashed lines) predominantly occurs beneath major hotspots, mid-ocean ridges, and subduction zones and lies at the base of the LVZ (fig. S5). Underside reflections from the G do not form where the seismic discontinuity has a weak velocity contrast or a broad velocity gradient (fig. S3).

the presence of volatiles within the upper mantle, though beneath ridges and hotspots, melt fractions are expected to be higher (*24*, *25*). Using a dry peridotite relationship between temperature and velocity (*26*), an estimated volume of 0.1 to 3% fractional melt is required to explain sharp negative velocity contrasts >5% (fig. S4). If volatiles such as H_2O or CO_2 are present in the LVZ (*25*), higher amounts of fractional melt are possible. Melt produced in the asthenosphere will migrate upward along grain boundaries (*27*), will be entrained into mantle flow (*28*), and will ultimately compact at the base of a less permeable lithosphere (*25*), forming a sharp, high-velocity-contrast seismic discontinuity.

The origin of asthenospheric melt production may take many forms, with multiple mechanisms likely present beneath different parts of the Pacific (Fig. 4). Examples include decompression melting at a mid-ocean ridge, shear-induced decompression melting from upwelling and corner flow around small-scale heterogeneities in mantle viscosity (*29*), decompression melting from the development of small-scale convection in fertile mantle (*30*), melting associated with the release of fluids from a subducting slab (*31*), and/or impingement of a mantle plume upon the lithosphere (*23*). Melt collecting at the LAB in the vicinity of the mid-ocean ridges will be too shallow to detect with the *SS* precursors (Fig. 4). A high-reflectivity G is detected near the Louisville hotspot and many of the volcanic island chains associated with the South Pacific Superswell, though other studies (*17*) resolve the shallow structure to the south (fig. S1). Beneath older and thicker lithosphere, the G brightens beneath the Hawaiian and Samoan hotspots, though Samoa is juxtaposed with subduction. Several detections of an enhanced G in regions away from recent surface volcanism and mantle hotspots may indicate the onset of decompression melting from secondary small-scale convective processes in the mantle (*30*) or localized hydration enhancement of the discontinuity (*19*). The circum-Pacific subduction zones also exhibit enhanced G reflectivity, though the long-wavelength sensitivity of the *SS* precursors makes it difficult to determine if this structure originates from subslab or mantle wedge–related fluids and/or melts at the LAB. Finally, regions lacking a G precursor are plausibly melt-free, confirming that the observed geophysical properties of the LVZ and asthenosphere do not necessitate the ubiquitous presence of melt.

References and Notes

1. M. H. Ritzwoller, N. M. Shapiro, S. J. Zhong, *Earth Planet. Sci. Lett.* **226**, 69 (2004).
2. K. Priestley, D. McKenzie, *Earth Planet. Sci. Lett.* **244**, 285 (2006).
3. J. X. Mitrovica, A. M. Forte, *J. Geophys. Res.* **102**, 2751 (1997).
4. S. Karato, H. Jung, *Earth Planet. Sci. Lett.* **157**, 193 (1998).
5. J. B. Gaherty, T. H. Jordan, L. S. Gee, *J. Geophys. Res.* **101**, 22291 (1996).
6. U. H. Faul, I. Jackson, *Earth Planet. Sci. Lett.* **234**, 119 (2005).
7. S. Karato, P. Wu, *Science* **260**, 771 (1993).
8. D. Anderson, C. Sammis, *Phys. Earth Planet. Inter.* **3**, 41 (1970).
9. M. A. Richards, W. S. Yang, J. R. Baumgardner, H. P. Bunge, *Geochem. Geophys. Geosyst.* **2**, (2001).
10. Y. Tan, D. V. Helmberger, *J. Geophys. Res.* **112**, B08301 (2007).
11. H. Kawakatsu *et al.*, *Science* **324**, 499 (2009).
12. C. A. Rychert, P. M. Shearer, *Science* **324**, 495 (2009).
13. H. Y. Yuan, B. Romanowicz, K. M. Fischer, D. Abt, *Geophys. J. Int.* **184**, 1237 (2011).
14. B. Gutenberg, *Z. Geophys.* **2**, 24 (1926).
15. K. M. Fischer, H. A. Ford, D. L. Abt, C. A. Rychert, *Annu. Rev. Earth Planet. Sci.* **38**, 551 (2010).
16. P. M. Shearer, *Nature* **344**, 121 (1990).
17. C. A. Rychert, P. M. Shearer, *J. Geophys. Res.* **116**, B07307 (2011).
18. Materials and methods are available as supporting material on *Science* Online.
19. S. Karato, *Earth Planet. Sci. Lett.* **321–322**, 95 (2012).
20. M. Nettles, A. M. Dziewonski, *J. Geophys. Res.* **113**, B02303 (2008).
21. B. Parsons, J. G. Sclater, *J. Geophys. Res.* **82**, 803 (1977).
22. E. Humler, C. Langmuir, V. Daux, *Earth Planet. Sci. Lett.* **173**, 7 (1999).
23. N. M. Ribe, U. R. Christensen, *Earth Planet. Sci. Lett.* **171**, 517 (1999).
24. M. M. Hirschmann, *Phys. Earth Planet. Inter.* **179**, 60 (2010).
25. G. Hirth, D. L. Kohlstedt, *Earth Planet. Sci. Lett.* **144**, 93 (1996).
26. H. Sato, I. S. Sacks, T. Murase, *J. Geophys. Res.* **94**, 5689 (1989).
27. W. L. Zhu, G. A. Gaetani, F. Fusseis, L. G. J. Montési, F. De Carlo, *Science* **332**, 88 (2011).
28. Y. Takei, B. K. Holtzman, *J. Geophys. Res.* **114**, B06205 (2009).
29. C. Conrad, T. A. Bianco, E. Smith, P. Wessel, *Nat. Geosci.* **4**, 317 (2011).
30. M. D. Ballmer, J. van Hunen, G. Ito, P. J. Tackley, T. A. Bianco, *Geophys. Res. Lett.* **34**, L23310 (2007).
31. D. L. Kohlstedt, H. Keppler, D. C. Rubie, *Contrib. Mineral. Petrol.* **123**, 345 (1996).

Acknowledgments: This work was supported by a Carnegie Institution of Washington Department of Terrestrial Magnetism Postdoctoral Fellowship and by the NASA Postdoctoral Program. The facilities of the IRIS Data Management Center were used for access to the data required in this study. I am grateful to three anonymous referees for constructive comments and reviews. I appreciatively recognize the contribution to this work of many prior discussions with Paul Silver (deceased).

Supporting Online Material

www.sciencemag.org/cgi/content/full/335/6075/1480/DC1
Materials and Methods
SOM Text
Figs. S1 to S5
Table S1
Additional Acknowledgments
References (*32*–*65*)

18 October 2011; accepted 14 February 2012
10.1126/science.1215433

The Aftermath of Megafaunal Extinction: Ecosystem Transformation in Pleistocene Australia

Susan Rule,[1,2] Barry W. Brook,[3] Simon G. Haberle,[1] Chris S. M. Turney,[4] A. Peter Kershaw,[5] Christopher N. Johnson[6]*

Giant vertebrates dominated many Pleistocene ecosystems. Many were herbivores, and their sudden extinction in prehistory could have had large ecological impacts. We used a high-resolution 130,000-year environmental record to help resolve the cause and reconstruct the ecological consequences of extinction of Australia's megafauna. Our results suggest that human arrival rather than climate caused megafaunal extinction, which then triggered replacement of mixed rainforest by sclerophyll vegetation through a combination of direct effects on vegetation of relaxed herbivore pressure and increased fire in the landscape. This ecosystem shift was as large as any effect of climate change over the last glacial cycle, and indicates the magnitude of changes that may have followed megafaunal extinction elsewhere in the world.

The disappearance of megafauna from most of the world's ecosystems was a major event in recent Earth history. Most research into these extinctions has focused on possible causes, which include climate and human colonization (*1*), and less attention has been paid to the consequences of the extinctions (*2*). Large herbivores have strong effects on ecosystems, by maintaining vegetation openness and patchiness, removing material that would otherwise fuel landscape fire, dispersing seeds, and physically disturbing soil and recycling nutrients (*3*). Therefore, megafaunal extinction might have caused major changes to vegetation and the functioning of ecosystems. We know little about this because we lack detailed ecological reconstructions able to distinguish the effects of large-herbivore extinctions from environmental changes that could have caused them. Recent studies from North

[1]School of Culture, History and Language, The Australian National University, Canberra ACT 0200, Australia. [2]School of Marine and Tropical Biology, James Cook University, Townsville, Qld 4811, Australia. [3]The Environment Institute and School of Earth and Environmental Science, University of Adelaide, Adelaide SA 5005, Australia. [4]Climate Change Research Centre, University of New South Wales, Sydney, NSW 2052, Australia. [5]School of Geography and Environmental Science, Monash University, Clayton Vic 3168, Australia. [6]School of Zoology University of Tasmania, Hobart Tasmania 7001, Australia.

*To whom correspondence should be addressed. E-mail: c.n.johnson@utas.edu.au

America show that megafaunal decline was followed by vegetation change and increased fire (*4*, *5*). However, these events happened in the latest Pleistocene during a time of rapid climate change, so it is difficult to resolve the contributions to them of megafaunal extinction versus climate.

Australia's megafauna included 20 or more genera of giant marsupials, monotremes, birds, and reptiles (*6*), which were extinct by 40 thousand years ago (ka) (*7*–*10*), soon after people colonized Australia (*11*), suggesting that people caused the extinction. Proposed mechanisms are overhunting (*6*, *12*), vegetation change due to landscape burning by people (*9*), or a combination thereof. Indications of increased fire and changed vegetation around the time of human arrival support a role for landscape burning (*9*, *13*), but it could be that fire increased as a consequence of the loss of large browsers and grazers, and fire then caused vegetation change (*14*). An alternative view is that Australia's megafauna was in long-term decline because of climate drying, and the human contribution to its ultimate disappearance was small (*15*).

We resolved relations among megafaunal extinction, fire, climate, and vegetation at the Lynch's Crater palaeolake/swamp in northeast Australia. Previous work at this site has documented an increase in charcoal and a shift from rainforest to sclerophyll vegetation beginning ~45 ka that is generally interpreted as a result of landscape burning by people (*13*, *16*). There is no archaeological record at the site, but regional archeology confirms that occupation may have begun as early as 49 ka and was widespread by 40 ka (*17*–*19*). We used pollen and charcoal to reconstruct vegetation, fire, and climate changes and spores of the fungus *Sporormiella* to indicate large-herbivore activity (*20*). *Sporormiella* depends on ingestion by herbivores to complete its life cycle; it sporulates in their dung. *Sporormiella* can be found in dung of herbivores across a wide range of body sizes, but spore counts are most strongly affected by activity of large herbivores (*21*, *22*) and thus provide a proxy for large-herbivore biomass (*4*, *5*, *21*–*24*).

We analyzed two cores, a long core ("core 1") spanning 130 to 24 ka (Fig. 1A) and another ranging from ~54 to 3 ka ("core 2"), which was sampled at ~100-year intervals between 54 and 24 ka (Fig. 1B). Core 1 encompasses two major climate transitions during the 80 thousand years (ky) preceding human arrival: (i) a shift from warm and humid to cool and dry conditions around 120 ka (termination of the last interglacial) and (ii) a further cooling and drying ~75 ka [onset of marine isotope stage 4 (MIS 4)]. Both events are marked by stepwise decline of rainforest angiosperms in favor of sclerophyll taxa and rainforest gymnosperms. Between 60 and 55 ka, high representation of rainforest gymnosperms indicates a return to somewhat warmer and more humid conditions, and after 55 ka, an increase in mid-storey plants and swamp/aquatic vegetation suggests a change from shallow lake to peat-swamp conditions. Most likely, the landscape at that time included a mix of vegetation types, with patches of grassland and sedges interspersed with mixed forest and woodland. High *Sporormiella* counts suggest that large herbivores ranged very close to or over the swamp surface.

These conditions ended around 41 ka, when *Sporormiella* counts dropped almost to zero. The timing of this decline agrees closely with estimates of the date of megafaunal extinction from fossil evidence elsewhere in Australia (*7*, *10*). At Lynch's Crater, it was associated with increased charcoal and grasses with a further rise in sclerophyll vegetation at the expense of rainforest angiosperms and (especially) gymnosperms. Unlike the two previous advances of sclerophyll vegetation, this shift has no climatic explanation. It preceded climate drying at the MIS 3/2 boundary by ~10 ky, and although sediment moisture conditions at Lynch's Crater show millennial scale fluctuations during the interval from 45 to ~25 ka (*25*), there is no discernible relation to the trend in

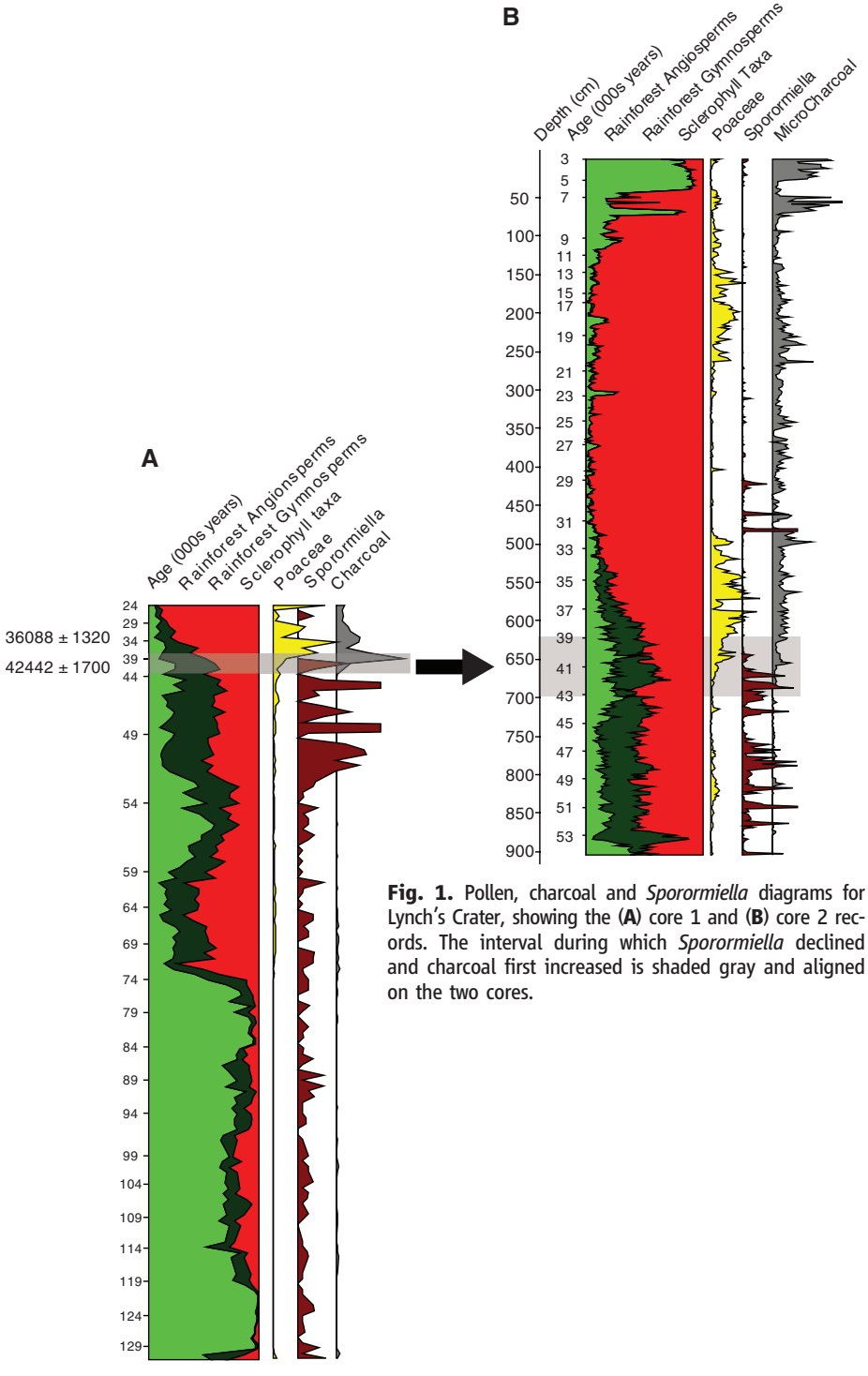

Fig. 1. Pollen, charcoal and *Sporormiella* diagrams for Lynch's Crater, showing the (**A**) core 1 and (**B**) core 2 records. The interval during which *Sporormiella* declined and charcoal first increased is shaded gray and aligned on the two cores.

Sporormiella. The transformation appears in both cores, with overlapping radiocarbon dates, and can be used to map core 2 onto core 1 (Fig. 1).

We analyzed this transformation in detail by focusing on the interval from 694 to 604 cm in core 2, which has an estimated age range from ~43 to 38 ka and encompasses the *Sporormiella* decline and charcoal rise (Fig. 2A). *Sporormiella* decline and charcoal increase were negatively correlated through this interval [correlation coefficient $r = -0.54$; 95% confidence interval (CI): −0.72 to −0.30], but neither was directly correlated with vegetation change [correlations with percent sclerophyll were 0.10 (95% CI: −0.20 to 0.38) for *Sporormiella* and 0.05 (95% CI: −0.33 to 0.45) for charcoal]. The reason that vegetation change was not directly correlated with *Sporormiella* and charcoal was that shifts in vegetation lagged behind changes in *Sporormiella* and charcoal (see below). This rules out fire as a cause of megafaunal extinction, because that hypothesis depends on fire causing vegetation change, which would then cause megafaunal decline. In that case, vegetation change should have led megafaunal decline, rather than following it.

The vegetation reorganization consisted of a succession of changes that unfolded over a range of time scales. There was a rapid rise in grass and a more gradual increase in sclerophyll plants as a proportion of the forest vegetation; these could represent phenological and successional responses in those plant groups to reduced herbivory or increased fire. Later, there was a large increase in total pollen influx from forest trees, which we interpret as a longer-term development of uniform sclerophyll forest (with a grassy understorey) in place of a previously more patchy forest structure (Fig. 2A). To clarify the timing of these events, we calculated a moving regression of each variable on depth, using nine depth intervals as the frame for each regression (equivalent to ~1000 years, according to our age model; see the supporting online material). This frame was shifted in steps of one depth interval (just over 100 years) for each successive regression calculation. Peaks and troughs in the plot of regression coefficients mark the onset of the steepest millennium-scale rises and falls in each variable (Fig. 2B). This analysis showed that the major

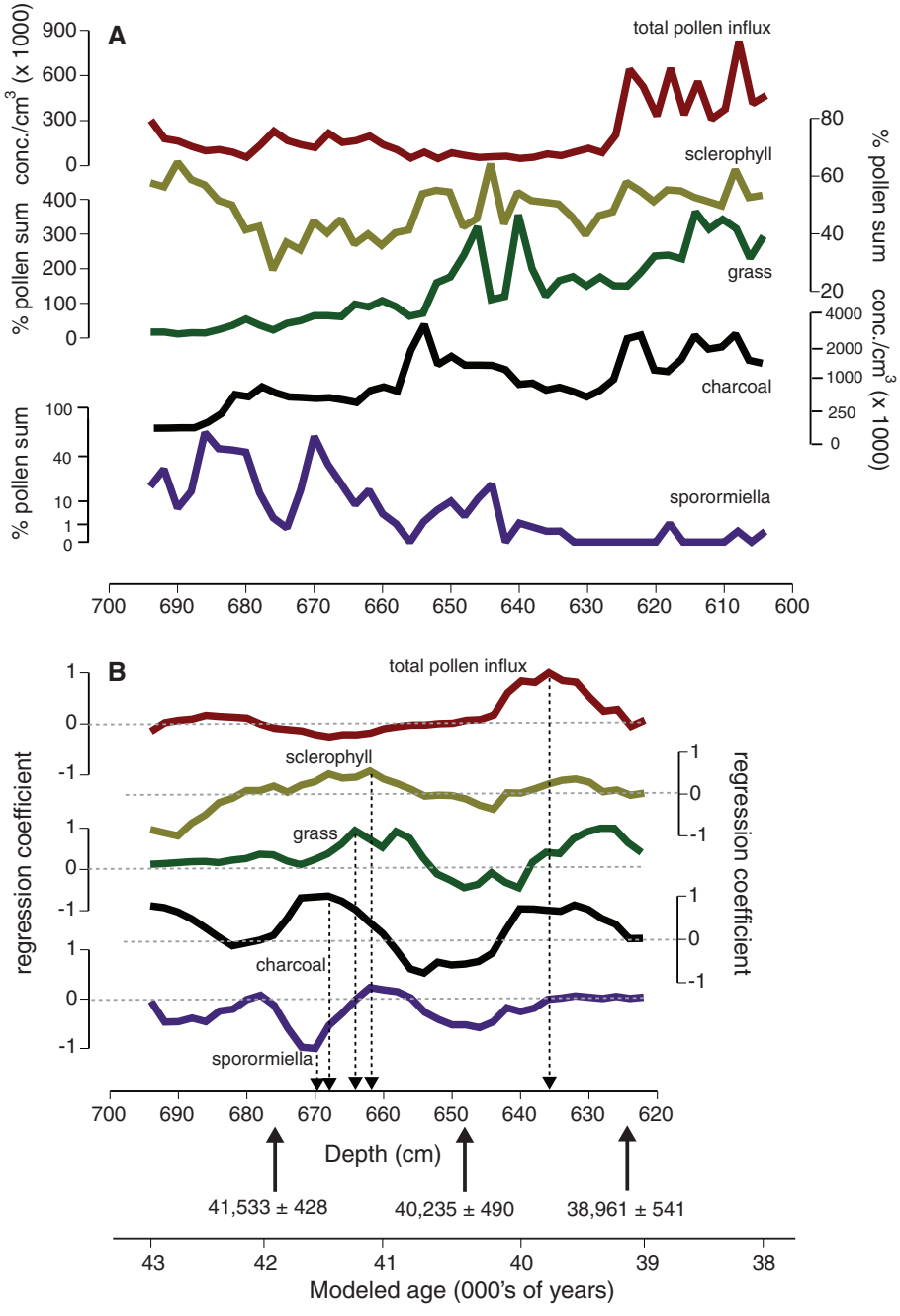

Fig. 2. Changes in *Sporormiella*, charcoal, and vegetation during the interval in the period around 41 ka, in core 2. (**A**) Pollen, charcoal, and *Sporormiella* counts, measured as percent of the pollen sum, except for charcoal (particles per cubic centimeter) and total pollen influx from forest trees (grains per square centimeter per year). (**B**) Moving regression analysis, showing the coefficient of the regression of each variable on time, recalculated for each point through the series. Dashed arrows mark the onset of the largest changes in each variable.

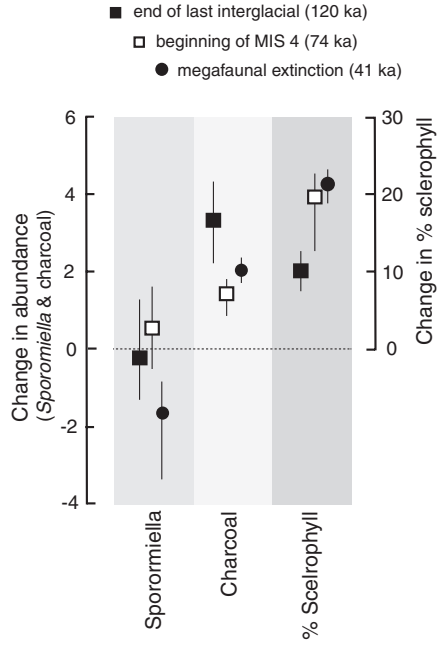

Fig. 3. Magnitudes of change in *Sporormiella* and charcoal counts and vegetation composition associated with two major climate shifts and megafaunal extinction. Changes in *Sporormiella* and charcoal are expressed as ratios of mean abundance during the 10 ky preceding each change to the 10 ky following it, converted to natural logs. Zero indicates no change. Vegetation changes are indicated by differences in percent sclerophyll for the 10 ky after and before each event. Confidence limits (95%) were derived by bootstrapping.

increase of charcoal lagged *Sporormiella* decline by ~100 years, grass followed *Sporormiella* decline by ~300 years, the rise in sclerophyll vegetation lagged *Sporormiella* decline by ~400 years, and total pollen influx from forest trees increased after 1600 years.

The fire increase that followed megafaunal decline could have been anthropogenic, but the extended trajectory of the rise in charcoal and its close matching with falling *Sporormiella* suggest instead that relaxation of herbivory directly caused increased fire, presumably by allowing the accumulation of fine fuel. The subsequent vegetation transformation could be explained in two ways: (i) by direct effects of relaxed herbivore pressure on vegetation density and composition or (ii) by release of fire as an ecological force, causing destruction of fire-sensitive rainforest vegetation with replacement by fire-tolerant sclerophyll taxa and grasses. We compared the importance of these two mechanisms by measuring the effects of *Sporormiella* and charcoal in linear models predicting changes in percent sclerophyll (lagged by four depth intervals, or ~400 years) over the interval shown in Fig. 2. We controlled temporal autocorrelation by fitting generalized least-squares models with an exponential correlation structure (*26*). The standardized regression coefficients (SRCs = coeffcients/SE) were –2.81 for *Sporormiella* and 2.53 for charcoal when fitted as single-term models; in a two-term model, the respective SRCs were –1.42 and 1.95. The changes in SRC values suggest that (i) there were independent contributions of both falling *Sporormiella* and rising charcoal to the subsequent rise in sclerophyll vegetation and (ii) the effect of charcoal was ~35% stronger.

After its initial rise charcoal remained high, and around 29 to 31 ka there was a large increase in macrocharcoal indicating that, for the first time in its history, the swamp itself was extensively burnt (*20*); short-lived spikes in *Sporormiella* associated with this burning probably represent grazing over the swamp bed by extant herbivores (probably kangaroos). Charcoal rose further in the Holocene, in complete contrast to the absence of fire in the previous interglacial.

Finally, we compared the magnitude of the ecological changes that followed megafaunal decline around 41 ka with earlier climate-driven shifts from 74 and 120 ka, by calculating standardized estimates of the sizes of effects of each event on *Sporormiella*, charcoal, and percent sclerophyll (Fig. 3). There was no significant effect on *Sporormiella* from the two episodes of climate drying, suggesting that the megafaunal extinction was not the culmination of a long-term decline driven by an increasingly arid climate. Had that been true, the Lynch's Crater record should have shown evidence of declines of megafaunal biomass at times when the climate of the region became substantially more arid. Instead, megafaunal biomass was insensitive to episodes of climate drying, before declining abruptly during a period of stable climate. The increase in charcoal counts and the compositional shift to sclerophyll vegetation that followed megafaunal extinction were as large or larger than changes in the same directions associated with the two major climate changes in the earlier part of the last glacial cycle.

References and Notes

1. P. L. Koch, A. D. Barnosky, *Annu. Rev. Ecol. Evol. Syst.* **37**, 215 (2006).
2. C. N. Johnson, *Proc. Biol. Sci.* **276**, 2509 (2009).
3. K. Danell, R. Bergstrom, P. Duncan, J. Pastor, *Large Herbivore Ecology, Ecosystem Dynamics and Conservation* (Cambridge Univ. Press, Cambridge, 2006).
4. J. L. Gill, J. W. Williams, S. T. Jackson, K. B. Lininger, G. S. Robinson, *Science* **326**, 1100 (2009).
5. G. S. Robinson, L. P. Burney, D. A. Burney, *Ecol. Monogr.* **75**, 295 (2005).
6. C. Johnson, *Australia's Mammal Extinctions: A 50,000 Year History* (Cambridge Univ. Press, Melbourne, 2006).
7. R. Gillespie, B. W. Brook, A. Baynes, *Alcheringa* **1**, 163 (2006).
8. R. G. Roberts *et al.*, *Science* **292**, 1888 (2001).
9. G. H. Miller *et al.*, *Science* **309**, 287 (2005).
10. R. Grün *et al.*, *Aust. J. Earth Sci.* **55**, 917 (2008).
11. P. Hiscock, *Archaeology of Ancient Australia* (Routeledge, London, 2008).
12. B. W. Brook, C. N. Johnson, *Alcheringa* **1**, 39 (2006).
13. C. S. M. Turney *et al.*, *J. Quat. Sci.* **16**, 767 (2001).
14. T. F. Flannery, *The Future Eaters* (Reed, Melbourne, 1994).
15. J. Field, M. Fillios, S. Wroe, *Earth Sci. Rev.* **89**, 97 (2008).
16. A. P. Kershaw, *Nature* **322**, 47 (1986).
17. B. David, R. Roberts, C. Tuniz, R. Jones, J. Head, *Antiquity* **71**, 183 (1997).
18. M. G. Leavesley *et al.*, *Aust. Archaeol.* **54**, 55 (2002).
19. G. R. Summerhayes *et al.*, *Science* **330**, 78 (2010).
20. See the supporting material available on *Science* Online.
21. J. R. Wood, J. M. Wilmshurst, T. H. Worthy, A. Cooper, *Quat. Sci. Rev.* **30**, 915 (2011).
22. O. K. Davis, D. S. Shafer, *Palaeogeogr. Palaeoclimatol. Palaeoecol.* **237**, 40 (2006).
23. D. A. Burney, G. S. Robinson, L. P. Burney, *Proc. Natl. Acad. Sci. U.S.A.* **100**, 10800 (2003).
24. O. K. Davis, *Quat. Res.* **28**, 290 (1987).
25. C. S. M. Turney *et al.*, *Nature* **428**, 306 (2004).
26. B. P. Murphy, G. J. Williamson, D. M. J. S. Bowman, *Global Ecol. Biogeogr.* **21**, 142 (2011).

Acknowledgments: This work was supported by the Australian Research Council, the National Geographic Society, Monash Univ., The Royal Society, Australian Institute of Nuclear Science and Engineering, and Natural Environment Research Council. We thank D. Bowman and E. Cameron for comments on the manuscript. The study was initiated by C.N.J. and B.W.B. and was designed by all authors. S.R. was responsible for data collection; B.W.B., C.N.J., S.R., and A.P.K. analyzed the data; C.S.M.T. developed the age model; C.N.J. led the writing; and all authors contributed to interpretation of results. The authors declare no competing interests. Original data will be provided by the corresponding author on request.

Supporting Online Material

www.sciencemag.org/cgi/content/full/335/6075/1483/DC1
Materials and Methods
Figs. S1 to S4
Table S1
References (*27*–*39*)

21 September 2011; accepted 3 February 2012
10.1126/science.1214261

Specialization and Rarity Predict Nonrandom Loss of Interactions from Mutualist Networks

Marcelo A. Aizen,[1,2]* Malena Sabatino,[1] Jason M. Tylianakis[3]

The loss of interactions from mutualistic networks could foreshadow both plant and animal species extinctions. Yet, the characteristics of interactions that predispose them to disruption are largely unknown. We analyzed 12 pollination webs from isolated hills ("sierras"), in Argentina, ranging from tens to thousands of hectares. We found evidence of nonrandom loss of interactions with decreasing sierra size. Low interaction frequency and high specialization between interacting partners contributed additively to increase the vulnerability of interactions to disruption. Interactions between generalists in the largest sierras were ubiquitous across sierras, but many of them lost their central structural role in the smallest sierras. Thus, particular configurations of interaction networks, along with unique ecological relations and evolutionary pathways, could be lost forever after habitat reduction.

Interspecific interactions link species within complex trophic and nontrophic webs (*1*–*3*). Disruption of individual interaction links can compromise both the survival of formerly interacting species pairs and of other species with whom they are directly or indirectly connected (*4*, *5*). For mutually beneficial interactions, such as those between plants and pollinators, the loss of interactions from a pollination web can jeopardize plant sexual reproduction directly through pollen limitation (*6*, *7*) and can reduce pollinator fitness by decreasing the availability of floral resources (*8*, *9*). Mutualists can persist to different extents after link disruption, depending on individual longevity, initial population abundance, generalization in the use of mutualistic partners, and importance of the pollination mutualism itself for species survivorship (*10*, *11*). Consequent-

[1]Laboratorio Ecotono—Centro Regional Universitario Bariloche (CRUB), Universidad Nacional del Comahue and Instituto de Investigaciones en Biodiversidad y Medioambiente (INIBIOMA), San Carlos de Bariloche, Río Negro 8400, Argentina. [2]Departamento de Botánica, Museo Argentino de Ciencias Naturales, Ángel Gallardo 470, Ciudad Autónoma de Buenos Aires 1405, Argentina. [3]School of Biological Sciences, University of Canterbury, Private Bag 4800, Christchurch, New Zealand.

*To whom correspondence should be addressed. E-mail: maizen@comahue-conicet.gob.ar

ly, loss of mutualistic interactions from a pollination web usually precedes species loss (*12*), as has been observed after habitat fragmentation (*9*, *13*) and species invasion (*14*, *15*). This extinction lag suggests that interactions, rather than species statistics, should be the main focus of studies of web dynamics and stability under different environmental change scenarios, and justifies the management of interspecific interactions as target activities of conservation and restoration programs (*16*).

Despite much progress in understanding the structure and dynamics of mutualistic webs, we still have a limited ability to predict species extinctions. This ability would improve if we could identify those interactions most susceptible to disruption. However, increasing predictive ability rests on two untested assumptions: (i) interactions are lost nonrandomly from webs following disturbance; and (ii), analogous to the "response traits" of species (*17*), particular traits that characterize mutualistic interactions increase their chance of disruption. Here, we explore these two hypotheses using 12 pollination webs from untilled hills or "sierras" that rise from the Pampas of Argentina (*18*). Ranging from tens to thousands of hectares, these sierras were once connected by a matrix of natural grassland, but are nowadays completely isolated by an intensively managed surrounding agricultural matrix. Therefore, they can be viewed as representing a gradient of habitat reduction. In addition to containing several endemic species of Gondwanan origin, these sierras still preserve many floristic elements that were formerly common in the surrounding plains and elsewhere in southern South America (*19*). Previous work revealed that the number of plant and pollinator species and interaction links between them increase with area of the sierras and that the rate of increase was half as great for species as it was for the number of links (*13*). However, why specific links are lost in smaller sierras, whereas others persist, remains unexplained.

Across all 12 pollination webs, we recorded 1170 distinct interactions (links) among 96 and 172 species of plants and flower visitors, respectively (Fig. 1 and fig. S1). When sierras were ordered by decreasing size, we found that interactions present in each sierra tended to be proper (i.e., nested) subsets (*20*) of those recorded in the next-larger sierra ($Z = 6.80$ and $Z = 5.43$ based on the completely randomized and marginal-conditioned null models, respectively; $P < 10^{-6}$ in both cases). This result is consistent with the hypothesis that mutualistic interactions are lost nonrandomly as habitat size decreases. Furthermore, interactions were more nested than plant and pollinator species themselves (fig. S2), which probably indicates their greater and more proximate susceptibility to habitat reduction (*13*). Thus, some mutualistic species could persist despite the disruption of some of their interactions, potentially because of mutualism redundancy and other buffering life-history traits (*10*) or simply as part of an extinction debt (*21*).

This pattern of nonrandom losses prompted the question of which traits of plant-pollinator interactions make them most susceptible to disruption. We analyzed two traits, interaction frequency and degree of generalization (estimated here as the average number of species with which the plant and pollinator interact), which required no detailed information about the species involved, beyond knowing with how many species they interacted and how frequently (*22*). We chose these traits because, first, locally rare plant-pollinator interactions should be particularly susceptible to habitat reduction because any further decrease in interaction frequency, perhaps related to declining species abundance, could trigger complete disruption (*22*, *23*). The second reason was that interactions between plant and pollinator species with limited numbers of alternative partners (i.e., interactions of low degree) should also be particularly susceptible beyond any confounding effect of interaction frequency, because they cannot be "subsidized" or "rescued" by third parties when, for instance, interacting species become spatially or phenologically isolated from each other (*4*, *24*). Thus, low-frequency interactions and/or interactions between specialists should be restricted to continuous habitat or large habitat fragments, whereas frequent interactions and/or interactions between generalists should be more resistant to habitat reduction and, therefore, be more ubiquitous (i.e., occur in habitat fragments of all sizes).

For each sierra, we characterized the ubiquity of each plant-pollinator interaction as the proportion of other sampled sierras in which it also

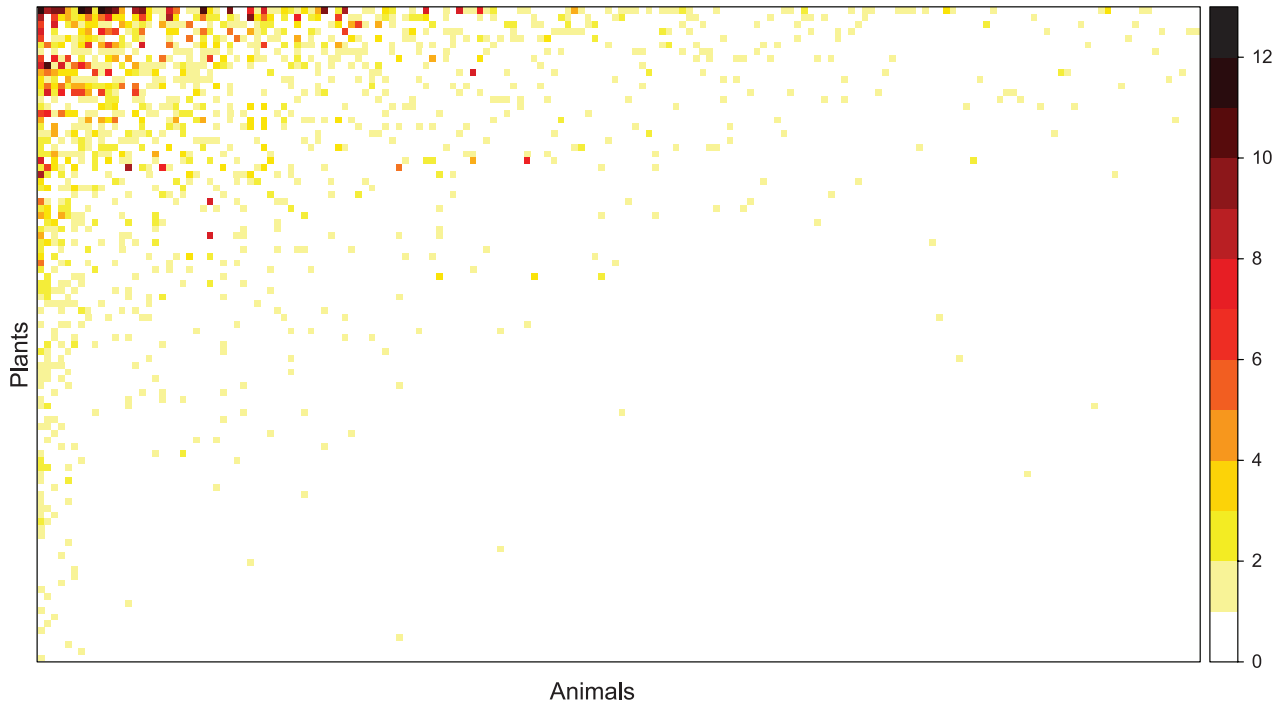

Fig. 1. Combined plant-animal pollinator interaction matrix depicting the 1170 distinct interactions among 96 and 172 species of plants and flower visitors, respectively, recorded across the 12 sierras. Species are ranked according to decreasing number of interactions per species. A colored cell specifies an observed interaction. Different colors and color hues indicate the number of sierras in which each interaction was found (from 1 to 12). Interactions occurring in most sierras, both large and small, are mostly restricted to the upper left corner of the matrix. The interaction matrix of each sierra is provided as Supporting Online Material (fig. S1).

occurred. Specifically, we predicted that interactions from a large sierra with a high frequency and/or degree (i.e., involving generalist species) should be more ubiquitous than interactions with a low frequency and/or degree, which are expected to be disrupted by habitat reduction and thus absent from the small sierras. Therefore, the positive relation between interaction ubiquity and the two interaction traits, frequency or degree, which we predicted for large sierras should weaken in the small sierras that have already been mostly depleted of fragmentation-susceptible pollination interactions.

Following our expectation, the relation between interaction ubiquity and its two predictors, local interaction frequency and degree of generalization, became increasingly positive with increasing sierra size (Fig. 2). Particularly, these relations were strongest among interactions recorded in sierras >100 ha (fig. S1, A to H) and became weaker or disappeared for interactions in sierras <100 ha (fig. S1, I to L). For example, on Volcan, one of the largest sierras (>2000 ha), expected ubiquity increased from 0.15 to 0.82 and from 0.09 to 0.76 over the range of interaction frequencies and degree of generalization, respectively (fig. S1B). In contrast, on Difuntito, one of the smallest sierras (13 ha), expected ubiquity increased only from 0.12 to 0.38 over the range of interaction frequencies and remained fairly constant (~0.15) over the range of interaction generalization (fig. S1J). The results from this small sierra also illustrate that the nonrandom loss of vulnerable interactions is, to some extent, unrelated to changes in interaction diversity, because the pollination web of Difuntito (the only fenced sierra protected from grazing and fire) was unexpectedly rich in species and interactions (*13*). Nevertheless, its position within the general pattern depicted in Fig. 2 was in no way anomalous, which suggested that this sierra lacked most of the vulnerable interactions recorded in the largest sierras. This result further stresses the importance of an area-per-se effect on the selective loss of interactions.

Interaction frequency and degree of generalization had largely independent effects on interaction loss. First, these two traits of interactions were correlated positively, but generally weakly within sierras ($r < 0.55$ in all cases), with the strength of this correlation increasing only marginally with sierra size (fig. S3). Second, and more important, the increasingly positive relation between interaction ubiquity and interaction frequency or degree of generalization with increasing sierra size (Fig. 2) persisted after accounting for any collinearity between the predictors by using partial model coefficients (fig. S4). Thus, particular traits of plant-pollinator interactions—specifically, low frequency and high specialization—contribute systematically and additively to their vulnerability to habitat reduction. Consequently, disruption of rare mutualistic interactions and those between reciprocal specialists may signal future biodiversity loss, and so they should be the focus of biodiversity monitoring and restoration programs. In particular, specialized interactions should be of primary concern, as their disruption could lead to the rapid loss of species that lack alternative efficient mutualists. Based on our results, a low interaction frequency would further increase the vulnerability of such interaction links.

Frequent interactions between generalist plants and pollinators establish the architectural core of pollination networks (*25*), which provides stability and resilience to the entire web (*1*, *2*, *25*, *26*). This core also governs coevolutionary dynamics of generalists engaged in strong interactions with other generalists and asymmetrically with most specialists (*27*, *28*). The differential loss of relatively specialized interactions in particular would accentuate this intrinsic asymmetry of networks (*29*, *30*) after habitat reduction, which was evidenced here by a weak but increasingly negative association between the specialization of plants and that of their interacting animal partners with decreasing sierra size (fig. S5). This result suggests that many specialists persist in fragmented landscapes by interacting with locally and regionally resilient generalists, around which interactions become increasingly concentrated. Such "supergeneralists," also described for pollination webs on islands and in communities with many invaders (*14*, *31*), should represent strong novel demographic and selection pressures for persisting specialists.

Our results also hint at subtle, but important, qualitative changes in the structure of the web core. Increasingly positive relations between interaction ubiquity and the two predictive interaction traits, frequency and degree of generalization (Fig. 2), indicate that the core in the largest sierras included a set of regionally widespread, robust interactions that were present in both large and small sierras (fig. S1). However, a trend toward decreasing frequency and degree of generalization of many of the most ubiquitous interactions (fig. S6) indicates their displacement from the inner core to relatively more marginal positions within the web as sierra size decreases. Even though some interactions [e.g., between species coded 32 and 108 (table S4)] remain part of this core, irrespective of the size of the sierra (fig. S1), the central structural role played previously by some of these ubiquitous interactions could remain vacant or be replaced by more facultative interactions present in one or a few small sierras [e.g., interaction between species coded 56 and 259 in Difuntito (fig. S1J and table S4)]. Thus, because of this core shift, species surviving in small habitat fragments could be subject to more variable ecological and evolutionary dynamics in space and perhaps time.

Functional redundancy in mutualistic interaction networks provides relative stability to minor or moderate random losses of species and interactions (*4*, *32*), but nonrandom disruption can affect species survival and adaptation more immediately and profoundly. Particularly, infrequently occurring and geographically restricted specialized interactions that involve efficient pollination for the plant and/or some critical floral resource for the pollinator can be highly relevant at both ecological and evolutionary time scales (*33*, *34*), and their disruption could lead to time-lagged species decline (*35*). Using a comparative interaction-network approach, we provide evidence that these particular interactions, occurring at low frequency and between species that lack alternative mutualists, are the most likely to be lost, which could accelerate the rate of species extinctions. In combination, our results suggest that nonrandom interaction disruption after habitat fragmentation and other anthropogenic disturbances will affect the most codependent and rare mutualisms and alter configurations of interaction networks, along with unique ecological relations and evolutionary pathways.

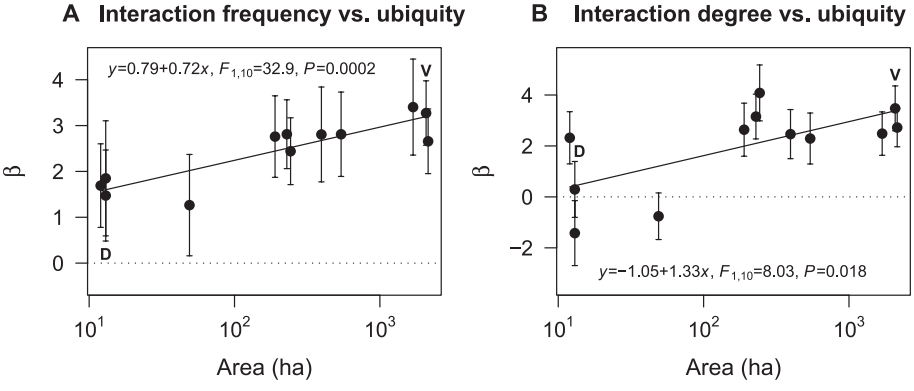

Fig. 2. The dependence on sierra size of the relation between interaction ubiquity and interaction (**A**) frequency and (**B**) degree of generalization. Dependence is represented by regression coefficients (β ± 95% confidence intervals) from binomial generalized linear models conducted for each of the 12 sierras. Individual coefficients whose confidence intervals do not overlap the dotted line differ significantly from zero. Solid lines and summary statistics indicate that the linear relation between ubiquity and each interaction trait increases significantly with sierra area. Specific results for Difuntito (D), a small sierra, and Volcan (V), a large sierra, discussed in the text are shown in fig. S1, B and J, respectively.

References and Notes

1. U. Bastolla *et al.*, *Nature* **458**, 1018 (2009).
2. T. Okuyama, J. N. Holland, *Ecol. Lett.* **11**, 208 (2008).
3. N. Rooney, K. McCann, G. Gellner, J. C. Moore, *Nature* **442**, 265 (2006).
4. C. N. Kaiser-Bunbury, S. Muff, J. Memmott, C. B. Müller, A. Caflisch, *Ecol. Lett.* **13**, 442 (2010).
5. L. P. Koh *et al.*, *Science* **305**, 1632 (2004).
6. C. Fontaine, I. Dajoz, J. Meriguet, M. Loreau, *PLoS Biol.* **4**, e1 (2006).
7. A. Pauw, *Ecology* **88**, 1759 (2007).
8. N. M. Williams, C. Kremen, *Ecol. Appl.* **17**, 910 (2007).
9. A. Müller *et al.*, *Biol. Conserv.* **130**, 604 (2006).
10. W. Bond, *Philos. Trans. R. Soc. Ser. B* **344**, 83 (1994).
11. N. M. Williams *et al.*, *Biol. Conserv.* **143**, 2280 (2010).
12. J. M. Tylianakis, R. K. Didham, J. Bascompte, D. A. Wardle, *Ecol. Lett.* **11**, 1351 (2008).
13. M. Sabatino, N. Maceira, M. A. Aizen, *Ecol. Appl.* **20**, 1491 (2010).
14. M. A. Aizen, C. L. Morales, J. M. Morales, *PLoS Biol.* **6**, e31 (2008).
15. B. Padrón *et al.*, *PLoS ONE* **4**, e6275 (2009).
16. J. M. Tylianakis, E. Laliberté, A. Nielsen, J. Bascompte, *Biol. Conserv.* **143**, 2270 (2010).
17. S. Lavorel, S. McIntyre, J. Landsberg, T. D. Forbes, *Trends Ecol. Evol.* **12**, 474 (1997).
18. Materials and methods are available as supporting material on *Science* Online.
19. J. Crisci, S. Freire, G. Sancho, L. Katinas, *Caldasia* **23**, 21 (2001).
20. M. Almeida-Neto, P. Guimaraes, P. R. Guimaraes Jr., R. D. Loyola, W. Ulrich, *Oikos* **117**, 1227 (2008).
21. D. Tilman, R. M. May, C. L. Lehman, M. A. Nowak, *Nature* **371**, 65 (1994).
22. D. P. Vázquez, M. A. Aizen, *Ecology* **84**, 2493 (2003).
23. D. P. Vázquez, R. Poulin, B. R. Krasnov, G. I. Shenbrot, *J. Anim. Ecol.* **74**, 946 (2005).
24. J. Memmott, P. G. Craze, N. M. Waser, M. V. Price, *Ecol. Lett.* **10**, 710 (2007).
25. J. Bascompte, P. Jordano, C. J. Melián, J. M. Olesen, *Proc. Natl. Acad. Sci. U.S.A.* **100**, 9383 (2003).
26. E. Thébault, C. Fontaine, *Science* **329**, 853 (2010).
27. P. R. Guimarães Jr. *et al.*, *Curr. Biol.* **17**, 1797 (2007).
28. J. N. Thompson, *The Coevolutionary Process* (Univ. of Chicago Press, Chicago, 1994).
29. J. Bascompte, P. Jordano, J. M. Olesen, *Science* **312**, 431 (2006).
30. D. P. Vázquez, M. A. Aizen, *Ecology* **85**, 1251 (2004).
31. J. M. Olesen, L. I. Eskildsen, S. Venkatasamy, *Divers. Distrib.* **8**, 181 (2002).
32. J. Memmott, N. M. Waser, M. V. Price, *Proc. Biol. Sci.* **271**, 2605 (2004).
33. B. Anderson, S. D. Johnson, *Evolution* **62**, 220 (2008).
34. K. E. Steiner, V. Whitehead, *Evolution* **44**, 1701 (1990).
35. A. Pauw, J. A. Hawkins, *Oikos* **120**, 344 (2011).

Acknowledgments: The authors thank J. M. Gómez, L. D. Harder, D. P. Vázquez, M. Verdú, N. M. Waser, and two anonymous referees for useful comments and suggestions; A. Saez and D. Porrini for field assistance; V. Izpizua and M. Nuciari for help in plant identification; and J. Farina and A. Roig-Alsina for help in identifying insects. Partial funding by the National Institute of Agricultural Technology (INTA), Balcarce (PNECO1302), the Argentina National Research Council (CONICET) (PIP 01623), the National Fund for Research (PICT 01300), and the National University of Comahue (B152/04) is acknowledged. M.A.A. is a career researcher and M.S. a fellow of CONICET. J.M.T. is funded by a Rutherford Discovery Fellowship administered by the Royal Society of New Zealand. Data used in the analyses are available in the Supporting Online Material.

Supporting Online Material

www.sciencemag.org/cgi/content/full/335/6075/1486/DC1
Materials and Methods
SOM Text
Figs. S1 to S6
Tables S1 to S4
References (*36*–*50*)

14 October 2011; accepted 14 February 2012
10.1126/science.1215320

Evolutionary Conservation of Species' Roles in Food Webs

Daniel B. Stouffer,[1,2] Marta Sales-Pardo,[3] M. Irmak Sirer,[4] Jordi Bascompte[1]

Studies of ecological networks (the web of interactions between species in a community) demonstrate an intricate link between a community's structure and its long-term viability. It remains unclear, however, how much a community's persistence depends on the identities of the species present, or how much the role played by each species varies as a function of the community in which it is found. We measured species' roles by studying how species are embedded within the overall network and the subsequent dynamic implications. Using data from 32 empirical food webs, we find that species' roles and dynamic importance are inherent species attributes and can be extrapolated across communities on the basis of taxonomic classification alone. Our results illustrate the variability of roles across species and communities and the relative importance of distinct species groups when attempting to conserve ecological communities.

Present-day ecosystems face threats, such as climate change and invasive species, that permeate entire communities (*1*). Partly for this reason, ecology has moved toward more holistic approaches that consider all species in an ecosystem and the network of interactions between them (*2*). This network approach has led to a greater understanding of the structural properties of ecological systems (*3*) and the community-wide consequences of empirically observed network structure (*4*, *5*). A drawback of this community focus is that the interplay between individual species and community-level dynamics has largely been ignored (*6*, *7*). Because conservation efforts are generally focused on species, this problem has precluded a deeper assessment of the conservation implications of network theory (*1*).

Here we focus on the species level, to understand the generality of species' roles and their dynamic importance when embedded in their community's network. The prevailing notion is that the ecological role of a species in a network is a direct result of its interactions with other species (*8*–*10*), in particular the prey it consumes and the predators that consume it. However, given structural definitions of species' roles, it is often unclear how to extrapolate from a species' structural role to its dynamic relevance. With this in mind, we introduce here a definition of species' roles based around the concept of "network motifs" (*11*).

Any network can be decomposed into a set of smaller subnetworks which, when reassembled, form the original network. Depending on the type of network studied, particular subnetworks appear more frequently than would be expected at random and represent fundamental building blocks: These are referred to as network motifs (*11*). Crucially, the number and type of motifs that make up a food web are known to directly affect the web's stability and persistence (*12*–*16*). In ecological networks, motifs provide a meso-scale characterization of community structure by quantifying how collections of three species come together to form a larger community (*17*, *18*). Here, we take network motifs one step further to better highlight the behavior of their most basic component: the individual species.

By definition, any motif of size n is composed of n species; for reasons of symmetry, however, each species does not necessarily appear in a unique position (Fig. 1). As an illustrative example, consider the two unique motifs made up of two species: $A \rightarrow B$ and $A \leftrightarrow B$ (*19*). In the first motif, the positions of A and B are not equivalent, because they allow us to distinguish between the two species. On the other hand, the positions of A and B are indistinguishable in the second motif. This implies that, formally, a motif of n species can have anywhere from 1 to n unique positions. If we consider three-species combinations, we find that there are 13 unique motifs composed of 30 unique positions (*20*, *21*) (fig. S1).

We examined the motif pattern of all species from 32 empirical food webs that describe which predator-prey interactions are observed in the community (*21*) (table S1). These food webs come from a variety of different environments, encompassing marine, terrestrial, freshwater, and estuarine habitats. To quantify the roles of all species in a food web, we directly enumerate, across all motifs, the frequency c_{ij} that species i appears in each position j. Therefore, in each network, the motif profile of any species i is provided by its vector $\vec{c_i} = \{c_{i1},c_{i2},\ldots,c_{i29},c_{i30}\}$.

[1]Integrative Ecology Group, Estación Biológica de Doñana (EBD-CSIC), calle Américo Vespucio sin número, 41092 Sevilla, Spain. [2]School of Biological Sciences, University of Canterbury, Christchurch 8140, New Zealand. [3]Departament d'Enginyeria Química, Universitat Rovira i Virgili, 43007 Tarragona, Spain. [4]Department of Chemical and Biological Engineering, Northwestern University, Evanston, IL, 60208, USA.

To better refine our definition of a species' role, we search for sets of species that exhibit statistically similar motif profiles. The resulting motif profile–based grouping of species provides the complete set of unique, empirically observed roles. Species with more interactions will appear in more motifs and will therefore be characterized by larger values of c_{ij}. To take this into account, we use a network-based method that identifies groups while explicitly controlling for the total number of motifs each species participates in (*21*–*23*) (figs. S2 and S3). In spirit, our methodology is akin to identifying sets of species that have similar normalized motif profiles $\vec{f_i} = \{f_{i1}, f_{i2},..., f_{i29}, f_{i30}\}$, where $f_{ij} = c_{ij}/\sum_k c_{ik}$, and the sum is across all positions (*24*). Because the sum gives the total number of times that species i appears in all of the motif positions, f_{ij} corresponds to the relative frequency that species i appears in position j (Fig. 2). Because our analysis controls for a species' total number of interactions, it provides an unbiased measure of the topological configuration of a species' interactions.

Now that we have a means to quantify species' roles, the next step is to extend our structural measure to its dynamic consequences. Simulations show that we can associate a "benefit" s_j to each position j across all motifs, determined by how much community persistence increases or decreases when a single motif j is added to the network (*16*). Because each position in a single motif appears with the same overall frequency, we necessarily assume that all positions from the same motif have the same associated benefit. Given the benefit of each position and our species-specific motif profiles, we can calculate a species' expected mean effect on community persistence. Mathematically, this is given by

$$b_i = \sum_{j}^{\text{positions}} f_{ij}\, s_j \qquad (1)$$

where b_i is the benefit of species i in terms of its effect on community persistence (*25*). Here, the benefit of each species provides an assessment of the degree to which each species in a community is a keystone species (*26*). A keystone species is one whose presence is particularly critical for a community's biodiversity maintenance, as compared to all other species present (*27*). Our analysis, therefore, allows us to quantify the complete gradient across which species contribute to the organization and dynamics of their network.

Across the 2468 empirical species and 32 webs, we observe 54 distinct empirical roles (table S1). At the network level, we find that some of the 32 webs contain species from just two distinct roles, whereas others contain species from up to 22 distinct roles (mean 7.4 ± 5.4). Intriguingly, the diversity of roles found in a food web is neither directly proportional to the amount of species diversity ($P = 0.63$) nor the amount of taxonomic diversity ($P = 0.82$) found within the community.

The majority of roles consist exclusively of intermediate species (46 out of the 54 roles), whereas the remaining roles are made up of either (i) basal and intermediate species or (ii) intermediate species and top predators. Roles, however, are not distributed proportionally across trophic levels; the 1026 basal, 991 intermediate, and 451 top species in the data are assigned to one of four, 53, or five roles, respectively. The interaction patterns of basal species and top predators therefore appear to be particularly constrained when they are part of a larger community. In addition, the diversity of roles played by intermediate species paints a more complex picture than the usual top-down versus bottom-up approach (*28*).

Building on the strong variability in roles across species and communities, we next aim to determine the extent to which a species' role is evolutionarily conserved. A strong tendency would help to predict the role of species in a new network; for example, after introduction or invasion. We find that species with the same role have a significant tendency to be homogenous both in terms of phylogenetic similarity and dynamic importance (*21*) (Fig. 3). In fact, we observe a large degree of phylogenetic signal in how species are embedded in their network and their subsequent dynamic importance (table S2). First, closely related species have a significant tendency to have similar motif profiles in a significant fraction of empirical webs (13 out of the 18 webs for which we have taxonomic data, $P < 10^{-4}$). Second, closely related species also have a significant tendency to be of similar benefit to their home community than would be expected at random (15 out of 18 webs, $P < 10^{-4}$). This relationship holds while controlling for the fact that phylogenetically related species also tend to have similar trophic positions (*21*, *29*).

Phylogenetic signal, as we have measured it here, is quantified at the scale of an individual community. We wish, however, to see if this result reflects an intrinsic property of each species and thus can be extrapolated across distinct communities composed of different species. To do so, we take advantage of specific details regarding our empirical data. Ten of the empirical webs come from third- or fourth-order tributaries of the same river in New Zealand (*30*). We compare the relative importance of the 150 species (out of 192 total) that occur in at least 2 of the 10 different networks. We find that, if a species is dynamically important in one web, it shows a significant tendency to be important in the other webs in which it appears, and vice versa (*21*).

To some degree, however, this result may be a direct consequence of (i) within-community phylogenetic signal and (ii) insufficient community variability between the 10 webs. Indeed, though the webs differ somewhat in the degree to which the adjacent land had been developed for pasture

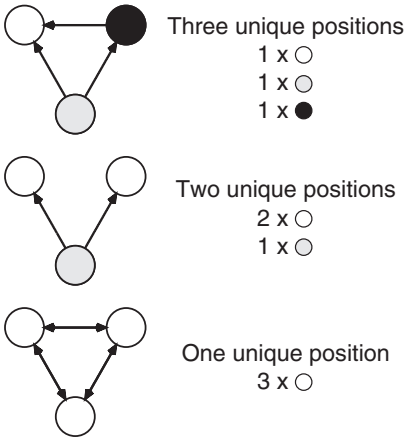

Fig. 1. Uniqueness of positions in three-species motifs. We show 3 of the 13 unique three-species motifs. Each circle represents a different species, and interacting species are connected by an arrow that goes from prey to predator. Although each motif consists of three species, not every position is unique for reasons of symmetry. From top to bottom, these motifs are made up of three, two, and one unique positions, respectively. In each motif, the different unique positions are shown in different colors (black, white, or gray).

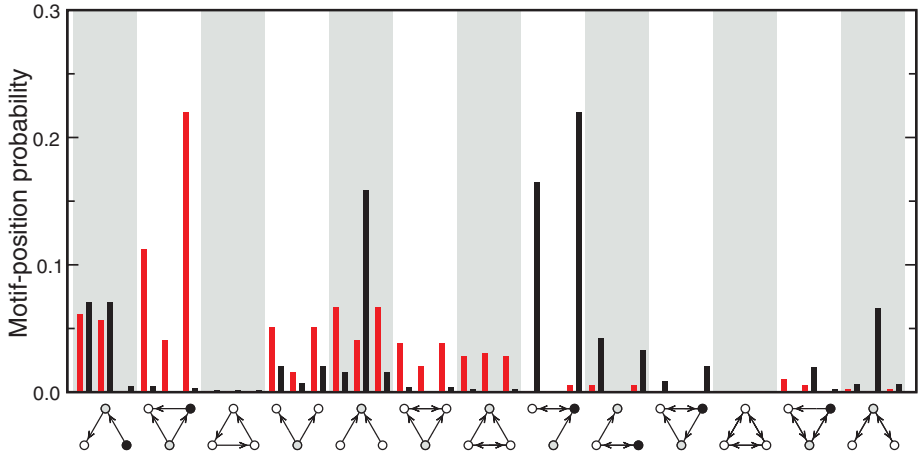

Fig. 2. Species differ in their tendency to appear in distinct motif positions. We show the species-specific motif profiles $\vec{f_i}$ for two different species from the empirical webs (red and black bars, respectively). The height of each bar is equal to the probability f_{ij} that the species appears in the position found immediately below.

(*30*), there is substantial overlap between them in terms of species composition. Given observed patterns of evolutionary conservation of ecological interactions (*31*–*33*), we cannot exclude the possibility that similarities in species composition across the 10 New Zealand webs are sufficient to account for the observed similarities in species' dynamic importance.

A stronger and more conclusive test of the generality of our results would be to compare species across the complete set of food webs, in which there is far greater variability of community composition. At the species level, we cannot extend this analysis to the other food webs, because none of the 192 species found in the New Zealand food webs appears elsewhere. Nevertheless, we can make comparisons at coarser levels of taxonomic aggregation. For example, we can compute the tendency of a given phylum of species to be important in the New Zealand webs and compare this to the tendency for the same phylum appearing in webs outside of New Zealand. Across all phyla, significant correlation could indicate that intrinsic factors are a stronger determinant of species' dynamic importance than are the properties of the community in which they occur.

In our comparative analysis, we find that dynamically important phyla in New Zealand also tend to be dynamically important elsewhere, and vice versa ($P = 0.036$; Fig. 4 and table S3). Moreover, we observe significant correlation at the class, order, and family levels ($P = 0.018$, $P = 0.012$, and $P = 0.005$, respectively). This implies that there are particular taxonomic groups of species that are expected to play an important dynamic role independent of the specifics of their particular ecological community. It therefore appears that species dynamic importance—the degree to which a species acts as a keystone species—may indeed be an intrinsic and inherent species attribute that arises as a consequence of species' evolutionary histories.

Our study of species' roles and their dynamic consequences has important implications about how best to decide which conservation actions will most successfully preserve ecological communities (*1*), linking species-specific variability to overall network persistence. The number and type of roles observed in a community do not increase systematically with increasing species or taxonomic diversity. This means that actions that focus on maintaining overall levels of biodiversity may not be sufficient to preserve an ecosystem's long-term viability. On the other hand, the dynamic implications of species' roles provide a potential starting point when deciding

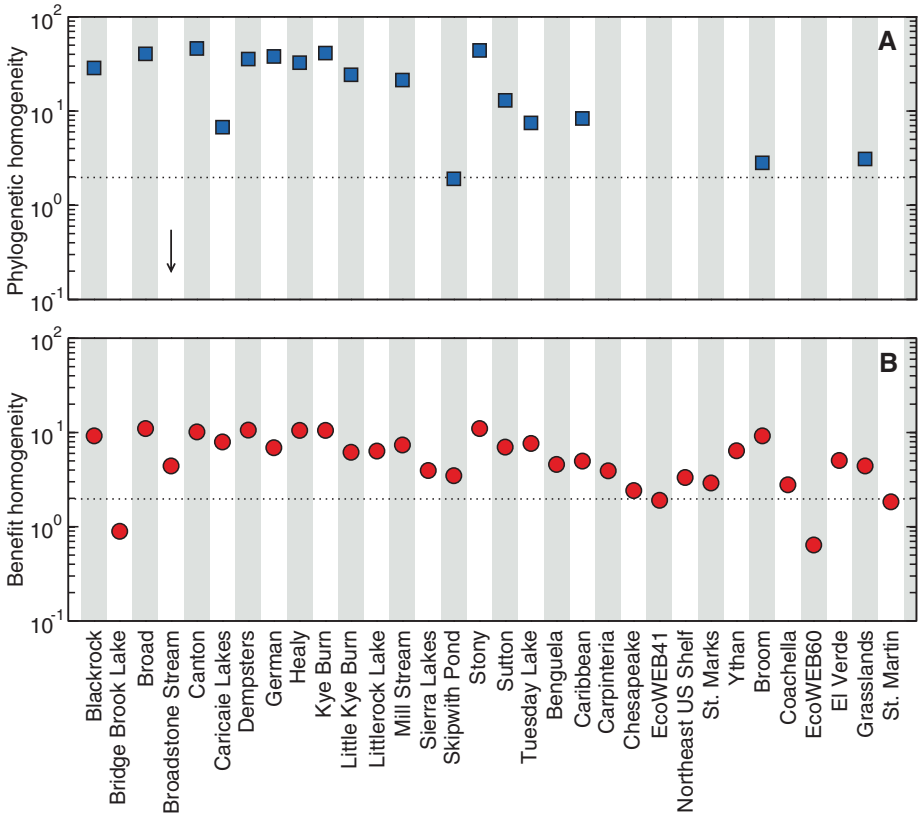

Fig. 3. Species' roles capture important components of the variability observed across species in a network. (**A**) Species' roles are phylogenetically homogeneous; that is, they have a significant tendency to be closely related phylogenetically. (**B**) Species' roles also tend to be homogeneous in terms of their dynamic importance to their community. Here, values of phylogenetic or benefit homogeneity close to zero indicate no tendency; in contrast, values greater than 2 (dotted line) indicate significant similarity within species' roles. We have ordered the webs so that the first 18 are from freshwater environments, the next 8 from marine environments, and the last 6 from terrestrial environments. The arrow in (A) indicates an observed value that is less than the *y*-axis minimum of 10^{-1}.

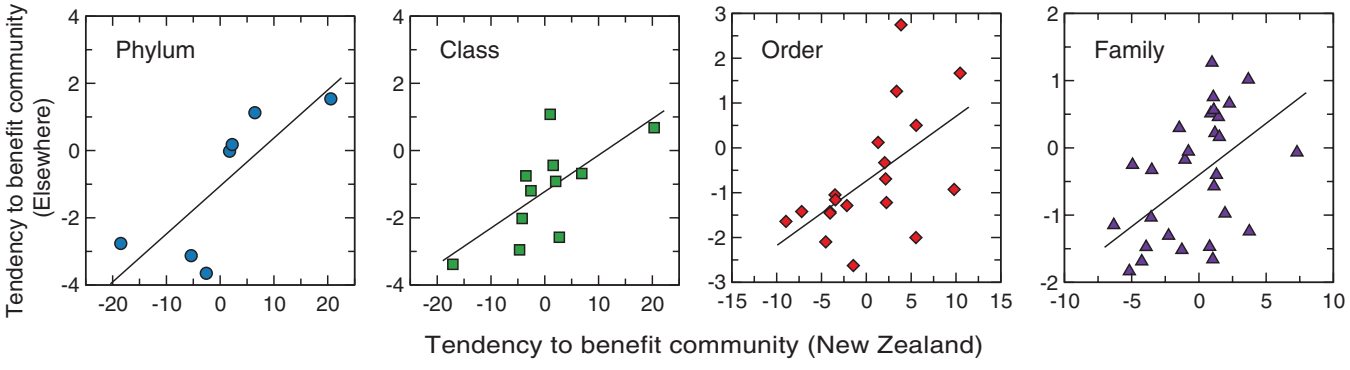

Fig. 4. Species dynamic importance is conserved across diverse ecological communities. We calculate whether specific groups of species are observed to benefit their home community as a result of their motif profiles. Values greater than 2 indicate a significant tendency to positively influence community persistence, whereas values less than −2 indicate a significant tendency to negatively influence community persistence. We repeat this analysis for every phylum, class, order, and family for which species appear both in the New Zealand webs and in the others. At each of these levels of classification, we observe significant correlation between species' tendencies to benefit their community ($P < 0.05$), irrespective of the community context in which they occur.

which species should receive priority in conservation efforts: those from groups that make the strongest contributions to the community persistence. Perhaps most importantly, our results indicate that this predictive power spans a broad range of taxonomic scales.

References and Notes

1. J. M. Tylianakis, E. Laliberté, A. Nielsen, J. Bascompte, *Biol. Conserv.* **143**, 2270 (2010).
2. J. Bascompte, *Science* **325**, 416 (2009).
3. M. Pascual, J. A. Dunne, Eds., *Ecological Networks: Linking Structure to Dynamics in Food Webs* (Oxford Univ. Press, Oxford, 2006).
4. E. Thébault, C. Fontaine, *Science* **329**, 853 (2010).
5. D. B. Stouffer, J. Bascompte, *Proc. Natl. Acad. Sci. U.S.A.* **108**, 3648 (2011).
6. D. Tilman, *Ecology* **80**, 1455 (1999).
7. D. B. Stouffer, *Funct. Ecol.* **24**, 44 (2010).
8. J. J. Luczkovich, S. P. Borgatti, J. C. Johnson, M. G. Everett, *J. Theor. Biol.* **220**, 303 (2003).
9. J. M. Olesen, J. Bascompte, Y. L. Dupont, P. Jordano, *Proc. Natl. Acad. Sci. U.S.A.* **104**, 19891 (2007).
10. S. Allesina, M. Pascual, *Ecol. Lett.* **12**, 652 (2009).
11. R. Milo *et al.*, *Science* **298**, 824 (2002).
12. A.-M. Neutel, J. A. P. Heesterbeek, P. C. De Ruiter, *Science* **296**, 1120 (2002).
13. M. Kondoh, *Proc. Natl. Acad. Sci. U.S.A.* **105**, 16631 (2008).
14. S. Allesina, M. Pascual, *Theor. Ecol.* **1**, 55 (2008).
15. J. L. García-Domingo, J. Saldaña, *Oikos* **117**, 336 (2008).
16. D. B. Stouffer, J. Bascompte, *Ecol. Lett.* **13**, 154 (2010).
17. J. Bascompte, C. J. Melián, *Ecology* **86**, 2868 (2005).
18. D. B. Stouffer, J. Camacho, W. Jiang, L. A. N. Amaral, *Proc. R. Soc. London Ser. B* **274**, 1931 (2007).
19. Here an arrow (→) indicates an interaction in the direction of mass and energy flow, from prey to predator.
20. We focus on three-species motifs because they provide both significant information content and reduced overall complexity (there are 199 and 9364 unique motifs composed of four and five species, respectively).
21. See the supporting material on *Science* Online.
22. M. Sales-Pardo, R. Guimerà, A. A. Moreira, L. A. Amaral, *Proc. Natl. Acad. Sci. U.S.A.* **104**, 15224 (2007).
23. R. Guimerà, M. Sales-Pardo, L. A. Amaral, *Phys. Rev. E Stat. Nonlin. Soft Matter Phys.* **76**, 036102 (2007).
24. All results reported here hold if we choose to focus on species' absolute motif profiles c_i instead of normalized motif profiles.
25. Just like the vector $\vec{c}_i$, the expected benefit b_i for a species i is calculated at the level of a single food web.
26. R. T. Paine, *Am. Nat.* **103**, 91 (1969).
27. L. S. Mills, M. S. Soulé, D. F. Doak, *Bioscience* **43**, 219 (1993).
28. M. E. Power, *Ecology* **73**, 733 (1992).
29. As for species' roles, we observe a significant relationship between species' benefits and whether that species is basal, intermediate, or a top predator ($P < 10^{-4}$). Nevertheless, phylogenetic relatedness is a signficant determinant of species' benefits even when controlling for the influence of species' trophic level (13 out of 18 webs, $P < 0.001$).
30. C. R. Townsend *et al.*, *Ecol. Lett.* **1**, 200 (1998).
31. E. L. Rezende, J. E. Lavabre, P. R. Guimarães, P. Jordano, J. Bascompte, *Nature* **448**, 925 (2007).
32. J. M. Gómez, M. Verdú, F. Perfectti, *Nature* **465**, 918 (2010).
33. A. Eklöf, M. R. Helmus, M. Moore, S. Allesina, *Proc. R. Soc. London Ser. B* 10.1098/rspb.2011.2149 (2011)

Acknowledgments: D.B.S. acknowledges the support of a Consejo Superior de Investigaciones Científicas–Junta para la Ampliación de Estudios Postdoctoral Fellowship and a Juan de la Cierva Fellowship from the Ministerio de Ciencia e Innovacion (MICINN), Spain. M.S.P. acknowledges the support of grant FIS2010-18639 from the MICINN, Spain; a Research Award from the James S. McDonnell Foundation; and grant PIRG-GA-2010-268342 from the European Union. M.I.S. acknowledges the support of a W. M. Keck Foundation grant. J.B. acknowledges the support of the European Research Council under the European Community's Seventh Framework Programme (FP7/2007-2013) through an Advanced Grant (grant agreement 268543). A list of references from which the food web data can be obtained is found in table S1. All figures were generated with PyGrace (http://pygrace.sourceforge.net).

Supporting Online Material

www.sciencemag.org/cgi/content/full/335/6075/1489/DC1
SOM Text
Figs. S1 to S3
Tables S1 to S3
References (*34*–*65*)

14 November 2011; accepted 14 February 2012
10.1126/science.1216556

Plant UVR8 Photoreceptor Senses UV-B by Tryptophan-Mediated Disruption of Cross-Dimer Salt Bridges

John M. Christie,[1,2] Andrew S. Arvai,[2] Katherine J. Baxter,[1]* Monika Heilmann,[1]* Ashley J. Pratt,[2] Andrew O'Hara,[1] Sharon M. Kelly,[1] Michael Hothorn,[3]† Brian O. Smith,[1] Kenichi Hitomi,[2,4,5] Gareth I. Jenkins,[1]‡ Elizabeth D. Getzoff[2]‡

The recently identified plant photoreceptor UVR8 (UV RESISTANCE LOCUS 8) triggers regulatory changes in gene expression in response to ultraviolet-B (UV-B) light through an unknown mechanism. Here, crystallographic and solution structures of the UVR8 homodimer, together with mutagenesis and far-UV circular dichroism spectroscopy, reveal its mechanisms for UV-B perception and signal transduction. β-propeller subunits form a remarkable, tryptophan-dominated, dimer interface stitched together by a complex salt-bridge network. Salt-bridging arginines flank the excitonically coupled cross-dimer tryptophan "pyramid" responsible for UV-B sensing. Photoreception reversibly disrupts salt bridges, triggering dimer dissociation and signal initiation. Mutation of a single tryptophan to phenylalanine retunes the photoreceptor to detect UV-C wavelengths. Our analyses establish how UVR8 functions as a photoreceptor without a prosthetic chromophore to promote plant development and survival in sunlight.

UVR8 (UV RESISTANCE LOCUS 8) orchestrates the expression of more than 100 genes in *Arabidopsis* in response to ultraviolet B (UV-B) wavelengths (280 to 315 nm) (*1*–*4*). The *uvr8* mutant exhibits UV-B sensitivity from decreased expression of genes conferring UV protection (*1*, *5*). UV-B exposure promotes both rapid UVR8 accumulation in the nucleus (*6*), where the protein binds chromatin via histones (*1*, *7*), and interaction with COP1 (CONSTITUTIVELY PHOTOMORPHOGENIC 1) to initiate transcriptional responses (*3*, *8*). In plant extracts and in heterologous systems, UV-B exposure triggers UVR8 dimer dissociation to initiate signaling (*9*). Tryptophan has been implicated in UV-B perception (*4*, *9*), but the absence of detailed three-dimensional information on dimer assembly precludes understanding of the mechanisms for UVR8 photoreception and signaling.

To investigate UVR8 structure/function relationships, we made recombinant *Arabidopsis* UVR8 (*10*) for biophysical analyses (figs. S1 and S2). Purified UVR8 (fig. S2A) is a homodimer that dissociates into monomers after exposure to narrowband, long-wavelength UV-B (fig. S2B); the dose-response relationship (fig. S2C) mirrors UVR8 behavior in plant extracts (*9*). Moreover, UV-B–induced monomerization is reversible; the active, dimeric photoreceptor spontaneously reassembles within hours in vitro and again responds to UV-B (Fig. 1A). UVR8 absorbs strongly at 280 nm (fig. S3), as expected from its complement of aromatic residues (14 Trp, 10 Tyr, and 8 Phe per 440-residue monomer). Photoactive, purified UVR8 lacks any bound cofactor, demonstrating that reversible UV-B–induced dimer dissociation is a property intrinsic to the protein.

The x-ray crystallographic structure of UVR8 (Fig. 1) was determined to 1.7 Å resolution (table S1) by molecular replacement with the RCC1 (Regulator of Chromosome Condensation 1) domain of E3 ligase HERC2 as the probe (*10*). UVR8 has a seven-bladed β-propeller fold, like

[1]Institute of Molecular, Cell and Systems Biology, College of Medical, Veterinary and Life Sciences, Bower Building, University of Glasgow, Glasgow G12 8QQ, UK. [2]Department of Molecular Biology and Skaggs Institute for Chemical Biology, The Scripps Research Institute, La Jolla, CA 92037, USA. [3]Plant Biology Laboratory, The Salk Institute for Biological Studies, La Jolla, CA 92037, USA. [4]Life Science Division, Lawrence Berkeley National Laboratory, Berkeley, CA 94720, USA. [5]Section of Laboratory Equipment, National Institute of Biomedical Innovation, 7-6-8, Saito-Asagi, Ibaraki, Osaka 567-0085, Japan.

*These authors contributed equally to this work.
†Present address: Structural Plant Biology Laboratory, Friedrich Miescher Laboratory of the Max Planck Society, Tuebingen, Germany.
‡In whose labs this research was jointly undertaken and to whom correspondence should be addressed. E-mail: gareth.jenkins@glasgow.ac.uk (G.I.J.); edg@scripps.edu (E.D.G.)

monomeric RCC1 and HERC2, but unexpectedly the topology is permuted (figs. S1 and S4). In HERC2 and RCC1, the N- and C-terminal sequences are linked because each contributes two of the four β strands to blade 1. In UVR8, however, each blade is contiguous in sequence with the N and C termini in the first and last blades, respectively (figs. S1 and S4), potentially permitting greater conformational flexibility.

Each doughnut-shaped UVR8 monomer is 40 to 50 Å in diameter, by ~35 Å high, with a central water-filled tunnel (Fig. 1B). Crystal packing of the trypsin-treated protein, which remains UV-B responsive (fig. S5), suggests two potential cylindrical dimer assemblies (Fig. 1C, inset). Small-angle x-ray scattering (SAXS) (table S2) clearly distinguishes the correct dimer in solution (Fig. 1C), by agreement between calculated and observed scattering profiles (*11*–*13*). The smaller, concave surfaces of the two subunits assemble face to face but offset by about 10 Å (Fig. 1, B and D). The two-fold dimer symmetry juxtaposes different blades from each subunit, except self-pairing blade 4 (Fig. 1B). SAXS results (Fig. 1D) show different lengths, but the same overall shape for full-length UVR8 and the trypsin-cleaved protein used for crystallography. Molecular envelopes derived from SAXS data on full-length UVR8 match the crystallographic dimer offset and diameter, and locate the C-terminal missing ~10% at distal ends of the dimer (Fig. 1D).

The dimer interface is remarkable for a preponderance of aromatic residues (7 Trp, 3 Phe, and 2 Tyr) (Fig. 1E) and charged side chains, which contribute to distinct regions of complementary electrostatic potential (Fig. 2A). The dimer offset and two-fold symmetry align rows of arginine and carboxylate side chains (Fig. 2B and fig. S6) to form a complex network of salt bridges across the dimer interface (fig. S7). In particular, doubly hydrogen-bonded salt bridges link R286 with D107 and R146 with E182 (Fig. 2C). Additional, singly hydrogen-bonded salt bridges join R286 with D96, R338 with D44, and R354 with E43 and E53. Interestingly, the dimer interface is composed of charged, hydrophilic, and aromatic residues only (except for hydrophobic A52), leading the PISA (Protein Interfaces, Surfaces and Assemblies) software (*14*) to assess dimer assembly as unstable. Yet, the solution scattering profile (Fig. 1C), size exclusion chromatography (SEC) (table S3), multiangle light scattering (MALS) (fig. S8A) and SDS-polyacrylamide gel electrophoresis (SDS-PAGE) analyses (*9*) (fig. S2B) demonstrate that UVR8 is a dimer.

To investigate the importance of ionic interactions in maintaining the UVR8 dimer, we showed that decreasing pH in vitro promotes monomerization (Fig. 2D) and examined the effects of mutating residues that participate in cross-dimer salt bridges. The UVR8^{R146A} and UVR8^{R286A} proteins, each lacking one dominant salt bridge, are dimers that undergo UV-B–induced monomerization, when assayed by SEC (table S3). However, unlike the wild-type protein, these mutants appear monomeric by SDS-PAGE without sample boiling (fig. S2D), indicating that the dimer has been destabilized. Double mutants lacking both dominant salt bridges (UVR8$^{R146A/R286A}$), the salt bridges of R286 with D107 and D96 (UVR8$^{D96N/D107N}$), or both the R286 and R338 salt bridges (UVR8$^{R286A/R338A}$) (Fig. 2C), are constitutive monomers (Fig. 2E and fig. S8), demonstrating a key role for the R286 salt bridges in dimer formation.

In each monomer, a striking cluster of nine aromatic residues dominates the interaction surface (Fig. 1E). A conserved Gly-Trp-Arg-His-Thr sequence repeat in blades 5, 6, and 7 (fig. S1) generates a triad of closely packed tryptophans—W233, W285, and W337—that are implicated in UVR8 photoreception (*9*). These pentapeptide repeats form protruding tight turns that project Trp and Arg residues outward and His residues (in all seven blades) inward to form a buried ring (Fig. 1E). Each triad Trp is flanked by the adja-

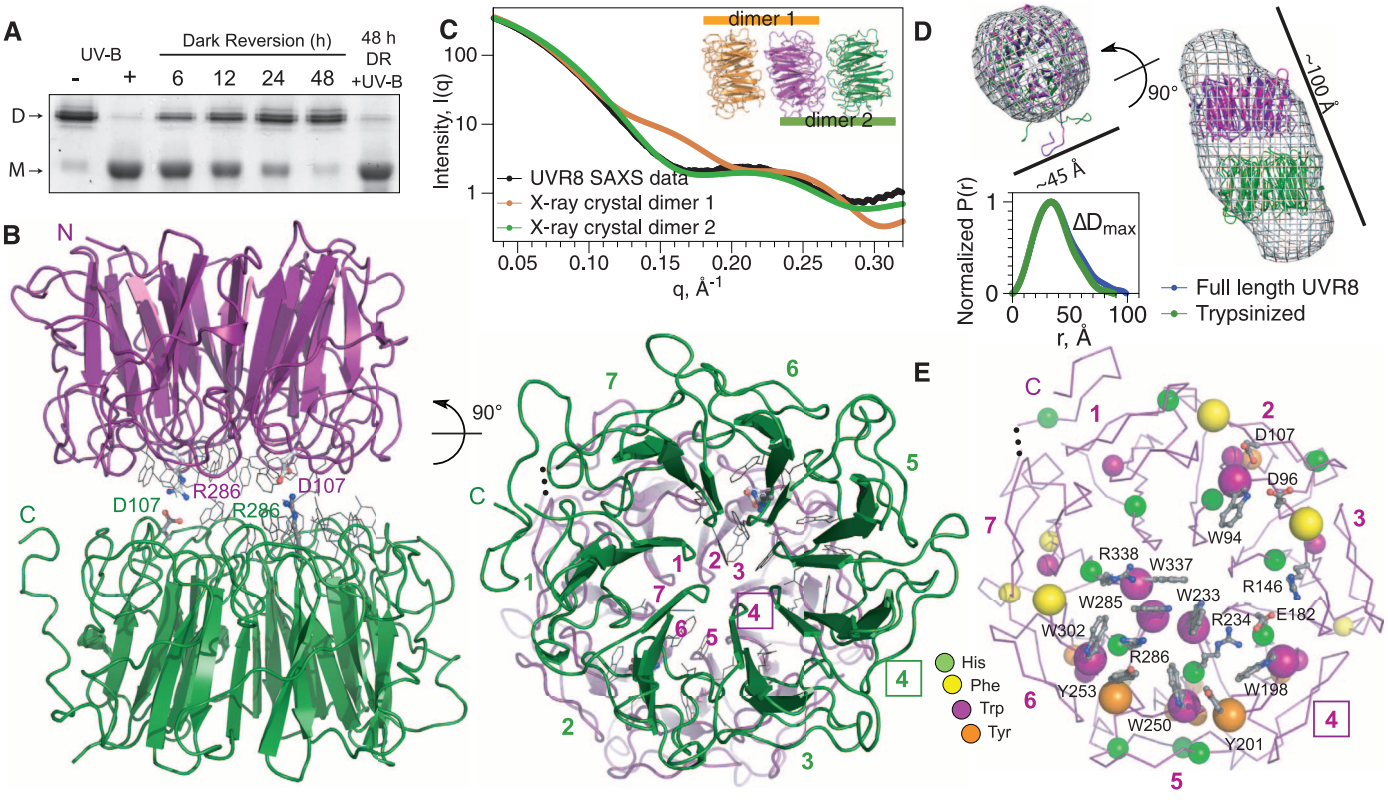

Fig. 1. Structure of *Arabidopsis* UVR8 dimer. (**A**) UV-B–induced dimer dissociation spontaneously reverses in the dark, regenerating photoactive dimers; analyzed by SDS-PAGE without sample boiling. (**B**) UVR8 forms a symmetric homodimer of seven-bladed β-propeller subunits (side and end views). Key salt bridges are shown as ball-and-stick. The end view is numbered to show blade pairing centered at blade 4 (box). (**C**) Experimental SAXS profile of UVR8 (crystallographic construct) compared with computed profiles for crystallographic dimers. (**D**) Crystallographic dimer docked into ab initio SAXS model of full-length UVR8 dimer (top) and pair-distance-distribution functions [*P*(*r*)] for full-length and trypsin-treated UVR8 (bottom), defining maximal diameter difference (ΔD_{max}). (**E**) Asymmetric localization of aromatic residues identifies center of photoreception. Key side chains (gray) are labeled.

cent Arg guanidinium moiety, but the side-chain orientation and packing differ among the three repeats (Fig. 3A). R234 and R338 are positioned as "book ends" flanking W285 and W233. Three more pairs of aromatic residues from blades 4, 5, and 6 (W198, Y201; W250, Y253; and W302, F305) create a perimeter fence of aromatic residues that isolates the Trp triad from solvent. At the center of the aromatic cluster, W285 and R286 are π-stacked between triad W337 and perimeter Y253 (Fig. 3A). W94 of the opposing monomer forms the apex of a Trp pyramid, with the Trp triad as the base (Fig. 3A and fig. S6). The close packing (less than 4.5 Å apart) of the Trp pyramid allows orbital overlap, permitting exciton coupling (*15*–*17*), which we assessed experimentally with far-UV circular dichroism spectroscopy (CD) (Fig. 3, B to G).

UV-B exposure of UVR8 strongly diminishes the large far-UV CD peak at 234 nm and trough at 221 nm that are characteristic (*15*) of exciton coupling between tryptophans (Fig. 3B). We mutated the pyramid Trps to investigate their contributions to exciton coupling and thus potentially to photoperception. The far-UV CD peak height is reduced in each of the single conservatively substituted W>F mutants (Fig. 3, D to F), most strongly in UVR8^{W233F} (Fig. 3D). Among four individual W>A side-chain truncation mutants (Fig. 3, C to F), UVR8^{W285A} revealed the greatest loss of exciton coupling, with its far-UV CD spectrum resembling those of triple-mutant UVR8$^{W233A/W285A/W337A}$ (Fig. 3G) and UV-B–treated wild type (Fig. 3B). UV-B has no effect on the altered CD signal of either the single UVR8^{W285A} (Fig. 3E) or the triple W>A (Fig. 3G) mutants, indicating a complete loss of photoreception. Similarly, UV-B has no effect on the CD signal of the UVR8^{W233F} and UVR8^{W285F} mutants, whereas it substantially reduces the CD signals of UVR8^{W337F} and UVR8^{W94A}, although to a lesser extent than in the wild-type protein (Fig. 3B and D to F). Consistent with these results, SEC analysis shows that UVR8^{W337F} and UVR8^{W94A} monomerize in response to UV-B, whereas UVR8^{W233F} and UVR8^{W285F} are constitutive dimers (table S3). Together, these observations indicate that the Trp pyramid is key to UVR8 photoperception, with W285 as the principal UV-B sensor. W233 is also important, not only in photoreception but particularly in maintaining exciton coupling, whereas W337 and W94 play auxiliary roles.

To examine the in vivo role of W285 in UV-B perception, we expressed green fluorescent protein (GFP)–UVR8^{W285A} in mutant *uvr8-1* plants and assayed UV-B induction of *HY5* transcripts, mediated by UVR8 (*1*). GFP-UVR8^{W285A} does not restore UV-B–mediated induction of *HY5* to *uvr8-1* mutants (Fig. 4A). However, loss of activity in the W285A mutant does not result from gross structural changes; SAXS analysis of UVR8^{W285A} confirmed that the dimer protein has dimensions similar to those of the wild type (Fig. 4B). Thus, these experiments show the in vivo functional importance of W285 in UV-B photoreception. Remarkably, although UVR8^{W285F} is unable to respond to UV-B, it does respond to UV-C, consistent with the shorter wavelength absorption of phenylalanine compared with tryptophan. Thus, UV-C exposure reduces the 234- and 221-nm CD features of UVR8^{W285F} (Fig. 4C) and initiates monomerization (Fig. 4D). Although UV-C is clearly less efficient in initiating photoreception in UVR8^{W285F} than UV-B in wild-type UVR8, these observations support the hypothesis that W285 has a key role in UVR8 photoreception. Furthermore, they demonstrate that the spectral sensing properties of the photoreceptor can be retuned by a single amino acid change, definitively establishing that UVR8 uses a tryptophan chromophore.

Salt-bridge mutations also influence exciton coupling as measured by far-UV CD. The constitutively monomeric, double salt-bridge mutants (table S3 and Fig. 2E) show a reduction in exciton coupling (Fig. 4E) consistent with the tight packing of arginine side chains with tryptophans within the aromatic cluster and the role of salt bridges in maintaining the cross-dimer Trp pyramid. The impact of these salt-bridge mutations on the exciton coupling is greater than that observed for the W94A (Fig. 3C) or W337A (Fig. 3F) mutants, which remove one tryptophan from the Trp pyramid. Indeed, the CD spectrum for UVR8$^{R146A/R286A}$ resembles that for UVR8^{W285A},

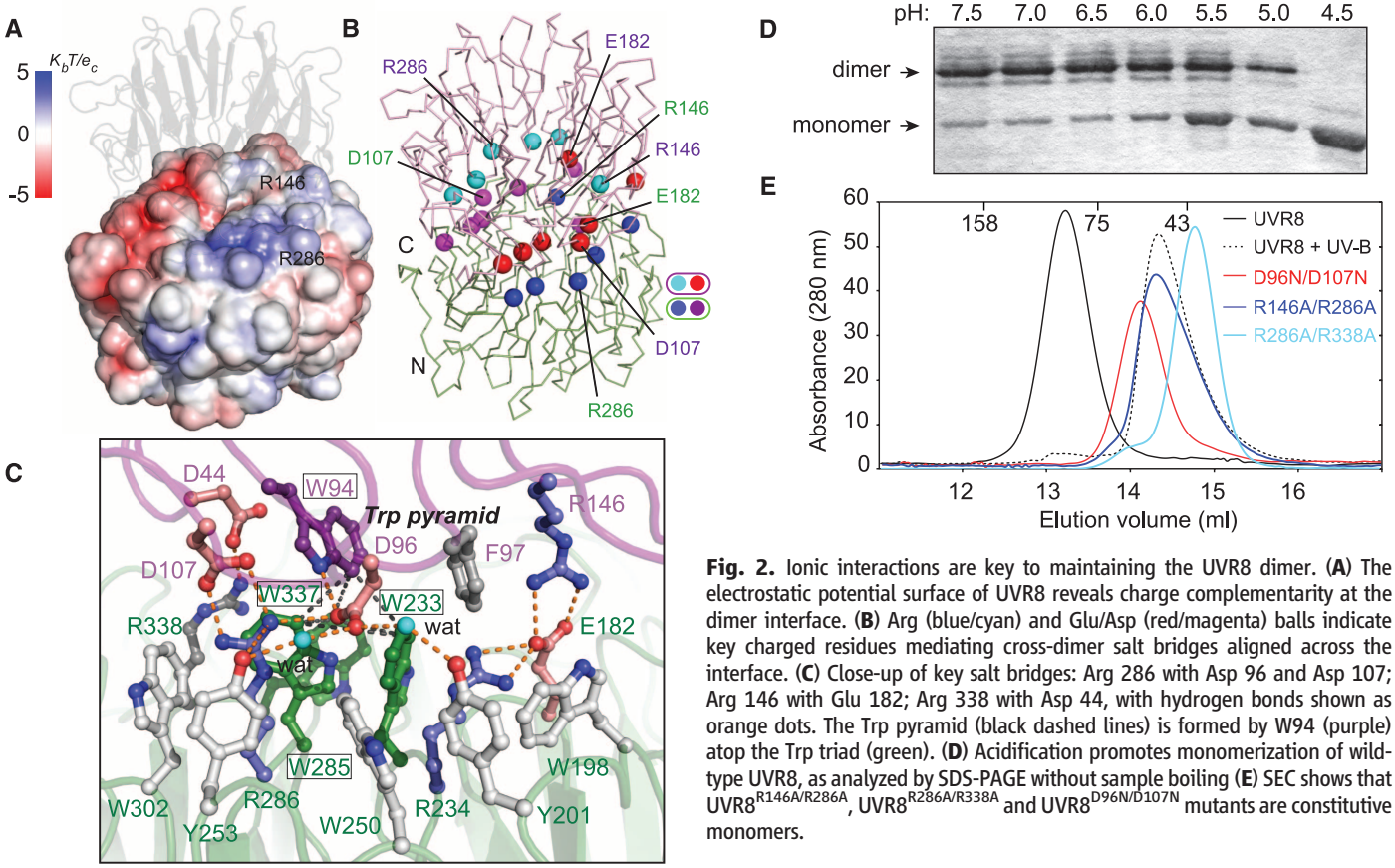

Fig. 2. Ionic interactions are key to maintaining the UVR8 dimer. (**A**) The electrostatic potential surface of UVR8 reveals charge complementarity at the dimer interface. (**B**) Arg (blue/cyan) and Glu/Asp (red/magenta) balls indicate key charged residues mediating cross-dimer salt bridges aligned across the interface. (**C**) Close-up of key salt bridges: Arg 286 with Asp 96 and Asp 107; Arg 146 with Glu 182; Arg 338 with Asp 44, with hydrogen bonds shown as orange dots. The Trp pyramid (black dashed lines) is formed by W94 (purple) atop the Trp triad (green). (**D**) Acidification promotes monomerization of wild-type UVR8, as analyzed by SDS-PAGE without sample boiling (**E**) SEC shows that UVR8$^{R146A/R286A}$, UVR8$^{R286A/R338A}$ and UVR8$^{D96N/D107N}$ mutants are constitutive monomers.

suggesting the importance of the π-stacking of these two residues in packing the Trp pyramid for exciton coupling.

Together, our findings indicate that UV-B photoreception by the excitonically coupled Trp pyramid leads to disruption of cross-dimer salt bridges, promoting UVR8 monomerization (Fig. 4F). Notably, the proximity and coupling of arginines and tryptophans suggest a specific mechanism whereby photoreception leads to monomerization. In particular, the key chromophore W285 stacks with adjacent R286, which has a crucial role in dimerization. This closely packed W285-R286 pair is therefore positioned to link UV-B photoreception and salt-bridge status (Fig. 2C). We propose that photoreception by the Trp pyramid, predominantly W285 and W233, results in the effective transfer of an

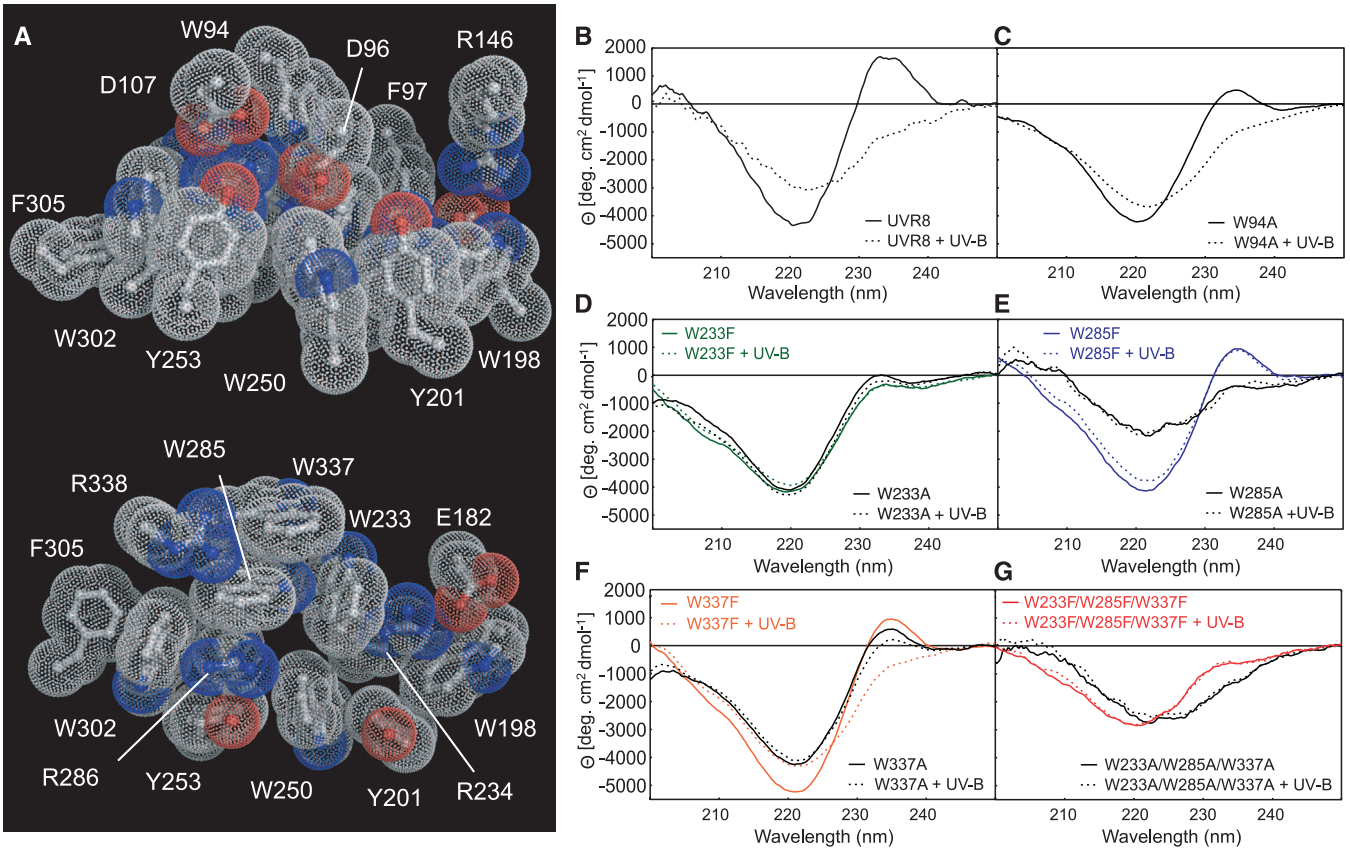

Fig. 3. Specific tryptophans mediate UV-B photoreception by UVR8. (**A**) Bulky aromatic residues tightly pack with key charged residues across the dimer (top) and within a monomer (bottom). (**B** to **G**) Far-UV CD spectrum change of UVR8 by UV-B. (B) Wild-type UVR8; (C) $UVR8^{W94A}$; (D) $UVR8^{W233F}$ and $UVR8^{W233A}$; (E) $UVR8^{W285F}$ and $UVR8^{W285A}$; (F) $UVR8^{W337F}$ and $UVR8^{W337A}$; (G) triple mutants $UVR8^{W233F/W285F/W337F}$ and $UVR8^{W233A/W285A/W337A}$.

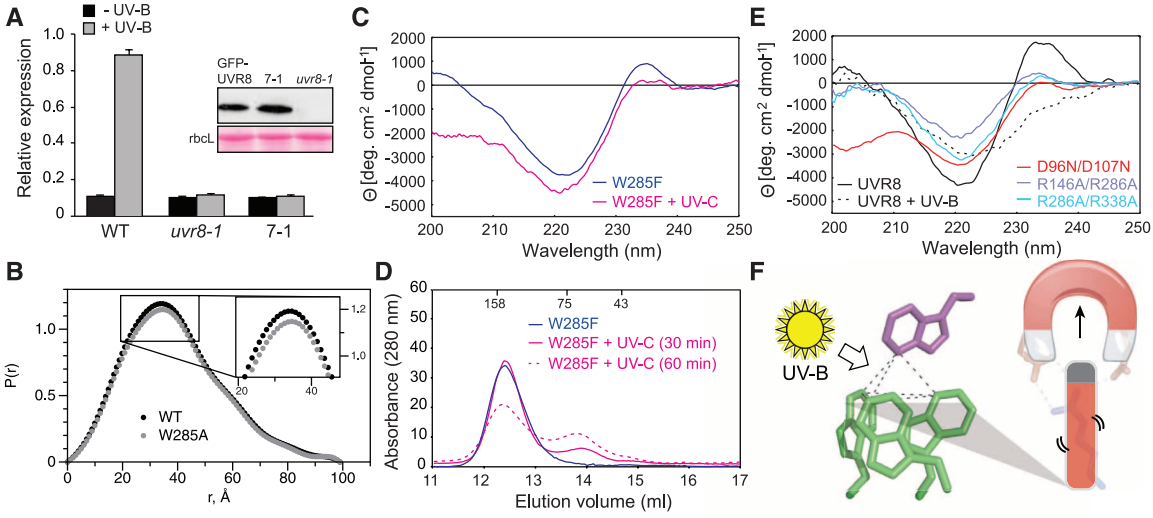

Fig. 4. Key features of UVR8 photoreceptor mechanism (**A**) Quantitative reverse transcription polymerase chain reaction analysis of UV-B induction of *HY5* transcripts in wild-type, *uvr8-1*, and *uvr8-1* expressing GFP-$UVR8^{W285A}$ (line 7-1). Inset shows Western blot of GFP-UVR8 in plant lines and Ponceau S staining of rbcL protein as loading control. (**B**) SAXS pair-distance-distribution functions [*P*(*r*)] show that $UVR8^{W285A}$ is dimeric, with only subtle conformational differences from wild type. (**C**) Far-UV CD spectra of $UVR8^{W285F}$ before and after exposure to 40 min UV-C. (**D**) SEC of $UVR8^{W285F}$ mutant protein exposed to UV-C (solid and dotted magenta lines). (**E**) Far-UV CD spectra of $UVR8^{R146A/R286A}$, $UVR8^{R286A/R338A}$, and $UVR8^{D96N/D107N}$ mutants. (**F**) Model for UV-B photoreception by UVR8. UV-B sensing (by Trp "pyramid") triggers dimer dissociation by disrupting salt bridges.

excited electron from the excitonically coupled Trp pyramid to adjacent arginine(s), leading to charge neutralization, consequent breakage of cross-dimer salt bridges, and thus dimer destabilization and dissociation (Fig. 4F). The complex packing assembly of the conserved aromatic cluster surrounding the Trp pyramid, and the interconnectivity of the conserved salt bridges that zip together the dimer interface, suggest that UVR8 has evolved a robust, concerted mechanism for UV-B perception and signaling.

In conclusion, we show that UVR8 is distinct from other known photoreceptors in exploiting the UV-B absorbance of its intrinsic tryptophans, rather than a bound chromophore. The presence of putative UVR8 orthologs in algae and mosses suggests that the photoreceptor may have evolved to promote plant survival when Earth's early atmosphere allowed high levels of UV-B exposure. β-propeller proteins interact with partners, often at the surface that UVR8 uses for dimerization (*18*, *19*). Hence, dimer dissociation is expected to facilitate interactions of UVR8 with proteins involved in downstream signaling or photoreceptor regulation.

References and Notes

1. B. A. Brown *et al.*, *Proc. Natl. Acad. Sci. U.S.A.* **102**, 18225 (2005).
2. B. A. Brown, G. I. Jenkins, *Plant Physiol.* **146**, 576 (2008).
3. J. J. Favory *et al.*, *EMBO J.* **28**, 591 (2009).
4. G. I. Jenkins, *Annu. Rev. Plant Biol.* **60**, 407 (2009).
5. D. J. Kliebenstein, J. E. Lim, L. G. Landry, R. L. Last, *Plant Physiol.* **130**, 234 (2002).
6. E. Kaiserli, G. I. Jenkins, *Plant Cell* **19**, 2662 (2007).
7. C. Cloix, G. I. Jenkins, *Mol Plant* **1**, 118 (2008).
8. A. Oravecz *et al.*, *Plant Cell* **18**, 1975 (2006).
9. L. Rizzini *et al.*, *Science* **332**, 103 (2011).
10. Materials and methods are available as supporting material on *Science* Online.
11. G. L. Hura *et al.*, *Nat. Methods* **6**, 606 (2009).
12. C. D. Putnam, M. Hammel, G. L. Hura, J. A. Tainer, *Q. Rev. Biophys.* **40**, 191 (2007).
13. N. Nishimura *et al.*, *Science* **326**, 1373 (2009).
14. E. Krissinel, K. Henrick, *J. Mol. Biol.* **372**, 774 (2007).
15. I. B. Grishina, R. W. Woody, *Faraday Discuss.* **99**, 245 (1994).
16. E. Ohmae, Y. Sasaki, K. Gekko, *J. Biochem.* **130**, 439 (2001).
17. D. Andersson, U. Carlsson, P. O. Freskgård, *Eur. J. Biochem.* **268**, 1118 (2001).
18. C. Xu, J. Min, *Protein Cell* **2**, 202 (2011).
19. C. U. Stirnimann, E. Petsalaki, R. B. Russell, C. W. Müller, *Trends Biochem. Sci.* **35**, 565 (2010).

Acknowledgments: We thank C. Cloix, E. Kaiserli, N. Fraser, C. Hitomi, R. Rambo, J. Holton, J. A. Tainer, and the Structurally Integrated BiologY for Life Sciences (SIBYLS) beamline staff for discussions and assistance. This research was supported by National Institutes of Health grant GM37684 (E.D.G.); The Skaggs Institute for Chemical Biology (K.H., A.J.P.); National Science Foundation Predoctoral Fellowship (A.J.P.); Royal Society University Research Fellowship (J.M.C.); Leverhulme Trust grant F/00179/AZ (G.I.J., J.M.C., B.O.S.); and UK Biotechnology and Biological Sciences Research Council Ph.D. studentship (A.O.). J.M.C., E.D.G., K.H., and G.I.J. designed the research; A.S.A., K.B., J.M.C., K.H., M.H., S.M.K, A.O., and A.J.P. performed the research; M. Hothorn provided reagents; A.S.A., K.B., J.M.C., E.D.G., K.H., M.H., G.I.J., S.M.K., A.O., A.J.P. and B.O.S. analyzed data; and J.M.C., E.D.G., K.H., G.I.J., and A.J.P. prepared the manuscript. Crystallography and SAXS data were collected at SIBYLS through the Integrated Diffraction Analysis Technologies program supported by the Department of Energy, Office of Biological and Environmental Research. Crystallographic coordinates and structure factors are deposited in the Protein Data Bank with accession code 4D9S.

Supporting Online Material

www.sciencemag.org/cgi/content/full/science.1218091/DC1
Materials and Methods
Figs. S1 to S8
Tables S1 to S3
References (*20*–*38*)

19 December 2011; accepted 30 January 2012
Published online 9 February 2012;
10.1126/science.1218091

MARF1 Regulates Essential Oogenic Processes in Mice

You-Qiang Su,[1] Koji Sugiura,[1]* Fengyun Sun,[1] Janice K. Pendola,[1] Gregory A. Cox,[1] Mary Ann Handel,[1] John C. Schimenti,[2] John J. Eppig[1]†

Development of fertilization-competent oocytes depends on integrated processes controlling meiosis, cytoplasmic development, and maintenance of genomic integrity. We show that meiosis arrest female 1 (MARF1) is required for these processes in mammalian oocytes. Mutations of *Marf1* cause female infertility characterized by up-regulation of a cohort of transcripts, increased retrotransposon expression, defective cytoplasmic maturation, and meiotic arrest. Up-regulation of protein phosphatase 2 catalytic subunit (PPP2CB) is key to the meiotic arrest phenotype. Moreover, *Iap* and *Line1* retrotransposon messenger RNAs are also up-regulated, and, concomitantly, DNA double-strand breaks are elevated in mutant oocytes. Therefore MARF1, by suppressing levels of specific transcripts, is an essential regulator of important oogenic processes leading to female fertility and the development of healthy offspring.

Oogenic processes essential for producing a "good" egg competent to support production of healthy offspring include accurate completion of meiosis (*1*), cytoplasmic maturational events that provide competence for fertilization and embryogenesis (*1*, *2*), and maintenance of genomic integrity by protection against disruptive factors such as retrotransposon activation (*3*). Precise control of these processes is critical for successful reproduction. Abnormalities in any of these events can lead to infertility, miscarriage, and/or birth defects and endanger future generations. We report here the identification of a regulator in mouse oocytes that is required for all of these oogenic processes and acts by suppressing levels of specific transcripts.

By using *N*-ethyl-*N*-nitrosourea (ENU) mutagenesis, we generated a line of mutant mice with a female-only autosomal recessive infertility phenotype (fig. S1) characterized initially by oocyte meiotic arrest; the mutation was designated ENU375-18. Ovaries of the mutant mice appeared normal (fig. S2, A to C), but oocytes did not resume meiosis even after a superovulatory regimen of gonadotropins and were ovulated at the immature germinal vesicle (GV) stage (Fig. 1A and fig. S2D). In contrast, both wild-type (WT) and heterozygous (HET) oocytes were ovulated at mature metaphase II (MII) stage (Fig. 1A and fig. S2D). Therefore, the hallmark of infertility in mutant females is oocyte meiotic arrest at the GV stage.

Positional cloning of the mutated gene revealed a G→T transition at the 5′-splice donor site of the 16th intron of the *4921513D23Rik* gene (fig. S3, A to C). This mutation causes the skipping of exon 16 during pre-mRNA splicing (fig. S3, B and D), resulting in expression of negligible levels of exon 16 mRNA in mutant fully grown oocytes (FGOs) (Fig. 1 B) and a frameshift in the coding sequence with creation of a premature stop codon (fig. S3, B and E). The 4921513D23RIK protein was not detected in mutant FGOs by an antibody targeting its C terminus (Fig. 1C). Only a trace amount of 5′-*4921513D23Rik* mRNA was detected in mutant FGOs by quantitative reverse transcription polymerase chain reaction (qRT-PCR) (Fig. 1B). This may be caused by nonsense-mediated decay of the truncated *4921513D23Rik* mRNA, suggesting that $4921513D23Rik^{ENU375\text{-}18}$ is unlikely to be a neomorph but rather an extreme hypomorph.

To verify that mutation of *4921513D23Rik* is responsible for the ENU-induced phenotype, we produced mice carrying a gene-trapped allele of $4921513D23Rik^{Gt(AS0671)Wtsi}$ (fig. S4, A to B) and mice with heteroallelic combination of $4921513D23Rik^{Gt(AS0671)Wtsi}$ and $4921513D23Rik^{ENU375\text{-}18}$ ($4921513D23Rik^{Gt(AS0671)Wtsi/ENU375\text{-}18}$). No 4921513D23RIK protein was detected in FGOs of $4921513D23Rik^{Gt(AS0671)Wtsi/Gt(AS0671)Wtsi}$ or $4921513D23Rik^{Gt(AS0671)Wtsi/ENU375\text{-}18}$ mice (Fig. 1C), and both types of mice phenocopied $4921513D23Rik^{ENU375\text{-}18/ENU375\text{-}18}$ (fig. S4, C to F). This noncomplementation of the two alleles indicates that the $4921513D23Rik^{ENU375\text{-}18}$ allele contains the causative mutation underlying the ENU-induced infertile phenotype. Hereafter, the *4921513D23Rik* gene will be referred to as *meiosis arrest female 1* (*Marf1*),

[1]The Jackson Laboratory, Bar Harbor, ME 04609, USA. [2]College of Veterinary Medicine, Cornell University, Ithaca, NY 14853, USA.

*Present address: Laboratory of Applied Genetics, Graduate School of Agricultural and Life Sciences, University of Tokyo, Tokyo, Japan.

†To whom correspondence should be addressed. E-mail: John.Eppig@jax.org

the *Marf1*$^{ENU375\text{-}18}$ allele as *Marf1*^{ENU}, and the gene-trapped allele as *Marf1*^{GT}.

Marf1 contains 27 exons that encode a 7765–base pair (bp) mRNA and 1736–amino acid (aa) peptide (fig. S5A). There is 86% amino acid identity between mouse and human MARF1. cDNA cloning and sequencing revealed that mouse oocytes express a unique variant of *Marf1* different from the isoform expressed in cumulus cells. This oocyte-specific variant lacks 537-bp nucleotides at the 3′ end of exon 3 (fig. S5B). By sequence analysis, MARF1 has three major domains: an N-terminal LK-Nuc domain belonging to the 5′→3′ nuclease domain superfamily of proteins having ribonuclease (RNase) activity, two RRM domains, and a C-terminal tandem repeat of LOTUS or OST-HTH novel domains also present in *Drosophila* Oskar and mammalian tudor domain–containing proteins (TDRD) 5 and 7 (*4*, *5*) (fig. S5C).

Marf1 mRNA is highly expressed in oocytes relative to other cell types (fig. S6A). There is ~60-fold higher expression of *Marf1* mRNA detected in oocytes than in granulosa cells (Fig. 2, A and B). MARF1 protein is also expressed predominantly by oocytes and barely detectable in granulosa cells (Fig. 2B). This was further confirmed by a β-galactosidase (GAL) reporter assay in *Marf1*$^{GT/GT}$ ovaries, with positive β-GAL staining in oocytes of follicles at all developmental stages but not in other ovarian cell types (Fig. 2C and fig. S6B). Moreover, the mutant meiotic arrest defect is oocyte-autonomous. *Marf1*$^{ENU/ENU}$ oocytes, when developed in vivo within reaggregated chimeric follicles composed of *Marf1*$^{ENU/+}$ somatic cells and *Marf1*$^{ENU/ENU}$ oocytes, displayed the meiotic arrest phenotype, whereas *Marf1*$^{ENU/+}$ oocytes acquired meiotic resumption competency when grown in reaggregated ovarian follicles composed of *Marf1*$^{ENU/ENU}$ somatic cells and *Marf1*$^{ENU/+}$ oocytes (table S1).

High levels of cyclic adenosine monophosphate (cAMP), produced in normal FGOs, maintain meiotic arrest (see fig. S7 for diagram illustrating meiotic control in FGOs). However, alleviation of cAMP inhibition, through pharmacological (fig. S8A) or genetic approaches (fig. S8, B and C), did not reverse meiotic arrest in *Marf1*$^{ENU/ENU}$ oocytes. Therefore, loss of MARF1 function affects processes downstream of relief from cAMP inhibition. No activation of oocyte maturation-promoting factor (MPF) was detected in *Marf1*$^{ENU/ENU}$ oocytes after administration of human chorionic gonadotropin (hCG) (fig. S9A), nor was there reduction of expression of key cell cycle regulators that activate MPF—*Cdk1*; *Ccnb1*; and *Cdc25a*, *b*, and *c*—in *Marf1*$^{ENU/ENU}$ FGOs (fig. S9B). However, microinjection of

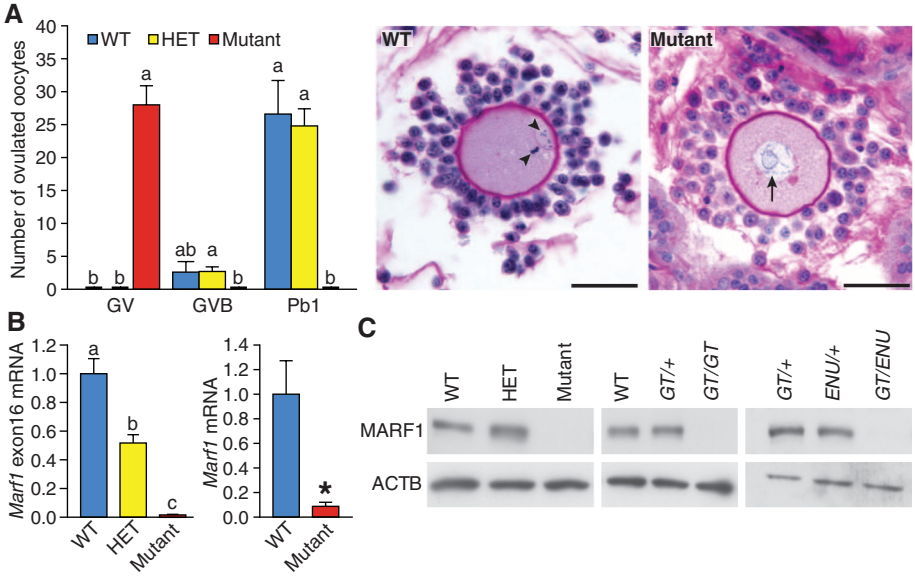

Fig. 1. Meiotic arrest and loss of *Marf1* expression in *Marf1* mutant oocytes. (**A**) Number of oocytes (graph) and histology of cumulus-oocyte complexes (photographs) ovulated in oviducts by WT, HET, and mutant *Marf1*^{ENU} females 14 hours after hCG injection. Pb1 indicates first polar body; scale bars, 50 μm; arrowheads, MII spindle and Pb1; Arrow, GV. (**B**) qRT-PCR of *Marf1* exon 16 (left) and 5′- (right) mRNA expression in WT, HET, and mutant *Marf1*^{ENU} FGOs. In this and subsequent figures, graphs show mean ± SEM. *$P < 0.05$ compared with WTs. Bars indicated with different letters (a, b, c) are significantly different, $P < 0.05$. (**C**) Western blot of MARF1 and beta actin (ACTB) protein in WT, HET, and mutant *Marf1*^{ENU} FGOs (left); WT, HET (*GT*/+), and mutant *Marf1*^{GT} (*GT/GT*) (middle); and *Marf1*$^{GT/+}$ (*GT*/+), *Marf1*$^{ENU/+}$ (*ENU*/+), and *Marf1*$^{GT/ENU}$ (*GT/ENU*) (right).

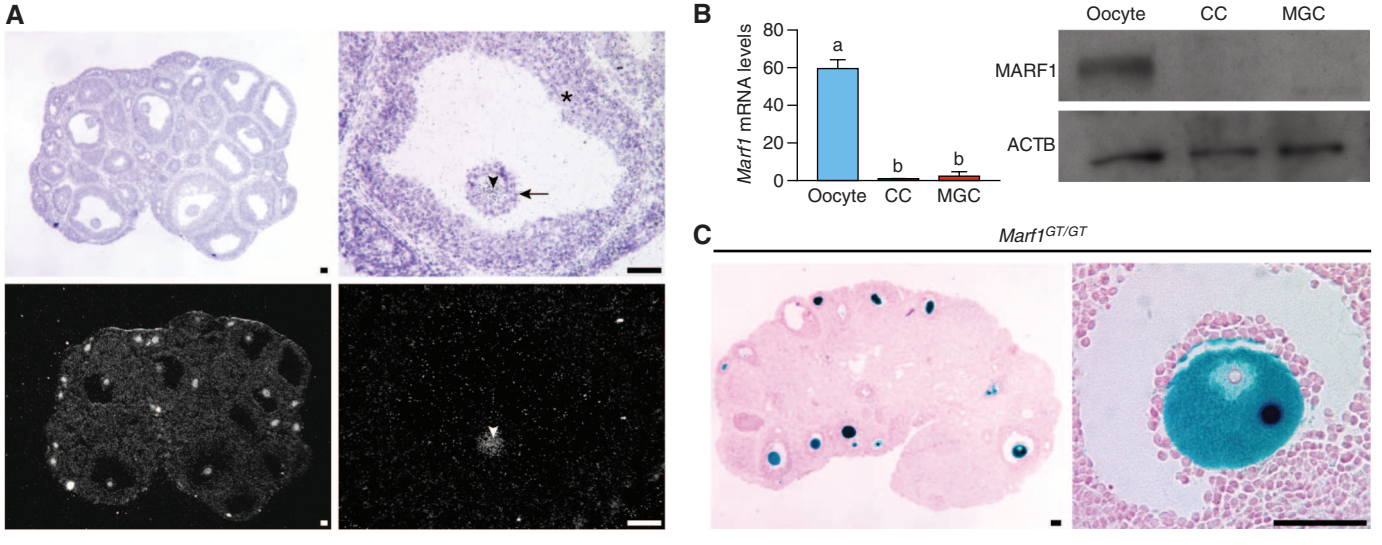

Fig. 2. Expression of *Marf1* by mouse oocytes. (**A**) In situ hybridization of *Marf1* mRNA in ovaries of 22-day-old B6SJLF1 mice 46 hours after equine CG (eCG) injection. Bright and dark field images are at the top and bottom, respectively. Arrowheads, oocytes; arrow, cumulus; and asterisks, mural granulosa cells (MGC). (**B**) qRT-PCR (left) and Western blot (right) analyses of *Marf1* mRNA and protein levels in oocytes, cumulus cells (CC), and MGC of eCG-primed F1 mice. (**C**) X-gal staining of *Marf1*$^{GT/GT}$ ovaries from eCG (46 hours)-primed 22-day-old mice. Scale bars, 50 μm.

mRNA encoding an active form of CDC25B into *Marf1*$^{ENU/ENU}$ FGOs reversed the meiotic arrest, with ~56% of injected oocytes resuming meiosis and activated MPF (Fig. 3C), of which ~42% progressed to MII with normal appearing spindles (Fig. 3, A and B, and fig. S9C). Therefore, defects in oocytes caused by *Marf1* mutation lie upstream of MPF activation.

To further determine the mechanisms of meiotic arrest in *Marf1* mutant oocytes, we examined the *Marf1*$^{ENU/ENU}$ oocyte transcriptome by using microarray analysis. A cohort of transcripts was markedly elevated in *Marf1*$^{ENU/ENU}$ FGOs, with 377 transcripts expressed ≥4-fold higher than in WT oocytes and only 27 transcripts down-regulated to the same extent (Fig. 3D and tables S3 and S4). This increased transcript expression and/or stability is consistent with proposed RNase activity of MARF1. Posttranscriptional control is also indicated by a lack of difference in the levels of unprocessed heterogeneous nuclear RNA (hnRNA) in mutant oocytes, despite dramatic increases in mRNAs (Fig. 3E).

We did not detect elevated levels of *Wee2* mRNA (fig. S9D); however, we found a profound, ~34-fold, up-regulation of *Ppp2cb* mRNA encoding the beta-isoform catalytic subunit of PPP2 [also known as protein phosphatase 2A (PP2A)] in *Marf1*$^{ENU/ENU}$ oocytes (Fig. 4A), and PPP2C protein was up-regulated ~50% in *Marf1* mutant oocytes (fig. S9E). Brief treatment of *Marf1* mutant oocytes with 2.5 μM okadaic acid (OA), an inhibitor of PPP2, was sufficient to reverse meiotic arrest in the majority (~70%) of *Marf1* mutant oocytes (Fig. 4B) and induce MPF activation (Fig. 3C). Moreover, microinjection of *Marf1*$^{ENU/ENU}$ oocytes with *Ppp2cb* small interfering RNA (siRNA) knocked down *Ppp2cb* mRNA by ~77% (fig. S9F) and induced about 46% GV breakdown (GVB) (Fig. 4C). Microinjection with *Ppp2cb* morpholinos also induced GVB in ~43% of mutant oocytes (Fig. 4D). Therefore, up-regulation of *Ppp2cb* is a key to meiotic arrest in *Marf1* mutant oocytes, although other factors are not excluded. Indeed, microarray analysis also revealed elevation of other transcripts in mutant oocytes that could be related to the meiotic arrest phenotype. For example, gene ontology (GO) analysis (http://proto.informatics.jax.org/prototypes/vlad-1.5/) indicates that ADNP, ADORA2B, and IMPDH2 participate in cyclic nucleotide production; HORMAD1 and MLH3 are meiotic proteins involved in synaptonemal complex assembly and recombination; CCNE1, CDK9, CDK19, CDKN2B, CSPP1, HEXIM1, ID2,

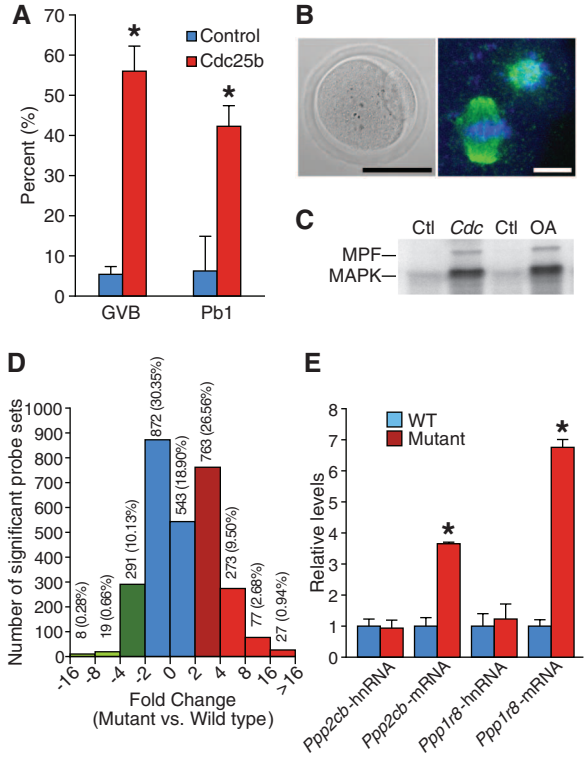

Fig. 3. Meiotic reversal by CDC25B and alteration of transcriptomes in *Marf1*$^{ENU/ENU}$ oocytes. (**A**) Effect of microinjection of *Cdc25b* mRNA (Cdc25b) on meiotic progression (GVB and Pb1 emission) in *Marf1*$^{ENU/ENU}$ oocytes. (**B**) *Marf1*$^{ENU/ENU}$ oocytes matured after *Cdc25b* injection. (Left) Differential image contrast (DIC) image. Scale bar, 50 μm. (Right) Chromosomes (blue) and spindles (green) staining. Scale bar, 10 μm. (**C**) MPF and mitogen-activated protein kinase (MAPK) activity in *Marf1*$^{ENU/ENU}$ oocytes with or without *Cdc25b* mRNA microinjection (*Cdc* and Ctl group, respectively) or treated with or without 2.5 μM OA (Ctl and OA group, respectively). (**D**) Distribution of significantly changed transcripts [represented by Affymetrix (Affymetrix, Incorporated, Santa Clara, CA) probe sets] at various magnitudes of difference in expression levels between *Marf1*$^{ENU/ENU}$ (Mutant) and WT FGOs detected by microarray analysis. The number and the percentage of each group of transcripts in total changed transcripts are indicated above each bar. (**E**) Levels of hnRNA and mRNAs measured by qRT-PCR in WT and *Marf1*$^{ENU/ENU}$ growing oocytes.

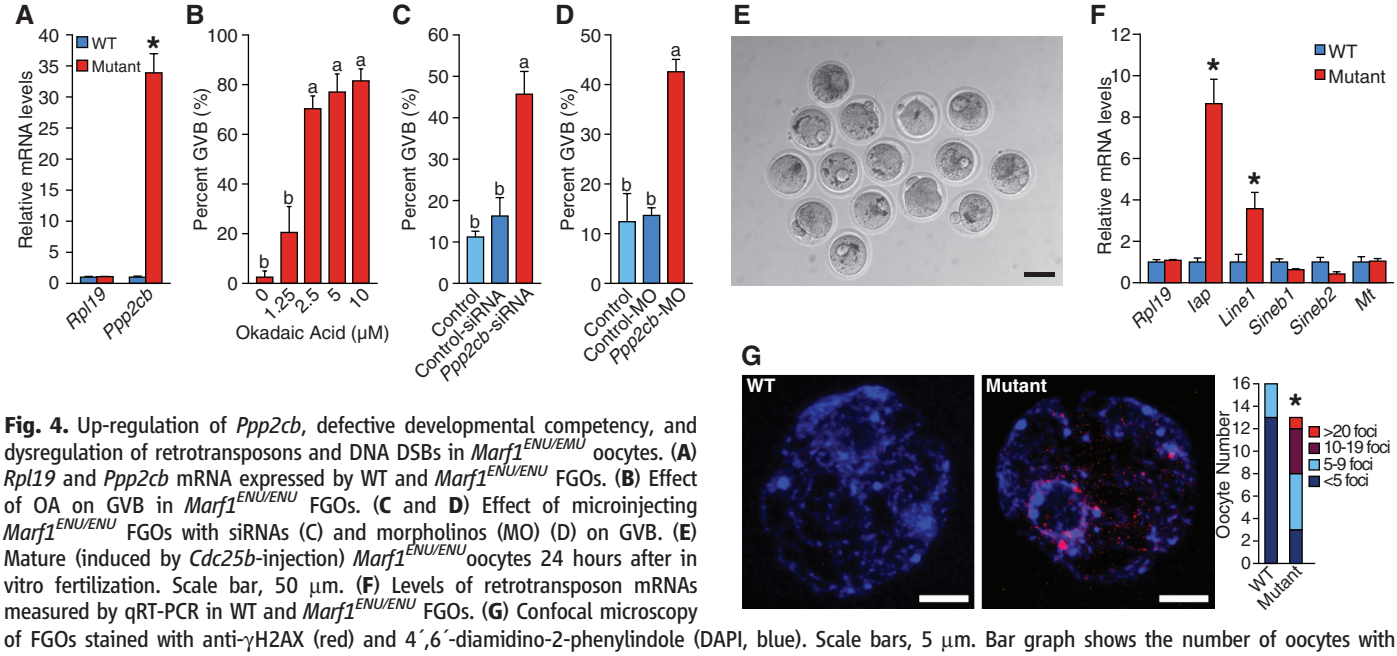

Fig. 4. Up-regulation of *Ppp2cb*, defective developmental competency, and dysregulation of retrotransposons and DNA DSBs in *Marf1*$^{ENU/EMU}$ oocytes. (**A**) *Rpl19* and *Ppp2cb* mRNA expressed by WT and *Marf1*$^{ENU/ENU}$ FGOs. (**B**) Effect of OA on GVB in *Marf1*$^{ENU/ENU}$ FGOs. (**C** and **D**) Effect of microinjecting *Marf1*$^{ENU/ENU}$ FGOs with siRNAs (C) and morpholinos (MO) (D) on GVB. (**E**) Mature (induced by *Cdc25b*-injection) *Marf1*$^{ENU/ENU}$ oocytes 24 hours after in vitro fertilization. Scale bar, 50 μm. (**F**) Levels of retrotransposon mRNAs measured by qRT-PCR in WT and *Marf1*$^{ENU/ENU}$ FGOs. (**G**) Confocal microscopy of FGOs stained with anti-γH2AX (red) and 4′,6′-diamidino-2-phenylindole (DAPI, blue). Scale bars, 5 μm. Bar graph shows the number of oocytes with various numbers of foci in the nucleus.

ID3, PSMG2, and RAD9 participate in regulation of cell cycle processes; and CDK9, OBFC2A, UBE2V2, and YY1 are involved in DNA repair. Moreover, among elevated transcripts there is a high representation of those encoding proteins that participate in regulation of cellular metabolism and gene expression (table S5). It is not known whether all of these transcripts are direct targets of regulation by MARF1 or whether some mRNA levels are abnormally high as a consequence of disruption of oogenic processes.

Consistent with the up-regulation of a cohort of transcripts potentially affecting oocyte development, after in vitro insemination there was no cleavage or embryonic development of the *Marf1* mutant oocytes induced to mature to metaphase II by microinjection with mRNA encoding an active form of CDC25B (Fig. 4E and fig. S10A). Therefore, defects in *Marf1* mutant oocytes are not restricted to those that directly influence meiotic progression; they include those crucial for acquisition of competence to undergo fertilization and embryogenesis.

Steady-state levels of transcripts for intracisternal A particles (*Iap*) and long interspersed repetitive element (*Line*) 1 (but not other retrotransposons analyzed) were also significantly higher in $Marf1^{ENU/ENU}$ mutant oocytes than in WT (Fig. 4F). Retrotransposons exert deleterious effects on genomic integrity, in part because their dysregulated insertion into the genome produces DNA double-strand breaks (DSBs) (*6*). Excess DSBs can affect meiotic progression in oocytes (*7*), and up-regulation of retrotransposons is associated with increased nuclear DSBs and meiotic arrest in mouse spermatocytes (*8*, *9*). Therefore, the effect of *Marf1* mutations on nuclear DSBs was examined by using γ histone 2AX (also known as H2AFX) immunolabeling. The numbers of DSBs in both $Marf1^{ENU/ENU}$ and $Marf1^{GT/GT}$ mutant FGOs were significantly elevated compared with those of WT controls (Fig. 4G and fig. S10B). Increased DSBs may contribute to the meiotic arrest phenotype of *Marf1* mutant oocytes, as does overexpression of PPP2CB. In somatic cells, DSBs trigger G_2/M checkpoints that inhibit entry of cells into mitosis. This checkpoint activation requires PPP2 and results in inhibition of CDC25 and subsequently CDK1 (*10*). It is unknown whether a similar mechanism regulates meiotic progression in mammalian oocytes, because oocytes from mice carrying mutations that affect DSB repair usually die before follicular development (*11*). Although it is not clear whether the increase in nuclear DSBs directly affects meiosis or activates a checkpoint control mechanism, MARF1 is shown to be involved in establishing both retrotransposon mRNA levels and competence to resume meiosis in mammalian oocytes.

Together, these observations reveal a pivotal role for MARF1 in regulating oogenic processes essential for meiotic progression, genomic integrity, acquisition of developmental competence, and female fertility. The phenotype of meiotic arrest was a window through which other functions of this unique regulator were identified, and the mutant phenotypes are likely linked through up-regulation of mRNAs. Aberrant mRNA expression levels can be due to transcriptional or posttranscriptional control. Although MARF1 does not possess domains typical of transcription factors, it contains a predicted RNase domain. The fact that hnRNA primary transcript levels are not affected in *Marf1* mutants, whereas their respective mRNAs are elevated provides support for misregulation of transcript processing and/or stability, suggesting involvement of MARF1 in RNA homeostasis. Indeed, posttranscriptional control of RNA levels is emerging as a regulatory mechanism of considerable importance in germ cell development (*12*), and its involvement in oocyte meiotic progression has been demonstrated by analyses of oocyte-specific conditional knockouts of *Dicer1* (*13*, *14*). Through its direct and indirect effects, MARF1 is pivotal in establishing the network of pathways essential for the development of a "good" egg.

References and Notes

1. J. J. Eppig, *Reprod. Fertil. Dev.* **8**, 485 (1996).
2. J. E. Swain, T. B. Pool, *Hum. Reprod. Update* **14**, 431 (2008).
3. N. Zamudio, D. Bourc'his, *Heredity* **105**, 92 (2010).
4. V. Anantharaman, D. Zhang, L. Aravind, *Biol. Direct* **5**, 13 (2010).
5. I. Callebaut, J. P. Mornon, *Bioinformatics* **26**, 1140 (2010).
6. D. J. Hedges, P. L. Deininger, *Mutat. Res.* **616**, 46 (2007).
7. C. Tatone *et al.*, *Hum. Reprod.* **26**, 1843 (2011).
8. S. F. Soper *et al.*, *Dev. Cell* **15**, 285 (2008).
9. L. Ma *et al.*, *PLoS Genet.* **5**, e1000635 (2009).
10. Y. Yan *et al.*, *Oncogene* **29**, 4317 (2010).
11. M. Di Giacomo *et al.*, *Proc. Natl. Acad. Sci. U.S.A.* **102**, 737 (2005).
12. E. Voronina, G. Seydoux, P. Sassone-Corsi, I. Nagamori, *Cold Spring Harb. Perspect. Biol.* **3**, a002774 (2011).
13. E. P. Murchison *et al.*, *Genes Dev.* **21**, 682 (2007).
14. O. H. Tam *et al.*, *Nature* **453**, 534 (2008).

Acknowledgments: We thank M. Conti for providing the *Cdc25b* plasmid and $Gpr3^{-/-}$ mice and K. Wigglesworth and M. O'Brien for technical assistance. Supported by NIH grant HD42137 (Y.-Q.S., K.S., F.S., J.K.P., M.A.H., J.C.S., and J.J.E.) and Scientific Services by grant CA34196 from the National Cancer Institute. Microarray data are deposited in the Gene Expression Omnibus (www.ncbi.nlm.nih.gov/geo, data set GSE 31985).

Supporting Online Material

www.sciencemag.org/cgi/content/full/335/6075/1496/DC1
Materials and Methods
Figs. S1 to S10
Tables S1 to S5
References (*15*–*29*)

30 September 2011; accepted 17 February 2012
10.1126/science.1214680

Trim28 Is Required for Epigenetic Stability During Mouse Oocyte to Embryo Transition

Daniel M. Messerschmidt,[1]† Wilhelmine de Vries,[2] Mitsuteru Ito,[3] Davor Solter,[1,4] Anne Ferguson-Smith,[3,5]* Barbara B. Knowles[1,6]

Phenotypic variability in genetic disease is usually attributed to genetic background variation or environmental influence. Here, we show that deletion of a single gene, *Trim28* (*Kap1* or *Tif1β*), from the maternal germ line alone, on an otherwise identical genetic background, results in severe phenotypic and epigenetic variability that leads to embryonic lethality. We identify early and minute epigenetic variations in blastomeres of the preimplantation embryo of these animals, suggesting that the embryonic lethality may result from the misregulation of genomic imprinting in mice lacking maternal *Trim28*. Our results reveal the long-range effects of a maternal gene deletion on epigenetic memory and illustrate the delicate equilibrium of maternal and zygotic factors during nuclear reprogramming.

Imprinting, the process resulting in gene expression specific to the parent of origin, is based on differential epigenetic modifications on chromosomes inherited from the father and mother. Imprinted gene loci are marked by differentially methylated regions (DMRs), disruptions of which can cause human defects or cancer (*1*). For instance, aberrant expression from the *Igf2/H19* cluster is involved in multiple cancers, the dwarfism Silver-Russell syndrome and the overgrowth Beckwith-Weidemann syndrome (*2*–*5*).

Protection of the inherited, germ line–derived methylation at imprinted loci is vital, especially during the oocyte-to-embryo transition (OET) when egg- and sperm-derived genomes undergo extensive epigenetic reprogramming to a totipotent state. Demethylation of the paternal genome is a key event during OET (*6*); however, it is

[1]Mammalian Development Group, Institute of Medical Biology, 138648 Singapore. [2]The Jackson Laboratory, 600 Main Street, Bar Harbor, ME 04609, USA. [3]Department of Physiology, Development and Neuroscience, University of Cambridge, Cambridge CB2 3EG, UK. [4]Duke-NUS, Graduate Medical School, 169857 Singapore. [5]Singapore Institute for Clinical Sciences, 117609 Singapore. [6]Department of Biochemistry, National University of Singapore, 117597 Singapore.

*No longer at Singapore Institute for Clinical Sciences.
†To whom correspondence should be addressed. E-mail: daniel.m@imb.a-star.edu.sg

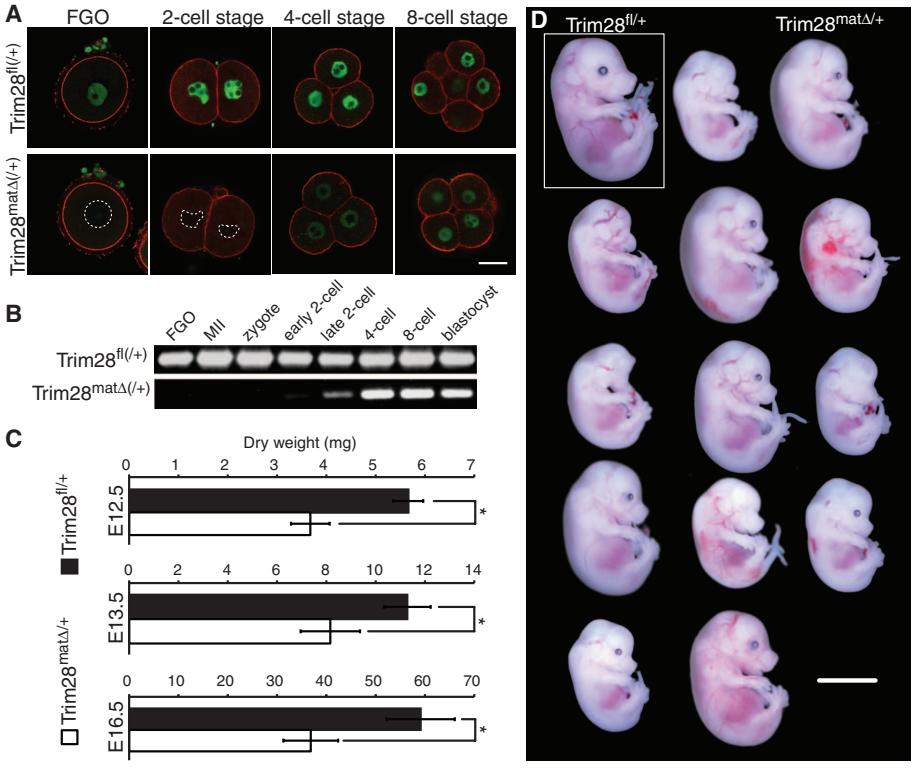

Fig. 1. Expression and maternal deletion of *Trim28*. (**A**) Immunofluorescence using antibody against TRIM28 (green) and phalloidin (red). Fully grown oocytes, two-cell–, four-cell–, and eight-cell–stage control and maternal mutant embryos are shown. Scale bar, 50 μm. (**B**) QPCR performed on control and maternal mutant oocytes and different preimplantation stage embryos (FGO, fully-grown oocyte; MII, metaphase II oocyte). (**C**) Quantification of growth restriction in maternal *Trim28* mutants compared with controls by measuring dry weight (mg) (Student's *t* test; $*P < 0.05$). (**D**) Mutant E15.5 embryos displaying large array of phenotypes and growth defects compared with a control embryo. Scale bar, 5 mm.

incomplete, as germline imprints and some other sequences retain their methylation state, which ensures inheritance from germ line to soma (*7*, *8*). Proteins such as PGC7 are known to protect the maternal genome from active demethylation during OET and to prevent DMR demethylation at several imprinted regions (*9*). Maternal-zygotic deletion of the Krüppel-associated box domain (KRAB)–zinc finger protein ZFP57 also results in loss of methylation at multiple imprinted loci, yet maternal deletion alone creates no phenotype in embryos, owing to paternal gene rescue (*10*).

A cohort of KRAB–zinc finger proteins mediate the interaction of TRIM28 (KAP1 or TIF1β), the central component of an epigenetic modifier complex, with specific genomic loci. TRIM28, in turn, recruits chromatin-modification and remodeling factors that are associated with the formation of repressive chromatin (*11*). We show that loss of maternal *Trim28* alone results in a highly pleiotropic, 100% lethal phenotype and demonstrate its requirement for maintaining genomic imprints and supporting a proper epigenetic environment during the OET.

Trim28 is highly expressed in oocytes and early embryos (Fig. 1, A and B). To address its maternal function, we used a Zp3-Cre mating scheme (fig. S1) to delete *Trim28* from oocytes, which were then fertilized by wild-type males. Embryos derived from this mating lack both *Trim28* RNA and protein until transcription from the paternal allele ensues after zygotic gene activation (ZGA) at the early two-cell stage. TRIM28 protein becomes detectable from the four-cell stage onwards.

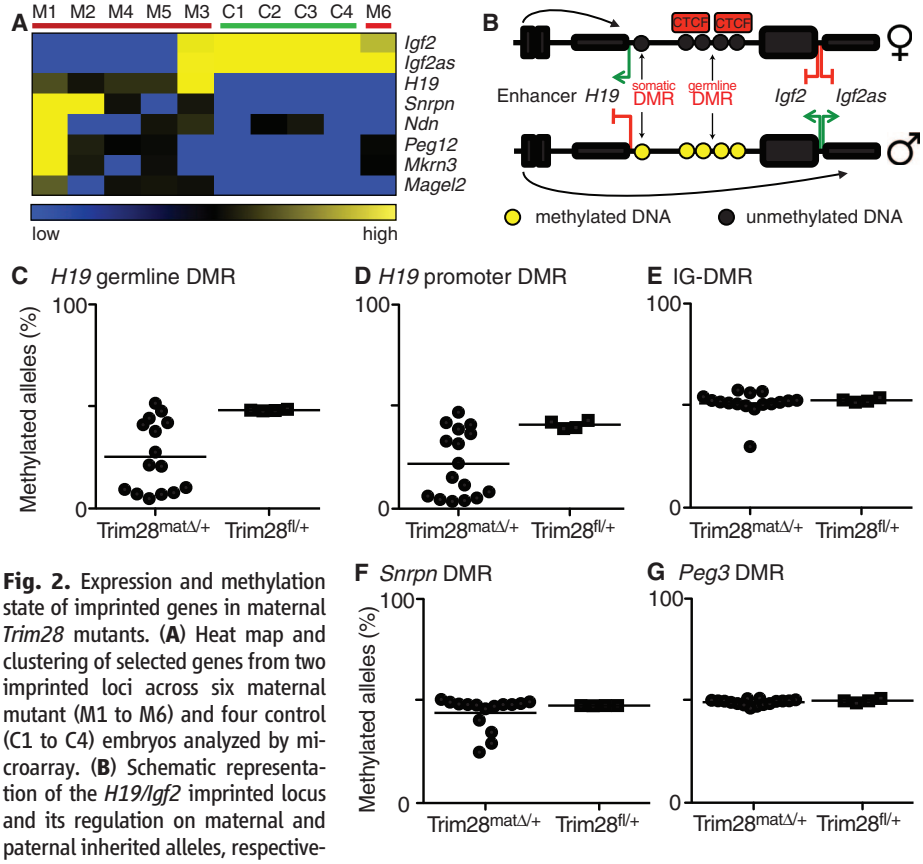

Fig. 2. Expression and methylation state of imprinted genes in maternal *Trim28* mutants. (**A**) Heat map and clustering of selected genes from two imprinted loci across six maternal mutant (M1 to M6) and four control (C1 to C4) embryos analyzed by microarray. (**B**) Schematic representation of the *H19/Igf2* imprinted locus and its regulation on maternal and paternal inherited alleles, respectively. (**C** to **G**) Methylation levels of DMRs examined by quantitative pyrosequencing after bisulfite conversion. Each dot represents an individual fetus (round, mutant; square, control). Analysis of the *H19* germline (C), *H19* promoter (D), IG- (E), *Snrpn* (F), and *Peg3* (G) DMRs is shown. Bar indicates median in each group.

Despite normal development to the blastocyst stage, viable offspring were never found. Detailed analysis at any postimplantation stage showed a highly pleiotropic phenotype, with 40 to 70% of the embryos being resorbed, which indicated partial postimplantation embryonic loss (table S1). Embryos surviving gastrulation undergo many normal aspects of embryonic development but never live after birth. Most are significantly growth restricted (Fig. 1C) and display great phenotypic variability, including edemas, craniofacial malformations, hemorrhage, and complete and hemianopthalmia (Fig. 1D). Often, such phenotypic variability is attributed to segregation of genetic modifiers on mixed genetic backgrounds, yet we backcrossed the *Trim28* floxed allele mice into C57BL/6J and confirmed the purity of their background by single-nucleotide polymorphism (SNP) genotyping (table S2). Hence, all experimental embryos are genetically identical. Zygotic heterozygous *Trim28* embryos do not display haploinsufficiency (*12*, *13*), which establishes that maternal *Trim28* is fundamental to proper embryonic development. Yet, its loss causes phenotypes long after OET and ZGA.

To address the molecular consequences of maternal *Trim28* deletion, we performed microarray analysis and found *Igf2* down-regulated in four of six mutants on embryonic day 12.5 (E12.5). *Igf2as* is also repressed in the affected embryos, whereas *H19* is up-regulated (Fig. 2A and fig. S2, A to C). All three genes are members of the imprinted *H19/Igf2* cluster, whose germline DMR (*H19* DMR) is paternally methylated, which promotes *Igf2/Igf2as* expression from the paternal and *H19* expression from the maternal allele (*14*–*19*) (Fig. 2B). Paternally inherited deletion of, or mutations and/or epimutations in, the *H19* DMR causes loss of *Igf2* expression and up-regulation of *H19* (*20*, *21*), as observed in maternal *Trim28*-null embryos.

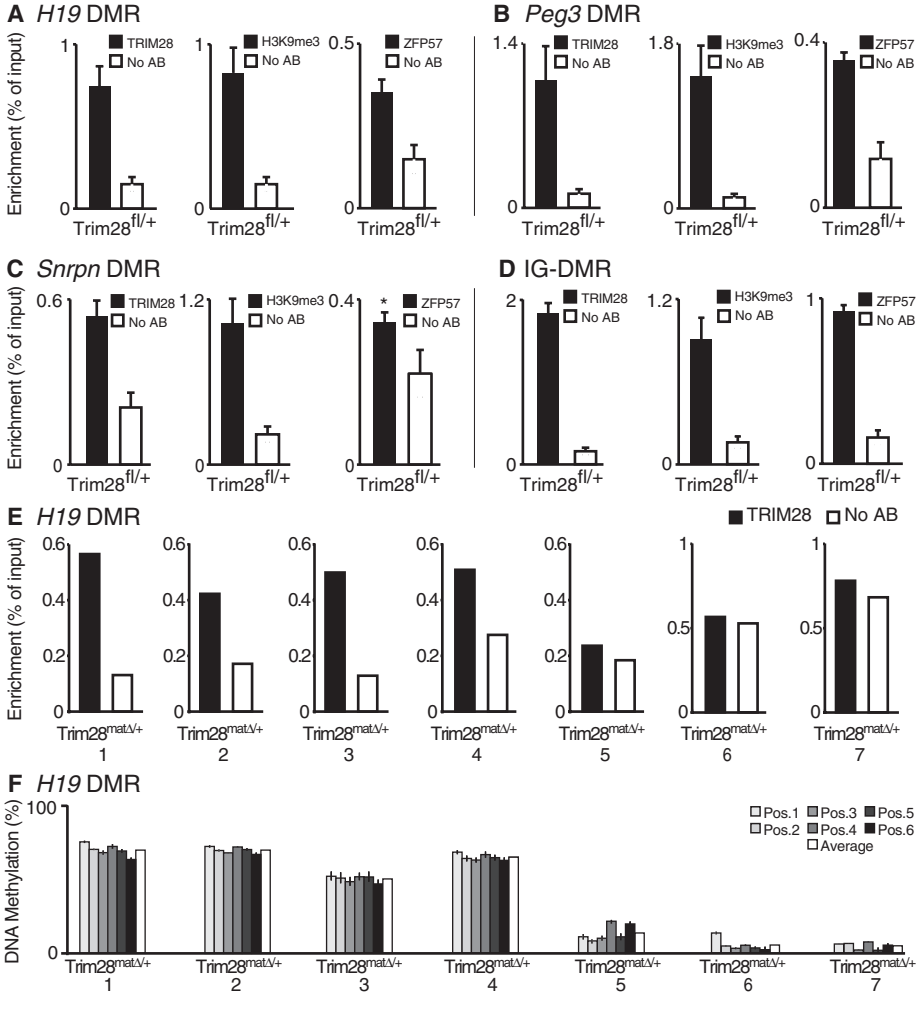

Fig. 3. TRIM28 binding to DMRs is methylation dependent. (**A** to **D**) ChIP shows enrichment of TRIM28, ZFP57, and H3K9me3 at the *H19* (A), *Peg3* (B), *Snrpn* (C), and IG-DMR (D), respectively. Depicted is the average enrichment over input in percent, with or without antibody, from five (TRIM28 and H3K9me3) or three (ZFP57) individual control E12.5 embryos (*$P < 0.05$). (**E**) Interaction of TRIM28 with the *H19* DMR in individual maternal mutants analyzed by ChIP. (**F**) DNA methylation analysis of the *H19* DMR by quantitative pyrosequencing of individual maternal mutants used for ChIP in (E). (Pos., position of CpG-island within the amplicon)

We determined the methylation state of the *H19* DMR by quantitative pyrosequencing after hydrogen sulfite (bisulfite) conversion. All control embryos show 50% methylation at the DMR (Fig. 2C). However in maternal *Trim28* mutants, *H19* DMR methylation varies between 50% and almost complete absence (Fig. 2C), a finding confirmed by combined bisulfite restriction analysis (COBRA) and by cloning and sequencing (fig. S3, A and B). Notably, the *H19* DMR methylation state correlates tightly with the *Igf2* expression levels in each of the respective mutants (fig. S3, C to E). Similar observations were also made at later stages (fig. S4). A secondary DMR in the *H19* promoter is established during preimplantation development and is subject to the germline *H19* DMR methylation state (*14*, *22*). Methylation levels of both DMRs correlate in all embryos (Fig. 2D and fig. S3, D and E). These findings show that after fertilization, maternal TRIM28 protects the *H19* DMR on the paternal chromosome from aberrant DNA demethylation.

To determine whether the effect is *H19/Igf2*-specific, we examined other imprinted genes. The intergenic (IG)–DMR is also paternally methylated but responsible for *Dlk1/Dio3* cluster regulation. Microarray-detected expression of genes in the *Dlk1/Dio3* imprinted cluster shows only marginal changes in the maternal *Trim28*-deleted embryos tested. Accordingly, differential methylation of the IG-DMR is just slightly affected (1 out of 16) (Fig. 2E). The Prader-Willi/Angelman syndrome cluster, normally methylated in the maternal germ line, contains a number of paternally expressed genes, such as *Snrpn*, *Mkrn3*, *Magel2*, *Ndn*, and *Peg12* (*23*). These are close to twofold up-regulated in one of six mutants (Fig. 2A and fig. S2, D to F). Hypomethylation at the *Snrpn* DMR can be detected in maternal mutants, albeit to a lower extent and frequency than at the *H19* DMR (Fig. 2F). The maternally methylated *Peg3* DMR is unaffected in embryos surveyed at E12.5 (Fig. 2G). Thus, correlating with the pleiotropic phenotype, we find a loss of methylation at DMRs, which is highly variable both between and within individual embryos (fig. S5). Notably, many embryos do not show demethylation of all DMRs at a given locus, which implies that they are chimeric for normal and aberrantly imprinted cells, a condition likely contributing to the highly variable phenotype.

To ascertain a relation between TRIM28, ZFP57, and the DMRs, we performed chromatin immunoprecipitations (ChIPs) followed by quantitative real-time fluorescence polymerase chain reaction QPCR in wild-type E12.5 embryos with normal methylation levels (Fig. 3 and fig. S6). TRIM28 and ZFP57 are enriched at the *H19* DMR, which indicates interaction. SETDB1, a component of the TRIM28 complex, catalyzes trimethylation of lysine residue 9 on histone 3 (H3K9me3), which is also significantly enriched at the *H19* DMR. Extending this analysis to other imprinted regions, we also find TRIM28, ZFP57, and H3K9me3 enriched at the *Snrpn*, IG-, and

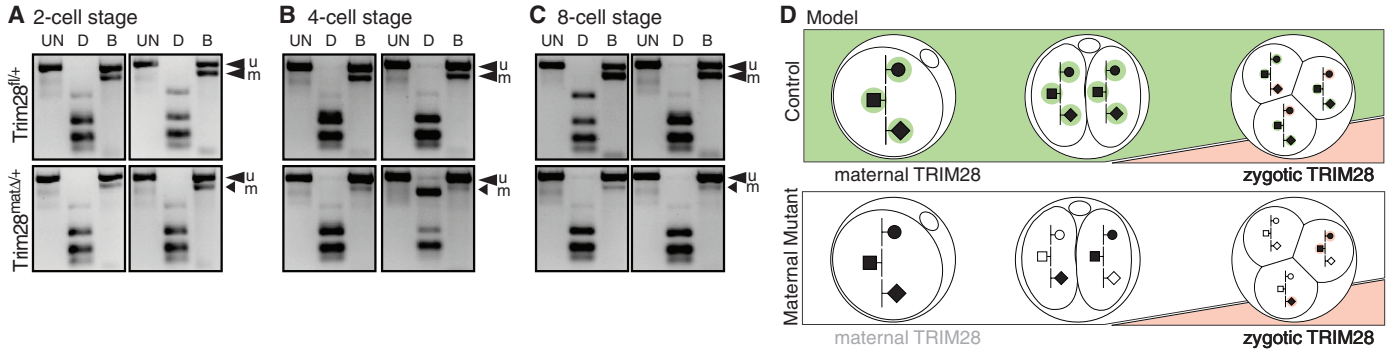

Fig. 4. Loss of *H19* DMR methylation in mutant preimplantation embryos. Combined bisulfite restriction analysis of the *H19* DMR methylation state in pooled (**A**) two-cell–, (**B**) four-cell–, and (**C**) eight-cell–stage controls and maternal mutants (UN, uncut; D, Dra I; B, Bst UI). Dra I digestion tests the efficiency of bisulfite conversion; the restriction site for Bst UI is protected from bisulfite mutagenesis if the CpG nucleotides within the site are methylated (u, unmethylated; m, methylated). Two individually analyzed embryo pools are shown for mutants and controls, respectively. (**D**) Model of TRIM28 function after fertilization and consequences of the maternal deletion. Symbols represent individual methylated (filled) or unmethylated (unfilled) DMRs. Colored outlines represent protective TRIM28 complexes at DMRs containing maternal (green) and later zygotic (red) TRIM28.

Peg3 DMR. In conclusion, the TRIM28 complex binds all tested DMRs, including those whose methylation state we find only slightly affected or unaffected by the loss of maternal *Trim28.* To address binding of TRIM28 to the *H19* DMR in maternal mutants, we queried seven individual E12.5 embryos. TRIM28 was enriched at the *H19* DMR in four mutants, which show normal *H19* DMR methylation, whereas no enrichment was detected in three others, which show severe hypomethylation (Fig. 3, E and F). Therefore, absence of maternal *Trim28* results in loss of DNA methylation and lack of paternal TRIM28 binding at later stages. This suggests that DNA methylation is required at the DMR for effective binding of the TRIM28 modifier complex, an observation further supported by recent ZFP57-binding studies in embryonic stem cells (*24*).

Our evidence suggests that maternal *Trim28* prevents DNA demethylation during OET, yet the global methylation state in mutant zygotes is not altered according to 5-methyl or 5-hydroxymethyl cytosine (*9*, *25*) immunofluorescence staining (fig. S7). We next addressed specifically DMR methylation in preimplantation embryos. We chose the *H19* DMR as the candidate most likely to display hypomethylation in pools of embryos, as it is most frequently affected in survivors of the first wave of lethality, at implantation. As *H19* DMR is paternally imprinted, it is not methylated in oocytes, but, at the two-cell stage, controls show methylation at about half the alleles (Fig. 4). In mutants, however, *H19* DMR methylation is reduced, a loss even more pronounced at the four- and eight-cell stages. Conversely, the *Peg3* DMR is maternally imprinted and fully methylated in control and mutant eggs (fig. S8). Thus, *Trim28* is not required to maintain this maternal imprint in the growing egg. After fertilization, the paternal, unmethylated allele is detectable, yet overall *Peg3* DMR methylation is not visibly affected in mutant two-cell– or eight-cell–stage embryos.

It is unclear why imprinted loci are not equally affected. Redundant mechanisms such as PGC7-mediated protection or locus-specific accessibility for modifiers could play potential roles. Additionally, early lethality at implantation and pooling of embryos at preimplantation stages could mask the detection of more affected DMRs. Indeed, when we analyzed individual E4.5 embryos for both *H19* and *Peg3* DMR methylation, we also found infrequent, yet complete, *Peg3* DMR hypomethylation (fig. S9). Such embryos appear unlikely to survive beyond implantation, as we detect only unaffected *Peg3* DMRs at later stages.

In maternal *Trim28* mutant embryos, demethylation of DMRs occurs slowly and inefficiently, although it still creates sufficient impact to cause lethality. This delay may be mediated by factors such as PGC7 and/or ZFP57 playing additional protective roles. This creates an environment in which paternal TRIM28, if present above a given threshold, can prevent complete DMR demethylation. However, once demethylated, the TRIM28 complex can no longer bind and recover this loss (see ChIP in Fig. 3E). Therefore, the molecular and phenotypic variability in maternal *Trim28*-deleted mutants emerges from a random combination of stochastically affected TRIM28 target loci (*26*). Because of ongoing cell division, this can further vary between blastomeres within an individual embryo. As a result, the embryo is a mosaic in which the degree of mosaicism and extent of gene disregulation determines the time and mode of embryonic and fetal lethality (Fig. 4D). Our findings illustrate the exquisite temporal and spatial balance between maternal and zygotic factors in the early embryo that are required to maintain epigenetic states. Perturbing this balance can cause a wide spectrum of phenotypic variability.

References and Notes

1. A. C. Ferguson-Smith, *Nat. Rev. Genet.* **12**, 565 (2011).
2. A. P. Feinberg, *Med. Pediatr. Oncol.* **27**, 484 (1996).
3. A. Kaneda, A. P. Feinberg, *Cancer Res.* **65**, 11236 (2005).
4. C. Gicquel *et al.*, *Nat. Genet.* **37**, 1003 (2005).
5. W. Reik *et al.*, *Hum. Mol. Genet.* **3**, 1297 (1994).
6. W. Reik, W. Dean, J. Walter, *Science* **293**, 1089 (2001).
7. H. D. Morgan, F. Santos, K. Green, W. Dean, W. Reik, *Hum. Mol. Genet.* **14**, (suppl. 1), R47 (2005).
8. S. A. Smallwood *et al.*, *Nat. Genet.* **43**, 811 (2011).
9. T. Nakamura *et al.*, *Nat. Cell Biol.* **9**, 64 (2007).
10. X. Li *et al.*, *Dev. Cell* **15**, 547 (2008).
11. S. Iyengar, P. J. Farnham, *J. Biol. Chem.* **286**, 26267 (2011).
12. N. C. Whitelaw *et al.*, *Genome Biol.* **11**, R111 (2010).
13. F. Cammas *et al.*, *Development* **127**, 2955 (2000).
14. M. S. Bartolomei, A. L. Webber, M. E. Brunkow, S. M. Tilghman, *Genes Dev.* **7**, 1663 (1993).
15. A. C. Bell, G. Felsenfeld, *Nature* **405**, 482 (2000).
16. M. S. Bartolomei, S. Zemel, S. M. Tilghman, *Nature* **351**, 153 (1991).
17. T. M. DeChiara, E. J. Robertson, A. Efstratiadis, *Cell* **64**, 849 (1991).
18. S. J. Giddings, C. D. King, K. W. Harman, J. F. Flood, L. R. Carnaghi, *Nat. Genet.* **6**, 310 (1994).
19. A. C. Ferguson-Smith, B. M. Cattanach, S. C. Barton, C. V. Beechey, M. A. Surani, *Nature* **351**, 667 (1991).
20. J. L. Thorvaldsen, K. L. Duran, M. S. Bartolomei, *Genes Dev.* **12**, 3693 (1998).
21. N. Engel, A. G. West, G. Felsenfeld, M. S. Bartolomei, *Nat. Genet.* **36**, 883 (2004).
22. A. C. Ferguson-Smith, H. Sasaki, B. M. Cattanach, M. A. Surani, *Nature* **362**, 751 (1993).
23. R. D. Nicholls, J. L. Knepper, *Annu. Rev. Genomics Hum. Genet.* **2**, 153 (2001).
24. S. Quenneville *et al.*, *Mol. Cell* **44**, 361 (2011).
25. M. Wossidlo *et al.*, *Nat Commun* **2**, 241 (2011).
26. H. O'Geen *et al.*, *PLoS Genet.* **3**, e89 (2007).

Acknowledgments: This research was financed by A*STAR, Singapore and by grants from the Wellcome Trust and UK Technology Strategy Board. We thank H. Wollmann, S. Balu, D. Tham, and K. Yamazawa for their help. Microarray data and accession nos. can be found in the Supporting Online Material.

Supporting Online Material

www.sciencemag.org/cgi/content/full/335/6075/1499/DC1
Materials and Methods
Figs. S1 to S9
Tables S1 and S2
References (*27*–*29*)
Array Data

3 November 2011; accepted 30 January 2012
10.1126/science.1216154

ApoE-Directed Therapeutics Rapidly Clear β-Amyloid and Reverse Deficits in AD Mouse Models

Paige E. Cramer,[1] John R. Cirrito,[2] Daniel W. Wesson,[1,3] C. Y. Daniel Lee,[1] J. Colleen Karlo,[1] Adriana E. Zinn,[1] Brad T. Casali,[1] Jessica L. Restivo,[2] Whitney D. Goebel,[2] Michael J. James,[4] Kurt R. Brunden,[4] Donald A. Wilson,[3] Gary E. Landreth[1]*

Alzheimer's disease (AD) is associated with impaired clearance of β-amyloid (Aβ) from the brain, a process normally facilitated by apolipoprotein E (apoE). ApoE expression is transcriptionally induced through the action of the nuclear receptors peroxisome proliferator–activated receptor gamma and liver X receptors in coordination with retinoid X receptors (RXRs). Oral administration of the RXR agonist bexarotene to a mouse model of AD resulted in enhanced clearance of soluble Aβ within hours in an apoE-dependent manner. Aβ plaque area was reduced more than 50% within just 72 hours. Furthermore, bexarotene stimulated the rapid reversal of cognitive, social, and olfactory deficits and improved neural circuit function. Thus, RXR activation stimulates physiological Aβ clearance mechanisms, resulting in the rapid reversal of a broad range of Aβ-induced deficits.

The most common form of Alzheimer's disease (AD) occurs sporadically late in life and is typified by deposition of β-amyloid (Aβ) within the brain (*1*). Individuals with late-onset AD produce Aβ peptides at normal levels but have an impaired ability to clear them from the brain (*2*). Elevated levels of Aβ are associated with perturbations of synaptic function and neural network activity that probably underlie the cognitive deficits in AD (*3*). Moreover, Aβ accumulation leads to its deposition into plaques and is thought to drive a pathologic cascade, which ultimately leads to neuronal death.

The most influential genetic risk factor for sporadic AD is allelic variation in the apolipoprotein E (*APOE*) gene. Possession of an APOE4 allele markedly increases disease risk (*4*). ApoE acts normally to scaffold the formation of high-density lipoprotein (HDL) particles, which promote the proteolytic degradation of soluble forms of Aβ (*5*, *6*).

The expression of apoE is transcriptionally regulated by the ligand-activated nuclear receptors, peroxisome proliferator–activated receptor gamma (PPARγ) and liver X receptors (LXRs) (*7*), which form obligate heterodimers with retinoid X receptors (RXRs). Transcriptional activity is regulated by ligation of either member of the pair (*8*). PPARγ:RXR and LXR:RXR act in a feed-forward manner to induce the expression of apoE, its lipid transporters ABCA1 and ABCG1, and the nuclear receptors themselves (*7*). Agonists of these receptors also act on macrophages and microglia to stimulate their conversion into "alternative" activation states (*9*) and promote phagocytosis (*10*). Chronic administration of LXR and PPARγ agonists reduces Aβ levels and improves cognitive function in mouse models of AD (*10*).

We reasoned that an RXR agonist would enhance normal Aβ clearance mechanisms by activating PPARγ:RXR and LXR:RXR, inducing apoE expression, facilitating Aβ clearance, and promoting microglial phagocytosis. Bexarotene (Targretin) is a highly selective, blood-brain barrier–permeant (fig. S3A), RXR agonist approved by the U.S. Food and Drug Administration (FDA) (*11*) with a favorable safety profile (*12*). Treatment of primary microglia or astrocytes with bexarotene stimulated the expression of apoE, ABCA1, and ABCG1 (fig. S1, A and B) and secretion of highly lipidated HDL particles (fig. S1, C and D). Bexarotene treatment of primary microglia and astrocytes facilitated degradation of soluble $A\beta_{42}$ (fig. S2, A and B) in a PPARγ-, LXR (fig. S2, C and D)–, and apoE (fig. S2, E and F)–dependent manner. The levels of Aβ proteases, insulin-degrading enzyme and neprilysin, were unchanged with bexarotene treatment (fig. S1, E and F).

Brain interstitial fluid (ISF) Aβ levels were monitored by hippocampal in vivo microdialysis (*13*) of 2-month-old APPswe/PS1Δe9 (APP/PS1) mice. Bexarotene rapidly lowered ISF $A\beta_{40}$ and $A\beta_{42}$ levels within 6 hours of administration, with a 25% reduction by 24 hours (Fig. 1, A and B). One dose of bexarotene significantly decreased ISF $A\beta_{40}$ and $A\beta_{42}$ levels by 25% for more than 70 hours (Fig. 1D), with a return to baseline by 84 hours. The suppression of ISF Aβ was due to increased clearance, as the $A\beta_{40}$ half-life was reduced from 1.4 to 0.7 hours (Fig. 1C). Bexarotene reduced murine Aβ levels in the C57Bl/6 mice to a similar extent as in APP/PS1 mice; however, it had no effect on Aβ levels in apoE-null mice (Fig. 1E), demonstrating that the enhanced clearance of soluble ISF Aβ required apoE.

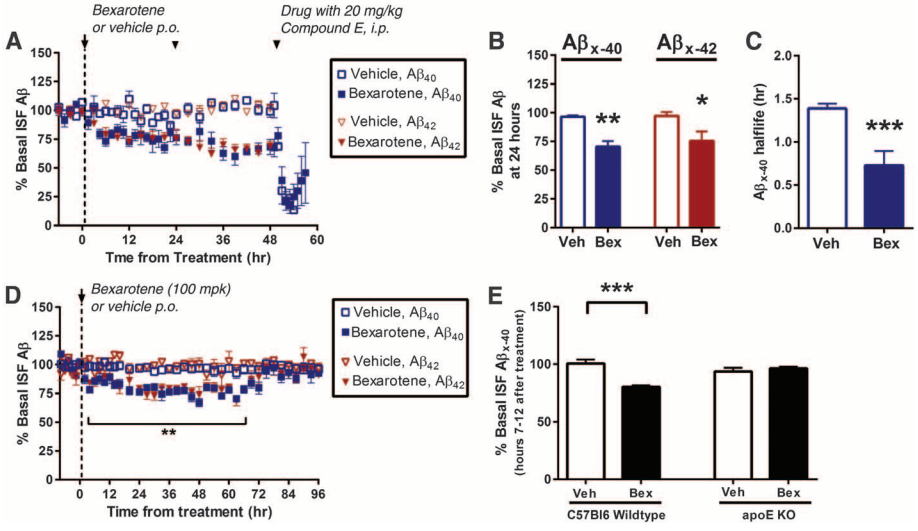

Fig. 1. ISF levels of Aβ decrease after bexarotene treatment. (**A** and **B**) ISF $A\beta_{x\text{-}40}$ and $A\beta_{x\text{-}42}$ levels were monitored by in vivo hippocampal microdialysis of 2-month-old APP/PS1 mice. Baseline Aβ levels were monitored for 6 hours, followed by daily orally administered bexarotene (100 mg kg^{-1} day^{-1}) (Bex) or vehicle (Veh; water) for 3 days. Mice were coadministered compound E [20 mg kg^{-1} intraperitoneally (i.p.)] on day 3. (**C**) The elimination half-life of ISF $A\beta_{x\text{-}40}$ was measured. In 2-month-old APP/PS1 mice, baseline ISF Aβ levels were sampled after administration of a single oral dose of bexarotene (100 mg kg^{-1}). (**D**) ISF $A\beta_{x\text{-}40}$ and $A\beta_{x\text{-}42}$ were sampled every 2 to 6 hours for 4 days after treatment. (**E**) Baseline ISF Aβ levels of nontransgenic (C57Bl/6) and apoE knockout (KO) mice (2 months) with and without bexarotene treatment. ISF $A\beta_{x\text{-}40}$ levels were measured between hours 7 and 12 after treatment; $n = 5$ mice per group (Student's t test; mean ± SEM, $^*P < 0.05$, $^{**}P < 0.01$, $^{***}P < 0.001$).

[1]Department of Neurosciences, Case Western Reserve University School of Medicine, Cleveland, OH 44106, USA. [2]Department of Neurology, Hope Center for Neurological Disorders, Knight Alzheimer's Disease Research Center, Washington University School of Medicine, St. Louis, MO 63110, USA. [3]Emotional Brain Institute, Nathan Kline Institute for Psychiatric Research and the New York University School of Medicine, Orangeburg, NY 10962, USA. [4]Center of Neurodegenerative Disease Research, Department of Pathology and Laboratory Medicine, Perelman School of Medicine, University of Pennsylvania, Philadelphia, PA 19104, USA.

*To whom correspondence should be addressed. E-mail: gel2@case.edu

We observed the rapid removal of both diffuse and compact Aβ plaques in the cortex and hippocampus of APP/PS1 mice after acute treatment with bexarotene (Fig. 2). We orally administered bexarotene or vehicle daily to 6-month-old APP/PS1 mice for 3, 7, or 14 days. We observed the progressively enhanced expression of apoE, ABCA1, and ABCG1 and elevated HDL levels in both the hippocampus and cortex of bexarotene-treated mice (fig. S3, B and C). There was a sustained 30% reduction in soluble Aβ levels throughout the 14-day treatment period (Fig. 2A). Insoluble Aβ levels were reduced by 40% after 72 hours and progressively decreased over the subsequent 14 days (Fig. 2A). Total (Fig. 2, B and C) and thioflavin-S^+ Aβ plaques (Fig. 2, E and F) were reduced by ~75% after 14 days of bexarotene treatment. Furthermore, we observed abundant Aβ-laden microglia after 3 days of bexarotene treatment, suggesting their involvement in the phagocytic removal of Aβ deposits (Fig. 2D).

To assess whether bexarotene could decrease Aβ burden in older animals with greater plaque deposition, we treated 11-month APP/PS1 mice with bexarotene for 7 days and found significantly reduced levels of soluble and insoluble $Aβ_{40}$ and $Aβ_{42}$ (fig. S4C), a 50% reduction in plaque number (fig. S4, D and E), and a concurrent increase in expression of apoE, the cholesterol transporters, and HDL levels (fig. S4, A and B). Thus, the efficacy of acute bexarotene treatment is evident in both early and later stages of pathogenesis in this mouse model.

We also tested the effect of chronic bexarotene treatment (3 months, daily) of APP/PS1 mice starting from 6 months of age. We found elevated levels of apoE, ABCA1, ABCG1, and HDL (fig. S5, A and B). Bexarotene reduced soluble Aβ levels by ~30%, consistent with its ability to enhance apoE-dependent Aβ proteolysis (fig. S6C). However, amyloid plaque burden was unchanged (fig. S5, D to G).

To evaluate the robustness of the effect of bexarotene, we treated an aggressive model of amyloidosis, the APPPS1-21 mouse (*14*), which possesses high levels of deposited Aβ at 7 to 8 months of age. APPPS1-21 mice treated for 20 days with bexarotene exhibited a reduced level of soluble and insoluble Aβ peptides (fig. S6C) and a 35% decrease in the number of thioflavin S^+ plaques (fig. S6, D and E). Bexarotene treatment enhanced the expression of ABCA1, ABCG1, apoE, and its lipidated forms (fig. S6, A and B).

There is persuasive evidence that the cognitive and behavioral deficits characteristic of AD arise, in part, from impaired synaptic function due to soluble forms of Aβ. Bexarotene treatment rapidly restored cognition and memory, as assessed by contextual fear conditioning in APP/PS1 mice treated for 7 days at both early (6 months) and later (11 months) stages of plaque pathogenesis. Similarly, chronic treatment of 6-month-old APP/PS1 mice for 90 days (analyzed at 9 months of age) (Fig. 3, A to C) showed drug-induced behavioral improvements in the contextual fear conditioning task. Additionally, APP/PS1 mice treated for 90 days and APPPS1-21 mice treated for 20 days exhibited improved hippocampal function after bexarotene treatment, as assessed by Morris water maze performance (Fig. 3, D and F), as well as in the contextual fear conditioning assay (Fig. 3E).

Nest construction is an affiliative, social behavior that becomes progressively impaired in Tg2576

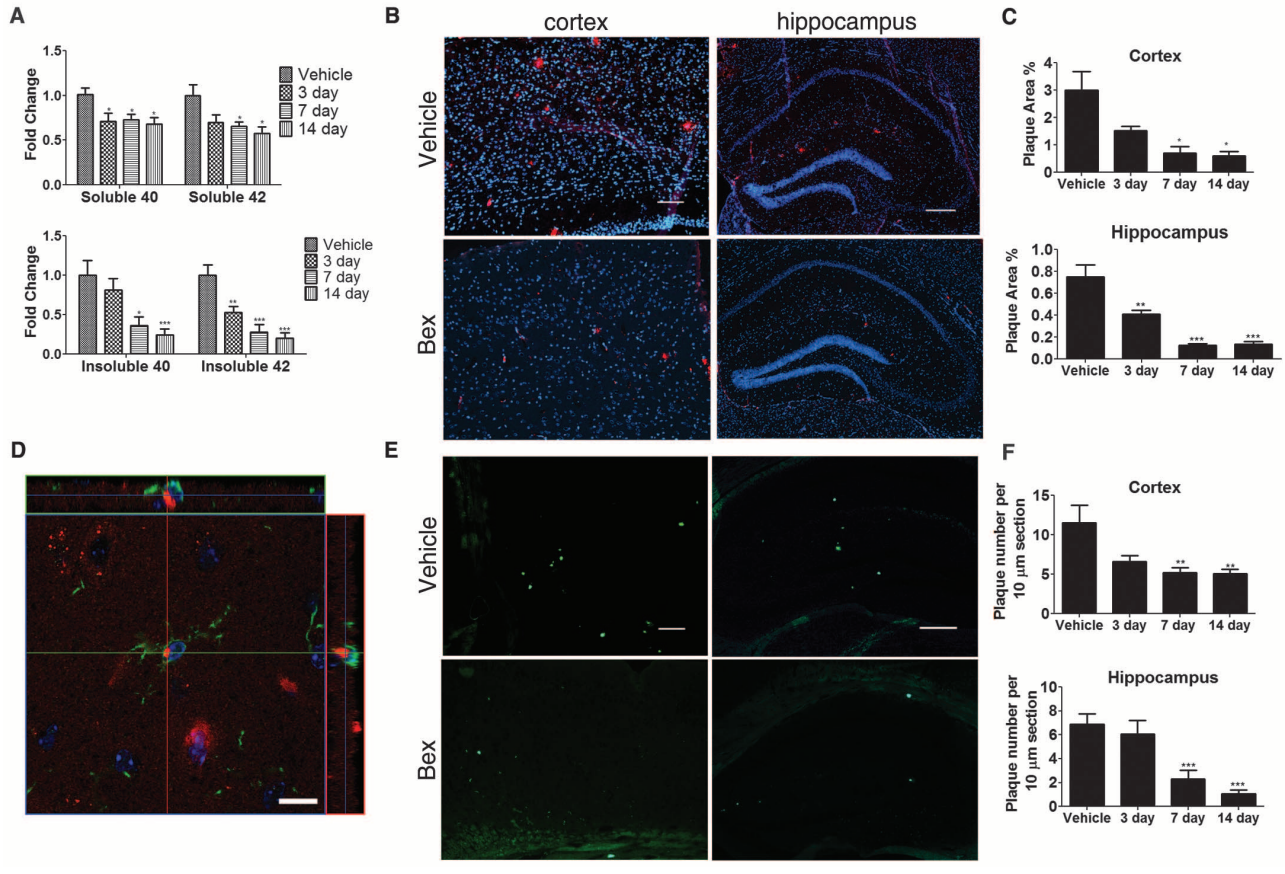

Fig. 2. Aβ levels and plaque burden are reduced by bexarotene treatment. APP/PS1 or nontransgenic (NonTg) mice (6 months) orally gavaged for 3, 7, and 14 days with bexarotene (100 mg kg^{-1} day^{-1}) or vehicle (water). Soluble and insoluble $Aβ_{40}$ and $Aβ_{42}$ levels were measured by enzyme-linked immunosorbent assay. (**A**) Fold changes based on vehicle: 7.0445 ng/mg protein and 14.529 ng/mg protein of soluble $Aβ_{40}$ and $Aβ_{42}$, respectively, and 30.349 ng/mg protein and 36.8 ng/mg protein of insoluble $Aβ_{40}$ and $Aβ_{42}$, respectively. (**B** and **E**) Representative cortex and hippocampus sections of vehicle and 14-day bexarotene-treated mice stained with antibody against Aβ (6E10) (B) or thioflavin S (E) are shown and (**C** and **F**) plaque levels quantified; $n \geq 5$ animals per group (Student's *t* test; mean ± SEM, $^*P < 0.05$, $^{**}P < 0.01$, $^{***}P < 0.001$). Scale bars (B and E): cortex, 100 μm; hippocampus, 200 μm. (**D**) Representative image of microglia in the cortex of a 6-month APP/PS1 mouse treated for 3 days with bexarotene (red: 6E10; green: Iba1; blue: DAPI). Scale bar: 10 μm .

mice (*15*). After just 72 hours of bexarotene treatment, nest construction behavior was restored in Tg2576 mice (Fig. 3G).

Finally, we explored whether bexarotene could rescue olfactory sensory impairments, (*16*), which are highly correlated with Aβ deposition in Tg2576 mice (*17*). Bexarotene treatment improved odor habituation behavior after 9 days of drug treatment in Tg2576 mice 12 to 14 months of age (Fig. 3H).

The improved behaviors observed in bexarotene–treated mice suggest global improvements of neural network function. Soluble Aβ interferes with synaptic function that subserves higher-order neural network information processing (*3*). Piriform cortex (PCX) circuit function is critical to odor-guided behaviors, and its disruption is implicated in impaired olfactory perception in both humans with AD and in Tg2576 mice (*18*). Therefore, we evaluated odor-evoked PCX local field potentials (LFPs) as a behaviorally relevant synaptic readout of neural circuit status. Odor-evoked high-frequency gamma-band oscillations (35 to 75 Hz) and beta-band oscillations (15 to 35 Hz), reflecting local circuit interactions and interregional network activity, respectively, are considered critical for normal olfactory function (*18*, *19*). Tg2576 mice (12 to 14 months) treated with vehicle exhibited significantly less odor-evoked beta- and gamma-band LFP power compared to drug-treated nontransgenic mice (Fig. 4, A and B), which was restored by 3 days of bexarotene treatment. Odor habituation after bexarotene treatment was improved in these same mice (fig. S7, B and C), indicating a rapid drug-dependent normalization of local and regional circuit function in the primary olfactory pathway.

RXR activation stimulates the normal physiological processes through which Aβ is cleared from the brain. The dependence of soluble Aβ clearance on apoE validates the mechanistic linkage between the principal genetic risk factor for AD and the cognitive impairment that characterizes the disease (*5*, *6*). Bexarotene acts rapidly to facilitate the apoE-dependent clearance of soluble forms of Aβ, accounting for the extremely rapid change in ISF Aβ metabolism. Bexarotene-mediated behavioral improvements were correlated with a reduction in soluble Aβ peptide levels of ~30%. These observations are consistent with previous observations that learning and memory

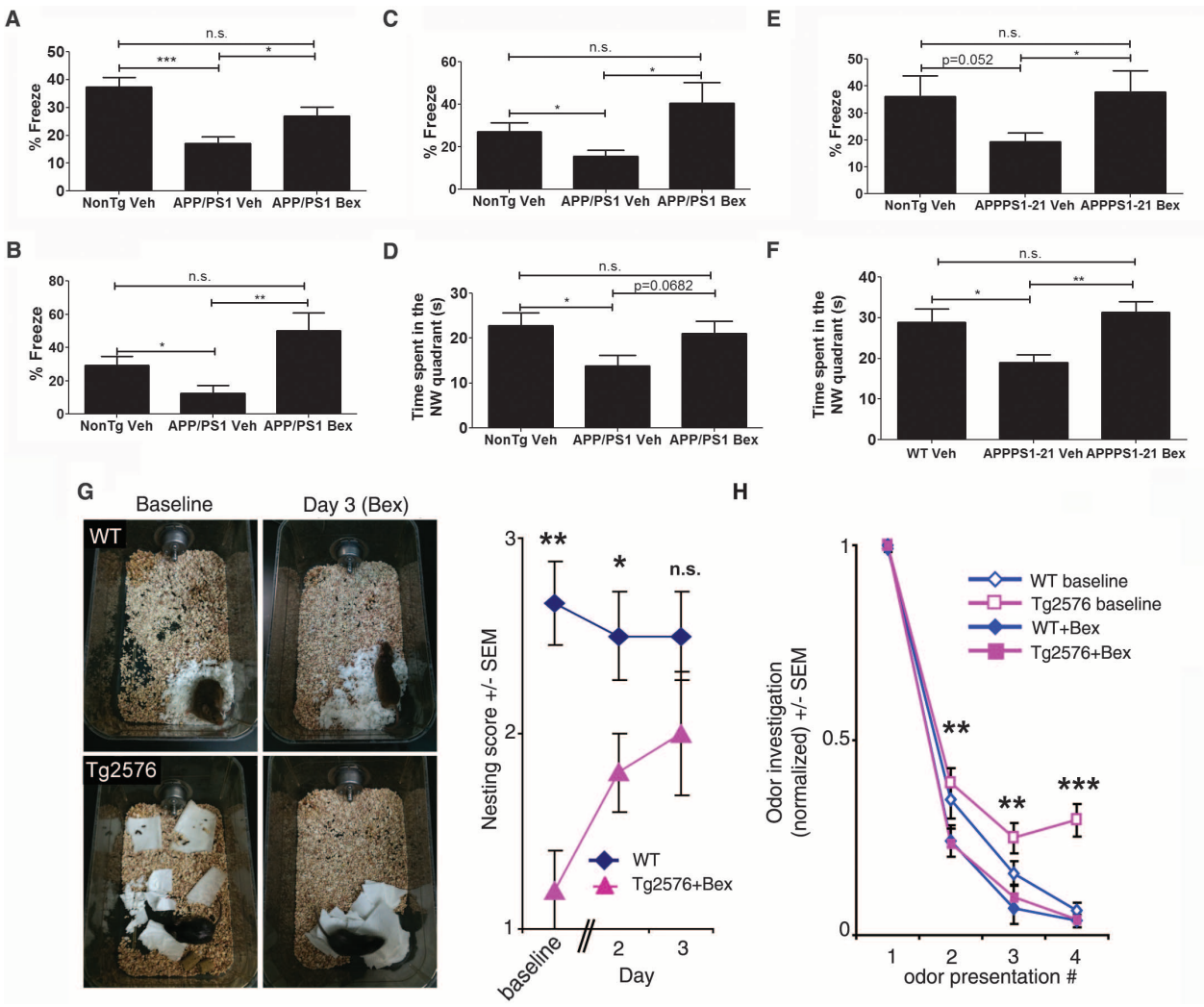

Fig. 3. Restoration of memory and cognition with bexarotene treatment. Contextual fear-learning assayed in (**A**) 6-month-old and (**B**) 11-month-old APP/PS1 mice treated for 7 days, or (**C**) in 9-month-old APP/PS1 mice treated for 90 days with vehicle or bexarotene. (**E**) APPPS1-21 mice 7 to 8 months of age were treated for 20 days and evaluated for performance. Percent time frozen was recorded in the 5-min test trial. (**D** and **F**) Spatial memory was assessed with the Morris water maze. Time spent in the northwest quadrant in the retention probe of (D) 9-month-old, 90-day-treated APP/PS1 mice and (F) 7- to 8-month-old, 20-day-treated APPPS1-21 mice with vehicle or bexarotene (Bex) (100 mg kg^{-1} day^{-1}). [Nontransgenic littermates were controls (NonTg), $n = 7$ to 14 mice per group (Student's t test; mean ± SEM, $^{*}P < 0.05$, $^{**}P < 0.01$)]. (**G**) Nest construction was quantified in 12- to 14-month NonTg and Tg2576 mice. Baseline data were obtained on day 0, after daily drug treatment and addition of paper towels in clean cages (two-tailed t test; $^{*}P < 0.05$, $^{**}P < 0.01$). (**H**) Odor habituation behavior in 12- to 14-month Tg2576 mice tested before (baseline) and after 9 days of bexarotene treatment; $n = 5$ mice per group (two-tailed t test; mean ± SEM, $^{**}P < 0.01$, $^{***}P < 0.001$ for Tg2576 baseline versus Tg2576 Bex).

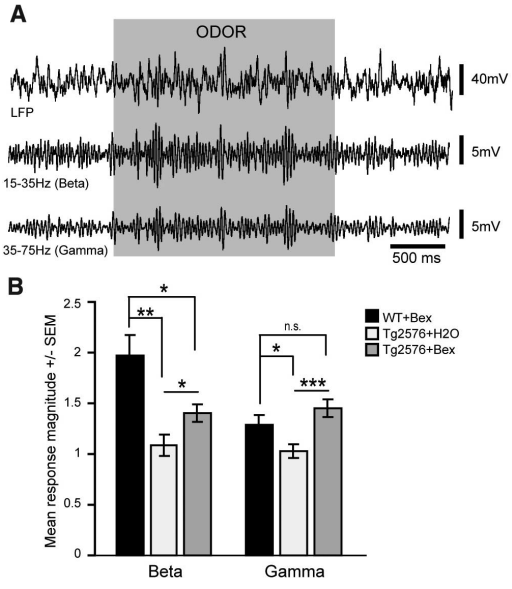

Fig. 4. Rescue of cortical network activity with bexarotene. LFP recordings of Tg2576 or nontransgenic (NonTg) mice (12 to 14 months) gavaged with bexarotene (Bex) (100 mg kg^{-1} day^{-1}) or vehicle (H_2O) for 3 days after implantation of electrodes into PCX. PCX LFPs in response to the odor ethyl valerate in an awake nontransgenic, bexarotene-treated mouse. (**A**) Fifteen- to 35-Hz beta- and 35- to 75-Hz gamma-band power traces (second-order band pass). (**B**) PCX odor-evoked response magnitudes (2 s odor/2 s pre-odor) ($n = 5$ mice per group, four odor presentations per mouse; $^*P < 0.05$, $^{**}P < 0.01$, $^{***}P < 0.001$, mean ± SEM, two-tailed t tests of mean odor-evoked magnitudes within LFP bins). ns, not significant.

can be improved through reducing brain-soluble Aβ levels, either upon the administration of ß- or γ-secretase inhibitors (*20*, *21*) or provision of antibodies against Aβ (*22*). However, the behavioral improvements were poorly correlated with the microglial-mediated removal of insoluble, deposited forms of Aβ. The dual actions of the nuclear receptors resulting in the enhanced expression and lipidation of apoE and modulation of the microglial-mediated immune response are consistent with recent genetic association analyses implicating them in the etiology of AD (*23*–*25*). The ability of bexarotene to rapidly reverse a broad range of deficits suggests that RXR agonists may be of therapeutic utility in the treatment of AD and its antecedent phases.

References and Notes

1. H. W. Querfurth, F. M. LaFerla, *N. Engl. J. Med.* **362**, 329 (2010).
2. K. G. Mawuenyega *et al.*, *Science* **330**, 1774 (2010).
3. J. J. Palop, L. Mucke, *Nat. Neurosci.* **13**, 812 (2010).
4. A. D. Roses, A. M. Saunders, *Curr. Opin. Biotechnol.* **5**, 663 (1994).
5. J. J. Donkin *et al.*, *J. Biol. Chem.* **285**, 34144 (2010).
6. Q. Jiang *et al.*, *Neuron* **58**, 681 (2008).
7. A. Chawla *et al.*, *Mol. Cell* **7**, 161 (2001).
8. P. Lefebvre, Y. Benomar, B. Staels, *Trends Endocrinol. Metab.* **21**, 676 (2010).
9. J. I. Odegaard, A. Chawla, *Annu. Rev. Pathol.* **6**, 275 (2011).
10. S. Mandrekar-Colucci, G. E. Landreth, *Expert Opin. Ther. Targets* **15**, 1085 (2011).
11. FDA, www.accessdata.fda.gov/drugsatfda_docs/nda/99/21055_Targretin.cfm (1999).
12. L. T. Farol, K. B. Hymes, *Expert Rev. Anticancer Ther.* **4**, 180 (2004).
13. J. R. Cirrito *et al.*, *J. Neurosci.* **23**, 8844 (2003).
14. R. Radde *et al.*, *EMBO Rep.* **7**, 940 (2006).
15. D. W. Wesson, D. A. Wilson, *Behav. Brain Res.* **216**, 408 (2011).
16. C. Murphy, *Physiol. Behav.* **66**, 177 (1999).
17. D. W. Wesson, E. Levy, R. A. Nixon, D. A. Wilson, *J. Neurosci.* **30**, 505 (2010).
18. D. W. Wesson *et al.*, *J. Neurosci.* **31**, 15962 (2011).
19. N. Kopell, G. B. Ermentrout, M. A. Whittington, R. D. Traub, *Proc. Natl. Acad. Sci. U.S.A.* **97**, 1867 (2000).
20. H. Fukumoto *et al.*, *J. Neurosci.* **30**, 11157 (2010).
21. T. A. Comery *et al.*, *J. Neurosci.* **25**, 8898 (2005).
22. J. C. Dodart *et al.*, *Nat. Neurosci.* **5**, 452 (2002).
23. L. Jones *et al.*, *PLoS ONE* **5**, e13950 (2010).
24. P. Hollingworth *et al.*, *Nat. Genet.* **43**, 429 (2011).
25. A. C. Naj *et al.*, *Nat. Genet.* **43**, 436 (2011).

Acknowledgments: We thank Dr. Mangelsdorf for discussions and M. Pendergast, G. Casadesus, and I. Nagle for technical assistance. This work was supported by the Blanchette Hooker Rockefeller Foundation, Thome Foundation, Roby and Taft Funds for Alzheimer's Research, Painstone Foundation, American Health Assistance Foundation, Cure Alzheimer's Fund, Coins for Alzheimer's Research Trust, and the National Institute on Aging (NIA) (grant AG030482-03S1 to G.E.L.); National Institute on Deafness and Other Communication Disorders (grant DC003906, RO1-AG037693 to D.A.W); NIA (grants K01 AG029524 and P50-AG005681), Shmerler family, and the Charles F. and Joanne Knight Alzheimer's Disease Research Center at Washington University (to J.R.C.); and Marian S. Ware Alzheimer Program (to K.R.B.). All raw data are archived on \\gel-server1 for authorized users. P.E.C. and G.E.L. hold U.S. Provisional Patent Application no. 61/224,709 regarding bexarotene as a potential therapeutic for Alzheimer's disease and are founding scientists of ReXceptor, Inc., which has licensing options from Case Western Reserve University on the use of bexarotene in the treatment of Alzheimer's disease.

Supporting Online Material

www.sciencemag.org/cgi/content/full/science.1217697/DC1
Materials and Methods
Figs. S1 to S7
References (*26*–*31*)

9 December 2011; accepted 20 January 2012
Published online 9 February 2012;
10.1126/science.1217697

Long-Range–Projecting GABAergic Neurons Modulate Inhibition in Hippocampus and Entorhinal Cortex

Sarah Melzer,[1]* Magdalena Michael,[1]* Antonio Caputi,[1]* Marina Eliava,[1] Elke C. Fuchs,[1] Miles A. Whittington,[2] Hannah Monyer[1]†

The hippocampus and entorhinal cortex play a pivotal role in spatial learning and memory. The two forebrain regions are highly interconnected via excitatory pathways. Using optogenetic tools, we identified and characterized long-range γ-aminobutyric acid–releasing (GABAergic) neurons that provide a bidirectional hippocampal-entorhinal inhibitory connectivity and preferentially target GABAergic interneurons. Activation of long-range GABAergic axons enhances sub- and suprathreshold rhythmic theta activity of postsynaptic neurons in the target areas.

The excitatory projections connecting the hippocampus and entorhinal cortex (*1*) account for the functional interdependence of these two brain regions (*2*–*4*). Excitatory neurons in the hippocampus and entorhinal cortex are under control of local γ-aminobutyric acid–releasing (GABAergic) interneurons (*5*, *6*). Some GABAergic neurons also project long distance. For example, long-range–projecting GABAergic cells connect hippocampus with medial septum (*7*–*9*) and other extra-hippocampal brain areas (*10*, *11*), suggesting that interregional GABAergic connectivity might be less rare than was previously assumed (*12*).

To test for the presence of hippocampal GABAergic neurons projecting to the medial enthorinal cortex (MEC), we injected the retrograde tracer fluorogold (FG) into the MEC of wild-type mice (fig. S1). In addition to the expected labeling of numerous excitatory cells, we found FG^+ neurons in stratum oriens and stratum radiatum of CA1 and in the hilus of the dentate gyrus (DG), indicating retrogradely labeled GABAergic cells. We detected FG-labeled cells coexpressing somatostatin (SOM) in stratum oriens of CA1 (23 cells, nine mice) and also in the hilus of the DG (14 cells, nine mice) (Fig. 1, A and B).

[1]Department of Clinical Neurobiology of the Medical Faculty of Heidelberg University and German Cancer Research Center (DKFZ), Im Neuenheimer Feld 280, 69120 Heidelberg, Germany. [2]Institute of Neurosciences, The Medical School, Newcastle University, Framlington Place, Newcastle, NE2 4HH, UK.

*These authors contributed equally to this work.
†To whom correspondence should be addressed. E-mail: h.monyer@dkfz-heidelberg.de

To provide direct evidence for the presence of hippocampal SOM$^+$ neurons projecting to the MEC, we injected the adeno-associated viral (AAV) vector AAV DIO *ChR2-mCherry* (*13*) into the dorsal hippocampus of *SOM^{Cre}* mice (Fig. 1C and fig. S2), achieving specific expression of the fluorescent fusion protein ChR2-mCherry in SOM$^+$ neurons (Fig. 1C). We detected mCherry-labeled axons of SOM$^+$ hippocampal neurons in the medial septum and the contralateral DG (Fig. 1D) (*14*, *15*). We also detected labeled axons originating from hippocampal SOM$^+$ neurons in the striatum (fig. S3) and MEC (Fig. 1E). In the MEC, long-range–projecting axons crossed orthogonally from layer VI (LVI) to LII, branched in the

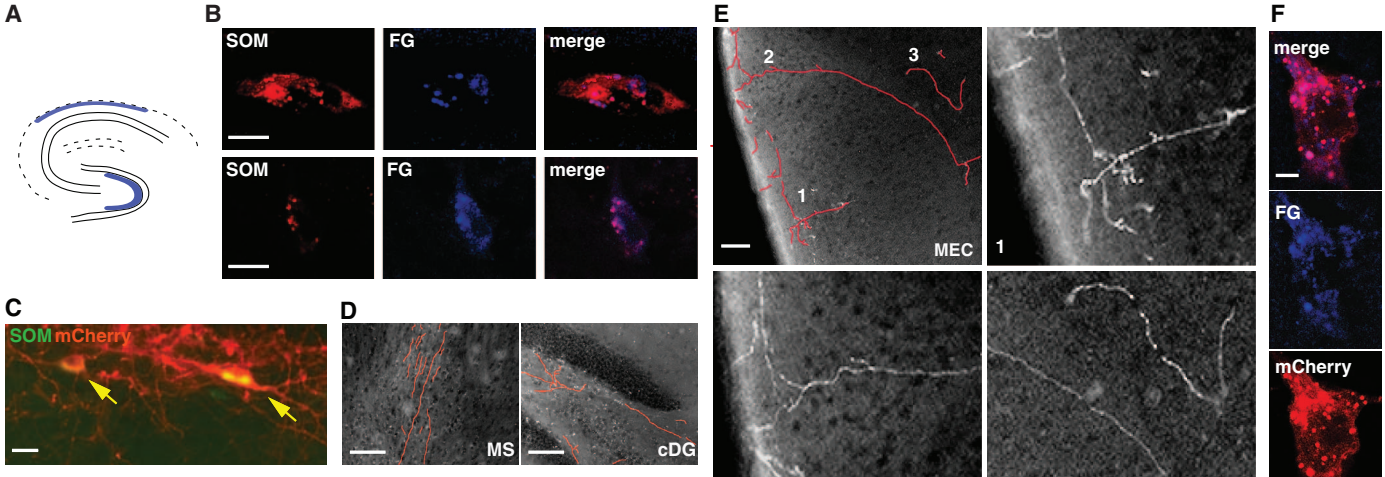

Fig. 1. Long-range–projecting hippocampal SOM$^+$ neurons target superficial layers in the MEC. (**A**) Schematic drawing showing the location of retrogradely labeled SOM$^+$ cells in CA1 and DG of the dorsal hippocampus after FG injection into the MEC. (**B**) Confocal images of a SOM$^+$/FG–labeled neuron in stratum oriens of CA1 (top row) and the hilus of the DG (bottom row). Scale bar, 10 μm. (**C**) Coexpression of SOM and ChR2-mCherry in CA1 stratum oriens after virus injection into the dorsal hippocampus in a *SOM^{Cre}* mouse. ChR2-mCherry expression was restricted to SOM$^+$ cells (yellow arrows). Scale bar, 30 μm. (**D**) Digitally encoded (red) mCherry$^+$ axons of long-range–projecting hippocampal SOM$^+$ cells detected in medial septum (MS, left) and contralateral DG (right). Scale bar, 100 μm. (**E**) Digitally encoded (red) mCherry$^+$ axons of long-range–projecting hippocampal SOM$^+$ cells in the MEC. Projections indicated by numbers are shown as higher magnification. Scale bar, 150 μm. (**F**) Confocal images of a mCherry and FG double-labeled cell in stratum oriens of the CA1 region after virus injection into dorsal hippocampus and FG injection into the MEC. Scale bar, 10 μm.

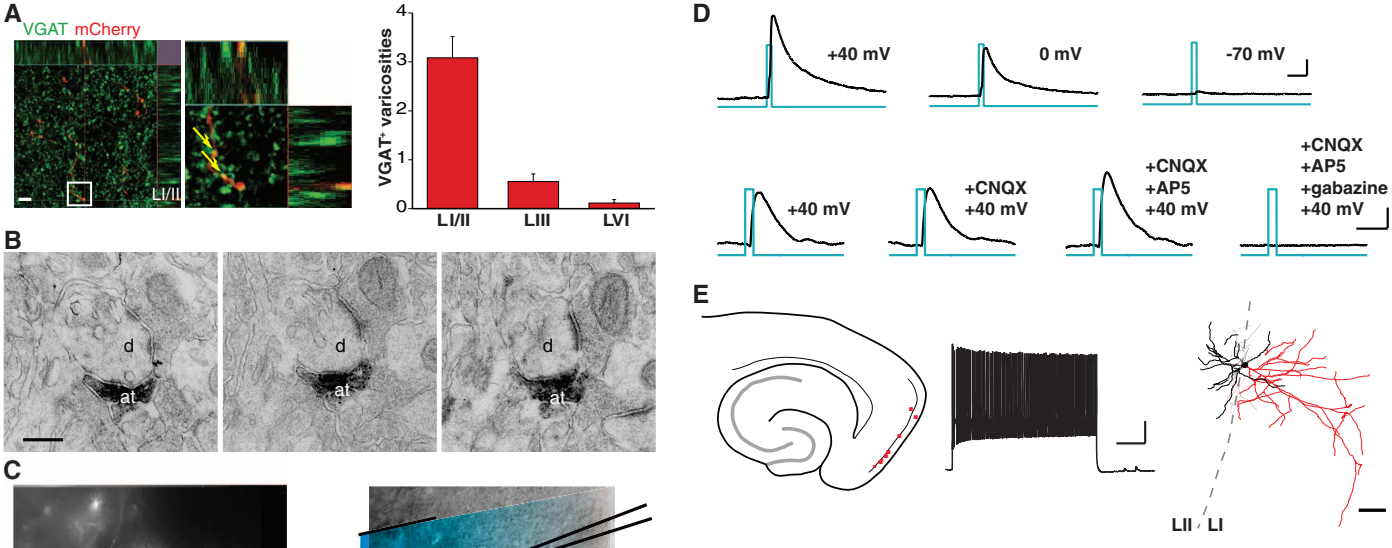

Fig. 2. Hippocampal SOM$^+$-projecting neurons form inhibitory synapses onto GABAergic neurons in the MEC. (**A**) VGAT$^+$ varicosities (arrows) of mCherry-labeled long-range projections in layer I/II of the MEC (left) and quantification in the indicated layers of the MEC. (Right) Bar histogram representing average number of VGAT$^+$ varicosities (60 optical sections, 2500 μm^2 each, mean ± SEM; five hemispheres of three mice). Scale bar, 5 μm. (**B**) Electronmicrographs showing serial sections of an immunogold-labeled ChR2-mCherry–expressing axon terminal (at) that forms a symmetric synapse onto a dendrite (d). Scale bar, 0.25 μm. (**C**) Fluorescence image of mCherry-labeled axons in the MEC (left). Asterisk indicates the location of a target cell shown in the DIC image (right). Presynaptic axon was stimulated with blue laser light, and PSCs were recorded in the target cell. Scale bar, 25 μm. (**D**) Inhibitory PSCs recorded in a target cell at indicated holding potentials. Responses could be blocked by gabazine but not CNQX and AP5. Scale bars, 20 ms and 50 pA. (**E**) Schematic drawing of a horizontal section showing the location of target neurons (red dots) that were biocytin-filled for subsequent reconstruction (left). Firing pattern most frequently found in MEC target cells (middle). Scale bars, 200 ms and 20 mV. (Right) A representative reconstructed target cell (dendrites, black; axon, red). Scale bar, 100 μm.

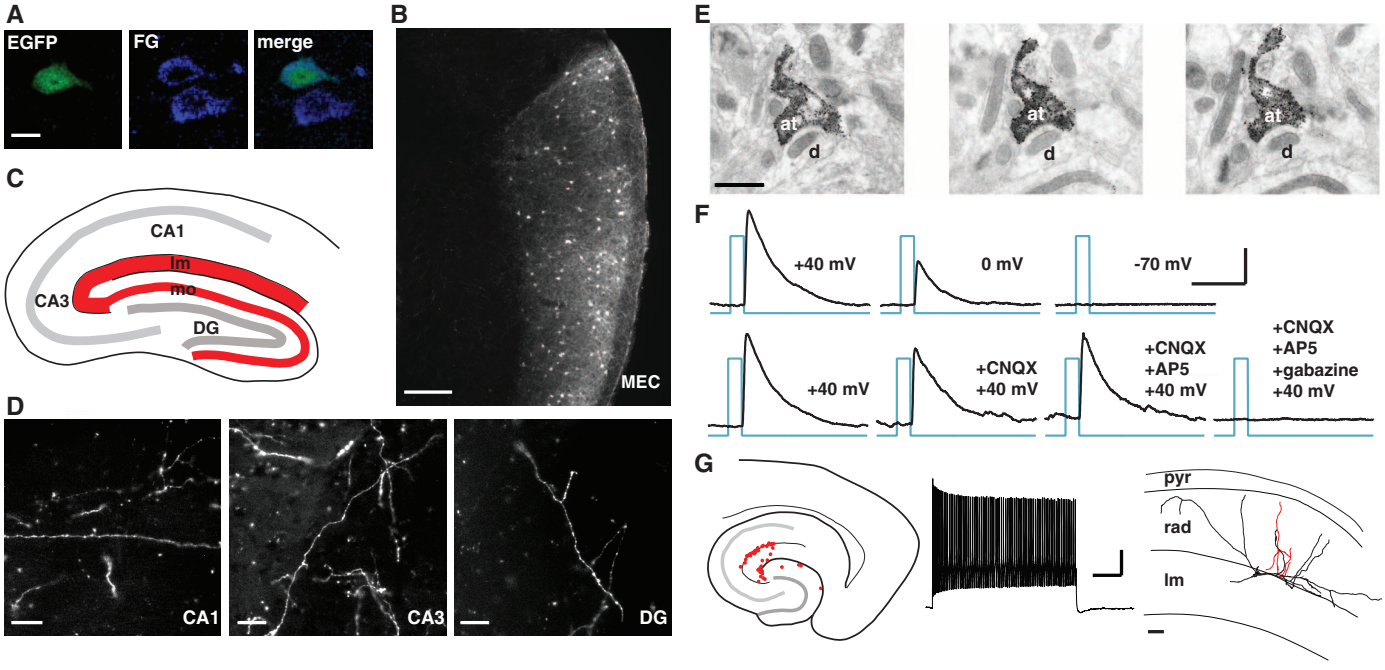

Fig. 3. MEC long-range GABAergic neurons form functional synapses onto GABAergic neurons in the hippocampus. (**A**) Retrogradely labeled GABAergic cell in the MEC after FG injection into the dorsal hippocampus of a *GAD67*^{EGFP} mouse. Scale bar, 10 μm. (**B**) mCherry expression in MEC GABAergic cells subsequent to AAV DIO *ChR2-mCherry* injection into a *GAD*^{Cre} mouse. Scale bar, 500 μm. (**C**) Schematic drawing of a sagittal hippocampal section indicating areas targeted by long-range–projecting MEC GABAergic neurons (red). (**D**) Fluorescent axons are located in stratum lacunosum-moleculare (lm) of the CA1 and CA3 areas and in stratum moleculare (mo) of the DG. Scale bars, 25 μm (CA1) and 12.5 μM (CA3 and DG). (**E**) Electronmicrographs showing serial sections of an immunogold-labeled ChR2-mCherry–expressing axon terminal (at) that forms a symmetric synapse onto a dendrite (d). Scale bar, 0.5 μm. (**F**) Inhibitory PSCs recorded in a target cell in stratum lacunosum-moleculare at indicated holding potentials. Response was blocked by gabazine but not CNQX or AP5. Scale bars, 20 ms and 50 pA. (**G**) Schematic drawing of a horizontal section of the intermediate hippocampus indicating the location of responsive target cells (red dots). Firing pattern most frequently found in hippocampal target cells (middle). Scale bars, 200 ms and 20 mV. (Right) Corresponding reconstruction in a sagittal section. Scale bar, 100 μm.

transition zone between LII and LI, and extended horizontally within LI over a distance of up to several 100 μm (Fig. 1E). We usually observed one to three projections per 50-μm section. Combining virus injection into the dorsal hippocampus with retrograde tracer injection into the MEC, we found individual CA1 neurons that were co-labeled with mCherry and FG (Fig. 1F). The population of hippocampal SOM$^+$ long-range–projecting neurons targeting the MEC appears to be distinct from the one projecting to the medial septum (fig. S4).

Using immmunohistochemistry, electron microscopy (EM), and whole-cell patch-clamp recordings, we subsequently investigated whether long-range–projecting hippocampal SOM$^+$ neurons form inhibitory synapses in the MEC. The mCherry-labeled axons were VGAT$^+$ and VGluT1-negative (Fig. 2A) and established symmetric synapses in LI and LII (Fig. 2B). We tested for functional synapses by laser-stimulating ChR2-mCherry–expressing terminals and recording from putative postsynaptic cells located in the vicinity of the labeled axons (Fig. 2C). Responses could be detected in 60 out of 686 patched cells (n = 41 mice). At +40 mV, the mean amplitude of the postsynaptic currents (PSCs) was 84.15 ± 11.94 pA, and the mean latency was 3.13 ± 0.22 ms (n = 37 cells). PSCs were inhibitory, as indicated by the reversal potential (~–70 mV, n = 25 out of 25 cells), the pharmacological block of the responses by the GABA type A ($GABA_A$) receptor antagonist gabazine (n = 17 out of 17 cells), and the lack of effect using the glutamatergic blockers 6-cyano-7-nitroquinoxaline-2,3-dione (CNQX) and (2*R*)-amino-5-phosphonovaleric acid (AP5) (n = 3 out of 3 cells) (Fig. 2D). All target cells identified through whole-cell recording were located close to or at the transition zone between LI and LII (Fig. 2E and fig. S5).

Hippocampal SOM$^+$ long-range–projecting neurons preferentially targeted GABAergic interneurons in the MEC. On the basis of their firing pattern, out of 20 target cells 16 could be classified as interneurons and 4 as stellate cells. The firing pattern of the interneurons was not uniform, indicating that they comprised different subtypes (fig. S6). Biocytin-filling revealed that axons of target cells arborized mainly in LI (n = 6 cells, three mice) (Fig. 2E).

FG injection into the MEC suggested that in addition to SOM$^+$ cells, other hippocampal GABAergic neurons project to the MEC (fig. S1B). AAV DIO *ChR2-mCherry* injection into the dorsal hippocampus of *GAD*^{Cre} mice (*16*) resulted in a larger number of labeled long-range–projecting axons that were VGAT$^+$ and covered additional target fields in the MEC (such as the presence of branches also in deeper layers) (fig. S7). Nineteen target cells were identified upon laser stimulation, and when tested, on the basis of the firing pattern all target cells were GABAergic (n = 12 out of 12 cells).

Retrograde labeling experiments have indicated the presence of long-range–projecting GABAergic cells in the opposite direction, from the entorhinal cortex to the hippocampus (*17*). When dorsal hippocampi of *GAD67*^{EGFP} mice were FG-injected, we detected FG/enhanced green fluorescent protein (EGFP) double-labeled cells in LII and LIII of the MEC (10 out of 1147 FG$^+$ cells counted, n = 5 mice) (Fig. 3A). We therefore injected AAV DIO *ChR2-mCherry* into the MEC of *GAD*^{Cre} mice (Fig. 3B) and readily detected mCherry-labeled axons in stratum lacunosum-moleculare/radiatum of the hippocampal CA areas, and stratum moleculare of the DG (Fig. 3, C and D).

We also analyzed the entorhinal-hippocampal connections anatomically and functionally. Fluorescently labeled long-range axons were VGAT$^+$ (fig. S8), and EM analysis of labeled axons in stratum lacunosum-moleculare/radiatum (n = 6 mice) showed that long-range projections formed symmetric synapses (Fig. 3E). Laser stimulation of presynaptic ChR2-expressing long-range projections allowed the identification of 86 responding target cells (out of ~1000 patched neurons from 65 mice) (mean amplitude and latency of PSCs at +40 mV was 101.45 ± 22.75 pA and 4.47 ± 0.50 ms, respectively; n = 19 cells) (Fig. 3F).

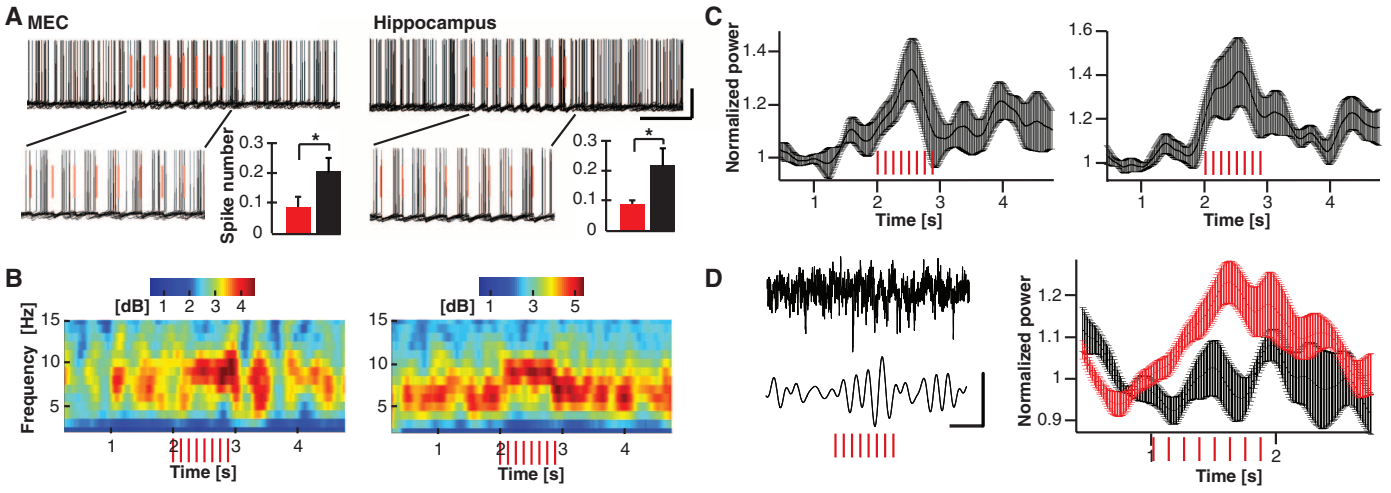

Fig. 4. Activation of GABAergic long-range projections enhances rhythmic activity in the MEC and the hippocampus. MEC target cells in hippocampal AAV DIO *ChR2-mCherry*–injected *SOM*^{Cre} mice [(A) to (C), left] and hippocampal target cells in MEC AAV DIO *ChR2-mCherry*–injected *GAD*^{Cre} mice [(A) to (C), right] cells were patched and depolarized to suprathreshold potentials. Long-range projections were stimulated at 8 Hz (red ticks). (**A**) Overlay of 20 unfiltered traces recorded in a target cell, with indicated enlargement of action potential firing during the stimulation period. Scale bars, 40 mV and 500 ms. Histogram below indicates mean number of spikes ± SEM within the first 62.5-ms interval directly after laser stimulation (red bar) and the subsequent 62.5-ms interval (black bar). (**B**) Spectrogram showing that activation of long-range–projecting axons entrains target cell to fire rhythmically at theta range frequency. (**C**) Increase in theta power (7 to 9 Hz) in target cells during laser stimulation. (**D**) Representative unfiltered (top) and filtered (3 to 7 Hz, bottom) trace of DHPG/NBQX–induced CA1 theta oscillations. (Right) Averaged power of 3- to 7-Hz oscillations normalized to power before stimulation for wild-type (black) and *GAD*^{Cre}-injected mice (red). Scale bars, 500 ms and 0.1 mV.

The GABAergic nature of these synapses was also confirmed by the reversal potential (n = 12 out of 12 cells) and selective gabazine blockage (n = 17 out of 17 cells). All detected target cells were located in dorsal and intermediate hippocampal areas that are known to contain interneurons only—namely, stratum lacunosum-moleculare and deep stratum radiatum in all CA areas and in stratum moleculare of the DG (Fig. 3G). In more than 110 pyramidal and granule cells that were patched, no PSCs could be detected, suggesting a preferential, if not even exclusive, targeting of GABAergic interneurons. The firing pattern (n = 26 cells) (Fig. 3G and fig. S9) and morphology (n = 19 cells) (Fig. 3G) of the target cells confirmed their interneuronal phenotype.

To establish the immunochemical identity of MEC GABAergic projection neurons, we combined FG retrograde labeling and immunohistochemistry, using different interneuron markers. FG/EGFP double-labeling in the MEC was found in a subpopulation of parvalbumin^{+} (PV) neurons (fig. S10A) and in additional GABAergic neurons of unknown immunochemical identity. Injection of AAV DIO *ChR2-mCherry* into the MEC of *PV*^{Cre} (*18*) mice further substantiated the finding that MEC PV^{+} cells projected to the hippocampus (fig. S10B) and formed functional synapses on hippocampal interneurons (n = 5 electrophysiologically identified target cells in CA1-3 and DG) (fig. S10, C and D).

To directly investigate whether long-range GABAergic cells modulate the activity of targeted cells, we recorded sub- and suprathreshold activity in targeted interneurons in slices of the MEC and the hippocampus during stimulation of long-range–projecting axons. Laser stimulation at 8 Hz for 1 s enhanced rhythmic firing of the postsynaptic neuron, as indicated by the reduction of the action potential number during the first half of each 125-ms-pulse interval in target cells in the MEC (n = 5 cells, P = 0.03) and in the hippocampus (n = 6 cells, P = 0.02) (Fig. 4A). Thus, axonal stimulation resulted in an increase in rhythmicity in theta range, as shown by the spectrogram of individual neurons (Fig. 4B) and the comparison of theta power during and before stimulation (n = 5 and 6 and P = 0.03 and 0.02 for MEC and hippocampus target cells, respectively) (Fig. 4C). There was no significant difference in the overall firing rate before, during, and after stimulation (fig. S11A). Axonal stimulation at 40 Hz frequency did not affect rhythmic firing of target cells (n = 7 and 5 for MEC and hippocampus, respectively) (fig. S11, B and C). Axonal stimulation at 8 Hz also increased subthreshold oscillations at theta frequency (n = 10 and 7 and P = 0.0002 and 0.02 for MEC and hippocampus target cells, respectively) (fig. S11, D to G).

Last, because theta oscillations can be induced pharmacologically in acute hippocampal slices (*19*) we analyzed whether recruitment of long-range GABAergic cells affected network activity. We recorded (*S*)-3,5-dihydroxyphenylglycine (DHPG)/2,3-dihydroxy-6-nitro-7-sulfamoyl-benzo[f]quinoxaline-2,3-dione (NBQX)–induced theta oscillations in the CA1 region. Hippocampal 8-Hz laser stimulation of MEC-derived axons increased theta power (3 to 7 Hz) significantly in slices obtained from MEC virus-injected *GAD*^{Cre} (n = 14 slices, $P < 0.05$) but not wild-type mice (n = 7 slices, $P > 0.1$) (Fig. 4D). Stimulation at 40 Hz did not change gamma power (n = 12 slices) (fig. S11H).

Using optogenetic viral tracing, we identified long-range GABAergic neurons connecting the hippocampus and the MEC. Furthermore, we provided functional evidence that long-range GABAergic neurons target local interneurons whose activity they modulate. It has been postulated that long-range–projecting GABAergic neurons might be an ideal substrate to precisely coordinate activity between distant brain regions (*20*). Long-range GABAergic neurons in the hippocampal-entorhinal formation might well account for the highly synchronized theta activity in the hippocampus and entorhinal cortex (*21*) and thus contribute to the proposed mechanisms underlying spatial and temporal coding and ultimately spatial memory (*22*, *23*).

References and Notes

1. C. B. Canto, F. G. Wouterlood, M. P. Witter, *Neural Plast.* **2008**, 1 (2008).
2. A. Bragin *et al.*, *J. Neurosci.* **15**, 47 (1995).
3. V. H. Brun *et al.*, *Neuron* **57**, 290 (2008).
4. A. Ylinen *et al.*, *Hippocampus* **5**, 78 (1995).
5. T. Klausberger, P. Somogyi, *Science* **321**, 53 (2008).
6. R. D. Traub, A. Bibbig, F. E. LeBeau, E. H. Buhl, M. A. Whittington, *Annu. Rev. Neurosci.* **27**, 247 (2004).
7. T. F. Freund, M. Antal, *Nature* **336**, 170 (1988).
8. V. T. Takács, T. F. Freund, A. I. Gulyás, *Eur. J. Neurosci.* **28**, 148 (2008).
9. K. Tóth, Z. Borhegyi, T. F. Freund, *J. Neurosci.* **13**, 3712 (1993).
10. S. Jinno *et al.*, *J. Neurosci.* **27**, 8790 (2007).
11. J. Apergis-Schoute, A. Pinto, D. Paré, *J. Neurosci.* **27**, 4061 (2007).
12. N. Tamamaki, R. Tomioka, *Front. Neurosci.* **4**, 202 (2010).

13. J. A. Cardin *et al.*, *Nat. Protoc.* **5**, 247 (2010).
14. S. Jinno, T. Kosaka, *Brain Res.* **945**, 219 (2002).
15. C. A. Zappone, R. S. Sloviter, *J. Comp. Neurol.* **441**, 324 (2001).
16. S. Tolu *et al.*, *FASEB J.* **24**, 723 (2010).
17. P. Germroth, W. K. Schwerdtfeger, E. H. Buhl, *Brain Res.* **494**, 187 (1989).
18. E. C. Fuchs *et al.*, *Neuron* **53**, 591 (2007).
19. M. J. Gillies *et al.*, *J. Physiol.* **543**, 779 (2002).
20. G. Buzsáki, J. J. Chrobak, *Curr. Opin. Neurobiol.* **5**, 504 (1995).
21. K. Mizuseki, A. Sirota, E. Pastalkova, G. Buzsáki, *Neuron* **64**, 267 (2009).
22. J. O'Keefe, L. Nadel, *The Hippocampus as a Cognitive Map* (Oxford Univ Press, Oxford, 1978).
23. M. P. Witter, E. I. Moser, *Trends Neurosci.* **29**, 671 (2006).

Acknowledgments: We thank K. Deisseroth for the AAVs, A. Vogt for help in generating mice, I. Preugschat-Gumprecht and R. Hinz for their technical assistance, and P. H. Seeburg for helpful discussions. This work was supported by a European Research Council grant (GABAcellsAndMemory grant 250047, to H.M.) and a German Ministry of Education and Research (BMBF) grant 01GQ1003A to H.M. and E.C.F.

Supporting Online Material
www.sciencemag.org/cgi/content/full/335/6075/1506/DC1
Materials and Methods
Figs. S1 to S11
References

28 November 2011; accepted 10 February 2012
10.1126/science.1217139

Glucocorticoids Can Induce PTSD-Like Memory Impairments in Mice

Nadia Kaouane,[1,2,3] Yves Porte,[1,2]* Monique Vallée,[2,3] Laurent Brayda-Bruno,[1,2,3] Nicole Mons,[1,2]† Ludovic Calandreau,[4] Aline Marighetto,[1,2,3] Pier Vincenzo Piazza,[2,3]‡§ Aline Desmedt[1,2,3]‡§

Posttraumatic stress disorder (PTSD) is characterized by a hypermnesia of the trauma and by a memory impairment that decreases the ability to restrict fear to the appropriate context. Infusion of glucocorticoids in the hippocampus after fear conditioning induces PTSD-like memory impairments and an altered pattern of neural activation in the hippocampal-amygdalar circuit. Mice become unable to identify the context as the correct predictor of the threat and show fear responses to a discrete cue not predicting the threat in normal conditions. These data demonstrate PTSD-like memory impairments in rodents and identify a potential pathophysiological mechanism of this condition.

Situations surrounding threatening events are better remembered than the ones accompanying neutral ones. This hypermnesia for environments and cues predicting threats is important for adaptation because it increases the probability of survival in uncontrolled environments. In humans, the exposure to threatening situations can also result in memory impairments culminating in severe pathological states such as posttraumatic stress disorder (PTSD) (*1*). In this case, a hypermnesia for the core traumatic event is associated with a memory deficit for peritraumatic contextual cues (*2*, *3*), impairing the capacity of the subject to identify the correct predictors of the threat and restrict fear to the correct place and/or to the correct cues. This deficit contributes to the intrusive recollection—re-experiencing the fear response in safe situations—that characterizes PTSD.

Animal models of traumatic memories and PTSD principally focus on the quantitative aspect of fear memories: an increased and persistent fear response (*4*). In contrast, the critical landmark of PTSD—the inability of the subject to restrict fear responses to the appropriate predictors—is largely neglected. As a consequence, the biological mechanisms of pathological PTSD-like memories remain largely unknown.

To address this issue, we analyzed whether PTSD-like memory impairments can be observed in mice. We therefore injected the stress hormone corticosterone, the major glucocorticoid in rodents, into the hippocampus of mice submitted to a fearful situation. Glucocorticoids increase in response to stress, enhance stress-related memories (*5*–*8*), and have been involved in the pathophysiology of PTSD (*9*, *10*). The hippocampus plays an important role in memory (*11*), is the major brain target of glucocorticoids (*12*, *13*), and seems impaired in PTSD (*14*, *15*).

We then developed a behavioral model that allows evaluating the ability of the individuals to restrict fear responses to the appropriate predictor of the threatening stimulus. Mice were first submitted to a threatening situation, the delivery of an electric footshock, when exposed to a discrete cue (a tone) in a specific context (conditioning cage). Twenty-four hours after this conditioning procedure, animals were re-exposed first to the cue alone in a familiar and safe environment and then to the conditioning context without the cue (*16*).

We used two distinct conditioning schedules that contained exactly the same nature and quantities of environmental stimuli but, differing in their associations, identified different predictors of the threat (*17*, *18*). In one schedule, the presentation of the tone was always followed by the delivery of the shock (predicting-cue group). In this case, animals identified the tone as the main predictor of the threat, showing conditioned fear when re-exposed to the cue alone but not to the context (Fig. 1A). During the second schedule, the tone presentation was never followed by the delivery of the shock (predicting-context group). In this case, animals identified the conditioning context as the correct predictor of the threat, showing conditioned fear when re-exposed to the context alone but not to the cue (Fig. 1A). As expected, in both conditions fear responses to the correct predictor progressively increased as a function of the threat intensity.

Corticosterone (10 ng per side) was infused into the dorsal hippocampus immediately after conditioning with three footshock intensities (0.3, 0.5, and 0.8 mA). In the predicting-cue group, corticosterone did not significantly modify fear responses (Fig. 1B). This is not surprising because the hippocampus is necessary for contextual conditioning but is dispensable for cue conditioning (*19*, *20*). In animals in which the context predicted the threat (predicting-context group), as expected (*6*, *7*) corticosterone administered after the lowest shock intensity (0.3 mA) enhanced conditioned fear to the context (Fig. 1B). However, when corticosterone followed the highest shock intensity (0.8 mA) PTSD-like memory impairments appeared. Animals did not show fear in response to the correct predictor of the threat, the context, but in response to the tone (Fig. 1B), which is normally not a relevant predictor of the threat for them. Animals infused with corticosterone also showed a fear response to a previously unexperienced cue (2 kHz tone) at some extent similar to the one (1 kHz tone) experienced during conditioning (Fig. 1C), but not in response to a completely different cue (white noise). In contrast, the fear response in the predicting-cue group was exclusively restricted to the conditioning cue. In conclusion, hippocampal corticosterone infusions impaired the ability of the subject to restrict fear responses to the appropriate predicting cues.

In physiological conditions, corticosterone increases systemically in response to stress. We then analyzed whether the exposure to a second stress, the restraint in a cylinder for 20 min, could also induce PTSD-like memory impairments. Similar to intrahippocampal corticosterone infusions, when the second stress followed the low shock intensity (0.3 mA) conditioned fear to the context

[1]CNRS UMR 5228, Centre de Neurosciences Intégratives et Cognitives, 33405 Talence, France. [2]Department of Life Science, Université de Bordeaux, 33077 Bordeaux, France. [3]INSERM U862, Neurocentre Magendie, 146 rue Leo Saignat, 33077 Bordeaux, France. [4]Institut National de la Recherche Agronomique (INRA) Centre de Tours Nouzilly, Physiologie de la Reproduction et des Comportements, CNRS UMR 6175, INRA UMR 85, Université de Tours–Haras Nationaux, 37380 Nouzilly, France.

*Present address: Institut des Maladies Neurodégénératives, CNRS UMR 5293, Universités Bordeaux 1 et 2, Avenue des Facultés, 33405 Talence, France.
†Present address: Institut de Neurosciences Cognitives et Intégratives d'Aquitaine, CNRS UMR 5287, Universités Bordeaux 1 et 2, Avenue des Facultés, 33405 Talence, France.
‡These authors contributed equally to this work.
§To whom correspondence should be addressed. E-mail: aline.desmedt@inserm.fr (A.D.); pier-vincenzo.piazza@inserm.fr (P.V.P.)

increased (Fig. 2A). However, when the second stress followed the high shock intensity (0.8 mA) PTSD-like memory impairments appeared. These effects of stress are attributable to stress-induced corticosterone secretion. Thus, systemic (intraperitoneal) corticosterone injections, in a range of doses (from 0.75 to 2.5 mg/kg) that encompasses the increase in corticosterone induced by several types of stress (fig. S1B), increased fear responses to

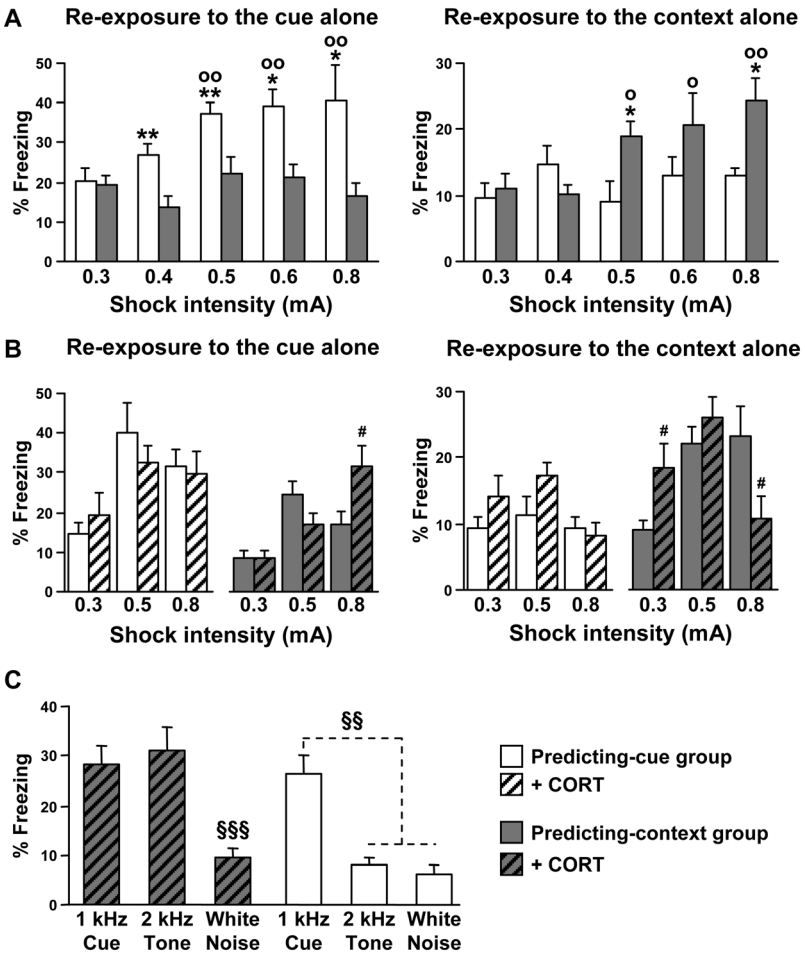

Fig. 1. Corticosterone infusion in the hippocampus induces PTSD-like memory impairments. (**A**) Increasing shock intensity progressively produced higher fear responses to the right predictor of the threat [all $F > 4.67$, $P < 0.01$]: in the predicting-cue groups to the cue alone (left) and in the predicting-context groups to the context alone (right). (**B**) In the context-predicting group, corticosterone (CORT) infusions in the hippocampus increased fear response to the context for a low-intensity threat (0.3 mA). After a high-intensity threat (0.8 mA), corticosterone induced PTSD-like memory impairments, suppressing the response to the correct predictor (the context) and increasing the fear response for the wrong predictor (the cue). (**C**) Corticosterone increased the response to a cue similar (2 kHz tone) to the one used for conditioning (1 kHz cue) but not to a very different cue (white noise). $^{*}P < 0.05$, $^{**}P < 0.01$, group comparisons; $^{\circ}P < 0.05$, $^{\circ\circ}P < 0.01$ versus 0.3 mA; $^{\#}P < 0.05$, aCSF versus CORT; §§$P < 0.01$, §§§$P < 0.001$ versus 1 kHz cue [Fisher's partial least-squares difference (PLSD)].

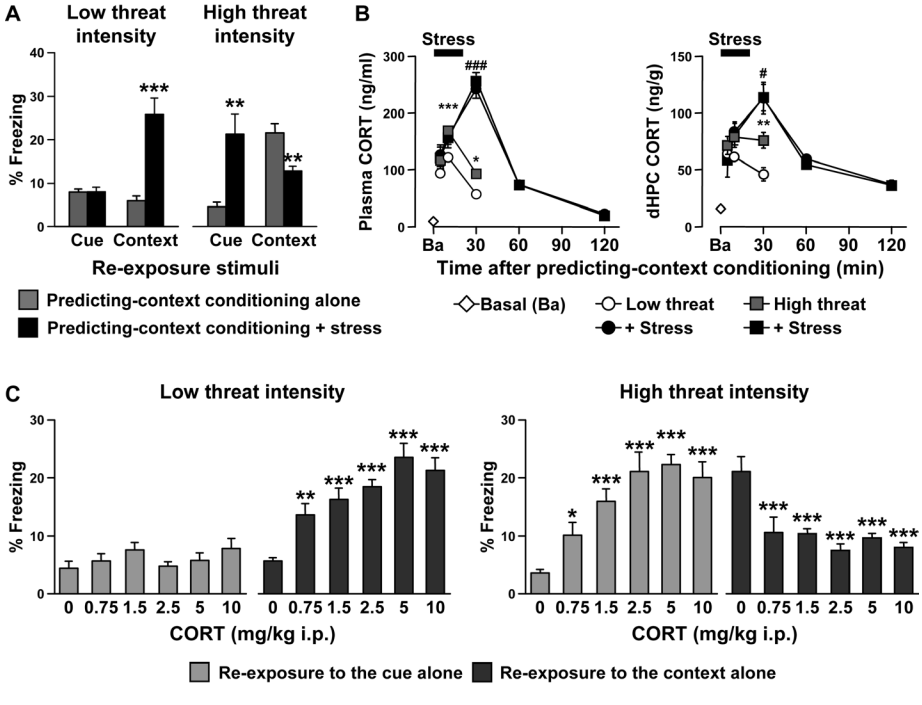

Fig. 2. Stress and systemic corticosterone injection induce PTSD-like memory impairments in the predicting-context group. (**A**) A second stress after conditioning with a low-intensity threat (0.3 mA shock) increased fear responses to the context. Stress after a high-intensity threat (0.8 mA shock) induced PTSD-like memory impairments, suppressing the response to the correct predictor (the context) and increasing the fear response for the wrong predictor (the cue). (**B**) Corticosterone (CORT) levels in the plasma and dorsal hippocampus (dHPC) were higher in the high-threat group and further increased after exposure to stress. (**C**) Intraperitoneal (i.p.) corticosterone injection after conditioning increased fear responses to the context for a low-intensity threat and induced PTSD-like memory impairments for a high-intensity threat. Ba, basal conditions; $^{*}P < 0.05$, $^{**}P < 0.01$, $^{***}P < 0.001$, versus control or 0 mg/kg CORT or low-intensity threat; $^{\#}P < 0.05$, $^{\#\#\#}P < 0.001$, versus high-intensity threat (Fisher's PLSD).

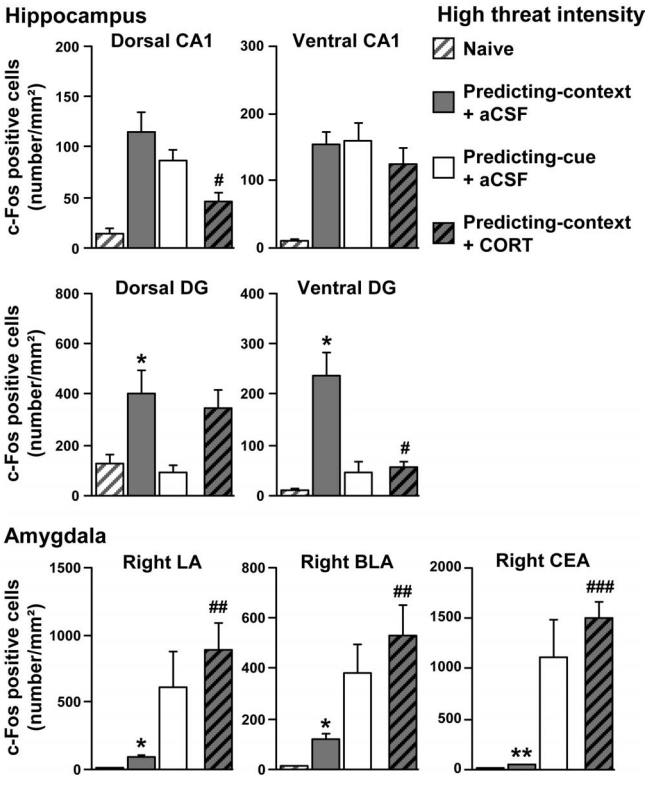

Fig. 3. PTSD-like memories were associated with an altered neural activity within the hippocampal-amygdalar circuit. In the control predicting-context group, c-Fos expression was high in the dentate gyrus (DG) of the hippocampus and low in the right amygdala [lateral (LA), basolateral (BLA), and central (CEA) nuclei]. The opposite pattern was observed in the predicting-cue group. Corticosterone (CORT) infusion in the predicting-context group decreased c-Fos expression in the dorsal CA1 and the ventral DG, whereas it increased c-Fos expression in the amygdala. $^{*}P < 0.05$, $^{**}P < 0.01$, Predicting-cue versus Predicting-context groups; $^{\#}P < 0.05$, $^{\#\#}P < 0.01$, $^{\#\#\#}P < 0.001$, aCSF versus CORT (Student's *t* test).

the context when injected after conditioning with a low threat (0.3 mA). In contrast, corticosterone, in the same range of concentrations, induced PTSD-like memory impairments when injected after conditioning with an intense threat (0.8 mA) (Fig. 2C). These differences between groups were maintained over the entire dose-response function of corticosterone, which included quite high doses (5 and 10 mg/kg) encompassing the entire range of corticosterone behavioral effects. Plasma and hippocampal corticosterone levels were higher in animals conditioned with the high shock intensity than in the ones conditioned with the low shock intensity (Fig. 2B). Stress or corticosterone injections increased corticosterone above the levels observed in the high shock intensity group, but differences between groups were suppressed (Fig. 2B), and this occurred even when the ED100 dose for the behavioral effects of corticosterone injections was studied (S1A). These results indicate that glucocorticoids induce PTSD-like memory impairments in a state-dependent manner. Corticosterone levels need to go above a certain threshold, and the threat needs to reach a certain intensity, for PTSD-like memory impairments to appear. These findings extend to PTSD state–dependent effects of glucocorticoids already described for the ability of these hormones to enhance the sensitivity to drugs of abuse (*21*), suggesting that this could be a general mechanism in the pathophysiology of stress-related disorders.

During acquisition of fear conditioning, the selection of the best predictor of the shock (tone versus context) requires different activations of the hippocampal-amygdalar circuit (*17*, *22*). The activation of these circuits, measured by the expression of the c-Fos protein, was analyzed 90 min after intrahippocampal infusion of either corticosterone (10 ng per side) or vehicle [artificial cerebrospinal fluid (aCSF)] in animals in the predicting-context group conditioned with the high shock intensity (0.8 mA). Because animals in the predicting-context group infused with corticosterone behaved similarly to control animals in the predicting-cue group, the latest group also was studied. In vehicle-infused mice, the correct identification of the context as predictor of the shock (predicting-context group) was associated with high levels of c-Fos expression in the dentate gyrus (DG) of the hippocampus and low levels of c-Fos expression in the amygdala. At the opposite, the identification of the cue as the correct predictor (predicting-cue group) was associated with low c-Fos levels in the DG and high c-Fos levels in the amygdala (Fig. 3). No significant differences between the two groups were observed in CA1 and CA3 (Fig. 3 and fig. S2). As previously observed (*23*), in the amygdala the response was completely lateralized and present only in the right hemisphere (Fig. 3 and fig. S2). Intrahippocampal corticosterone infusions in the predicting-context group decreased c-Fos expression in the dorsal CA1 and the ventral DG, whereas it increased c-Fos expression in the right amygdala. Thus, the pattern of c-Fos expression in the predicting-context group infused with corticosterone approximated the one observed in control animals for which the correct predictor was the cue.

During conditioning with an intense threat, an increase in glucocorticoid level in the hippocampus can generate PTSD-like memory impairments in mice. Animals in the predicting-context group infused with corticosterone after conditioning with the highest shock intensity did not show conditioned fear in response to the conditioning context, the correct predictor of the threat. These animals showed instead a fear response to salient cues that did not predict the threat in normal conditions: a tone that was part of the stressful experience but was never associated with shock delivery, and even a tone resembling the previous one but never experienced before. This impairment is very similar to the one observed in PTSD patients in which contextual peritraumatic cues are often forgotten, whereas salient but irrelevant ones are strongly remembered. These salient cues, and others more or less similar to them, can then induce a strong fear response in contexts different from the traumatic one (*1*, *2*).

PTSD-like memory impairments were associated with a switch in neural activation within the hippocampal-amygdalar circuit. In controls, the identification of the context as the right predictor of the threat was associated with low amygdalar activation and high activation in the DG, whereas the opposite pattern was observed in animals identifying the cue as the correct predictor. After corticosterone infusions, when the animals in the predicting-context group identified the cue instead of the context as the predictor of the threat, the activation of the right amygdala increased, whereas it decreased in the ventral DG and the dorsal CA1 of the hippocampus. This hippocampal subregion selectivity is consistent with both the critical role of the dorsal CA1 in the processing of contextual information and with the high sensitivity of the ventral DG to stress (*24*, *25*). The observed alterations in neural activation are also very similar to those observed in PTSD patients, showing an impaired hippocampal function, which is sometimes associated with decreased hippocampal volume (*14*), and an amygdalar hyperactivation in response to trauma-related cues (*26*), in particular in the right hemisphere (*27*, *28*). The relevance of an imbalance between the activity of the right and the left amygdala is also supported by the development of PTSD in a patient in which the left amygdala was surgically ablated (*29*).

These results provide solid evidence for the existence of PTSD-like memory impairments in rodents and identify one of the potential pathophysiological mechanisms of this condition. Understanding the molecular mechanisms through which high levels of glucocorticoids in the hippocampus can modify neural activation in the hippocampal-amygdalar circuit could open new avenues for the development of innovative treatments of PTSD.

References and Notes

1. APA, *Diagnostic and Statistical Manual of Mental Disorders IV—Text Revision* (American Psychiatric Press, Washington, DC, 2000).
2. B. M. Elzinga, J. D. Bremner, *J. Affect. Disord.* **70**, 1 (2002).

3. B. Layton, R. Krikorian, *J. Neuropsychiatry Clin. Neurosci.* **14**, 254 (2002).
4. S. Tronel, C. M. Alberini, *Biol. Psychiatry* **62**, 33 (2007).
5. J. L. McGaugh, B. Roozendaal, *Curr. Opin. Neurobiol.* **12**, 205 (2002).
6. J. M. Revest *et al*., *Nat. Neurosci.* **8**, 664 (2005).
7. J. M. Revest *et al*., *Mol. Psychiatry* **15**, 1125, 1140 (2010).
8. C. Sandi, M. T. Pinelo-Nava, *Neural Plast.* **2007**, 78970 (2007).
9. M. van Zuiden *et al*., *Biol. Psychiatry* **71**, 309 (2011).
10. R. Yehuda, *J. Clin. Psychiatry* **62** (suppl. 17), 41 (2001).
11. L. R. Squire, *Psychol. Rev.* **99**, 195 (1992).
12. B. S. McEwen, R. M. Sapolsky, *Curr. Opin. Neurobiol.* **5**, 205 (1995).
13. E. R. de Kloet, E. Vreugdenhil, M. S. Oitzl, M. Joëls, *Endocr. Rev.* **19**, 269 (1998).
14. J. D. Bremner, J. H. Krystal, S. M. Southwick, D. S. Charney, *J. Trauma. Stress* **8**, 527 (1995).
15. M. W. Gilbertson *et al*., *Nat. Neurosci.* **5**, 1242 (2002).
16. Materials and methods are available as supporting material on *Science* Online.
17. L. Calandreau *et al*., *J. Neurosci.* **26**, 13556 (2006).
18. A. Desmedt, R. Garcia, R. Jaffard, *J. Neurosci.* **18**, 480 (1998).
19. R. G. Phillips, J. E. LeDoux, *Behav. Neurosci.* **106**, 274 (1992).
20. J. J. Kim, M. S. Fanselow, *Science* **256**, 675 (1992).
21. P. V. Piazza, M. Le Moal, *Brain Res. Brain Res. Rev.* **25**, 359 (1997).
22. P. Trifilieff, L. Calandreau, C. Herry, N. Mons, J. Micheau, *Neurobiol. Learn. Mem.* **88**, 424 (2007).
23. A. P. Scicli, G. D. Petrovich, L. W. Swanson, R. F. Thompson, *Behav. Neurosci.* **118**, 5 (2004).
24. S. Brummelte, L. A. Galea, *Neuroscience* **168**, 680 (2010).
25. M. R. Hunsaker, R. P. Kesner, *Neurobiol. Learn. Mem.* **89**, 61 (2008).
26. I. Liberzon *et al*., *Biol. Psychiatry* **45**, 817 (1999).
27. S. L. Rauch *et al*., *Arch. Gen. Psychiatry* **53**, 380 (1996).
28. L. M. Shin *et al*., *Am. J. Psychiatry* **156**, 575 (1999).
29. S. D. Smith, B. Abou-Khalil, D. H. Zald, *J. Abnorm. Psychol.* **117**, 479 (2008).

Acknowledgments: We thank F. Naneix for helpful discussions and C. Dupuy, A. Faugere, A. Grel, and F. Rougé-Pont for technical help. N.K., A.D., and P.V.P. conceived and designed the experiments. N.K., M.V., N.M., Y.P., L.B.B., L.C., and A.D. performed the experiments. N.K., M.V., and A.D. analyzed the data. N.K., A.M., A.D., and P.V.P. wrote the manuscript. This work was supported by Centre National de la Recherche Scientifique, Institut National de la Santé et de la Recherche Médicale, Fondation pour la Recherche sur le Cerveau, Conseil Régional d'Aquitaine, Ministère de l'Enseignement supérieur et de la Recherche, and University of Bordeaux.

Supporting Online Material

www.sciencemag.org/cgi/content/full/science.1207615/DC1
Materials and Methods
Figs. S1 and S2
References

28 April 2011; accepted 9 February 2012
Published online 23 February 2012;
10.1126/science.1207615

Generation of a Synthetic Memory Trace

Aleena R. Garner,[1,2] David C. Rowland,[3] Sang Youl Hwang,[1] Karsten Baumgaertel,[1] Bryan L. Roth,[4] Cliff Kentros,[3] Mark Mayford[1,2]*

We investigated the effect of activating a competing, artificially generated, neural representation on encoding of contextual fear memory in mice. We used a *c-fos*–based transgenic approach to introduce the hM_3D_q DREADD receptor (designer receptor exclusively activated by designer drug) into neurons naturally activated by sensory experience. Neural activity could then be specifically and inducibly increased in the hM_3D_q-expressing neurons by an exogenous ligand. When an ensemble of neurons for one context (ctxA) was artificially activated during conditioning in a distinct second context (ctxB), mice formed a hybrid memory representation. Reactivation of the artificially stimulated network within the conditioning context was required for retrieval of the memory, and the memory was specific for the spatial pattern of neurons artificially activated during learning. Similar stimulation impaired recall when not part of the initial conditioning.

Direct electrical stimulation can be used to define functional domains in the brain, elicit stereotyped behavioral responses, drive self-stimulation behavior, and serve as conditioned or unconditioned stimuli in conditioning paradigms (*1*–*4*). This type of stimulation has typically been focal, using either microelectrodes or, more recently, genetically encoded mediators of neural excitability such as channelrhodopsin (*5*, *6*). Although such discrete, temporally coordinated, focal stimulation can drive behavior, we know much less about the effects of stimulating broadly distributed neural networks. The mammalian cortex displays substantial nonrandom, spontaneous neural activity that is internally generated rather than arising from sensory inputs, and this activity influences the processing of natural sensory stimuli (*7*–*10*). How does this internally generated activity influence the formation of a new memory representation?

To investigate this question, we used transgenic mice (Fig. 1A) in which the hM_3D_q receptor is expressed in an activity-dependent manner by a *c-fos* promoter–driven tTA transgene ($hM_3D_q^{fos}$ mice) (*11*, *12*). hM_3D_q is a G_q-coupled receptor that responds specifically to clozapine-*N*-oxide (CNO) and produces strong depolarization and spiking in pyramidal neurons (*12*). Transgenic mice exposed to a particular environmental stimulus will express hM_3D_q in those neurons that are sufficiently active to induce the *c-fos* promoter, and this naturally occurring neural ensemble can be subsequently reactivated artificially in the transgenic mice by delivery of CNO. Artificial activity induced in this manner will retain the spatial character of the neural ensemble, but will not preserve the temporal dynamics achieved by natural stimuli.

The expression of hM_3D_q is widely distributed in the brain of $hM_3D_q^{fos}$ double transgenic mice in the absence of doxycycline (Dox), enabling tTA-driven transcription (Fig. 1, B and C). Within a given brain area, expression is limited to a fraction of excitatory neurons that are sufficiently active to drive the *c-fos* promoter. Dox can be used to control the specific time window in which active neurons are genetically tagged with hM_3D_q by modulating tTA-driven transcription (*11*, *13*). To test the kinetics of CNO-based neural activation in these animals, we performed in vivo recording in the hippocampus of anesthetized animals. We found an increase in neuronal activity that reached a maximum intensity between 30 and 40 min after CNO injection (Fig. 1D). To examine the increase in neural activity more broadly, we used endogenous *c-fos* expression as an indicator of neural activity (Fig. 1, E and F). Relative to controls, we found significant increases (by a factor of 2 to 20) in *c-fos* labeling across multiple brain regions in CNO-injected $hM_3D_q^{fos}$ transgenic mice (table S1). Labeling for *c-fos* was found in both hM_3D_q-positive and hM_3D_q-negative neurons, with 91 ± 2% of hM_3D_q-positive neurons in CA1 colabeled with *c-fos* (fig. S2).

In standard contextual fear conditioning, animals develop a memory for the conditioning chamber in which they receive a footshock. The ability to form the context association is dependent on the hippocampus, which participates in encoding a representation of the environment (*14*, *15*). To test the effects of competing circuit activation on the formation of a memory trace, we designed the fear-conditioning protocol outlined in Fig. 2A. On day 1, $hM_3D_q^{fos}$ mice were exposed to a novel context (ctxA) in order to drive expression of the hM_3D_q transgene into neurons activated in that context. On day 2, mice were injected with Dox to inhibit further hM_3D_q receptor expression and with CNO to stimulate activity in the spatial pattern of neurons that expressed the receptor. The mice were then fear-conditioned in a distinct context (ctxB), and 24 hours later, memory performance was tested in the absence and presence of CNO. Thus, we fired the neurons active in ctxA while the mice were fear-conditioned in ctxB.

We anticipated three potential outcomes. The strong synthetic activation of ctxA neurons could be dominant and serve as a conditioned stimulus

[1]Department of Cell Biology and Dorris Neuroscience Center, The Scripps Research Institute, 10550 North Torrey Pines Road, La Jolla, CA 92037, USA. [2]Neurosciences Graduate Program, University of California, San Diego, 9500 Gilman Drive, La Jolla, CA 92037, USA. [3]Department of Psychology, Institute of Neuroscience, University of Oregon, Eugene, OR 97403, USA. [4]Departments of Pharmacology, Chemical Biology, and Medicinal Chemistry and Program in Neuroscience, University of North Carolina Chapel Hill Medical School, Chapel Hill, NC 27599, USA.

*To whom correspondence should be addressed. E-mail: mmayford@scripps.edu

to produce an associative fear memory. This would lead to a fear response to CNO, or possibly even a fear response to ctxA itself, if the artificial and natural activation of the neurons were sufficiently similar. This was not observed, as the level of freezing in ctxA was not significant in transgenic mice either with or without CNO injection (Fig. 2B). A protocol in which ctxA neurons were activated by CNO and mice were shocked immediately in ctxB [to prevent formation of a ctxB representation (*13*)] also failed to produce a CNO-dependent memory (fig. S3). Similarly, when the neurons active during conditioning itself were tagged with the hM_3D_q transgene, CNO did not produce significant freezing (fig. S5). Thus, the synthetic activity alone could not serve as a conditioned stimulus in fear conditioning. A second possibility was that the natural sensory experience in ctxB would dominate and transgenic mice would show normal conditioning to ctxB. The $hM_3D_q^{fos}$ mice displayed a severe deficit in freezing to ctxB, which suggests that the CNO-induced activity was interfering with normal encoding of memory for ctxB (Fig. 2C). A third possibility was that mice would form a hybrid representation, incorporating elements of both the CNO-induced artificial stimulation and the natural sensory cues from ctxB. This appears to be the case, as the transgenic mice showed a significant increase in freezing in response to CNO delivered in the ctxB setting during the 24-hour memory test (Fig. 2C).

We observed similar results in two separate experiments when a different contextual setup for ctxA neural labeling was used (figs. S1 and S4). The requirement for reactivation of the transgene-expressing neurons during memory retrieval suggests that their activity was incorporated into the memory trace. Consistent with this idea, we found a correlation between freezing during memory retrieval and the degree of neural activation, as assessed by *c-fos* expression in the hippocampus (Fig. 2, D and E).

Retrieval of a memory representation likely involves the reactivation of some neurons that were active during the initial learning (*11*, *16*–*18*). To test the susceptibility of this spatial code to competing neural network activation, we exposed $hM_3D_q^{fos}$ mice to ctxA to allow expression of the hM_3D_q transgene but then conditioned them in ctxB without CNO stimulation of the ctxA neural ensemble (Fig. 3). As expected, these mice developed wild-type levels of freezing to ctxB 24 hours after conditioning. Now, however, activation of the hM_3D_q-expressing neurons impaired memory performance during retrieval in ctxB. This suggests that CNO-induced activation of a competing neural network interferes with the learned spatial code and degrades recognition if this activity was not present during the initial training. This is not surprising, given that even limited focal hippocampal stimulation has been shown to disrupt spatial memory (*19*).

Does the hybrid fear memory formed by $hM_3D_q^{fos}$ mice incorporate the specific pattern of ctxA neurons activated by CNO during learning, or are the mice responding to a less specific alteration in brain state? To distinguish between these possibilities, we conditioned mice in the presence of CNO-induced firing of ctxA-labeled neurons but then placed the mice on Dox to allow turnover of the hM_3D_q receptor. Two days later, we removed Dox from the animals' diet and placed them in a new home cage to allow de novo expression of the hM_3D_q receptor in a distinct group of neurons (ctxC). Fourteen days after initial conditioning, we tested memory performance as assessed by freezing scores in ctxB in the absence and presence of CNO-induced synthetic activation. We found no increase in freezing in $hM3D_q^{fos}$ mice in response to CNO (Fig. 4, A

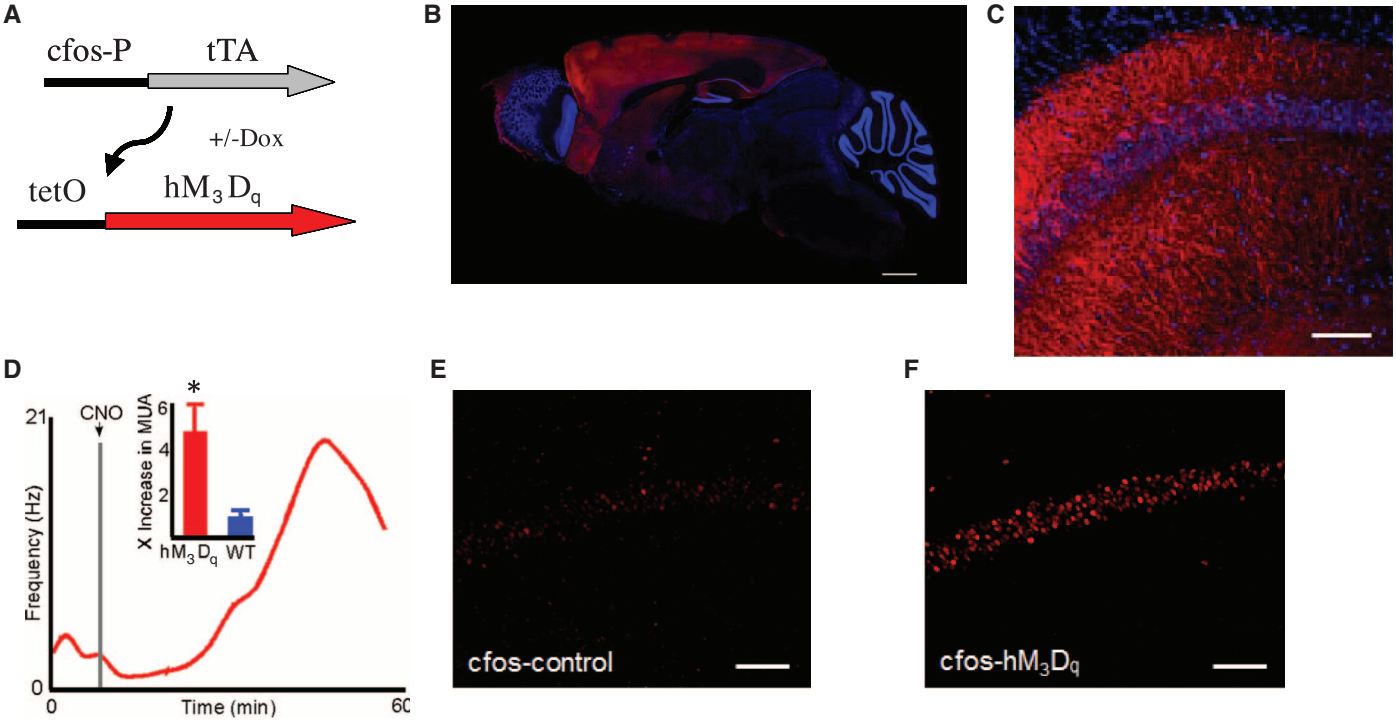

Fig. 1. Expression and activation of the hM_3D_q transgene. (**A**) Transgenic mice used in this study carry two transgenes. The first expresses the tetracycline transcriptional activator (tTA) under control of the activity-regulated *c-fos* promoter. The second transgene allows expression of hM_3D_q under the tet operator (tetO), which is activated upon binding of tTA but is inhibited by Dox. (**B**) Overall spatial expression profile of the hM_3D_q transgene in mice off Dox maintained in the home cage. Immunofluorescence was strong in hippocampus, in basolateral amygdala, and throughout the cortex. Fluorescence was also observed to a small extent in the pontine nucleus and brainstem. Scale bar, 1000 μm. (**C**) Expression in the CA1 region of the hippocampus, showing sparse and distributed expression of the hM_3D_q transgene. Scale bar, 100 μm. (**D**) CNO injection caused increased neural activity in $hM_3D_q^{fos}$ mice. Red curve shows multi-unit activity (MUA) recorded from dorsal CA1 of an anesthetized $hM_3D_q^{fos}$ mouse over time. Inset shows relative increase in MUA [mean MUA 30 to 40 min after injection compared to mean pre-injection baseline, 4.76 for $hM_3D_q^{fos}$ mice ($n = 6$) versus 0.9 for wild-type (WT) mice ($n = 6$); Wilcoxon signed-rank test, $^*P < 0.01$]. (**E** and **F**) *c-fos* induction 1.5 hours after CNO administration in a control (left) and $hM_3D_q^{fos}$ (right) mouse. $hM_3D_q^{fos}$ mice showed on average a factor of 2.5 increase in *c-fos* expression in the hippocampal CA1 region relative to control mice (see table S1; $hM_3D_q^{fos}$, $n = 10$; control, $n = 10$; t test, $P < 0.02$). Scale bars, 100 μm.

and C); this finding demonstrates a requirement for reactivation specifically of the learned (ctxA) neural ensemble, rather than a generalized change in brain state caused by CNO-induced activity.

To further address the issue of ensemble specificity, we preexposed mice to the fear-conditioning context (ctxB) on day 1 to express the hM_3D_q receptor in neurons that were activated in that context. We reasoned that the synthetic activation of this pattern of neurons would more likely overlap with the natural activity during learning in ctxB and should therefore not interfere with the production of a normal ctxB representation. When mice were fear-conditioned after injection of CNO to artificially activate the ctxB ensemble during learning, they developed wild-type levels of 24-hour context fear memory that were independent of CNO stimulation (Fig. 4, B and D). This is in contrast to the deficit produced in mice preexposed to the novel ctxA and further supports the hypothesis that there must be a match in the spatial pattern of neural activity at learning and retrieval.

Several recent studies have suggested flexibility in the specific neurons incorporated into a fear memory trace in the amygdala through a selection mechanism in which more excitable neurons are preferentially incorporated into the trace (*16*–*18*). Our results do not appear to be attributable to this type of selection, as the reactivation of the neurons with CNO is required for retrieval, whereas in the previous studies the stimulated neurons were part of a representation that could be naturally retrieved. This difference may be due to different requirements for forming simple associations in the amygdala versus more complex representations in the hippocampus and cortex.

In our study, the artificially stimulated neural ensembles become incorporated into the memory and the amount of activation in CA1 and CA3 during retrieval is correlated with the strength of memory performance in transgenic mice. In one recent study, ChR2 stimulation of a random population of neurons in the piriform cortex combined with odorant during conditioning found that either the artificial stimulation or the odorant alone could produce recall, which suggests independent and noninterfering representations (*20*). In contrast, we found that the CNO activation alone could not act as an independent cue. These studies differed in a variety of parameters, including anatomy and size of the artificially stimulated ensembles; one critical difference may be that the activity induced by hM_3D_q is not temporally coordinated in response to the inducing stimulus (CNO), as is the case with ChR2-driven stimulation by light. However, the sensory input during conditioning and retrieval in ctxB may coordinate the activity of the CNO-depolarized cells to provide some degree of temporal coordination to the CNO-driven neurons and account for the requirement for the compound stimulus. Alternatively, it is possible that the uncoordinated

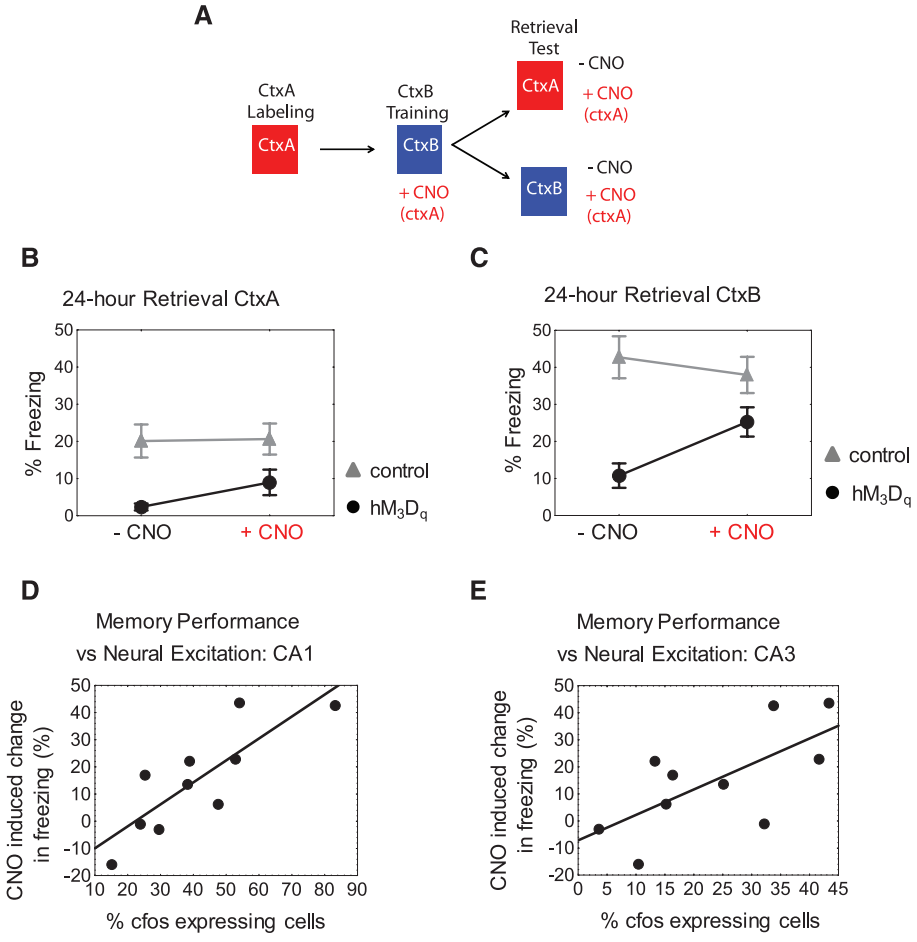

Fig. 2. Incorporation of synthetic neural activity into a 24-hour memory representation. (**A**) Schematic of experimental procedure. (**B**) Freezing in ctxA 24 hours after conditioning in ctxB. $hM_3D_q^{fos}$ mice ($n = 14$) froze significantly less than did control mice ($n = 13$) in ctxA in both the absence and presence of CNO [repeated-measures analysis of variance (ANOVA): main effect of genotype, $F(1,26) = 10.96$, $P < 0.005$]. CNO had no significant effect on freezing in either group (post hoc Bonferroni test: $hM_3D_q^{fos}$, $P = 0.192$; control, $P = 1.00$). (**C**) Transgenic $hM_3D_q^{fos}$ mice showed impaired 24-hour memory for ctxB that was rescued by injection of CNO [repeated-measures ANOVA: genotype × CNO interaction, $F(1.25) = 10.15$, $P < 0.005$]. $hM_3D_q^{fos}$ mice froze significantly less than did control mice in ctxB in the absence of CNO (post hoc Fisher's least significant difference test; $P < 0.001$) but were statistically similar in ctxB in the presence of CNO ($P = 0.117$) and showed a significant increase in freezing in ctxB with CNO relative to ctxB alone ($P < 0.001$). (**D** and **E**) Correlation between the difference in freezing scores in the presence and absence of CNO and endogenous *c-fos* expression 1 hour after memory testing in hippocampal areas CA1 (D) ($r = 0.8276$, $P < 0.005$) and CA3 (E) ($r = 0.6742$, $P < 0.05$).

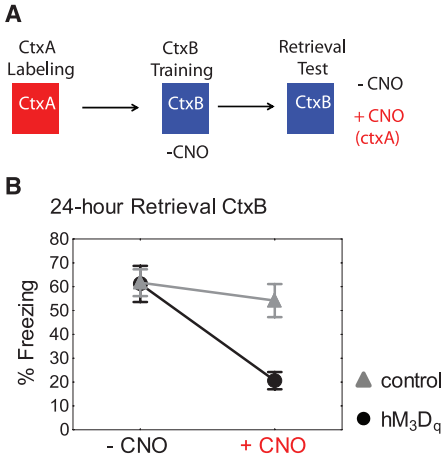

Fig. 3. Disruption of memory retrieval by synthetic neural activation. (**A**) Schematic of experiment. (**B**) Transgenic $hM_3D_q^{fos}$ mice developed a normal 24-hour context memory when conditioned in the absence of CNO. This memory was disrupted by CNO injection to activate the competing ctxA representation [$hM_3D_q^{fos}$, $n = 12$; control, $n = 12$; repeated-measures ANOVA: main effect of genotype, $F(1,22) = 5.3$, $P < 0.05$; CNO, $F(1,22) = 28.6$, $P < 0.001$; genotype × CNO interaction, $F(1,22) = 13.5$, $P = 0.001$]. hM_3D^{fos} mice froze significantly less in the presence of CNO relative to before CNO administration (post hoc Fisher's least significant difference test; $P < 0.001$) and froze significantly less than did control mice in the presence of CNO ($P < 0.001$).

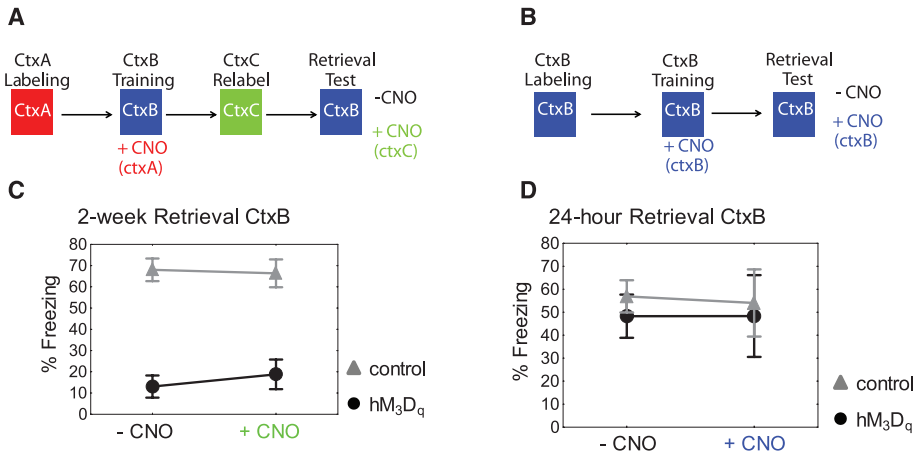

Fig. 4. Memory performance during synthetic reactivation is network-specific. (**A** and **C**) When CNO-induced synthetic activation did not occur in identical neural populations during memory formation and memory retrieval, a memory deficit was observed. $hM_3D_q^{fos}$ mice showed significantly less freezing than did control mice in ctxB, both in the absence and presence of CNO [$hM_3D_q^{fos}$, $n = 14$, control, $n = 17$; repeated-measures ANOVA: main effect of genotype, $F(1,23) = 51.15$, $P < 0.001$]. (**B** and **D**) When $hM_3D_q^{fos}$ mice were exposed to ctxB off of Dox to induce hM_3D_q expression and then fear-conditioned on Dox after CNO injection in ctxB, synthetic activation by CNO was not necessary for memory recall in ctxB [ctxB – CNO: $hM_3D_q^{fos}$, $n = 9$; control, $n = 10$; ctxB + CNO: $hM_3D_q^{fos}$, $n = 5$; control, $n = 6$; repeated-measures ANOVA: $F(2,18) = 0.0474$, $P = 0.954$].

CNO-based stimulus could serve as a conditioned stimulus if it was limited to a discrete primary sensory area, such as the piriform cortex.

Current views of sensory processing recognize the role of internally generated (spontaneous) neural activity in generating a representation from a given sensory input (*8*). This activity is not random but has spatial and temporal structure that is thought to represent defined ensembles formed through previous learning-related plasticity. Moreover, in psychology, the idea of a schema as a preexisting framework of relationships that modulates learning suggests that new memories are not produced de novo; rather, coding of new learned information depends on preexisting circuit activity (*21*, *22*). Although the CNO-based stimulation does not replicate the temporal dynamics of this naturally occurring internal activity, the approach allows the activation of a distributed spatial pattern of neurons recruited during a specific experience (ctxA exposure). Our results show that this spatial pattern of activity at the time of learning and retrieval must match for appropriate recall. The results imply a strong spatial component to coding in this form of learning and support the idea that the internal dynamics of the brain at the time of learning contribute to memory encoding.

References and Notes

1. R. W. Doty, *Annu. Rev. Psychol.* **20**, 289 (1969).
2. P. G. Shinkman, R. A. Swain, R. F. Thompson, *Behav. Neurosci.* **110**, 914 (1996).
3. R. Romo, A. Hernández, A. Zainos, E. Salinas, *Nature* **392**, 387 (1998).
4. H. Jasper, W. Penfield, *Epilepsy and the Functional Anatomy of the Human Brain* (Little, Brown, Boston, ed. 2, 1954).
5. D. Huber *et al.*, *Nature* **451**, 61 (2008).
6. L. Luo, E. M. Callaway, K. Svoboda, *Neuron* **57**, 634 (2008).
7. T. Kenet, D. Bibitchkov, M. Tsodyks, A. Grinvald, A. Arieli, *Nature* **425**, 954 (2003).
8. J. Fiser, C. Chiu, M. Weliky, *Nature* **431**, 573 (2004).
9. J. N. MacLean, B. O. Watson, G. B. Aaron, R. Yuste, *Neuron* **48**, 811 (2005).
10. D. L. Ringach, *Curr. Opin. Neurobiol.* **19**, 439 (2009).
11. L. G. Reijmers, B. L. Perkins, N. Matsuo, M. Mayford, *Science* **317**, 1230 (2007).
12. G. M. Alexander *et al.*, *Neuron* **63**, 27 (2009).
13. N. Matsuo, L. Reijmers, M. Mayford, *Science* **319**, 1104 (2008).
14. S. G. Anagnostaras, G. D. Gale, M. S. Fanselow, *Hippocampus* **11**, 8 (2001).
15. P. W. Frankland, V. Cestari, R. K. Filipkowski, R. J. McDonald, A. J. Silva, *Behav. Neurosci.* **112**, 863 (1998).
16. J. H. Han *et al.*, *Science* **316**, 457 (2007).
17. J. H. Han *et al.*, *Science* **323**, 1492 (2009).
18. Y. Zhou *et al.*, *Nat. Neurosci.* **12**, 1438 (2009).
19. G. Girardeau, K. Benchenane, S. I. Wiener, G. Buzsáki, M. B. Zugaro, *Nat. Neurosci.* **12**, 1222 (2009).
20. G. B. Choi *et al.*, *Cell* **146**, 1004 (2011).
21. D. Tse *et al.*, *Science* **333**, 891 (2011); 10.1126/science.1205274.
22. D. Tse *et al.*, *Science* **316**, 76 (2007).

Acknowledgments: We thank K. Cowansage for helpful discussions. Supported by National Institute of Mental Health (NIMH) grant R01MH057368 and National Institute on Drug Abuse grant R01DA028300 (M.M.), NIMH grant U19MH82441 and the Michael Hooker Distinguished Chair in Pharmacology (B.L.R.), and a graduate fellowship from the California Institute for Regenerative Medicine (A.R.G.).

Supporting Online Material

www.sciencemag.org/cgi/content/full/335/6075/1513/DC1
Materials and Methods
Figs. S1 to S5
Table S1
References (*23*, *24*)

7 October 2011; accepted 30 January 2012
10.1126/science.1214985

New Products

ICP-OES SPECTROMETERS

The new Spectroblue sets new standards among compact, mid-range ICP-OES spectrometers for simplified operation, low maintenance, and high sample throughput while achieving the lowest cost of ownership in its class. The plasma generator uses novel air-cooled technology that eliminates the need for expensive external cooling. The new and unique OPIAir axial optical plasma interface needs no external cooling either, and offers sensitivity improvements of up to six times compared to conventional radial plasma observation, achieving detection limits at parts per billion levels. At the same time the generator's ample power reserves enable it to handle extreme sample loading while providing exceptional uptime, stability, and reliability. Spectro's unique UV-PLUS sealed optical system virtually eliminates gas purging. The Paschen-Runge optical layout combines high optical transparency with a wavelength range from 165 to 770 nm, and 8 pm resolution in the important analytical region from 165 to 285 nm for ease of processing line-rich spectra.

Spectro Analytical

For info: + 44-(0)-1162-462950 | www.spectro.com

AUTOMATED SAMPLE DECAPPER

The QIAensemble Decapper automation system can facilitate the handling of liquid-based cytology and various other types of liquid samples that are processed by clinical laboratories around the world. This open platform system enables laboratories to automate many tedious manual steps required for unscrewing (or "decapping") the lids of clinical sample vials, extracting the sample material, pipetting it into testing vials, and then recapping the clinical sample vial. QIAensemble Decapper has a capacity to process up to approximately 800 samples per shift (excluding setup time and postprocessing requirements). It has been designed specifically for the handling and transfer of sample materials, and the addition of reagents. The instrument accommodates a variety of fluid types of variable viscosity for both samples and reagents. The software system, which is operated by an intuitive graphical user interface, provides laboratory staff with a comprehensive and user-friendly report for each run.

Qiagen

For info: 800-426-8157 | www.qiagen.com

PCR INSTRUMENT

The Eppendorf Mastercycler nexus family of polymerase chain reaction (PCR) instruments offer excellent reproducibility, low noise emission, and the versatility to use all types of consumables. Up to three units may be combined for higher throughput, while software capability enables users to access a booking schedule for the instrument and receive e-mail notification when the PCR cycle is finished. Designed to be affordable, flexible, and reliable, the Mastercycler nexus incorporates Eppendorf's flexlid concept with automatic height adjustment of the lid. In combination with the universal block this allows use of the widest variety of PCR consumables, from large 0.5 mL tubes down to low profile plates and strips. The Mastercycler nexus gradient model provides a true gradient with 12 different temperatures and features SteadySlope technology to ensure that the heating and cooling ramp rates are identical in both optimization and routine experiments.

Eppendorf

For info: +44-(0)-1223-200440 | www.eppendorf.co.uk

LAB MOISTURE ANALYZER

Moisture analysis is quick, easy, and accurate using the versatile Kern MLB 50-3N moisture analyzer. With a readout of 0.001 g or 0.01% moisture and connected to an optional companion printer, the MLB 50-3N moisture balance supports GLP/ISO record keeping data consisting of time, date, and sample identification number. Data include: Moisture content as a percent, current temperature, active drying process, previous sample drying time, and the switch-off mode by time or constant weight. Utilizing a 400 W halogen heater the MLB 50-3N moisture analyzer has a temperature range of 50°C to 160°C, a maximum weighing capability of 50 g, reproducibility of 0.003 g, and linearity of ±0.003 g. Technicians can select four heating profiles—standard, soft, fast, and step—based on the properties of the material being tested.

Tovatech

For info: 973-913-973 | www.tovatech.com

OMNIPREP SOIL DNA

The OmniPrep Soil DNA kit is designed for the rapid extraction of polymerase chain reaction (PCR)-ready DNA from environmental samples. The kit provides all the reagents necessary to isolate DNA samples ready for PCR from a large variety of environmental samples. The OmniPrep Soil DNA kit is primarily designed for use with environmental samples that contain a high humic acid content. This includes difficult soil samples such as compost, manure, and sediment. A major issue with high humic acid samples is that the humic acids, as well as metals and polysaccharides, inhibit subsequent PCR. OmniPrep Soil DNA SoilOUT columns remove these interfering agents, thus allowing for successful PCR. The kit applies a rapid precipitation technique that uses unique precipitation reagents to isolate genomic DNA free from proteins and RNA. Pure genomic DNA is isolated in about 60 minutes. The resulting genomic DNA is passed through the SoilOUT columns to remove the humic acid and is then ready for PCR.

G-Biosciences

For info: 314-991-6034 | www.gbiosciences.com

Electronically submit your new product description or product literature information! Go to **www.sciencemag.org/products/newproducts.dtl** for more information.

Newly offered instrumentation, apparatus, and laboratory materials of interest to researchers in all disciplines in academic, industrial, and governmental organizations are featured in this space. Emphasis is given to purpose, chief characteristics, and availability of products and materials. Endorsement by *Science* or AAAS of any products or materials mentioned is not implied. Additional information may be obtained from the manufacturer or supplier.

EPITOMICS®
BETTER ANTIBODIES • BETTER SCIENCE

SPECIAL OFFER
$129 AKT RABMABS
Find out more @
www.epitomics.com/products/promo

RabMAbs® = Better AKT Antibodies

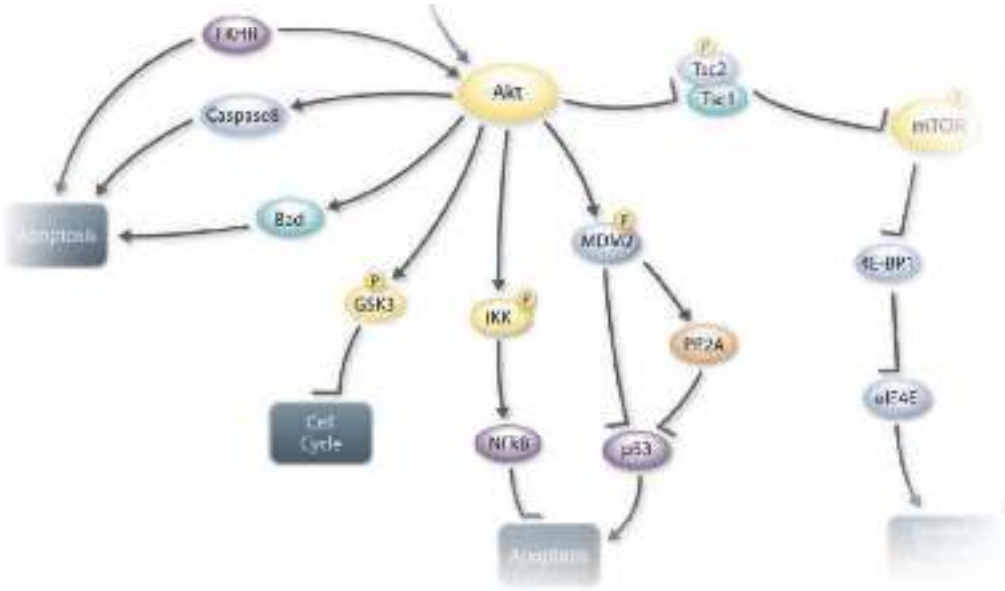

- **High quality antibodies to Akt and related proteins**
- **Validated in WB, IHC, IF, IP and FACS**
- **Over 7000 antibodies and counting**

At Epitomics, we provide a wide range of high quality antibodies to Akt and related proteins. Using our patented Rabbit Monoclonal Antibody (RabMAb®) technology, we have developed a collection of high quality Akt specific antibodies. Each Akt specific RabMAb offers superior antigen recognition of the rabbit immune system and the specificity of a monoclonal antibody.

Find out more@ www.epitomics.com/akt

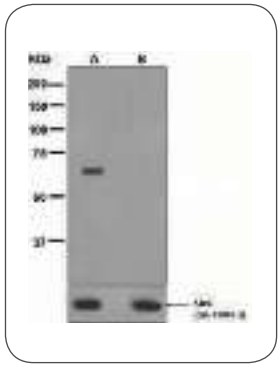

Akt1 Phospho (pT450)

Western blot analysis on NIH/3T3 cell lysate using anti-Akt1 Phospho (pT450) RabMAb (cat. #3188-1). Cells were either (A) untreated or (B) treated with Lambda Phosphatase.

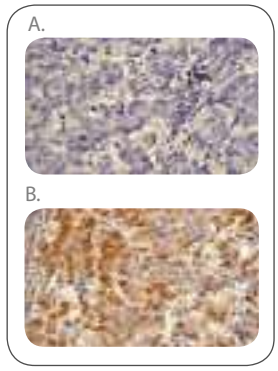

Akt1 Phospho (pS473)

Immunohistochemical staining of human cervical carcinoma tissue using anti-Phospho-Akt1 (pS473) RabMAb (cat. # 2118-1). Tissue was (A) phosphatase treated and (B) untreated.

100% SATISFACTION GUARANTEE *Antibody Satisfaction Guarantee*

www.epitomics.com

US & Canada | 1-877-772-2622
Outside NA | 650-583-6688
info@epitomics.com

gairdner

LES PRIX CANADA GAIRDNER AWARDS

CONGRATULATIONS TO THE 2012 CANADA GAIRDNER AWARD RECIPIENTS

For their pioneering discoveries concerning the biological clock responsible for circadian rhythms.

CANADA GAIRDNER INTERNATIONAL AWARD
JEFFREY C. HALL PhD

Professor of Biology Emeritus, Brandeis University, Waltham, MA

CANADA GAIRDNER INTERNATIONAL AWARD
MICHAEL ROSBASH PhD

Investigator, Howard Hughes Medical Institute and Professor of Biology, Brandeis University, Waltham, MA

CANADA GAIRDNER INTERNATIONAL AWARD
MICHAEL W. YOUNG PhD

Richard and Jeanne Fisher Professor, VP Academic Affairs, Head, Laboratory of Genetics, The Rockefeller University, NY, NY

CANADA GAIRDNER INTERNATIONAL AWARD
THOMAS M. JESSELL PhD

Professor of Neuroscience; Investigator, Howard Hughes Medical Institute, Columbia University, NY, NY

For research in defining the genetic and molecular pathways leading to the complex development of the spinal cord, with implications for therapeutic applications.

CANADA GAIRDNER INTERNATIONAL AWARD
JEFFREY V. RAVETCH PhD MD

Theresa and Eugene Lang Professor, and Head, Leonard Wagner Laboratory of Molecular Genetics and Immunology, The Rockefeller University, NY, NY

For his seminal work in identifying the Fc receptors of antibodies, which play a key role in the immune response, and for establishing their critical role in autoimmune diseases and cancer.

CANADA GAIRDNER GLOBAL HEALTH AWARD
BRIAN M. GREENWOOD MD

London School of Hygiene & Tropical Medicine, London, UK

For contributions to significantly reducing mortality in children due to meningitis and acute respiratory infection and for contributions to malaria prevention.

CANADA GAIRDNER WIGHTMAN AWARD
LORNE A. BABIUK OC SOM PhD DSc FRSC

Vice-President (Research), University of Alberta, Edmonton, AB

For his extraordinary national and international leadership in vaccine development and research on human and veterinary infectious disease control.

Gairdner recognizes the world's most creative and accomplished biomedical scientists.
Join our growing community at **www.gairdner.org**

The future of qPCR is here, and it's digital.

That's **ddPCRevolutionary.**

Bio-Rad's QX100™ Droplet Digital™ PCR system provides a measure of target DNA molecules with unrivaled precision and accuracy. The QX100 system partitions each sample into 20,000 individual nanoliter-sized droplets. PCR-positive and PCR-negative droplets from every sample are then counted to provide absolute target quantification in digital form. The QX100 system provides a revolutionary approach to target DNA quantification.

- Detect rare target sequences with unmatched sensitivity for cancer and viral research
- Measure small differences in target copy number variations (down to 1.2x differences)
- Determine gene expression levels without a standard curve or ΔΔCq

Visit **www.bio-rad.com/ad/DropletPCR** or contact your Bio-Rad Sales Representative to learn more.

Research. Together.

To find your local sales office, visit **www.bio-rad.com/contact**.
In the U.S., call toll free at 1-800-4BIORAD (1-800-424-6723).

Visit us at www.bio-rad.com

BIO-RAD

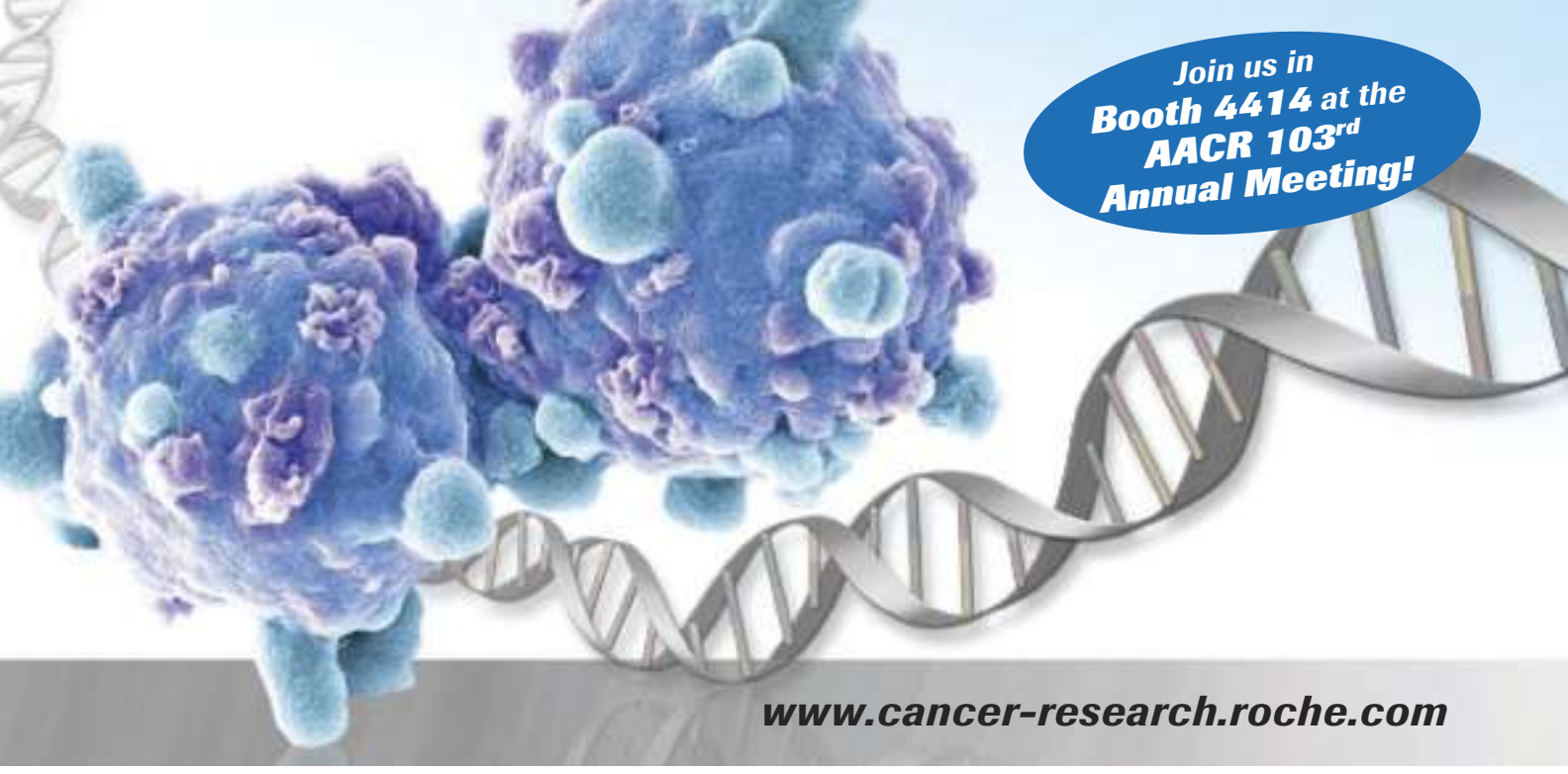

Choose a Trusted, Experienced Partner

To Help You Advance Your Cancer Research Faster

Quantify Gene Expression

Analyze DNA Methylation

Detect and Characterize Genomic Variations

Research Proliferation, Apoptosis, and Cytotoxicity

Continuously Monitor Cell Invasion and Migration

Study the Role of Proteins in Cancer

Hoping to advance your cancer research more quickly? Start by combining **Roche Applied Science**'s world-class reagents and instruments to rapidly, accurately study cancer at the level of the gene, transcript, protein, and cell.

As part of the world's leading supplier of oncology treatments (Roche Pharmaceuticals/Genentech) and tissue-based diagnostics, Roche Applied Science is uniquely qualified to be your primary partner in cancer research, offering:

- **Performance you can trust, plus innovation:** Combine time-tested reagents with novel instrumentation that enables you to study cancer in new ways.
- **Flexible, efficient solutions that help you make more from less:** Obtain more results faster in many applications.
- **Our commitment to you:** Confidently rely on our dedicated service professionals, on-site reagent stocking, customized research solutions, and much more.

Let Roche help you reveal the cellular and molecular mechanisms of cancer. Learn more by visiting *www.cancer-research.roche.com*

Roche Diagnostics Corporation
Roche Applied Science
Indianapolis, Indiana

For life science research only.
Not for use in diagnostic procedures.

advancing the life sciences 1912-2012

FASEB

Federation of American Societies for Experimental Biology

Proudly celebrating 100 years of service to the biological and biomedical sciences community

Stand Up for Science!

We Support Scientists By:

- Advocating for funding for biological research
- Advancing policies that facilitate research and reduce regulatory burden
- Improving the environment for science training and education

FASEB, the voice of biological and biomedical researchers, represents 26 scientific societies and over 100,000 scientists and engineers.

Join our e-Action Alert

Help us communicate with Congress on key research issues by visiting **www.faseb.org/StandUp** to join our e-Action list and keep up with the latest policy news.

Join a FASEB Member Society

Benefits include reduced fees for scientific meetings, conferences, and journals; access to continuing education, professional development and career resources; and opportunities to contribute to science policy, advocacy, and public education.

The American Physiological Society
American Society for Biochemistry and Molecular Biology
American Society for Pharmacology and Experimental Therapeutics
American Society for Investigative Pathology
American Society for Nutrition
The American Association of Immunologists
American Association of Anatomists
The Protein Society
Society for Developmental Biology
American Peptide Society
Association of Biomolecular Resource Facilities
The American Society for Bone and Mineral Research
American Society for Clinical Investigation
Society for the Study of Reproduction
Teratology Society
The Endocrine Society
The American Society of Human Genetics
Environmental Mutagen Society
International Society for Computational Biology
American College of Sports Medicine
Biomedical Engineering Society
Genetics Society of America
American Federation for Medical Research
The Histochemical Society
Society for Pediatric Research
Society for Glycobiology

Free up your time

Automated sample and assay technologies by QIAGEN

Automated solutions from sample to result:

- **The widest choice of sample processing protocols**
- **Low-, medium-, and high-throughput automation**
- **Leading solutions for molecular testing**
- **Plug-and-play automated sample preparation**
- **Quantitative, real-time PCR detection**
- **Automated analysis of DNA fragments and RNA**
- **High-resolution sequence-based DNA detection and quantification**

Making improvements in life possible — www.qiagen.com

QIAGEN®

Sample & Assay Technologies

AUTOPorff1111S1WW

Little Genius

BLItz

BLItz brilliantly packs the power of Dip and Read™ label-free analysis into a personal assay system. Give BLItz a drop of your sample and it does the rest!

- Protein presence/absence in seconds
- Binding kinetics assays at your bench
- Protein quantitation in seconds
- Develop immunoassays in minutes
- Easily analyze crude samples

Cleverly priced under $20K so you can have your own little genius.

Want to try BLItz in your lab? Visit BlitzMeNow.com or call 855.BLITZ.ME.

fortéBIO

life technologies™

8 trusted brands. 600,000 citations.

Life Technologies.

We're committed to your success

That's why we've united the most trusted life science brands. Our wide range of innovative products and services delivers the high quality you expect, and they're backed by our #1 rated support team. That's the value of life.

Visit us at our American Association for Cancer Research booth #4419.

Invitrogen™ | Applied Biosystems® | Gibco® | Molecular Probes® | Novex® | TaqMan® | Ambion® | Ion Torrent™

lifetechnologies.com

Quickly find the cancer mutations that matter

Human genome sequencing in a single day*

Ion Proton™ Sequencer

*The content provided herein may relate to products that have not been officially released and is subject to change without notice.

life technologies™

Understanding which genetic and epigenetic changes have biological and clinical significance is a big challenge. At Life Technologies, we are committed to transforming your cancer research by providing highly accurate and affordable sequencing and real-time PCR systems for basic and translational research. Whether you need whole genome or whole exome sequencing, or focused cancer gene panels and mutation validation, we're here to help you reach your next breakthrough.

Whole genome & whole exome sequencing

Sequence whole genomes and whole exomes on a fast, simple, and scalable benchtop device that any lab can afford.

Ion Proton™ Sequencer

Targeted resequencing

Get same-day sequencing results for multiple oncogenic regions from tumor samples using Ion AmpliSeq™ Cancer Panels and Ion semiconductor sequencing.

Ion PGM™ Sequencer
& Ion AmpliSeq™ Cancer Panel

Mutation validation

Rapidly validate mutations using allele-specific TaqMan® Mutation Detection Assays or gold-standard Sanger sequencing.

QuantStudio™ 12K Flex
Real-Time PCR System
& 3500 Genetic Analyzer

IN PURSUIT OF A WORLD WITHOUT CANCER

To advance your pursuit, we have the solutions that deliver the performance you expect—backed by our #1 rated support.
Visit us at our American Association for Cancer Research booth #4419, or to see our full offering go to lifetechnologies.com/cancerbiomarkers

Invitrogen™ Applied Biosystems® Gibco® Molecular Probes® Novex® TaqMan® Ambion® Ion Torrent™

Discover the noncoding RNAs that regulate cancer

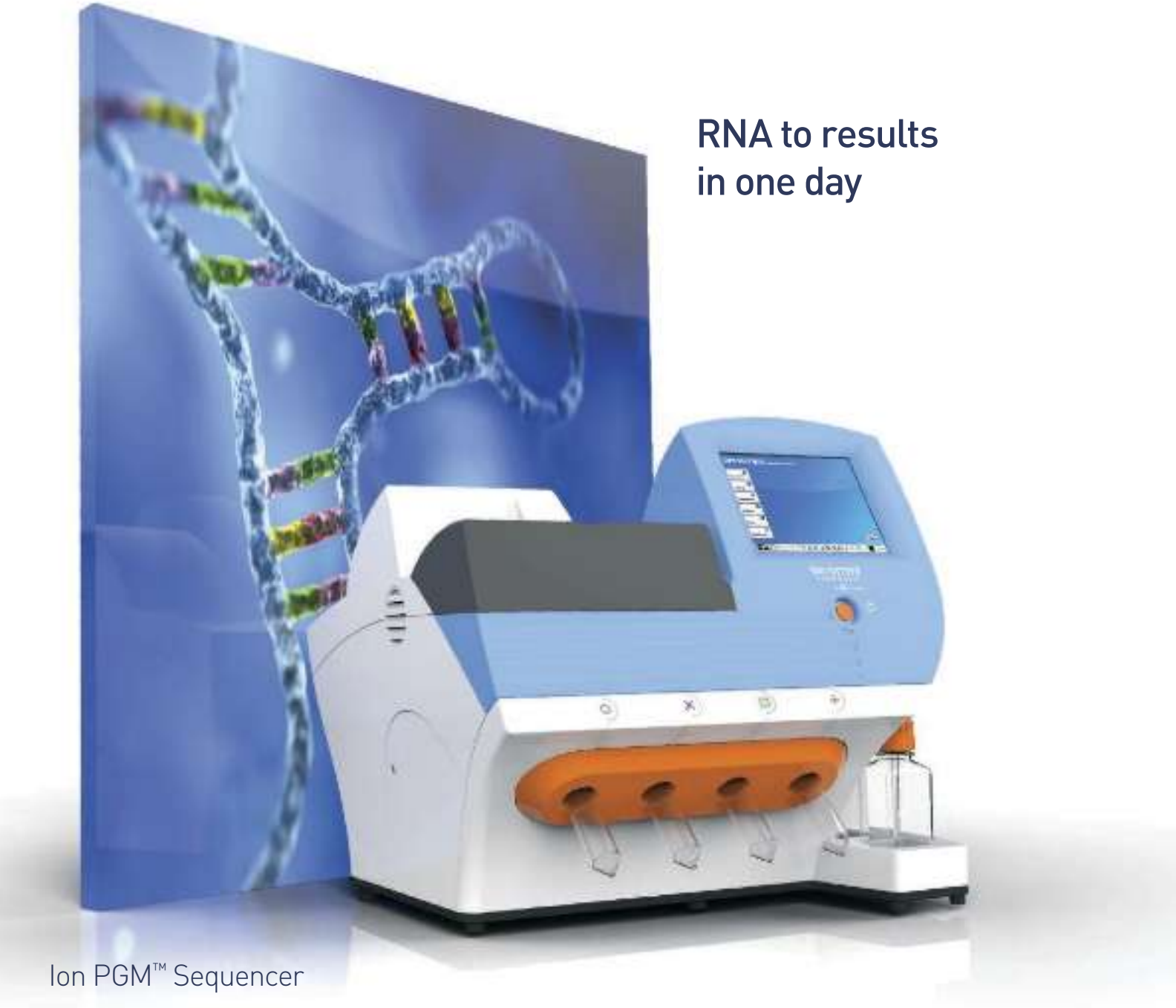

RNA to results in one day

Ion PGM™ Sequencer

life technologies™

Discovering how noncoding RNAs regulate gene expression will lead to new approaches to understanding cancer. At Life Technologies, we're developing sensitive methods to uncover new RNAs, solutions to profile and validate microRNAs, and functional analysis tools to help you define the most important noncoding RNAs in human cancer.

RNA discovery

Expand your RNA research beyond microarrays and discover differentially expressed noncoding RNAs, novel transcripts, and splice variants from tumor samples using fast, scalable, and affordable Ion semiconductor sequencing.

Ion PGM™ Sequencer
& Ion Total RNA-Seq Kit

MicroRNA profiling & validation

Quickly discriminate differential microRNA profiles from cancer tissues using predesigned and custom TaqMan® microRNA panels with a flexible, scalable real-time PCR platform.

QuantStudio™ 12K Flex Real-Time PCR System
& TaqMan® OpenArray® MicroRNA Panels

MicroRNA regulation

Functionally analyze microRNAs *in vitro* or *in vivo* with easy-to-transfect microRNA mimics or inhibitors.

*mir*Vana™ miRNA mimics and inhibitors,
Lipofectamine® RNAiMAX
& Invivofectamine® 2.0 reagents

IN PURSUIT OF A WORLD WITHOUT CANCER

To advance your pursuit, we have the solutions that deliver the performance you expect—backed by our #1 rated support.
Visit us at our American Association for Cancer Research booth #4419, or to see our full offering go to lifetechnologies.com/cancerRNA

Invitrogen™ Applied Biosystems® Gibco® Molecular Probes® Novex® TaqMan® Ambion® Ion Torrent™

Unlock the mysteries of the cancer cell

Click. Print. Love. Simple cell imaging

FLoid™ Cell Imaging Station

life technologies™

Understanding the biology of cancer cells is critical to improving the future of cancer treatment. We're committed to helping you ask new questions and more easily find answers at every step of your basic and translational research. With expertise that spans from cell culture, RNAi, and gene expression analysis to innovative rapid protein detection and cell imaging, we have affordable, high-quality solutions designed to help navigate your fastest path from genotype to phenotype.

Cellular imaging

Visualize intracellular changes in cancer cells right on your benchtop using Molecular Probes® assays and the FLoid™ Cell Imaging Station.

FLoid™ Cell Imaging Station
& Molecular Probes® assays

Cell signaling

Analyze cancer cell signaling pathways with ease using rapid, multiplex protein detection assays.

MAGPIX® System,
antibodies & ELISAs

RNA expression

Reliably quantify changes in mRNA and noncoding RNA expression levels from cancer cells and archived FFPE samples using TaqMan® Assays.

QuantStudio™ 12K Flex Real-Time
PCR System & TaqMan® Assays

IN PURSUIT OF A WORLD WITHOUT CANCER

To advance your pursuit, we have the solutions that deliver the performance you expect—backed by our #1 rated support.
Visit us at our American Association for Cancer Research booth #4419, or to see our full offering go to lifetechnologies.com/cancercells

Invitrogen™ Applied Biosystems® Gibco® Molecular Probes® Novex® TaqMan® Ambion® Ion Torrent™

Be the next winner!

2011 Winner
Dr. Tiago Branco
Postdoctoral
Research Fellow
University College
London

Get recognized!
US$ 25,000 Prize

Deadline for entries:
June 15, 2012

It´s easy to apply! Learn more at:
www.eppendorf.com/prize

eppendorf & Science PRIZE FOR NEUROBIOLOGY

Eppendorf & Science Prize for Neurobiology

Congratulations to Dr. Tiago Branco on winning the 2011 Eppendorf & *Science* Prize for his studies on how dendrites discriminate temporal input sequences and apply different integration rules depending on input location. The results of Dr. Branco's research provide insight on how the brain performs computations, and suggest that even single neurons can solve complex computational tasks.

You could be the 11th winner of this award.
The annual Eppendorf & *Science* Prize for Neurobiology honors young scientists for their outstanding contributions to neurobiological research based on methods of molecular and cell biology. The winner and finalists are selected by a committee of independent scientists, chaired by *Science's* Senior Editor, Dr. Peter Stern.

To be eligible, you must be 35 years of age or younger. If you're selected as this year's winner, you will receive US$ 25,000, have your work published in *Science* and be invited to visit Eppendorf in Hamburg, Germany. Past winners and finalists have come from as far a field as China, Chile, India and New Zealand.

Yes, it can happen to you. Enter your research now!

eppendorf
In touch with life

Science AAAS

Kurstin Roe Photography

The Wonders of Science & Technology
PAST, PRESENT, AND FUTURE

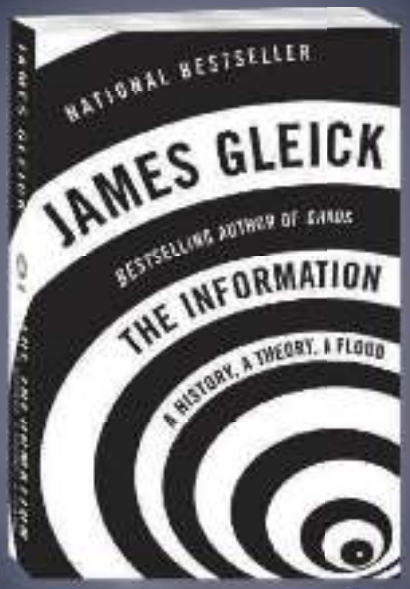

"Ambitious, illuminating and sexily theoretical."
—The New York Times

"Gleick does what only the best science writers can do: take a subject of which most of us are only peripherally aware and put it at the center of the universe." *—Time*

From the bestselling author of *Chaos and Genius* — a thoughtful and provocative exploration of the big ideas of the modern era.

A *New York Times* Notable Book
A *Los Angeles Times* and *Cleveland Plain Dealer* Best Book of the Year

NOW IN PAPERBACK

"Fascinating.... A wide-ranging tour of what to expect from technological progress over the next century or so."
—The Wall Street Journal

"Has the ability to surprise and enthrall and frighten."
—The New York Times

"A whirlwind tour of technological possibility."
—New Scientist

Michio Kaku, bestselling author of *Hyperspace* and *Physics of the Impossible*, forecasts a century of earthshaking advances in technology that could make even the last centuries' leaps and bounds seem insignificant.

NOW IN PAPERBACK

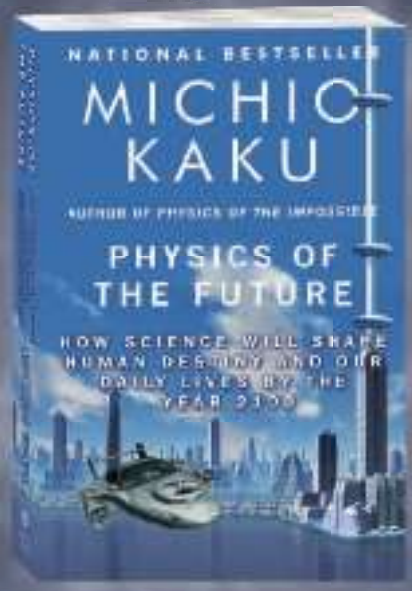

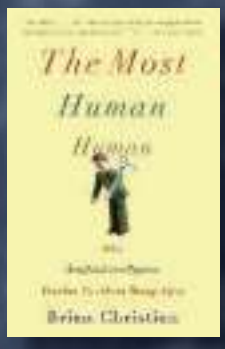

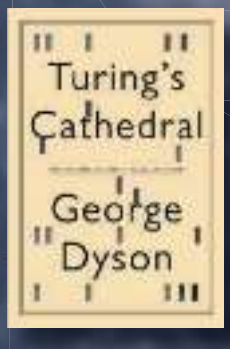

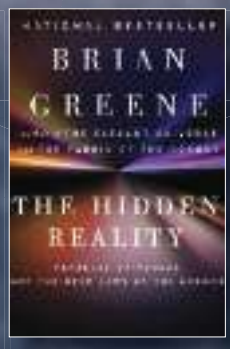

Now available wherever books and eBooks are sold
The Knopf Doubleday Publishing Group
www.knopfdoubleday.com

For desk and examination copies: Knopf Doubleday Academic
1745 Broadway, 12th Floor New York, NY 10019
www.aaknopf.com/academic • acmart@randomhouse.com

New Products

ICP-OES SPECTROMETERS

The new Spectroblue sets new standards among compact, mid-range ICP-OES spectrometers for simplified operation, low maintenance, and high sample throughput while achieving the lowest cost of ownership in its class. The plasma generator uses novel air-cooled technology that eliminates the need for expensive external cooling. The new and unique OPIAir axial optical plasma interface needs no external cooling either, and offers sensitivity improvements of up to six times compared to conventional radial plasma observation, achieving detection limits at parts per billion levels. At the same time the generator's ample power reserves enable it to handle extreme sample loading while providing exceptional uptime, stability, and reliability. Spectro's unique UV-PLUS sealed optical system virtually eliminates gas purging. The Paschen-Runge optical layout combines high optical transparency with a wavelength range from 165 to 770 nm, and 8 pm resolution in the important analytical region from 165 to 285 nm for ease of processing line-rich spectra.

Spectro Analytical
For info: + 44-(0)-1162-462950 | www.spectro.com

AUTOMATED SAMPLE DECAPPER

The QIAensemble Decapper automation system can facilitate the handling of liquid-based cytology and various other types of liquid samples that are processed by clinical laboratories around the world. This open platform system enables laboratories to automate many tedious manual steps required for unscrewing (or "decapping") the lids of clinical sample vials, extracting the sample material, pipetting it into testing vials, and then recapping the clinical sample vial. QIAensemble Decapper has a capacity to process up to approximately 800 samples per shift (excluding setup time and postprocessing requirements). It has been designed specifically for the handling and transfer of sample materials, and the addition of reagents. The instrument accommodates a variety of fluid types of variable viscosity for both samples and reagents. The software system, which is operated by an intuitive graphical user interface, provides laboratory staff with a comprehensive and user-friendly report for each run.

Qiagen
For info: 800-426-8157 | www.qiagen.com

PCR INSTRUMENT

The Eppendorf Mastercycler nexus family of polymerase chain reaction (PCR) instruments offer excellent reproducibility, low noise emission, and the versatility to use all types of consumables. Up to three units may be combined for higher throughput, while software capability enables users to access a booking schedule for the instrument and receive e-mail notification when the PCR cycle is finished. Designed to be affordable, flexible, and reliable, the Mastercycler nexus incorporates Eppendorf's flexlid concept with automatic height adjustment of the lid. In combination with the universal block this allows use of the widest variety of PCR consumables, from large 0.5 mL tubes down to low profile plates and strips. The Mastercycler nexus gradient model provides a true gradient with 12 different temperatures and features SteadySlope technology to ensure that the heating and cooling ramp rates are identical in both optimization and routine experiments.

Eppendorf
For info: +44-(0)-1223-200440 | www.eppendorf.co.uk

LAB MOISTURE ANALYZER

Moisture analysis is quick, easy, and accurate using the versatile Kern MLB 50-3N moisture analyzer. With a readout of 0.001 g or 0.01% moisture and connected to an optional companion printer, the MLB 50-3N moisture balance supports GLP/ISO record keeping data consisting of time, date, and sample identification number. Data include: Moisture content as a percent, current temperature, active drying process, previous sample drying time, and the switch-off mode by time or constant weight. Utilizing a 400 W halogen heater the MLB 50-3N moisture analyzer has a temperature range of 50°C to 160°C, a maximum weighing capability of 50 g, reproducibility of 0.003 g, and linearity of ±0.003 g. Technicians can select four heating profiles—standard, soft, fast, and step—based on the properties of the material being tested.

Tovatech
For info: 973-913-973 | www.tovatech.com

OMNIPREP SOIL DNA

The OmniPrep Soil DNA kit is designed for the rapid extraction of polymerase chain reaction (PCR)-ready DNA from environmental samples. The kit provides all the reagents necessary to isolate DNA samples ready for PCR from a large variety of environmental samples. The OmniPrep Soil DNA kit is primarily designed for use with environmental samples that contain a high humic acid content. This includes difficult soil samples such as compost, manure, and sediment. A major issue with high humic acid samples is that the humic acids, as well as metals and polysaccharides, inhibit subsequent PCR. OmniPrep Soil DNA SoilOUT columns remove these interfering agents, thus allowing for successful PCR. The kit applies a rapid precipitation technique that uses unique precipitation reagents to isolate genomic DNA free from proteins and RNA. Pure genomic DNA is isolated in about 60 minutes. The resulting genomic DNA is passed through the SoilOUT columns to remove the humic acid and is then ready for PCR.

G-Biosciences
For info: 314-991-6034 | www.gbiosciences.com

Electronically submit your new product description or product literature information! Go to **www.sciencemag.org/products/newproducts.dtl** for more information.

Newly offered instrumentation, apparatus, and laboratory materials of interest to researchers in all disciplines in academic, industrial, and governmental organizations are featured in this space. Emphasis is given to purpose, chief characteristics, and availability of products and materials. Endorsement by *Science* or AAAS of any products or materials mentioned is not implied. Additional information may be obtained from the manufacturer or supplier.

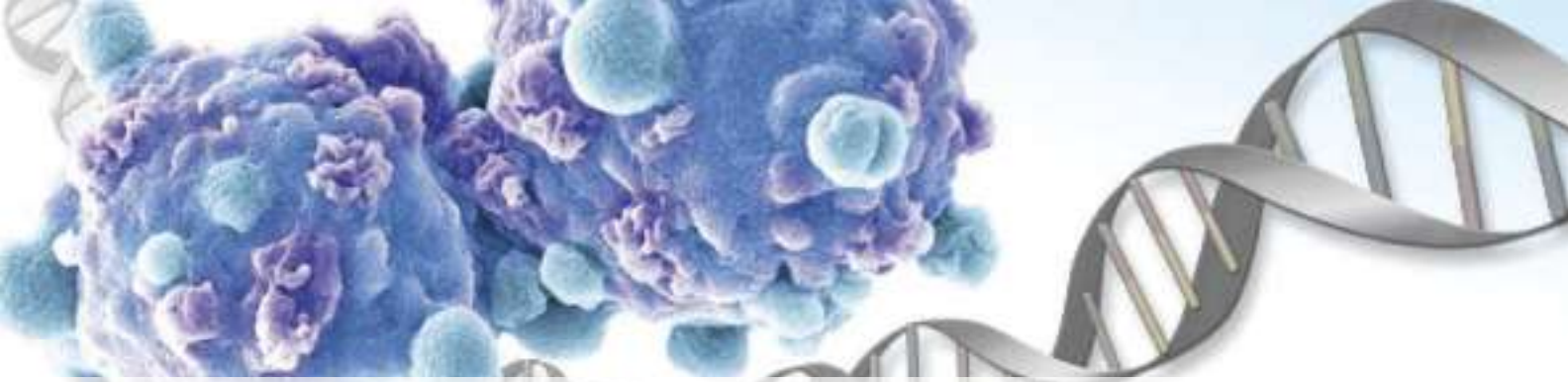

WEBINAR

Targeting Tumor Vulnerabilities

Unmasking Novel Targets Using Real-time, Label-free Cell Analysis

April 11, 2012
12 noon ET, 9 a.m. PT, 4 p.m. GMT, 5 p.m. UK

In the ongoing effort to identify novel therapeutic targets against common and aggressive cancers, new methods are being utilized to better understand the molecular pathways of disease. In particular, the molecular mechanisms employed by cancer cells to achieve chemoresistance and evade immune monitoring, as well as the pathways to metastasis, are being intensively investigated. The challenges to discover and develop targeted agents that hold the potential to enhance tumor cell sensitivity to chemotherapy and to inhibit metastasis are being complemented by the use of real-time, label-free cell analysis in monitoring T cell activity, tracking drug resistance, and modeling tumor cell invasion. In this webinar, a panel of experts will discuss their research and describe the use of real-time, label-free cell monitoring in their investigation of novel cancer targets and the impact of their work on translational research and drug development.

Webinar viewers will:

- Discover how these scientists are incorporating real-time, label-free cell analysis to aid the hunt for novel therapeutic targets
- Hear about applications for monitoring chemoresistance and metastasis in real time
- Discover how label-free technology can be an enabling tool for cellular analysis
- Have an opportunity to ask the panelists questions—live!

SPEAKERS

Keith L. Knutson, Ph.D.
Mayo Clinic
Rochester, MN

Aykut Üren, M.D.
Georgetown University Medical Center
Washington, DC

REGISTER NOW!
webinar.sciencemag.org

Brought to you by the *Science*/AAAS Custom Publishing Office

Science AAAS

Webinar sponsored by

Roche

xCELLigence

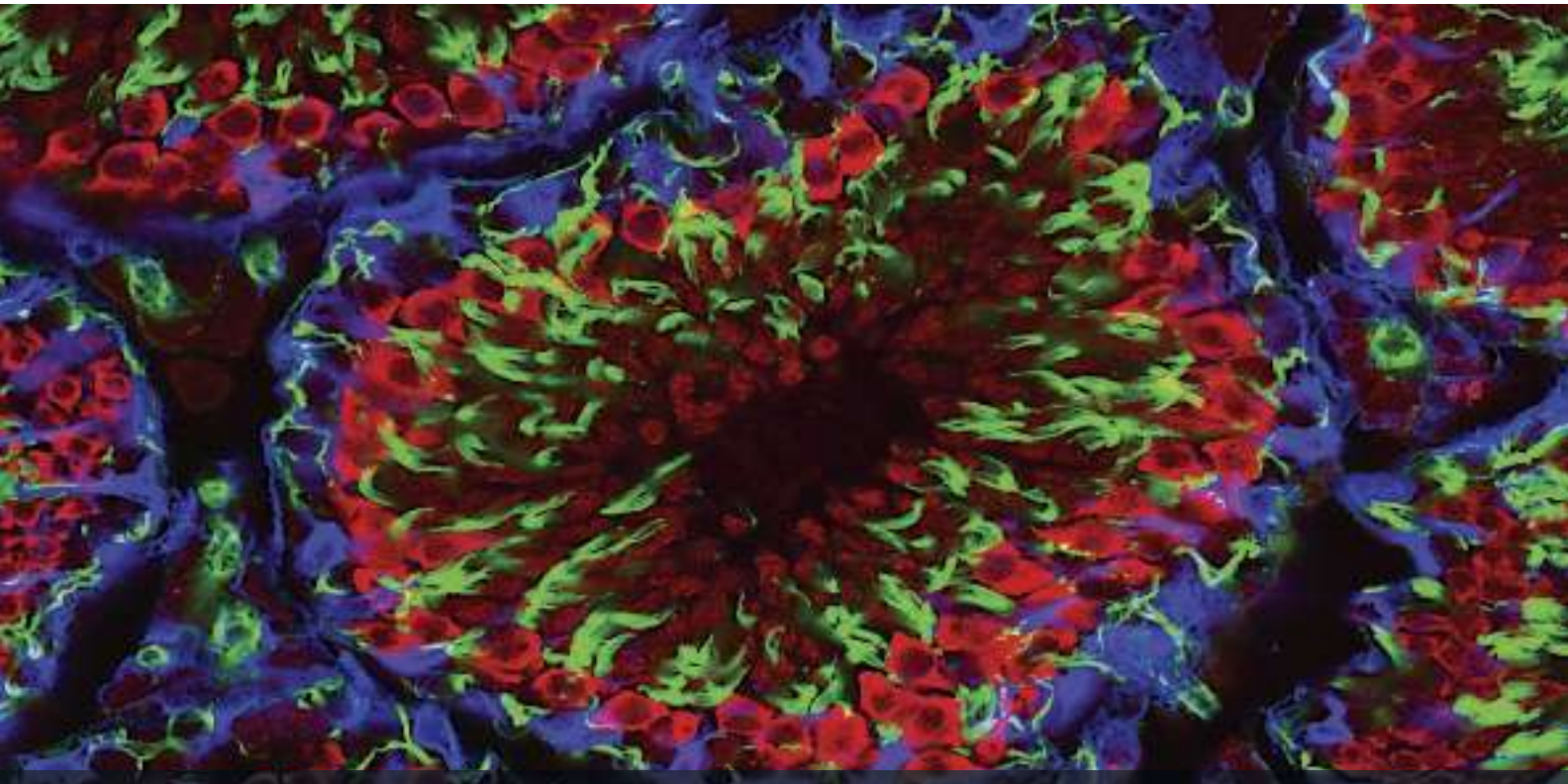

XP® Monoclonal Antibodies,
one antibody, multiple applications

Unparalleled product quality, validation, and technical support.

XP® monoclonal antibodies are a line of high quality rabbit monoclonal antibodies exclusively available from Cell Signaling Technology. Any product labeled with XP has been carefully selected based on superior performance in the most relevant applications.

XP monoclonal antibodies are generated using XMT® technology, a proprietary monoclonal method developed at Cell Signaling Technology. This technology provides access to a broad range of antibody-producing B cells unattainable with traditional monoclonal technologies, allowing more comprehensive screening and the identification of XP monoclonal antibodies.

eXceptional specificity
As with all of our antibodies, the antibody is specific to your target of interest, saving you valuable time and resources.

+ eXceptional sensitivity
The antibody will provide a stronger signal for your target protein in cells and tissues, allowing you to monitor expression of low levels of endogenous proteins, saving you valuable materials.

+ eXceptional stability and reproducibility
XMT technology combined with our stringent quality control ensures maximum lot-to-lot consistency and the most reproducible results.

= eXceptional Performance™
XMT technology coupled with our extensive antibody validation and stringent quality control delivers XP monoclonal antibodies with eXceptional Performance in the widest range of applications.

Above: Confocal IF analysis of rat testis using Miwi (D92B7) XP® Rabbit mAb #6915 (red pseudocolor) and Vimentin (D21H3) XP® Rabbit mAb (Alexa Fluor® 647 Conjugate) #9856 (blue pseudocolor). Actin filaments were labeled with DY-554 phalloidin (green pseudocolor).

For experimental details, additional information, and a complete list of available XP® monoclonal antibodies visit…
www.cellsignal.com

Cell Signaling TECHNOLOGY®

Orders (toll-free) 1-877-616-2355 | **Technical support** (toll-free) 1-877-678-8324 support@cellsignal.com | **Inquiries** info@cellsignal.com | **Environmental Commitment** eco.cellsignal.com

Science Careers Advertising

For full advertising details, go to ScienceCareers.org and click For Employers, or call one of our representatives.

Tracy Holmes
Worldwide Associate Director
Science Careers
Phone: +44 (0) 1223 326525

UNITED STATES & CANADA
E-mail: advertise@sciencecareers.org
Fax: 202-289-6742

Tina Burks
Midwest/West Coast/
South Central/Canada
Phone: 202-326-6577

Elizabeth Early
East Coast & Corporate
Phone: 202-326-6578

Marci Gallun
Sales Administrator
Phone: 202-326-6582

Online Job Posting Questions
Phone: 202-312-6375

EUROPE & REST OF WORLD
E-mail: ads@science-int.co.uk
Fax: +44 (0) 1223 326532

Simone Jux
Phone: +44 (0)1223 326529

Lucy Nelson
Phone: +44 (0)1223 326527

Kelly Grace
Phone: +44 (0) 1223 326528

JAPAN
Yuri Kobayashi
Phone: +81-6-6627-9250
E-mail: ykobayas@aaas.org

CHINA & TAIWAN
Ruolei Wu
Phone: +86-1367-1015-294
E-mail: rwu@aaas.org

Science Careers
From the journal *Science* AAAS

SIU School of Medicine

Chair and Professor Department of Medical Microbiology, Immunology, and Cell Biology

Southern Illinois University's School of Medicine at Springfield invites applications and nominations for the position of Chair of the Department of Medical Microbiology, Immunology and Cell Biology (MMICB) **www.siumed.edu/mmi**. The MMICB department has twelve faculty members each with an active research program in areas ranging from virology, neuroscience, reproductive immunology and host response to infection, to a major cancer biology group. The Department has an excellent record of research funding from the NIH, DOD, foundations, and contracts. The Department's graduate program is part of the integrated Molecular Biology, Microbiology and Biochemistry Program (46 participating faculty members) which is composed of the Departments of MMICB and Biochemistry and Molecular Biology in the School of Medicine and the Department of Microbiology in the SIU College of Science. The program hosts approximately 90 master's and Ph.D. students of which 40 reside in the MMICB department. The Department occupies 28,000 sq. ft. in new and renovated laboratory space. The Department shares a 2500+ sq.ft. CDC certified BSL3 laboratory with the Illinois Department of Public Health. The Department is supported by excellent Core Research facilities.

We seek an accomplished scientist with a strong record of academic and administrative leadership. Special emphasis will be given to experience in both medical student and graduate education, the mentoring of junior faculty, and a sustained record of extramural research funding. The successful candidate will have an exciting vision for the future of the department's integrated research, education and training programs. Candidates who specialize in medical microbiology, immunology, or cell biology will be considered. Candidates whose research complements existing departmental strengths in cancer and cell biology will be of particular interest.

Candidates must possess a Ph.D. and/or an M.D. degree, and have academic credentials for a tenured appointment as Professor.

To apply, please send via e-mail, a letter of application or nomination, with curriculum vitae, statement of research interests and goals as Department Chair and the names of three references in a single PDF to:

Ross D. Silverman, J.D., M.P.H.
Chair, MMICB Search Committee
c/o pamitai@siumed.edu
Southern Illinois University
School of Medicine

Review of applications will begin on **May 15, 2012** and continue until the position is filled.

The Southern Illinois University School of Medicine is an Equal Opportunity, Affirmative Action Employer. Background investigation required.

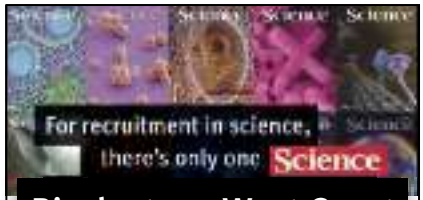

Bioclusters: West Coast

Special Career Feature: May 4
Reserve your ad by
April 17 to guarantee space.

Bioclusters engage their communities, raise local scientific awareness, and diversify regional economic opportunities. The Western U.S. is home to three such areas—San Francisco, San Diego, and Seattle—each with a different history, a unique personality, and a distinct area of focus. These cities all compete for the best scientific talent, and *Science*'s May 4 feature allows your company to stake its claim as a vital entity within these clusters while drawing the best scientific minds to your career opportunities.

700,000 scientists from around the world will read about the exciting careers on the West Coast. Whether you are recruiting or need to promote your company beyond U.S. borders, this issue offers your organization a unique chance to entice both active and passive job seekers worldwide. Make sure your company maximizes this recruitment and branding opportunity.

To book your ad:
E-mail: advertise@sciencecareers.org
Or telephone us:
US: 202-326-6582
Europe/RoW: +44 (0) 1223 326500
Japan: +81-6-6627-9250
China/Korea/Singapore/Taiwan/
Thailand: +86-1367-1015-294

ScienceCareers.org

Produced by the *Science*/AAAS
Custom Publishing Office

Where your leading-edge research becomes tomorrow's real-world results.

VISIT US AT AACR BOOTH 4603

What kind of difference can you make for the future?

At USA Mitchell Cancer Institute (MCI), you'll have the opportunity to stand at the forefront of cancer detection and screening. We are an expanding cancer research and treatment facility, combining a robust, interactive and entrepreneurial research environment with enhanced diagnostic, prognostic and prevention treatments to battle cancer on all fronts—from the "bench to bedside."

Please see our companion ad in this issue for more information on current opportunities.

UNIVERSITY OF SOUTH ALABAMA
MITCHELL CANCER INSTITUTE

1660 Springhill Avenue
Mobile, Alabama 36604
251-665-8000

www.usamci.com

Cancer Research

Overcoming Challenges

Renewed Focus on Cancer Vaccines

No longer treated as myth, the cancer vaccine field has materialized over the past decade. Researchers have overcome numerous challenges and more vaccines are poised to enter the market. The field is growing rapidly, which makes it an opportune time for graduate and postdoctoral fellows to enter it.
By Jacqueline Ruttimann Oberst

"So much exists that is unknown, and this fact represents a unique opportunity for investigators, especially young scientists, to find a foothold and make very important contributions."
—Philip Vernon

Until recently, **Olivera Finn** would come across articles or meeting sessions describing her field as "Fact or Fiction." "It used to drive me crazy," she says.

Finn, a chair of the Department of Immunology at the University of Pittsburgh, and others who work on cancer vaccines have finally seen their field vindicated. Three vaccines have been approved by the U.S. Food and Drug Administration and five U.S. phase III clinical trials are poised to report data by this year. Worldwide, over a dozen cancer vaccines have been approved.

Cancer vaccines as a field have been slow to emerge but have come into its own. Researchers have learned the reasons, scientific and regulatory, for many past failures and are poised to meet future challenges. Graduate and postdoctoral fellows who choose to enter this field are doing so when it is hitting its stride, allowing the possibility for a rewarding and potentially lucrative career.

FINDING THE PROVERBIAL NEEDLE IN A HAYSTACK: CANCER VACCINE HISTORY

Treating cancer has historically relied on a trifecta of treatments—surgery, chemotherapy, and radiation—known colloquially as "slash, poison, and burn."

Vaccines have a potential advantage over these three options in that the body's response is longer lasting (on a scale of years as opposed to weeks or months), which could possibly eradicate the micro-metastases that often linger after standard treatments end. Moreover, cancer vaccines have similar minor side effects to traditional vaccines: inflammation at the injection site and flu-like symptoms.

Some say that this method probably won't eradicate cancer altogether, but vaccines could enable physicians to manage it more like a chronic disease.

"I anticipate that we'll get to the point where if you do get cancer, then it will be more manageable or cured more easily," says **Christian Ottensmeier,** a medical oncologist and director of the Experimental Cancer Medicine Centre at the University of Southampton in the United Kingdom.

Opines **Eric von Hofe,** president and CEO of Antigen Express, a cancer vaccine biotechnology company: "We're not going to replace chemotherapy, radiation, and surgery, but in 5 to 10 years, vaccines will be much more an accepted part of clinical oncology."

Cancer vaccines require rethinking the term "vaccine." Most patients are familiar with vaccines given to healthy people to prevent bacterial or viral infections, such as diptheria and mumps. These traditional vaccines require using weakened or killed viruses, bacteria, or other germs to trigger an immune response in the body via activation of B cells and killer T cells. Although some cancer vaccines (e.g., Gardasil and Cervarix for cervical cancer) work in this fashion and are for prophylactic purposes, others are used as a therapeutic, to retrain the immune system to attack a disease that already exists (e.g., Provenge for prostate cancer). Therapeutic vaccines use cancer cells, parts of cells, or pure antigens—sometimes from the individual patient—in combination with other substances called adjuvants to further boost the immune response. Thus these vaccines all fall under the umbrella of immunotherapy.

The first foray into immunotherapy was in 1893, when William Coley, a New York surgeon, injected a cocktail of attenuated bacteria, *Streptococcus pyogenes* and *Serratia marcescens,* into sarcoma patients. Today, this approach is only used in superficial bladder cancers; live Bacillus Calmette-Guérin is injected after surgical resection.

Beginning in the 1970s, the discovery and refinement of techniques to create monoclonal antibodies, which can bind to a single target, has enabled the identification of cancer-specific cell-surface proteins or antigens. Whereas antigens detected by these antibodies offer a whole armamentarium for vaccine creation, most of them are also found in normal cells. This raises the risk of a patient's immune system turning on itself and creating autoimmunity. Yet all is not lost for this type of treatment: Cancer cells often express more of these antigens than normal cells, and the "friendly fire" or immune-induced injury of normal cells may be reversible. Furthermore, vaccines can elicit antibodies that do not act directly upon the tumor cells; some neutralize growth factors, cytokines, or the blood supply needed by cancer cells to inhibit the tumor's expansion and continued »

UPCOMING FEATURES

Bioclusters: Eastern United States—April 6
Bioclusters: Western United States—May 4
Biotech/Pharma: Navigating Mergers/Acquisitions—June 8

CREDITS: (FROM LEFT) ©ISTOCKPHOTO.COM/ AYDINMUTLU; LABORATORY OF MICHAEL T. LOTZE, UNIVERSITY OF PITTSBURGH CANCER INSTITUTE


CHINA RETURNEES
家
(HOME)
LET LIFE TAKE YOU THERE NOW.
A lot has happened since you've been away. Your mother turned 70. Your sister graduated from college. Your nephew took his first steps. Your China has transformed from a third world country to a world-class economy. And Life Technologies, the world's most innovative biotechnology company formed with the merger of Applied Biosystems and Invitrogen, is growing fast in China. So now there's no reason to keep missing out on the chance to be closer to your family and to be part of a team that makes science easier and life better everyday.
For more information, visit lifetechnologies.com/careers/cn.
life technologies™
Invitrogen™ Applied Biosystems® Gibco® Molecular Probes® Novex® TaqMan® Ambion® Ion Torrent™

Cancer Research

"The development of synthetic vaccines via genetic engineering over the last decade has [also] been a game-changer."
—Philip Arlen

others target the connective tissue or stroma between tumor cells. The discovery of cancer-testis antigens, whose expression is limited only to cancer cells and immune-protected sperm cells, has opened up new immunotherapy approaches that avoid healthy cells altogether.

The late 1980s and early 1990s ushered in better cell culturing techniques, allowing immune cells, such as killer T cells, to be retrieved from the patients and grown in the lab. In the 1990s and 2000s, the development of spontaneous mouse tumor models closed the loop from bench-to-cage-to-bedside. Instead of using xenographs or transplantable tumors in immunocompromised mice, researchers can now observe tumorigenesis in the context of an intact immune system. These improvements have facilitated better preclinical testing of cancer vaccines and their safety.

"The development of synthetic vaccines via genetic engineering over the last decade has [also] been a game-changer," says **Philip Arlen,** president and CEO of Neogenix Oncology, another prominent cancer immunotherapy company. "Previously vaccines came from the tumors themselves. Now we are using peptides and vectors and not introducing biologic material from the tumor itself to humans."

According to many in the field, it will take a village of researchers to help create these vaccines.

"This is a very active field of translational research requiring clinical investigators as well as scientists in both academia and biotech as it increasingly attracts big pharma attention," says von Hofe. "At the practical level, biomarker discovery, including gene profiling and the study of immunological parameters, are clearly areas in need of candidates with bioinformatics expertise, as well as a tumor immunology background, to help guide the discovery of second generation cancer immunotherapeutics."

Finn, whose students are part of an interdisciplinary graduate program at the University of Pittsburgh School of Medicine, admits that she's "shameless about convincing new students to choose immunology."

"We teach students the power of the immune system and how the immune system operates. One can't do anything nowadays that doesn't involve the immune system. It affects such ailments as obesity and stress," adds Finn, claiming that as a result, psychology, and bioengineering students have entered the immunology department to work in the cancer vaccine field.

Tumor biologists and immunologists are not the only experts that are required for this field.

"A whole slew of skills are needed," says Arlen. "There's the issue of discovery in which tumor biologists and immunologists contribute, but then there's sequencing of proteins or peptides for which molecular biologists are needed. Virologists and microbiologists can contribute to design of viral vectors, and those with regulatory and peptide synthesis skills are desired for production/manufacturing work." He adds that individuals with vivarium expertise are also in demand, as various animal models, such as mice, dogs, pigs, and monkeys, are needed for preclinical studies.

STICKING POINTS: CANCER VACCINE CHALLENGES

Over the years, numerous tumor immunotherapies have had "false starts," with early-stage successes but failing in phase III clinical trials. Many reasons account for these failures, including insufficient knowledge of the biology and inappropriate patient populations.

"The understanding of the immune system 30–35 years ago is archaic compared to what we know today," says Arlen. "We now have a much more comprehensive understanding of the checks and balances of how the immune system works—the subsets of cells, how they function, and how immunocompetency can be compromised or lead to autoimmunity when the immune system is not in check."

"Although immunologists are still needed, someone versed in regulatory affairs is also required," continues Arlen. "We'll need someone who can go through the IND process, understands the rationale for treating patients, and who has expertise in developing animal studies." Those who possibly fit the bill include physicians, nurses, and veterinarians.

According to Finn, the earlier clinical trials have taught cancer vaccine researchers two things: "One, there really is no window of opportunity; patients with cancer are already immunocompromised to varying degrees so they might not respond well to a vaccine. Second, we have learned more about the specifics of how a tumor changes the immune system. For example, too many regulatory T cells observed in many cancer patients will prevent an immune response to the vaccine, so we need to get rid of these. Likewise, if there are too many exhausted T cells, we need to help them by interrupting their negative signaling pathways."

This knowledge has spurred the vaccine field into a new industry: immunotherapeutic antibodies that prime the cancer patient's immune system so vaccines can work. One example is the emerging class of anti-inhibitory antibodies called checkpoint blockades, such as anti-CTLA-4 and anti-PD-1, which bypass the immune system's natural off switches, sustaining the cellular immune response long enough to make an impact on cancer. To aid in the construction of these antibodies, biochemists and researchers with expertise in X-ray crystallography are also highly desired.

Clinical trial designs also need revamping in the cancer vaccine field. With traditional drugs, clinical trials tend to include individuals whose cancer is at an advanced stage to prove efficacy. This is often because these patients are more willing to try the treatment. Essentially, they have nothing to lose, having already been treated with other agents that have failed. Moreover, companies have found that treating this population often results in positive effects showing up more quickly than in patients with either early-stage or fully-resected tumors.

However, Ottensmeier says, "cancer vaccines have forced clinical trial design to stand on its head" because clinical trials have indicated that vaccines will likely work best in patients with earlier-stage cancers or in those whose tumor burden has been reduced to the microscopic level by surgery or chemotherapy. continued »

Leading-edge opportunities in a real-world paradise.

Emerging and Established Faculty positions in oncologic sciences and interdisciplinary clinical oncology

The Opportunity: We seek outstanding, energetic, first-time faculty candidates to develop a successful independent basic/translational research program and established, well-funded faculty candidates to develop key programmatic basic/translational and/or clinical research programs aligned with the institutional mission. Successful candidates will receive generous and competitive start-up funding packages to grow and/or expand the individual's research program and the institution's research grant funding base. Candidates are expected to be highly interactive with existing research groups focused on cancer biology, metastasis, drug discovery, cancer stem cells, cancer metabolism, and biomarkers. An entrepreneurial spirit with a focus on translational outcomes is strongly encouraged.

State-of-the-art Facilities: USA Mitchell Cancer Institute provides a robust, interactive scientific environment with fully-equipped laboratories and access to core facilities including flow cytometry, tissue biobank, BL3 laboratory, genomics, laser microdissection, atomic absorption, high content screening and drug discovery, proteomics, metabolomics, advanced live cell imaging, and super-resolution and stochastic optical reconstruction microscopy.

Community Environment: Located in Mobile, Alabama, USA Mitchell Cancer Institute brings the best of the Gulf Coast to your doorstep. The area features many attractions, along with exciting outdoor adventures, fresh delicious seafood, Delta excursions, fascinating museums, twenty-one world-class golf courses, a thriving arts community, beautiful historic homes, and, of course, beautiful white sandy beaches. There's no place like the Mobile Bay area, the home of the original Mardi Gras!

Requirements: The successful candidate(s) must have a Ph.D., M.D., or M.D./Ph.D. degree, evidence of prior research accomplishments, a minimum of one to two years of postdoctoral training, and excellent interpersonal skills. Emerging faculty are expected to establish a high quality, independent basic/translational or clinical cancer research program having the potential for NIH level grant support within a 2-3 year period and to meet the criteria for appointment as a tenure-track Assistant Professor. Established faculty are expected to bring a well-funded and recognized program in basic/translational or clinical cancer research, exhibit strong leadership potential, and qualifications appropriate for tenured appointment as Associate or Full Professor.

Application Process: Applicants should send letter of interest and CV to Michael R. Boyd, M.D., Ph.D., 1660 Springhill Avenue, Mobile, Alabama 36604, or e-mail to sallen@usouthal.edu.

UNIVERSITY OF SOUTH ALABAMA
MITCHELL CANCER INSTITUTE
COMPREHENSIVE ONCOLOGY HEALTHCARE & RESEARCH

USA is an Affirmative Action and Equal Opportunity Employer.

Cancer Research

"After decades of using in vitro culture systems and animal models, it is fantastic to now have access to samples from patients that can provide us with truly informative answers. Our findings may indeed improve the treatment or even cure cancer patients one day."
—Angelica Cazaly

Finn's lab is testing early intervention in patients with premalignant lesions such as advanced colon polyps. Her group has seen that vaccinating patients who have had these polyps removed elicited a robust immune response never before seen in patients with colon cancer. She hopes that this strong immune response will prevent the polyps from either recurring or reverting to colon cancer.

MAGIC BULLET OR NOT?

Most researchers in the cancer vaccine field believe that because cancers are ever-changing in their nature, adopting a one-size-fits-all approach for cancer vaccines is not likely.

"The future is in two directions: vaccines as one more addition to a very complex and comprehensive therapy for cancer patients, or alone as prophylaxis," predicts Finn.

Combining vaccines with chemotherapy might prove to be a formidable match.

"There's a long-held belief that any chemotherapy has a negative impact on the immune system. However, low-dose chemotherapies actually release antigens that trigger cancer-specific immune responses and can give a whole new set of markers to monitor," says **Jill O'Donnell-Tormey,** CEO and director of scientific affairs at the Cancer Research Institute, a non-profit organization dedicated to advancing the field of cancer immunology. She adds that there is a need to optimize cancer vaccines (i.e., dosing, timing, alone or in combination, and the identification of prognostic and diagnostic biomarkers that can be modulated by cancer vaccines)—as such, epidemiologists and those studying public health are in high demand in the field.

Arlen points out that the chemotherapy agents may change their spots: Many of the drugs used to damage cancer cells, once thought to be immunosuppressive, appear to have unexpected beneficial effects on the immune system. "When used at a proper dose, [chemotherapy] can reduce or lower regulatory T cells that block tumor response, making the tumor more susceptible to the immune responses generated by cancer vaccines," he says.

WHY GO INTO THIS FIELD?

For Ottensmeier, a medical oncologist and immunologist, this field has the best of all worlds.

"It's an interplay of learning in a lab, testing in people, and going back to the lab," he says. And because patients understand the general concept of vaccines, they also get excited to see their lab results and whether their bodies are fighting the cancer, he adds.

His postdoctoral fellow, **Angelica Cazaly,** agrees: "After decades of using in vitro culture systems and animal models, it is fantastic to now have access to samples from patients that can provide us with truly informative answers. Our findings may indeed improve the treatment or even cure cancer patients one day."

The field is also not a fait accompli, yielding more opportunities for students to contribute.

"It's a great field to enter because of how much we still have to learn about how the immune response to tumors is initiated, the complex interplay of molecules and cells that render it effective, and how it can contract appropriately. Knowledge of all these processes increases the opportunity for therapeutic intervention," says **Adam Farkas,** Finn's graduate student.

Laboratories that focus on cancer vaccines are becoming abundant at university cancer centers and at government facilities such as the National Cancer Institute (NCI) and the National Institutes of Health. There are also positions in the cancer vaccine field for M.D.s. Many U.S. medical oncology training programs provide physicians with either training in the laboratory or developing clinical trials and treating patients with experimental cancer vaccines. Furthermore, now that the industry is focusing on developing these therapies, basic research laboratories in both pharmaceutical and biotechnology companies provide a basis for additional training in this cutting-edge oncology field.

"So much exists that is unknown, and this fact represents a unique opportunity for investigators, especially young scientists, to find a foothold and make very important contributions," says **Philip Vernon,** another graduate student in Finn's NCI-sponsored training program. "This reality allows scientists to pursue their own ideas because of the relative paucity of established 'dogma.'"

This latitude of scientific exploration, as well as preliminary positive results has steered the field, according to Arlen, from "'this is really voodoo' to now being validated and approved."

FEATURED PARTICIPANTS

Featured Participants

Antigen Express
www.antigenexpress.com

Cancer Research Institute
www.cancerresearch.org

National Cancer Institute
www.cancer.gov

Neogenix Oncology
www.neogenix.com

University of Pittsburgh
www.pitt.edu

University of Southampton
www.southampton.ac.uk/medicine

Additional Resources

American Cancer Society
www.cancer.org

Cancer Research UK
info.cancerresearchuk.org

Cancer Immunity
www.cancerimmunity.org

NIHR Experimental Cancer Medicine Centres, UK
www.ecmcnetwork.org.uk

CVAX: The Cancer Vaccine Magazine
www.cvax.org

Jacqueline Ruttimann Oberst is a freelance writer living in Chevy Chase, Maryland.

DOI: 10.1126/science.opms.r1200116

MAYO CLINIC

Research Scientist position in the Division of Hematology Thrombosis, Hemostasis or Vascular Biology with focus on Thrombosis

Heal the sick, advance the science, share the knowledge.

The Division of Hematology in the Mayo Clinic Department of Internal Medicine is seeking a Research Scientist in the field of Thrombosis, Hemostasis or Vascular Biology. A research focus on Hemostasis and Thrombosis is preferred. The successful candidate should be an established investigator with national recognition and current NIH (or similar) grant funding. Candidates must have a PhD, MD/PhD, MD or DVM degree and rank of at least assistant professor.

Recognized by *U.S. News and World Report* as one of America's Best Hospitals, Mayo Clinic is an excellent choice for the candidate who is seeking to join and partner with a highly successful group of research scientists. Mayo Clinic has over 200 biomedical research laboratories, institutionally supported state-of-the-art facilities and diverse clinical patient populations providing opportunities to readily translate discovery to the bedside. In addition to colleagues in Hematology and Biochemistry, candidates will have the opportunity to collaborate with scientists and clinicians in the Mayo Clinic Cancer Center, the Mayo Clinic Thrombophilia Center, the Mayo Clinic Hemophilia Treatment Center, the Kogod Center on Aging, the Center for Regenerative Medicine, the Divisions of Cardiovascular Diseases and Hematopathology, and the Department of Oncology – all world-renowned for achievements and innovation. We offer a compensation package that includes a highly competitive start-up, sustained intramural funding, outstanding laboratory facilities and capital equipment funding, as well as exceptional benefits.

Mayo Clinic in Rochester combines the comfort of small city living with easy access to additional cultural and entertainment opportunities in nearby Minneapolis/St. Paul and has been recognized by *FORTUNE* magazine as one of the "100 Best Companies to Work For."

Interested candidates are invited to learn more about this position, Mayo Clinic and Rochester at **www.mayoclinic.org/scientist-jobs/** and reference job posting **9617BR**. Applications should include a letter of interest and curriculum vitae. Specific questions related to the posting should be directed to:

John A. Heit, M.D., Professor of Medicine
Division of Cardiovascular Diseases
Mayo Clinic
200 First Street SW • Rochester, MN 55905
E-mail: heit.john@mayo.edu

Mayo Foundation is an affirmative action and equal opportunity educator and employer. Post-offer/pre-employment drug screening is required.

MEDICAL COLLEGE OF WISCONSIN CANCER CENTER

Tenure Track Assistant and Associate Professor Positions in Cancer Cell Biology

The Medical College of Wisconsin (MCW) Cancer Center invites applications for tenure-track positions at the Assistant or Associate Professor level. The successful applicant will be expected to develop a program aligned with major ongoing research efforts in Cancer Cell Biology at the MCW Cancer Center. We encourage applications from junior and mid-level investigators with expertise in the following areas relevant to cancer:

Cell Signaling
Redox Mechanisms and Metabolism
Mitochondria and Bioenergetics
Epigenetics
Genomic Instability
Chemokines and Inflammatory Mediators

The candidate is expected to establish a vigorous and extramurally funded research program, and participate in collaborative and interdisciplinary projects. Teaching at the graduate level is also expected. Applicants must have a doctoral degree in a relevant area, a minimum of two years of post-doctoral experience, and a strong record of research accomplishments.

The MCW Cancer Center is an integrated partnership of more than 200 cancer research scientists and physicians at the Medical College of Wisconsin, Froedtert Hospital, Children's Hospital of Wisconsin, Clement Zablocki VA Medical Center, and the BloodCenter of Wisconsin. The MCW Cancer Center occupies 30,000 sq. ft. with newly completed space dedicated to cancer-related basic science research on the MCW campus, and an additional 50,000 sq. ft. of space adjacent to Froedtert Hospital in the MCW medical complex.

Candidates should send by e-mail (**kedwards@mcw.edu**) a complete curriculum vitae, bibliography, statement of research interests, and names of at least three references to: **Kate Edwards, Cancer Cell Biology Search, Medical College of Wisconsin Cancer Center, 8701 Watertown Plank Road, Milwaukee, WI 53226.**

NYU Langone MEDICAL CENTER

Faculty Position

- Leon H. Charney Division of Cardiology -
http://medicine.med.nyu.edu/cardiology/

- Kimmel Center for Stem Cell Biology -
www.kimmelstem.med.nyu.edu

The Leon H. Charney Division of Cardiology and the Helen L. and Martin S. Kimmel Center for Stem Cell Biology at NYU Langone Medical Center invite applications for tenure-track positions at the assistant, associate or full professor level for a leadership position in a new program in Cardiovascular Regenerative Medicine. We seek applicants with an exceptional record of achievement in any area of stem cell biology and regenerative medicine to facilitate the translation of stem cell discovery related to cardiovascular disease - building on fundamental laboratory investigations to clinical evaluation and application. The Leon H. Charney Division of Cardiology and the Kimmel Center for Stem Cell Biology are highly interdisciplinary, and combine research strengths and clinical trial expertise at the NYU Langone Medical Center and the College of Arts and Sciences.

The NYU Langone Medical Center offers excellent resources to support new faculty, including generous start-up packages and core facilities for siRNA screening, cell sorting, imaging, proteomics, mouse molecular genetics, genomics and structural biology. Successful candidates are expected to maintain vigorous independent research programs that will enrich and be enriched by the highly collaborative environment throughout the NYU research community.

This is an electronic application process only. Please create your application packet by formatting it as a single PDF document. Use the following page order: 1) Cover Letter; 2) Curriculum Vitae; 3) Research Statement, highlighting the most significant research accomplishments and the relevant publications. Email the application packet to **stemcellsearch@med.nyu.edu** by April 30, 2012. Three letters of reference should be sent independently to the same email address. NYU Langone Medical Center was founded in 1841 and is an equal opportunity affirmative action employer. Women and minority candidates are encouraged to apply.

FOCUS ON CANCER RESEARCH

Weill Cornell Medical College in Qatar

TYPE 2 DIABETES SENIOR INVESTIGATOR

BIOMEDICAL RESEARCH PROGRAM **FACULTY POSITION**

Weill Cornell Medical College in Qatar (WCMC-Q), a branch of Weill Medical College of Cornell University, seeks a Type 2 Diabetes Senior Investigator to join its biomedical research program.

WCMC-Q is presently in its 10th year of operations and continues to pursue excellence in education, research, and clinical care. In a pioneering international initiative, the WCMC-Q research program was established in partnership with the Qatar Foundation for Education, Science and Community Development to address the most pressing health challenges in Qatar and the region by employing an integrated basic, translational and clinical approach.

WCMC-Q seeks a highly qualified candidate at the associate or full-professor level with an established research program in the cellular/molecular basis of Type 2 Diabetes. The successful candidate will have a stellar track record of research accomplishments and an enthusiasm for building new research initiatives. Candidates must have an MD and/or PhD degree and must be willing to relocate to Doha, which is rapidly growing as a research hub. The level of appointment will be commensurate with credentials and experience. A comprehensive and highly competitive salary and foreign service benefits package and a competitive start-up package will be provided.

The WCMC-Q research program offers a collaborative, multidisciplinary team environment, endowed with a comprehensive support infrastructure. The successful applicant will be able to draw on state-of-the-art facilities, including genomics, proteomics, imaging, and computational and biostatistics cores. Details regarding the WCMC-Q research program and facilities can be accessed at **http://qatar-weill.cornell.edu/research/index.html**.

Qualified applicants are invited to submit a letter of application, which should outline their interest in the position and a description of research interests and future research plans (3-5 pages), along with their curriculum vitae to:

http://job.qatar-med.cornell.edu

Applications may be submitted until June 30, 2012. Please note that, due to the high volume of applications, only short-listed candidates will be contacted.

Cornell University is an equal opportunity, affirmative action educator and employer.

Weill Cornell Medical College in Qatar

CENTER FOR LIFE SCIENCES

Faculty and Postdoctoral Positions at Center for Life Sciences

Applications are invited for Principal Investigator (PI) and Postdoctoral positions at Center for Life Sciences (**http://www.cls.edu.cn/english/**).

As a pilot program of the National Plan for Education Development and Reform, Center for Life Sciences aims to combine excellence in research and education. We are recruiting scientists with the best potential to carry out creative research of long-term significance in the life sciences. Positions are open at all ranks from Assistant, Associate, Full Investigatorship, to Postdoctoral positions.

The Center of Life Sciences, Peking University side is looking for the best researchers in life sciences regardless of specific areas of research, although our relative emphasis will be in bioinformatics, cancer researches, epigenetics, cell biology, chemical biology, computational biology, human genetics, genetics, genomics, molecular medicine, molecular neuroscience and cognitive neuroscience, modern imaging, physiology, plant biology, synthetic biology, and systems biology.

Each PI holds a joint appointment in one of the departments or schools at Peking University (such as Chemistry, Computer science, Engineering, Life Sciences, Mathematics, Medical School, Physics and Psychology) where the PI will hold a tenure track or tenured position. **Contact person for PI positions: Ms. Fangmin Li (gsmkyb@pku.edu.cn) For Postdoc positions: Ms. Siyuan Gong(clsbsh@ctb.pku.edu.cn)**

Each PI holds a joint appointment in one of the departments or schools at Tsinghua University, including but not limited to Chemistry, Computer Science, Information Technology, Life Sciences, Mathematics, Medicine, Physics, Psychology, Public Health and all engineering departments/ schools, where the PI will hold a tenure-track or tenured position.

In Tsinghua University, scholarship is our top consideration regardless of specific areas of research, although some emphasis will be given to systems biology, developmental biology, cancer research, cellular biochemistry, computational and system neuroscience, microbiology and virology, immunology, plant molecular biology, and all inter-disciplinary research areas that engage life sciences. **Contact person for PI positions: Ms. Jiang Yi (yijiang@biomed.tsinghua.edu.cn) For Postdoc positions: Ms. Hong Zhang (zhanghong@biomed.tsinghua.edu.cn)**

Center of Life Sciences offers a stimulating and interdisciplinary research environment, outstanding core research facilities, and internationally competitive packages for both PI and postdoctoral researchers. Award-winning kindergartens and exceptional elementary schools will be available to the children of all PIs and postdocs. Applications from both Chinese and non-Chinese nationals will be evaluated on an equal opportunity basis.

Please send your application materials (a cover letter, a CV, a brief summary of past research accomplishments, and a brief description of your future research plan) in a single PDF file to the contact person. For postdoc applicants, please indicate in your cover letter 1 or 2 laboratories as your intended host. The research areas of all PIs can be found at **http://www.cls.edu.cn/english/PrincipalInvestigator/**.

HM Government

Government Chief Scientific Adviser

The Government Chief Scientific Adviser (GCSA) is the principal source of guidance and counsel to the Prime Minister and wider government on science. S/he provides clear and authoritative analysis of some of the most important challenges the country faces. The GCSA must comment on a very wide range of scientific matters. In addition, it is also the role of the GCSA to articulate measured and comprehensible messages to the general public, often in times of crisis.

As Head of Profession, the GCSA is responsible for the management and leadership of the Government Office for Science and for leading the science and engineering profession within the whole Civil Service. The GCSA reports to the Cabinet Secretary.

Candidates for the role will be eminent scientists with a strong track record of research in their chosen discipline. They will also bring recognition and a professional network beyond their own area of specialisation. This breadth of scientific understanding will be complemented by experience in the communication of science to the public and of working with internal and external stakeholders. Familiarity and ease in working with the media will be crucial in helping to inform national opinion.

The Cabinet Office has retained Russell Reynolds Associates to assist with this appointment.

For further information on the position, additional details on qualifications, requirements, terms and conditions of service and application instructions, please visit: **www.rrapublicsector.com**

The closing date for applications is 23rd April 2012.

RUSSELL REYNOLDS ASSOCIATES

University of Nebraska Lincoln

Professor and Chair Department of Statistics

The University of Nebraska-Lincoln invites applications for the position of Professor and Chair, Department of Statistics. This is a full-time, 12-month appointment responsible for the academic leadership of the research, teaching and service activities in the Department of Statistics as well as for the professional development of the faculty and staff. In this position, you will have a primary focus on the continued development of the Department as an internationally recognized program in statistics along with the opportunity and expectation for developing a high level, internationally recognized campus-wide bioinformatics and computational biology initiative. The Department Chair reports to the Dean of the College of Arts and Sciences (CAS), and deans of the College of Agricultural Sciences and Natural Resources (CASNR) and the Agricultural Research Division (ARD) within the Institute of Agriculture and Natural Resources (IANR) on matters related to the department.

To succeed in this role, you will need an earned doctoral degree in Statistics or closely related field; must meet qualifications for appointment as a tenured professor; and have a record of excellent interpersonal, organizational, and leadership skills. Previous administrative experience is preferred.

If this sounds like the job for you, please access the web site **http://employment.unl.edu**. Search for **requisition number 120174**. Complete the faculty academic administrative information form. Attach a letter of application, curriculum vitae, and contact information for three professional references.

Review of applications will begin **May 15, 2012**, and will continue until the position is filled or the search is closed.

The University of Nebraska has an active National Science Foundation ADVANCE gender equity program, and is committed to a pluralistic campus community through affirmative action, equal opportunity, and dual careers.

NANJING UNIVERSITY

NBRI

Nanjing Biomedical Research Institute of Nanjing University

南京大学—模式动物生物医学研究院

Full-time Associate Professor or Full Professor

The Model Animal Research Center (MARC) of Nanjing University invites applications for full-time faculty positions, at academic ranks of Associate or Full Professor. Individuals with demonstrated accomplishments in, but not limited to, the following areas are encouraged to apply – neurobiology, immunology, development biology, metabolic disease and cancer biology. Highly competitive research support will be provided in an interactive and nurturing environment. Individuals will have an opportunity to establish a state-of-the-art independent research program in newly renovated space and to interact with a strong group of affiliated scientists. For more information and to apply visit website: **http://www.nicemice.cn/.**

Our institute's research interests emphasize on programs in the studies on human diseases using different model animal systems such as mouse, zebrafish, fruit fly, and nematode worm. Now MARC has established an excellent platform for functional analysis of transgenic and knockout mice, with AAALAC accredited SPF animal facility with more than 50,000 mouse cages. Interested individuals, regardless of their nationalities, should submit a detailed letter of interest, curriculum vitae, PDFs of three of their best publications, and three letters of recommendation to: **Ruimin Zhu, HR supervisor of Model Animal Research Center, Nanjing University, 12 Xuefu Road, Nanjing, Jiangsu 210061**, China or preferably electronically to **syyxzrm@sina.com or zhurm@nicemice.cn**. The positions are available immediately. Applications will be evaluated by faculty search committee upon receipt until the positions are filled.

KOREA UNIVERSITY

Faculty Openings

Korea University, in Seoul, South Korea, seeks candidates to join the faculty in the fall semester of 2012 beginning September 1. We are recruiting enthusiastic, well-trained scholars who wish to refine their teaching experience and research in this part of the world. Korea University, founded in 1905, is ranked one of the top universities in Korea by major global assessment reports. The positions available for the candidates are assistant, associate, or full professors (a two or three year tenure track appointment, OR non-tenure track appointment). All candidates are expected to have ample university-level teaching experience, a strong commitment to excellence in scholarship, and dedication to teaching and research in their fields.

[Education Requirement] - Ph.D. at the Time of Application

[Online Application] - How to apply : http://kuweb.korea.ac.kr/faculty
- Application Deadline : April 25, 2012

[Point of Contact] - Phone : +82-2-3290-1072
- Fax : +82-2-929-9164
- E-mail : faculty@korea.ac.kr

KOREA UNIVERSITY

Assistant/Associate Professor of Plant Breeding & Genetics (Tenure Track)

Molecular Breeding & Genetics for Nutritional Quality – Research 60%; Teaching 40%

Dept. of Plant Breeding & Genetics - NY State College of Agriculture & Life Sciences - Cornell University - Ithaca, NY

Great universities depend on the **talents** of great people

Cornell University fosters the pursuit of knowledge and inspires excellence. Join our global community that teaches tomorrow's thought leaders to think otherwise.

Responsibilities: Advances in biochemistry, metabolomics, and metabolic engineering, and the availability of genomic sequences for food crop species are opening new and valuable research opportunities for plant breeding. This molecular breeding position will have responsibility for conducting innovative research exploring genetic/epigenetic/quantitative variation in plants and the association with phenotypic variation in traits relating to human and animal health and nutrition made accessible by the latest technologies. These efforts could be applied to traditional or specialty crops chosen specifically for their unique attributes. The range of possible outcomes would span foods with new nutritional and health-promoting functions or bioavailability, to the chemistry of flavors and texture to new bioactive food components. Because this is part of a cluster hire, preference will be given to candidates interested in forming collaborations with other faculty with complementary expertise in nutritional sciences, food science, and animal science, among others. Appointee will be expected to develop an externally funded research program; release novel lines, germplasm or genetic stocks; supervise graduate students; teach courses at both the undergraduate and graduate levels related to plant breeding, plant genetics and genomics; and contribute to specialized courses, seminars, and team-taught courses, as well as to graduate training in plant breeding/plant genetics/genomics/plant molecular biology. We are seeking highly motivated individuals with strong research and teaching credentials. Strength in quantitative genetics/statistics is highly desirable. This position will have a 60:40 research and teaching responsibility. For more information visit our web site **http://plbrgen.cals.cornell.edu**.

Qualifications:

- Ph.D. in plant breeding, plant genetics/genomics, or plant molecular biology
- Experience in teaching, student advising, and research related to this position, either post-doctoral or pre-doctoral
- Evidence of ability to work with other researchers in interdisciplinary inquiry
- Evidence of ability to attract extramural support and lead an innovative research/breeding program
- Postdoctoral and/or other relevant experience desirable

Salary: Competitive and commensurate with background and experience. An attractive fringe benefits package is available.

Applications: Candidates are requested to submit a letter of application; detailed resume; a personal statement of research and teaching experience, leadership efforts, and contribution to diversity; copies of university transcripts; copies of one or two publications; and names and contact information for three references combined into a single file in pdf format. Send by e-mail to **Ms. Michelle Steigerwald (md464@cornell.edu) or by mail to Department of Plant Breeding and Genetics, 240 Emerson Hall, Cornell University, Ithaca, NY 14853.** Applications are reviewed as received and will continue until a suitable applicant is identified. Inquiries may be sent to Mark Sorrells, 240 Emerson Hall, Cornell University, Ithaca, NY.

Find us online at http://hr.cornell.edu/jobs or Facebook.com/CornellCareers

Cornell University is an Affirmative Action Equal Opportunity Employer and Educator

MRC Laboratory of Molecular Biology

Cambridge, UK

Programme Leaders in Neurobiology

Coinciding with the move of the MRC Laboratory of Molecular Biology (LMB) into a new state-of-the-art research building in October 2012 (http://www2.mrc-lmb.cam.ac.uk/about-lmb/new-building), the Division of Neurobiology wishes to recruit talented scientists interested in developing an independent programme of research. We are particularly interested in individuals working on the function of neural circuits using electrophysiological or imaging techniques, and we envisage that such work would make use of organisms open to genetic manipulation. Current interests in the Division include visual and olfactory processing, circadian rhythms, mechanisms of synaptic transmission and protein misfolding in relation to neurodegenerative diseases (www2.mrc-lmb.cam.ac.uk/NB/). Scientific excellence and potential for major impact are paramount. Synergy with existing research programmes would be an advantage.

The LMB provides an excellent environment for hands-on research. Core-funding by the Medical Research Council provides long-term support for ambitious projects, while administrative duties are minimal and no teaching is required. Interactions across the four Divisions of the Laboratory are encouraged. There is extensive central support, including electronic and instrumentation workshops, imaging and transgenic mouse facilities. The University of Cambridge and affiliated institutions form a vibrant Neuroscience community (http://www.neuroscience.cam.ac.uk/).

Candidates should have a PhD and/or MD and will have completed a period of postdoctoral training or equivalent, with an excellent track record, and show outstanding potential for independent research. You will lead a small team and substantial funding will be available.

These appointments will be made at either Programme Leader or Programme Leader-track level, depending on achievements and experience. Candidates for Programme Leader positions should have a strong international track record of relevant independent research and a proven ability to lead a research team, pursuing original approaches to long-term research goals. Programme Leader-track appointments will be made for those who demonstrate the potential to develop into Programme Leaders within six years. Candidates with appropriate levels of experience may be given responsibility for oversight of core scientific activities within the LMB. Salaries are competitive (Programme Leader-track £35,935 - £48,000 per annum; Programme Leader £45,213 - £70,000 per annum).

These positions will remain open until they are filled; applications received by 6th April 2012 will be given priority.

Informal enquiries can be addressed to Michel Goedert (mg@mrc-lmb.cam.ac.uk).

Applications should include a covering letter and full CV, an outline of current research interests (1 page) and a proposal for future research (up to 2 pages), along with the names and addresses of three professional referees who have agreed to be contacted prior to interview. Applications for this post must be made online at https://ext.ssc.rcuk.ac.uk inputting the reference IRC47968. If you do not have access to the internet, or experience technical difficulties, please contact 01793 867003.

This position is subject to pre-employment screening.

For further information about the MRC visit www.mrc.ac.uk
The Medical Research Council is an Equal Opportunities Employer

POSITIONS OPEN

PHARMACEUTICAL SCIENCES FACULTY POSITION
The University of Tennessee College of Pharmacy

The Department of Pharmaceutical Sciences in the College of Pharmacy at the University of Tennessee Health Science Center in Memphis, Tennessee, is seeking applications for a 12-month full-time, tenure-track faculty position at the **FULL, ASSOCIATE,** or **ASSISTANT PROFESSOR** level that is state supported. The successful candidate is expected to devote greater than a 60% effort to research. The applicant should have core expertise in medicinal chemistry, pharmacology, pharmaceutics, chemical biology, biomedical engineering, structural biology, or a related discipline focused on drug discovery and development. Candidates with a well-funded program in cancer, diabetes, antibiotics, drug delivery, nano-medicine, nano-technology, bio-imaging, or lipid research are highly encouraged to apply. The successful candidate is expected to have a Ph.D. or equivalent degree, the ability to acquire sustained external, investigator-initiated funding, including National Institutes of Health principal investigator funding, a commitment to excellence in teaching, and excellent oral and written communication skills. Applications will be processed until the position is filled. Please submit curriculum vitae, summary of research interests, contact information, and three letters of reference to: **Isaac Donkor, Ph.D. Professor and Vice Chair, Chair of Faculty Search Committee, Department of Pharmaceutical Sciences, 847 Monroe Ave, Suite 327, Memphis, TN 38163.** The University of Tennessee Health Science Center is located in Memphis, TN, an economically vibrant center, with a metropolitan population of more than 1.3 million, reflecting the richness along the bluffs of the mighty Mississippi River. The College of Pharmacy is located in a new, 187,000 square-foot building on the Health Science Center complex.

The University of Tennessee Health Science Center is an Equal Opportunity/Affirmative Action Employer.

POSTDOCTORAL FELLOW POSITION
The Center for Research Excellence in Bioactive Food Components
University of North Carolina at Greensboro

Responsibilities: This position will perform NIH-funded research projects with a research area of alcoholic liver disease. The research projects aim at understanding the pathogenesis of alcohol-induced liver damage, and exploring preventive and/or therapeutic interventions. This position is also responsible for data analysis, presentation of research findings at national/international meetings, and preparation of manuscripts for publication.

Qualifications: The minimum qualifications for this position include a Ph.D. degree in the field of biomedicine with 0–3 years of post-degree research experience; (2) well trained with advanced laboratory techniques in biochemistry, molecular biology and pathology; and (3) ability of research design, laboratory analysis and data interpretation. In addition, previous experience with animal and cell culture studies on intestinal barrier and alcoholic liver disease and strong records in scientific publications are required.

Salary: Fair market salary.

Contact: Please send a letter of interest, curriculum vitae, and a list of three references electronically to **e-mail: z_zhou@uncg.edu** (**Zhanxiang Zhou,** Ph.D.).

POSTDOCTORAL POSITION
Germline Stem Cells

Studies include culture, differentiation, and gene activity of male germline stem cells. See *Science* **316:**404, 2007 & *PNAS* **106:**21672, 2009. Send curriculum vitae, names of three references, and a letter describing research experience to: **R. L. Brinster, School of Veterinary Medicine, University of Pennsylvania. E-mail: cpope@vet.upenn.edu.**